ROMA TRE
UNIVERSITÀ DEGLI STUDI

SCUOLA DOTTORALE IN GEOLOGIA DELL'AMBIENTE E DELLE RISORSE (SDIGAR)
SEZIONE GEOLOGIA DELLE RISORSE NATURALI

XXVI CICLO

A crystal-chemical study of cordierite, synthesis and stability at variable H_2O and CO_2 concentration: geological and technological applications

Dottorando:
Francesco Radica

firma

Tutor:
Prof. Giancarlo Della Ventura

firma

Coordinatore:
Prof. Claudio Faccenna

firma

UNIVERSITA' DEGLI STUDI "ROMA TRE"

SCUOLA DOTTORALE IN GEOLOGIA DELL'AMBIENTE E DELLE RISORSE

(SDIGAR)

SEZIONE GEOLOGIA DELLE RISORSE NATURALI

- XXVI CICLO-

A crystal-chemical study of cordierite, synthesis and stability at variable H_2O and CO_2 concentration: geological and technological applications

PhD Candidate

Francesco Radica

Advisor: **Prof. Giancarlo Della Ventura**

Co-advisors : **Dr. Fabio Bellatreccia**

Dr. Carmela Freda

Thesis reviewers: **Dr. Gianluca Iezzi** and **Dr. Jannick Ingrin**

Defense committee: **Prof. G. Diego Gatta**, **Dr. Roberto Sulpizio** and **Dr. Luca Aldega**

Head of the Doctoral School: **Prof. Claudio Faccenna**

A.A. 2014/2015

AI MIEI NONNI

"Though we cannot SEE angles, we can INFER them, and this with great precision. Our sense of touch, stimulated by necessity, and developed by long training, enables us to distinguish angles far more accurately than your sense of sight, when unaided by a rule or measure of angles."

—Edwin Abbott Abbott, Flatland: A Romance of Many Dimensions—

Table of contents

ACKNOWLEDGMENTS

This project couldn't have been accomplished without the help of many precious people that have accompanied me through these years of work and amusement.

First and foremost, I want to express all my gratitude to my supervisor Prof. Giancarlo Della Ventura who guided and supported me during these years, in particular during the last year for helping me with my terrible English and trying to decipher my thoughts and express them in the text.

My sincere gratitude goes to my co-supervisors for their precious help: Fabio Bellatreccia for his advices and for fulfilling my continuous doubts and solving my problems with great patience, and to Carmela Freda for introducing me to the world of experimental petrology.

A special thanks goes to Matteo Masotta, who transferred me all the secrets of the QuickPress, for the great time spent inside and outside the INGV laboratory and for being a good friend.

I'm deeply indebted to all people that supported me during the experiments and the analysis at INGV: Piergiorgio Scarlato, Valeria Misiti, Silvio Mollo, Andrea Cavallo, Elisabetta del Bello, Serena Granati and all people gravitating or passing by the HP-HT laboratory for helping me out with advices and joyful company.

Sincere thanks are due to several people I met at INFN-LNF: Claudio Marcelli, Mariangela Cestelli Guidi, Antonio, Agostino, Diego Sali, for solving all problems I had with the FTIR spectrometer …and the OPUS software.

A special thanks goes to Dr. Gianfelice Cinque and all people at Diamond Light Source for their help with the synchrotron-beam work.

Heartfelt regards are due to Prof. Harald Behrens for his willingness to hosting me in Hannover, and to all people I met during my stay in Germany: Sara, Juan Carlos, Simone, Gabriele, Paola and so on.

Thanks to Dr. Mikey Gunter (Moscow, Idaho) transmitted me the secrets and the beauty of optical mineralogy and in particular of the use of the spindle stage to orient the crystals for

FTIR polarized-light measurements; most of this thesis would have been impossible without this elegant, unfortunately almost lost, technique.

I'm very grateful to Prof. Simon Harley (University of Edinburgh) for the SIMS data, Prof. Frank Hawthorne (University of Manitoba, Winnipeg) for the LA-ICP-MS analysis, Giuseppe Chita (IC-CNR, Bari) and Francesco Capitelli (CNR, Roma) for X-ray data collection, Dr. Luca Tortora (Roma Tre University) for the TOF-SIMS maps, Vincenzo Mangione (Roma Tre University) for the help with the optical profilometer and Massimo Piccinini (Porto Conte Ricerche, Alghero) for the Raman spectra.

Thanks to Mr. R. Pagano and Dr M. D. Welch (Natural History Museum, London) for providing some of the studied cordierite samples, while Dr. B. Rondeau (Nantes) and Dr. J.J. Chiappero (Museum National d'Histoire Naturelle, Paris) gently provided the beautiful and hystorical emeralds which have been used for the experiments.

A very special thanks goes to Dr. Gianluca Iezzi (Università G. D'Annunzio, Chieti), Dr. Jannick Ingrin (Univerité Lille 1, Lille) and Prof. Charles Geiger (University of Salzburg, Salzburg) for their careful revision of a preliminary draft of my Thesis and for their precious suggestions.

Thanks to all people I met during these years of travelling and conferencing, especially to Ruggero, hope to see you soon.

Un grandissimo ringraziamento va ai miei vecchi e nuovi colleghi/amici che mi hanno accompagnato e mi hanno dato forza in questi anni, in special modo Stefano (preparati per agosto!), Umberto, Fabietto, Lidia, una serie infinita di Gabriele, Marco e Andrea, Ines, Ileana, Giorgia, Silvia, Roberta, Chiara, Alessandro, Riccardo, Martina e Francesco. Se ho dimenticato qualcuno sono una pessima persona.

Un grazie di cuore va ai miei genitori, a mio fratello e specialmente ai miei nonni che sono venuti a mancare in questi anni, grazie per l'amore che mi donate quotidianamente in terra e dal Cielo.

Ovviamente un ringraziamento speciale va ai miei amici storici e recenti, non mi dilungherò nei nomi - sarebbero troppi e, per come sto combinato adesso, sicuramente dimenticherei qualcuno - vi basti sapere che il vostro nome è nascosto dietro questi quadratini □□□□□□□□□□□□□.

…ad maiora!

ABSTRACT

Cordierite is a relatively widespread mineral, having a peculiar ability to trap H_2O and CO_2 up to very high pressure and temperature. This is a unique property for a rock forming silicate, and has a significant role in the mineralogical equilibria in *HT* and *UHT* metamorphism (Harley and Thompson, 2004). In this work, great attention was paid to the study of the diffusion mechanisms of carbon dioxide inside these channel-like structures. Considering that carbon dioxide is probably one of the major responsible for long-term climate change on Earth (IPCC, 2005), the ability of these minerals to entrap CO_2 could provide insights for future research for the permanent CO_2 storage in minerals.

The aim of this Thesis was to investigate the diffusion of CO_2 across cordierite, and address possible implications from both a geological and a technological point of view. The work was completed by the parallel study of beryl, which is structurally correlated to cordierite.

The text is divided into four major sections:

1) In the first section (**Chapter 1 and 2**) I introduce the issues related to the qualitative and quantitative analysis of H_2O and CO_2 in cordierite by means of Fourier-Transform Infrared Spectroscopy (hereafter FTIR). In detail I show the crystal-chemical and spectroscopic study of chemically different samples, from an almost Mg-cordierite end-member to its Fe-analogue sekaninaite. Additionally I will discuss the calibration of the molar absorption coefficient ε, an indispensable coefficient for quantitative measurement in FTIR micro-spectroscopy. Both these chapters have been published in first-rank mineralogical and petrological journals and are thus reported here as they are published.

2) In the second section (**Chapter 3 and 4**) I'll focus in mechanism of outward CO_2 diffusion: to this purpose, oriented single-crystal cordierite slabs were heated by using a

heating-stage under the FTIR microscope and investigated using *in situ* FTIR μ-spectroscopy. Part of this study was done using a synchrotron-light source (SR-FTIR) to improve the signal-to-noise ratio and attain higher spatial resolution in the data. In this section I studied in particular the absorbance variation at constant temperature as a function of time, and evaluated the kinetic and diffusion parameters for CO_2 expulsion from the matrix.

3) In the third section (**Chapter 5**) I discuss the mechanism of inward diffusion of CO_2 within the structural channel of cordierite and beryl under different pressure, temperature and time conditions. The experimental work was done using a piston cylinder apparatus. In this section I'll make extensive use of high resolution single-crystal FTIR Focal Planar Array (FTIR-FPA) imaging to characterize possible inhomogeneity in the CO_2/H_2O across the samples, and identify the possible pathways for CO_2 diffusion. As it will be shown, the spectroscopic imaging was also necessary to locate the analytical spots for CO_2 measurements in the sample.

4) The last part (**Chapter 6, 7 and 8**) covers additional features observed during the work. In particular, chapter 6 deals with a multidisciplinary study of a peculiar diffusion pattern of CO_2 across an hourglass zoned beryl. This chapter relates on advances in techniques such as Time Of Flight Secondary Ion Mass Spectroscopy (TOF-SIMS) chemical imaging, polarized light FPA imaging and High Resolution SR-FTIR mapping. Chapter 7 deals with changes in coordination environment and physical state of H_2O in low-water beryl and cordierite. Chapter 8 eventually presents a summary of the work and illustrates the technological applications of CO_2 diffusion in beryl.

RIASSUNTO

La cordierite è un minerale abbastanza diffuso che ha la capacità di intrappolare H_2O and CO_2 anche ad altissime pressioni e temperature. Questa è una proprietà unica per un silicato diffuso nelle rocce che gioca un ruolo fondamentale negli equilibri mineralogici nel metamorfismo di alta o altissima temperatura (Harley and Thompson, 2004). In questo lavoro ci siamo dedicati allo studio approfondito dei meccanismi di diffusione nell'anidride carbonica all'interno di strutture cristalline a "canale". Inoltre, considerando che l'anidride carbonica è uno delle principali cause dei cambiamenti climatici terrestri a lungo termine (IPCC, 2005), la capacità di questi minerali di intrappolare la CO_2 potrebbe fornire spunti per future ricerche sullo stoccaggio permanente della CO_2 nei minerali.

Lo scopo di questa tesi è quindi quello di studiare la diffusione della CO_2 nella cordierite, e individuare le possibili implicazioni da un punto di vista geologico e tecnologico. Il lavoro è stato arricchito con lo studio in parallelo della diffusione della CO_2 nel berillo, che è strutturalmente correlato alla cordierite.

Il lavoro di tesi è suddiviso in quattro sezioni principali:

1) Nella prima sezione (**Capitoli 1 e 2**) introduco le problematiche relative all'analisi qualitativa e quantitativa di H_2O e CO_2 nella cordierite attraverso la Spettroscopia Infrarosso a Trasformata di Fourier (più comunemente FTIR). In particolare illustro lo studio cristallochimico e spettroscopico di campioni di variegata composizione chimica, a partire da cordieriti di Mg fino all'analogo estremo ferrifero sekaninaite. Inoltre illustrerò la messa a punto della calibrazione del coefficiente di assorbimento molare ε, un parametro indispensabile per misure quantitative in micro-spettroscopia FTIR. Entrambi i capitolo sono

stati pubblicati su riviste di mineralogia e petrologia di alto impatto e qui riportati come da pubblicazione.

2) La seconda sezione (**Capitoli 3 e 4**) è focalizzata sui meccanismi di espulsione della CO_2: a questo proposito sono state riscaldate delle lamelle orientate provenienti da cristalli singoli di cordierite attraverso un tavolino riscaldante installato direttamente su di un microscopio FTIR ed analizzati tramite micro-spettroscopia FTIR *in situ*. Parte dello studio è stato condotto utilizzando una sorgente di luce di sincrotrone (SR-FTIR) in modo da aumentare il rapporto segnale-rumore e raggiungere una migliore risoluzione spaziale. In questa sezione ho studiato in dettaglio la variazione degli assorbimenti in funzione del tempo a temperatura costante, e ho ricavato i parametri cinetici e di diffusione per l'estrazione della CO_2 dai canali strutturali della cordierite.

3) Nella terza sezione (**Capitolo 5**) discuto il meccanismo di diffusione della CO_2 attraverso i canali strutturali di cordierite e berillo riequilibrate a varie condizioni di pressione, temperatura e tempo. La procedura sperimentale è stata condotta usando un apparato di tipo *piston-cylinder*. In questa sezione farò uso intensivo di *imaging* FTIR bidimensionale (FTIR-FPA) ad alta risoluzione su cristallo singolo per individuare possibili inomogeneità nella distribuzione di H_2O/CO_2 nei campioni trattati, ed identificare i possibili percorsi di diffusione della CO_2. Inoltre l'*imaging* FTIR è indispensabile per localizzare i punti analitici per la misura quantitativa della CO_2.

4) Nell'ultima parte del manoscritto (Capitoli 6, 7 e 8) discuterò ulteriori problematiche incontrate durante il lavoro di tesi. In particolare, il capitolo 6 illustrerà uno studio multidisciplinare su di un peculiare percorso di diffusione della CO_2 osservato in un berillo zonato a clessidra. Questo capitolo illustra alcune tra le tecniche più innovative nell'analisi mineralogica come le mappe composizionali in *Time Of Flight Secondary Ion Mass Spectroscopy* (TOF-SIMS), *imaging* FTIR-FPA in luce polarizzata e mappatura SR-FTIR and altissima risoluzione. Il capitolo 7 è focalizzato sulle variazioni di coordinazione e speciazione dell'H_2O in berilli e cordieriti con poca acqua. Infine il capitolo 8 riporta un riassunto dell'intero lavoro svolto e illustra le implicazioni tecnologiche della diffusione della CO_2 nel berillo.

INTRODUCTION

1. Structural details of cordierite and beryl and their relevance on technology

Carbon dioxide (CO_2) generated by the combustion of fossil fuels is by far the most abundant greenhouse gas; its reduction in the atmosphere is therefore a primary environmental concern. Due to several reasons, it can be easily understood that fossil fuels will continue to play a significant role in the world's economy at least in the following decades, thus emphasis must be placed on improving methods to decrease the amount of CO_2 dispersed in the environment. The reduction of CO_2 from the atmosphere can be achieved by efficiency improvements in power plants, use of alternative energy technologies, sequestration of CO_2, or some combination of these methods. Up to the present, several techniques have been considered, and these include: 1) forestation, where CO_2 is removed from the atmosphere by biological activity; 2) aquifer storage, in which CO_2 is injected into terrestrial aquifers where it is trapped hydro-dynamically; 3) deep sea storage, where CO_2 is injected into the ocean at approximately 3,000 meter depths, where it is believed to remain stable; and 4) mineral carbonation, in which CO_2 is reacted with minerals to form solid carbonates. This final form of sequestration is the most efficient method, because the carbonates are stable over geologic time periods (millions of years), rather than the hundreds to thousands of years of stability expected for the first three forms of sequestration. This process is however highly expensive and energy consuming, therefore research in material science has focused in the last decade at developing technically feasible processes for mineral sequestration of carbon dioxide alternative to carbonation.

Actually, many minerals contain carbon as a major to trace constituent, however the carbon content analysed in naturally occurring silicates is traditionally assigned to CO_3^{2-}

groups in the structure, whereas the possible presence of molecular CO_2 in these phases is almost completely ignored. Up to the present, the only accepted CO_2-bearing minerals are beryl (Wood and Nassau, 1967) and cordierite (Armbruster and Bloss, 1980, Della Ventura *et al.*, 2009, 2012). Indeed these two isostructural minerals are able to trap CO_2 because of their peculiar structural channels.

Cordierite is a framework alumino silicate with the ideal formula $(\square,Na)(Mg,Fe)_2Al_4Si_5O_{18}(\square,H_2O,CO_2)$ and a continuous solid solution between the Mg^{2+} end-member and the Fe^{2+} end-member (sekaninaite) exists (e.g. Černý *et al.*, 1997, Radica *et al.*, 2013). The cordierite framework can be described as a stacking of pseudo-hexagonal Si/Al layers of tetrahedra and mixed layers of tetrahedra and octahedra (Fig. 1a). Alkali cations such as Na, K, Ca, and molecules such as H_2O and CO_2 may be allotted within the resulting pseudo-hexagonal channel, occupying sites on the c axis at the height of the narrow "bottle necks" for Na, and of the large cavities for H_2O and CO_2 (Gibbs, 1966, Hochella *et al.*, 1979; Malcherek *et al.*, 2001; Yakubovich *et al.*, 2004).

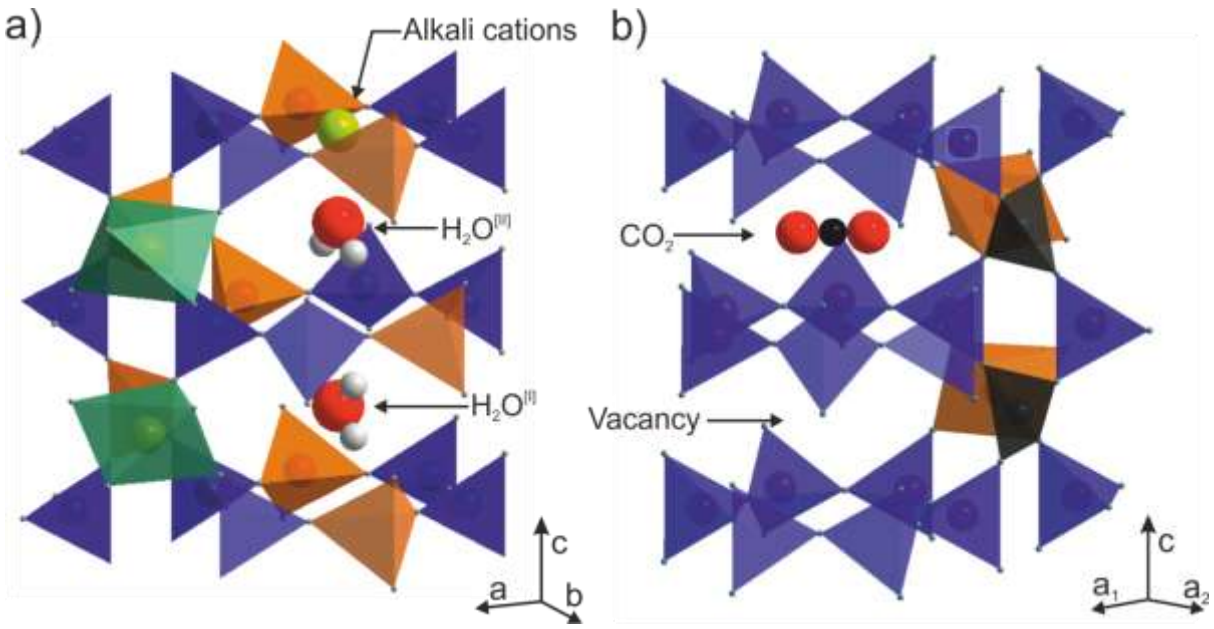

Figure I - Schematic view of a portion of the cordierite (a) and beryl (b) structures emphasizing the channels parallel the *c* axis. Si-containing tetrahedra are shown in blue, Al in tetrahedral and octahedral coordination is shown in orange, Be- containing distorted tetrahedra in dark gray and Mg-octahedra in dark green. The structural position of the channel alkali cations, both orientation types of H_2O and CO_2 are shown (modified after Radica *et al.*, 2013)

Beryl (ideal formula $(\square,Na)Be_3Al_2Si_6O_{18}(\square,H_2O,CO_2)$ is isostructural with cordierite (Fig. 1b). Its framework is constituted by 6-fold Si-centered tetrahedral rings stacked along

the c axis. The hexagonal rings are interconnected parallel to [001] by distorted Be-centered tetrahedra. Al occupies the octahedral sites (Gibbs *et al.*, 1968). Beryl also has structural channels running along the *c* axis that can contain alkali cations and volatile molecules (Wood and Nassau, 1968).

Extra-framework H_2O groups occur in the structural channels with the molecular plane parallel to (100). In both cordierite and beryl H_2O can be oriented in two different ways: type I H_2O (hereafter $H_2O^{[I]}$) has its H–H vector oriented parallel to the *c* axis, and type II H_2O ($H_2O^{[II]}$) has its H–H vector normal to the c axis (parallel to the *b* axis in cordierite). H_2O groups of the latter type are locally associated with channel cations (Goldmann *et al.*, 1977; Hawthorne and Černý, 1977). Winkler *et al.* (1994) proposed that $H_2O^{[I]}$ in synthetic Mg-cordierite is rotationally disordered about [001] and that a purely static description is inappropriate to describe its behavior in the channel cavity. They proposed a model whereby the H...H vector remains parallel to [001] and the H_2O molecule rotates in two different positions about its center of mass with an estimated hopping time of about 6 picoseconds at room temperature; this feature however cannot be observed by using FTIR spectroscopy. The linear CO_2 molecules are systematically oriented normal to the c axis and parallel to the crystallographic *a* axis for cordierite (Aines and Rossman, 1984;Kolesov and Geiger, 2000; Khomenko and Langer, 2005).

The molecular dimension of H_2O is 2.8 X 3.2 X 3.7 Å and CO_2 is 2.8 X 2.8 X 5.0 Å (Wood and Nassau, 1968). However the CO_2 molecule barely fits inside the cage, so once inside it tends to be wedged to the structure behaving as a “plug” (Aines and Rosmann, 1984; Vry *et al.*, 1990). On the opposite, the smaller H_2O polar molecules are bonded to the structure mainly by electrostatic interactions with the structural oxygens ($H_2O^{[I]}$) and alkali cations ($H_2O^{[II]}$).

Additionally, because of its thermal and mechanical properties, cordierite is used in industrial applications such as high-tech ceramics or as a catalyst in petroleum industry. Beryl is a pegmatitic mineral and has a lower thermal and baric stability; it is well known for providing some of the most notable gemstones, such as the varieties emerald (green), aquamarine (light-blue), heliodor (yellow) or bixbite (red).

2. The petrological relevance of cordierite

This PhD Thesis work has been mainly focused on cordierite because it represents the only case of a widespread microporous mineral (pore size under 2 nm, Rouquérol *et al.*, 1994; McCusker *et al.*, 2001) that is able to trap significant amounts of molecular H_2O and CO_2 (Schreyer and Yoder 1964; Mirwald *et al.*, 1979; Newton and Wood, 1979; Armbruster and Bloss 1982; Kurepin 1985) under extreme geological (P, T) conditions. Cordierite stability extends from the amphibolite facies to ultra-high temperature metamorphism to crustal anatexis conditions (Mirwald and Schreyer, 1977; Vry *et al.*,1990; Carrington and Harley, 1996; Smith 1996; Kalt 2000; Harley *et al.*, 2002; Bertoldi *et al.*, 2004; Sarkar *et al.*, 2010). The analysis of the volatile constituents of cordierite can used to determine the composition of the fluid pahse during crystallization (Vry *et al.*, 1990; Carrington and Harley, 1996; Harley *et al.*,2002; Kurepin, 2010). H_2O and CO_2 contents affect the stability of cordierite (Schreyer 1985; Carey 1995; Harley *et al.*, 2002). Therefore, a quantitative determination of its channel constituents is crucial in petrologic studies.

Among the wide range of cordierite occurrences, the most investigated is the ultra high-temperature metamorphism of pelitic rocks. Dehydration melting of biotite-bearing pelites with moderate to high X_{Mg} variations (X_{Mg}/X_{Mg+Fe} >0.5) is often controlled by cordierite-forming reactions in migmatites and leuco-granites at 200–700 MPa and 700–900° C (Fitzsimons, 1996; Harley *et al.*, 2002). Thus understanding the role of cordierite as an H_2O and CO_2 bearing phase is essential for understanding melting processes and for thermodynamic calculation of fluid activities during these events (Harley and Thompson, 2004). Kurepin (2010) made calculations of the dependence of H_2O and CO_2 contents in cordierite as a function of *P, T* and fluid composition for the aforementioned P-T conditions, and his thermodynamic model showed a non-ideality of thermodynamic behavior of H_2O and CO_2 mixing. In addition evaluation of the H_2O and CO_2 activities showed that cordierites in high temperature and pressure assemblages were formed under fluid-saturated conditions over a wide range of H_2O/CO_2 ratios (Vry *et al.*, 1990; Kurepin, 2010).

In order to understand these mechanisms, several experimental studies on the solubility of volatile components in cordierite have been performed, in particular H_2O (Schreyer and Yoder 1964; Mirwald *et al.*, 1979, Harley and Carrington, 2001 among the

others), CO_2 (Armbruster and Bloss, 1982, Armbruster, 1985; Le Breton and Schreyer, 1993), and mixed H_2O – CO_2 (Johannes and Schreyer 1981; Thompson *et al.*, 2001).

As a result of these studies, there is agreement that pressure exerts a stronger influence on the solubility of both H_2O and CO_2 than does temperature. Both H_2O and CO_2 contents slightly decrease with increasing temperature, while increasing pressure favors higher concentrations (*e.g.* Fig. 2, modified after Harley and Thompson, 2004). It is important to note that the maximum H_2O content obtained at 700 MPa is about 2.4 wt.%, which is close to the maximum theoretical value of 2.9 wt.% or 1 molecule per formula unit in the channel (Deer *et al.*, 2004). The maximum calculated value for CO_2 is about 2.2 wt.% (Deer *et al.*, 2004) corresponding to about 0.3 molecules per formula unit.

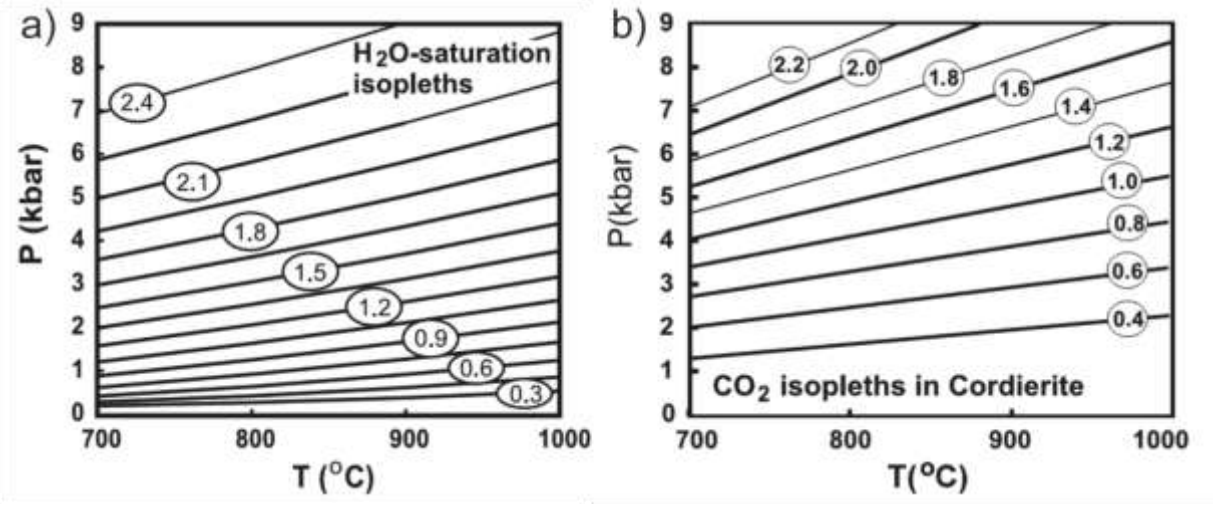

Figure 2 – (a) Pressure – temperature phase diagram of the isopleths of H_2O (expressed in wt.%) for X_{Mg} = 0.75 cordierite coexisting with pure H_2O fluid, as calculated by Harley and Carrington (2001); (b) isopleths of CO_2 (expressed in wt.%) for X_{Mg} = 0.80 cordierite in a pure fluid after Thompson *et al.*, (2001) and Harley *et al.*, (2002).

Studies on X_{CO2}, where $X_{CO2} = CO_2/(CO_2+H_2O)$, partitioning between melt and cordierite have shown that H_2O tends to be incorporated preferentially into the cordierite structure, while CO_2 preferentially remains in the melt (Fig. 3b and Johannes and Schreyer, 1981). This behavior is only slightly changed at higher temperatures (Harley and Carrington, 2001), while X_{CO2} increases with increasing pressure, facilitating CO_2 uptake (Johannes and Schreyer, 1981). Moreover, increasing X_{CO2} decreases significantly the amount of H_2O+CO_2 diffused into the mineral. In particular, there is a decrease of H_2O (Fig. 3a) probably because the presence of CO_2 obstructs its diffusion to the channel ways. This behavior, which is observed also in natural samples (Vry *et al.*, 1990), can be explained by the configuration of

the CO_2 molecule inside the channels. Another factor that decreases the total amount of diffused fluids is the alkali content within the structural channels (Johannes and Schreyer, 1981; Vry *et al.*, 1990). There is evidence suggesting that CO_2 (and possibly alkali cations) may act as plugs in the channel ways obstructing inward and outward molecule diffusion, drastically slowing down the time of degassing and re-equilibration in case of pressure drop (Johannes and Schreyer, 1981; Kalt, 2000). This behavior complicates the possibility to predict the diffused molecules coexisting with mixed H_2O and CO_2 fluids, although a theoretical approach has been attempted by Kurepin (2010).

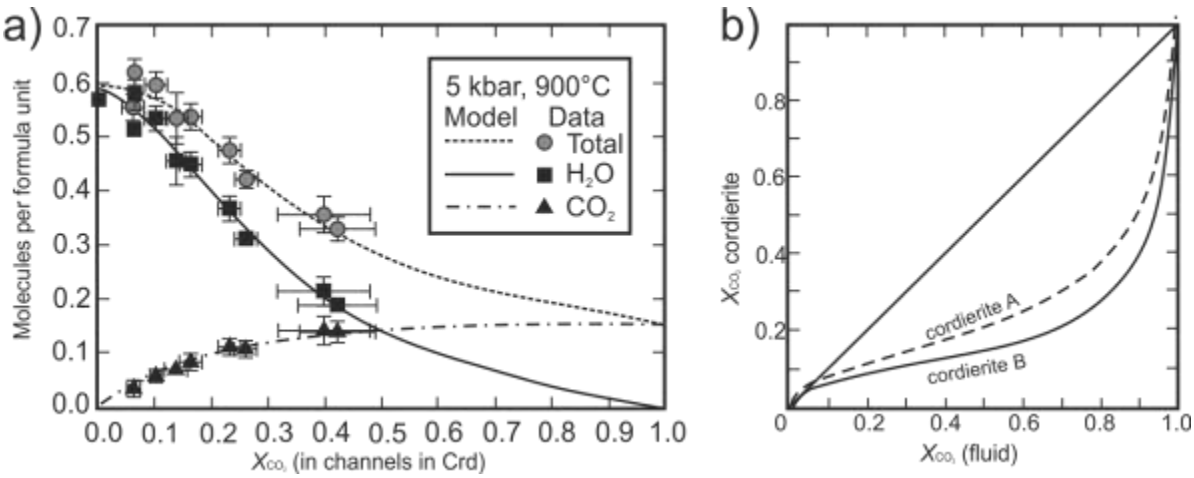

Figure 3 (a) variation of the volatile composition in cordierite (X_{Mg} = 0.68) channels with fluid-saturated, intermediate H_2O - CO_2 fluid composition. The lines show the calculated values atThompson *et al.* (2001). Squares = H_2O, triangles = CO_2, circles = total number of molecules per formula unit (modified after Thompson *et al.*, 2001). (b) partition curves showing X_{CO2} fractioning between cordierite and coexisting fluid at 500 MPa and 600°C fort two different synthetic cordierites A and B (modified after Johannes and Schreyer, 1981).

The experiments were performed with small cordierite grains as starting materials (about 200 µm in Armbruster and Bloss, 1982 and Armbruster, 1985; 125-250 µm in Thompson *et al.*, 2001) in order to maximize the surface-to-volume ratio, and were carried out for a long duration (up to a few weeks) in order to achieve fluid/mineral equilibration. However there is still no agreement on the results, among the different authors. For instance, Johannes and Schreyer (1981) obtained different results as a function of different starting material (Fig. 2b) or grain size of cordierite, and Le Breton and Schreyer (1993) observed a nonlinear behavior of the CO_2 contents between 15 minutes to 3 weeks experimental runs. Major problems arise with CO_2 diffusion, because its “sluggish” nature delays or even prevents sample saturation. Thus, the study of the run products cannot be addressed by conventional bulk methods, such as coulometric tritation (Armbruster and

Bloss, 1982; Johannes and Schreyer, 1981) or powder FTIR spectroscopy (Vry *et al.*, 1990) or single spot micro-analytical techniques, such as SIMS (secondary ion mass spectrometry) (Thompson *et al.*, 2001), which do not allow characterizing the inhomogeneous distribution of the target element. For this reason, we have predominantly used, in this Thesis, single-crystal FTIR spectroscopy to examine the run products, and have developed in particular novel FTIR procedures to characterize the sample inhomogeneities.

3. Advances in FTIR micro-spectroscopy

Several times during this introduction we mentioned that FTIR micro-spectroscopy was chosen as a principal probing tool, and the reason is that FTIR is one of the main tool in Earth Science able to deal with light and crucial elements like H (both as H_2O and OH^-) and C (both as CO_2 and CO_3^{2-} groups). Several complementary techniques were developed in the last decades to overcome some of the most common issues occurring in Earth Science.

1) Focal Plane Array (FPA) FTIR imaging and FTIR mapping are extremely important imaging techniques capable of detecting and quantify the distribution of an absorber across a sample. In Earth Science materials these techniques are useful to examine the possible inhomogeneity of natural samples, such as chemical zoning, but also melt/fluid inclusions, structural defect of the occurrence of included micro-phases. Several works have been devoted to this topic, in particular Della Ventura *et al.* (2010, 2014) revised the data in literature and illustrated the possibilities offered by imaging techniques in Earth Science. During the present Thesis I made extensive use of this technique, in particular each experimental sample was preliminary analyzed through 2D FTIR FPA imaging in order to locate the most suitable spots for CO_2 quantitative measurement.

Polarized-light FTIR single spot analysis (Libowitzky and Rossman, 1996) was used for quantitative measurements and to define the orientation of the absorbers in the samples. In addition in Chapter 6 I describe the results of FPA imaging done on oriented single crystals using polarized radiation (Fig. 4a); this is the first time that polarized imaging is applied in Earth Science and the data show that this technique opens interesting scenarios: for instance the work presented in chapter 6 shows how it is possible to map in detail the distribution of absorbers with different orientation in the same section.

In this work I also illustrate the possibilities offered by synchrotron-light FTIR mapping. In FTIR spectroscopy the increased brilliance of a synchrotron source translates into improved signal to noise ratio in 2D FPA imaging and thus in a higher spatial resolution for spot measurements and mapping (Della Ventura *et al.*, 2014). In Figure 4 I reported for comparison the contour map of CO_2 distribution in the same area of a thermally-treated beryl sample obtained using a conventional Globar source (Fig. 4b) and a synchrotron source (Fig. 4c).

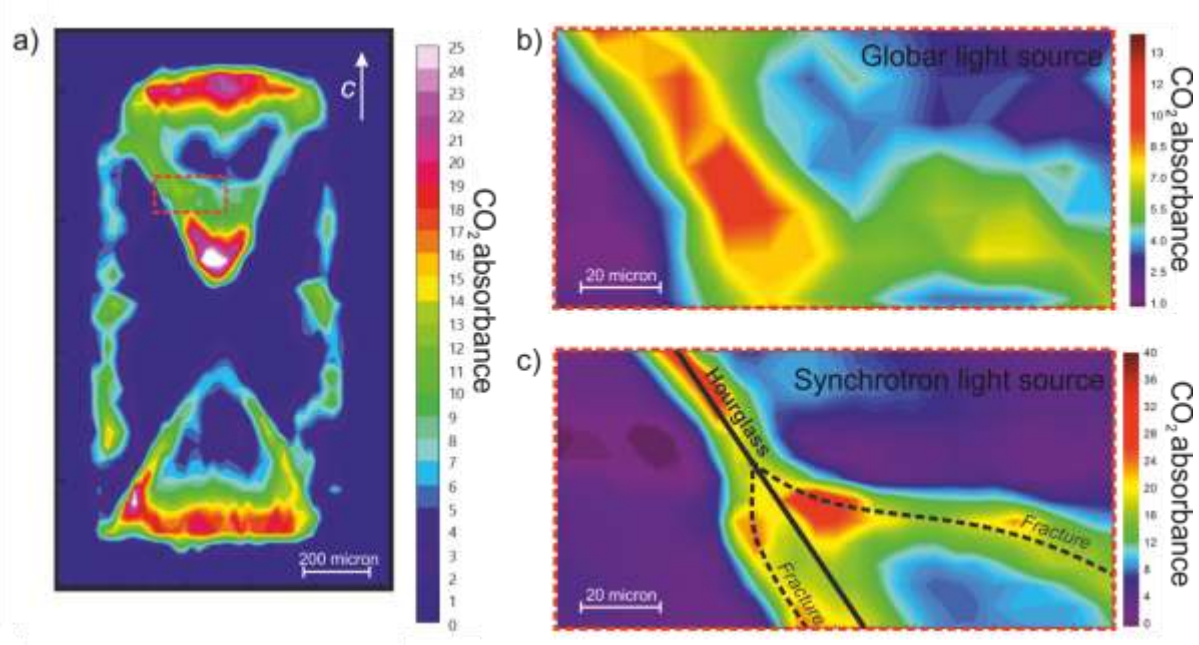

Figure 4 – (a) FTIR-FPA contour map of CO_2 distribution collected for E⊥c in a beryl sample treated at 800 °C and 500 MPa, 4 days. (b) Enlargement of (a) showing the CO_2 distribution obtained with conventional light, spot size 20 x 20 µm, sampling step 10 µm, and (c) obtained with synchrotron light with spot size 10 x 10 µm, sampling step 5 µm. Chromatic scale is proportional to the CO_2 content, units are arbitrary. See Chapter 6.

2) *In-situ* FTIR techniques were developed to study phase equilibria and kinetic process at extreme pressures and temperatures using diamond anvil cells (DAC) and heating stages (Koch-Müller *et al.*, 2003, Iezzi *et al.*, 2006, 2009, Keppler and Smyth, 2006; Hawthorne *et al.*, 2007, Welch *et al.*, 2007, Della Ventura *et al.*, 2010, 2014). In Chapter 3 and 4 of this Thesis I will describe the CO_2 absorbance variations in cordierite up to 1200 °C and the kinetic of CO_2 expulsion from the structural channels. *In-situ* high temperature measurements up to 1200 °C could be performed for the first time using a modified heating stage capable to operate at extreme temperatures directly under the IR microscope (Fig. 5a).

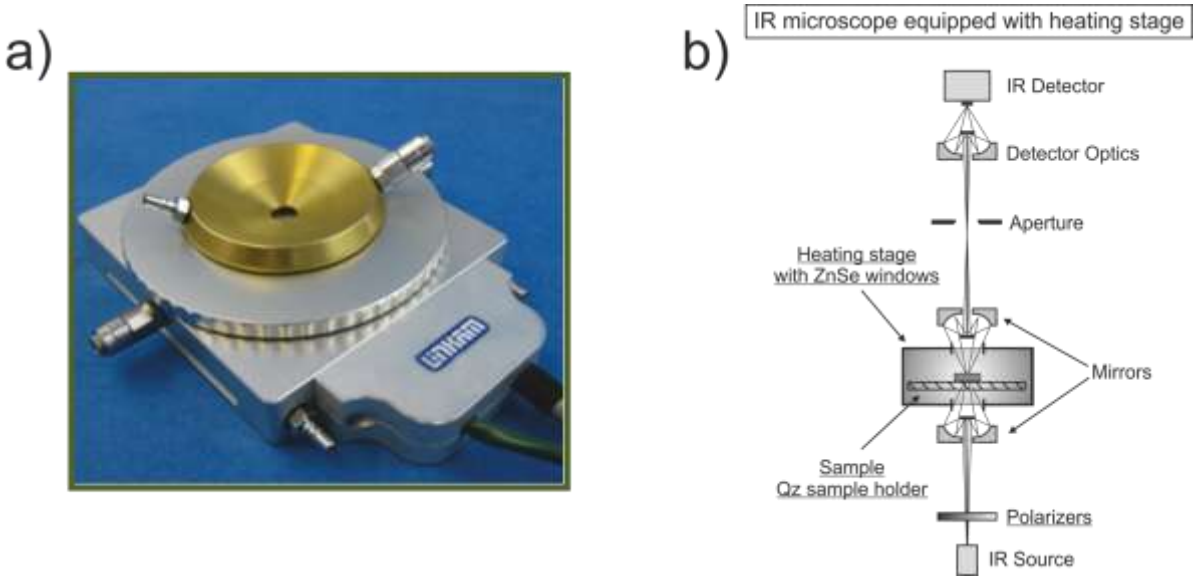

Figure 5 - The used Linkam TS 1400XY Heating stage, modified to work under the FTIR microscope (a). Schematic layout (b).

The kinetic of CO_2 expulsion was studies using two different sections with different thickness; to collect the spectra for the thinner 19 µm slice with enough S/R we used a synchrotron light source, because the reduced thickness of the samples coupled with the strong beam absorbance caused by the stage windows, sample holder and polarizers (Fig. 5b) affected significantly the transmitted signal.

SUMMARY

Section I: Structural and spectroscopic characterization of cordierite (Chapters 1 and 2).

Eight different cordierite samples (Chapter 1) from different localities and geological occurrences were chosen to cover a wide range in H_2O/CO_2 ratio.

Single-crystal X-ray diffraction data were collected on optically clean grains free from inclusions and alteration products at CNR Istituto di Cristallografia (Bari) with a Nonius Kappa CCD area detector diffractometer, revealing all samples to be orthorhombic *Cccm*. Major oxides were analysed by EMPA while H and C were quantified by SIMS (secondary ion mass spectrometry). Accordingly, the Si:Al ratio is close to 5:4; X_{Mg} ranges from 76.31 to 96.63; extraframework K and Ca are negligible, with Na up to 0.84 apfu. SIMS shows H_2O up to 1.52 and CO_2 up to 1.11 wt%.

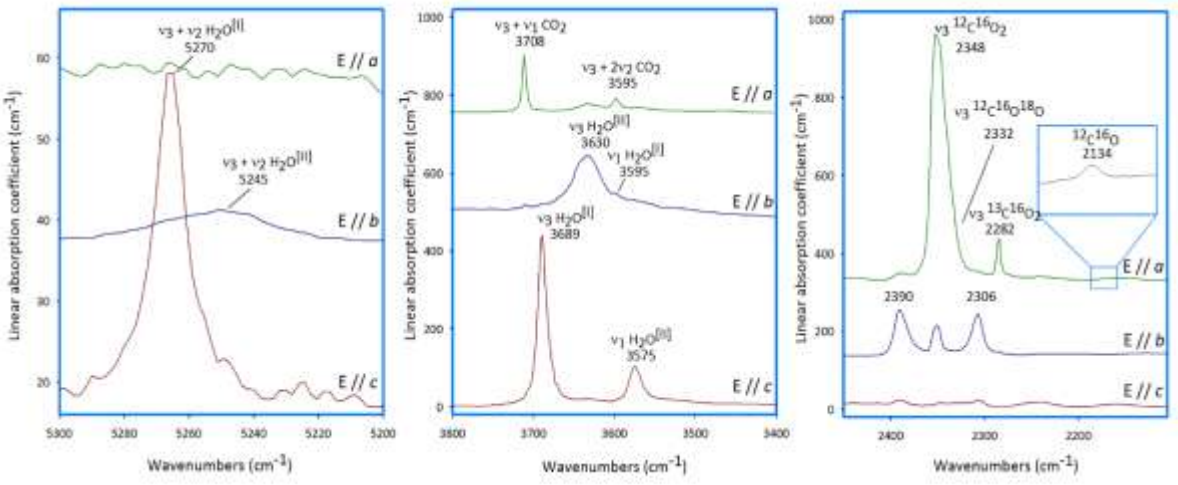

Figure 1 - Selected single-crystal polarized-light FTIR spectra of cordierite along the principal optical directions, peak identification after Della Ventura *et al.*, (2009).

Optically transparent single-crystals were oriented using the spindle-stage and examined by FTIR micro-spectroscopy under polarized light. The observed bands were assigned to water molecules in two different orientations $H_2O^{[I]}$ and $H_2O^{[II]}$, and to CO_2 molecules in the structural channels (Fig. 1). Prior to the quantitative analyses, the samples were examined for their water and carbon dioxide distribution using a focal-plane-array (FPA) of detectors. The evidence was that at the µm-scale the distribution of H and C in cordierite were significantly inhomogeneous, particularly for H_2O, whose zoning within the crystal can be strongly affected by the geological history of the mineral after its formation.

The core of this work was the quantitative calibration of H_2O and CO_2 in cordierite based on single-crystal FTIR micro-spectroscopy (Fig. 1), based on the Beer-Lambert relationship.

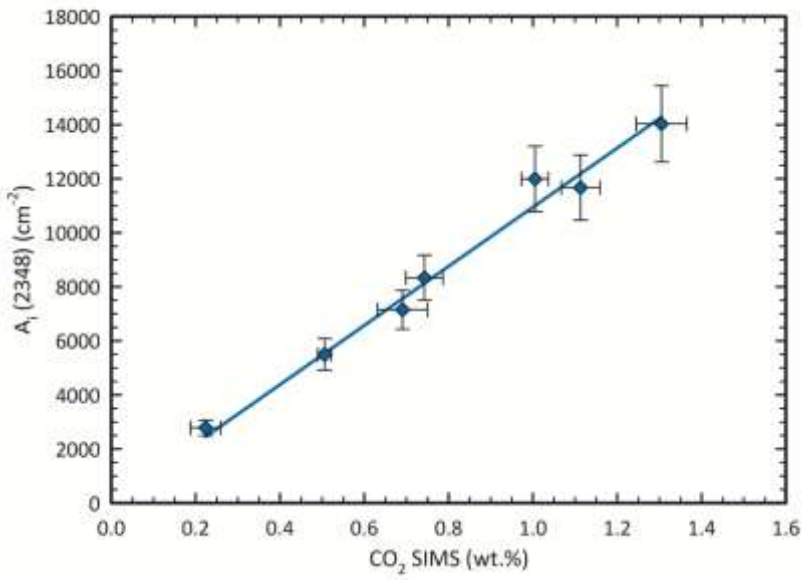

Figure 2 - Relationship between the analysed (SIMS) CO_2 content and the integrated absorption coefficient ($a_i=A_i/t$) for the studied cordierites. The calibration curve provides the specific absorption coefficient (ε) to be used in the Beer-Lambert equation for the spectroscopic quantitative analysis of CO_2 in cordierite.

For H_2O the integrated molar coefficients for type I and type II water molecules were calculated separately and turned out to be $^{[I]}\varepsilon = 5000 \pm 1000$ l·mol^{-1}·cm^{-2} and $^{[II]}\varepsilon = 13200 \pm 500$ l·mol^{-1}·cm^{-2}, respectively. For CO_2 the integrated coefficient is $\varepsilon_{CO2} = 19000 \pm 1000$ l·mol^{-1}·cm^{-2}. The same procedure just illustrated was then applied to the Fe end-member of the cordierite group, sekaninaite (Chapter 2). Additionally single crystal X-ray refinement, laser ablation mass-spectroscopy for Li^+ and Raman spectroscopy characterization were performed.

Electron-micro-probe analysis shows the sample to be close to the Fe end-member [X_{Fe} = Fe/(Fe+Mg) = 94%) with significant Mn (1.48 wt.%); laser ablation mass-spectrometry showed the presence of 0.42 wt.% Li_2O. H_2O and CO_2 contents (1.48 and 0.17 wt.%, respectively) were determined via secondary-ion mass-spectrometry (SIMS). X-ray site occupancy refinement suggested that the lack of monovalent charge at the octahedral site due to the presence of Li^+, is counter-balanced by the presence of Na^+ in the channel.

Sample homogeneity was confirmed by FPA imaging (Fig. 3) and single-crystal FTIR spectroscopy confirmed the presence of two types of H_2O groups in different orientations (with prevalence of the type II orientation).

Using the Beer-Lambert relation, integrated molar coefficients ε_i were calculated for both types of H_2O (ε_i $H_2O^{[I]}$ = 6000±2000; ε_i $H_2O^{[II]}$ = 13000±1000) and for CO_2 (ε_i CO_2 = 2000±1000).

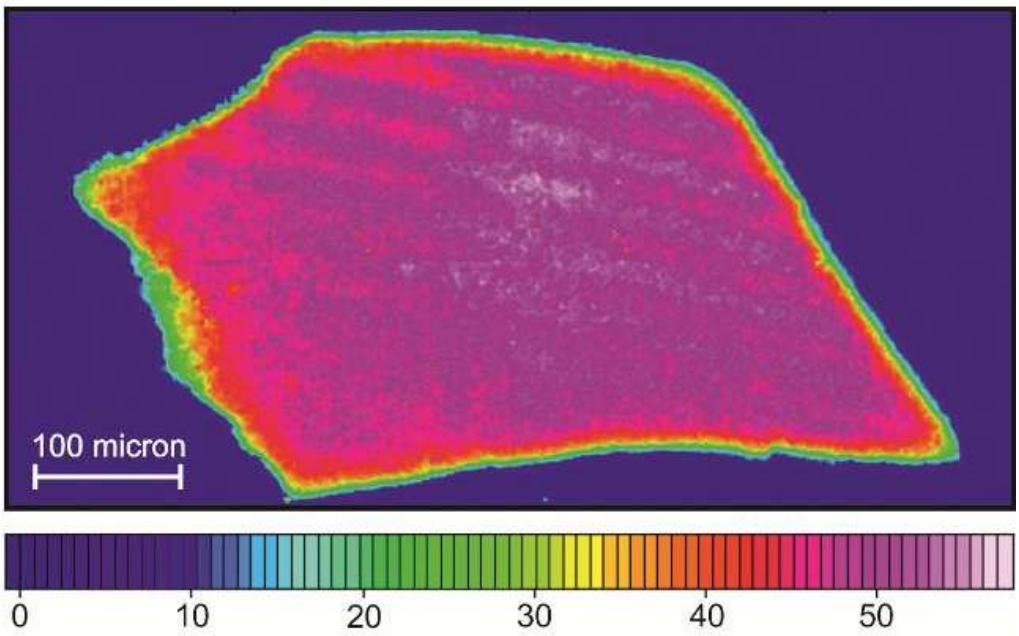

Fig. 6. FTIR FPA image of the (100) section, 47 µm thick slab of sekaninaite. Integration of the H_2O stretching bands in the range 3500-3700 cm^{-1}. The chromatic scale is proportional to volatile contents, units are arbitrary.

The integrated molar absorption coefficients ε for H_2O are very close to those reported for Mg-rich cordierite in Chapter 1. On the other hand, the value of $\varepsilon_{i\ CO2}$ obtained here cannot be considered reliable because of the uncertainty of the SIMS data, which is > 50%. However, it is close to the one calibrated by Della Ventura *et al.* (2006) from a CO_2-poor cordierite.

Section II: *In-situ* HT-IR spectroscopy and kinetic study of CO_2 expulsion from cordierite (Chapters 3 and 4).

In this section I will describe the *in situ HT*-FTIR micro-spectroscopy of cordierite and will evaluate the kinetic and diffusion parameters of CO_2 expulsion as a function of increasing *T*. Experiments were performed using a Linkam TS 1400 XY heating stage at LNF-INFN and at beamline B22, Diamond Light Source laboratory Oxford (UK). Fragments of two natural cordierites, BM 96512 from Cabo de Gata (Almaria region, Spain) and Rp 3237 from Kragero (Arendal region, Norway) were used.

In a first series of step-heating experiments, the (001) section of cordierite Rp 3237 was heated up to 1000 °C with a rate of 20 °C/min and FTIR spectra were collected for every step. At the end of the run, the sample was allowed to cool down to *RT* and a spectrum was measured, than was heated up at 1100 °C (rate 100 °C/min) and then cooled down again at *RT*; spectra were collected at 1100 °C and at *RT*. A second series of experiments was performed heating up the (010) section with a rate of 100 °C/min up to 600 °C; measurements were performed every 100°C during the ramp. Then the sample was cooled down to RT and heated up again up to 600 °C with a rate of 100 °C/min. The same procedure was repeated at 800, 900, 1000, 1100 and 1200 °C. FTIR spectra were collected at *RT* and at any target temperature every 50 °C. After each experiment FPA-FTIR images were collected to check for the homogeneity of residual CO_2.

In-situ measurements on (001) oriented sections that up to $T > 800$ °C there is a significant intensity increase of the CO_2 stretching mode at 2348 cm^{-1}, followed by a sudden decrease for $T > 900$°C; the absorbance is virtually zero at 1000°C (Fig. 7a). On the opposite, the integrated absorbance (A_i) of the CO_2 ($\nu_3 + \nu_1$) combination mode at 3708 cm^{-1} (Fig. 7a) is almost constant up to about 450 °C, then decrease up to 850 °C. For higher *T* the intensity decreases with a much faster rate; the band disappears at 950°C. Similar trends for the (010) section cut out from the same cordierite crystal (Fig. 7c).

The evolution of the H_2O absorbance as a function of increasing *T* is extremely different to that of CO_2 (Fig. 7a and b, in purple), and shows a linear and constant decrease of ~50% of the intensity up to 800°C; in the 800°-900°C range there is a sudden drop and at 950°C the sample is completely anhydrous. Similarly to what observed for CO_2, the data collected on quenched samples show a different scenario: the integrated H_2O absorbance is

constant up to 800°C and suddenly drops in the 800-900°C range. At 1000° the sample is completely anhydrous

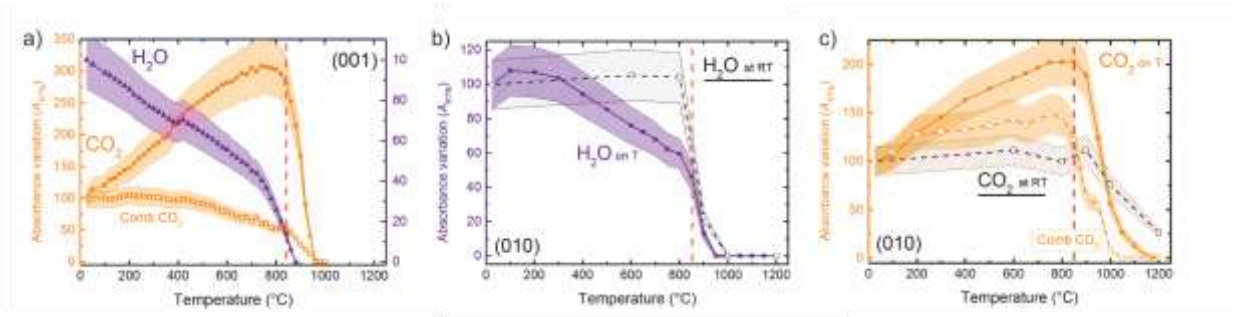

Figure 7 - (a) Sample Rp 3237 (001) section: integrated absorbance variation ($A_{RT\%}$ in %) of H_2O (purple triangles), CO_2 stretching mode (filled orange squares) and CO_2 combination mode (open orange squares). Sample Rp 3237_14 (010) section: integrated absorbance variation ($A_{RT\%}$ in %) of H_2O (b) and CO_2 (c) absorptions. In (b) and (c) the intensities measured after quencing the sample are given for comparison (dashed black lines). The shaded areas represent the estimated error on $A_{RT\%}$.

Several authors (*e.g.* Keppler and Bagdassorov, 1993; Yamagishi *et al.*, 1997; Zhang *et al.*, 2007; Tokiwai and Nakashima, 2010b) revised recently the absorbance in minerals and glasses in HT-FTIR spectroscopy and showed that the intensity measured during *in situ* data collection is not related to the concentration of the target absorber via the same Beer-Lambert relationship calibrated at room-*T*. This feature is shown in Figure 7, where it is evident that *in situ* FTIR data collection does not provide a real estimate of the CO_2 and H_2O behavior in cordierite as a function of increasing *T*. In particular, based on the Beer-Lambert relationship, assuming no or negligible change in the sample thickness across the studied *T* range, the trends of Figure 7 suggest a significant change in the molar absorption coefficients ε for both volatile species at varying *T*.

Interestingly, as already observed for H_2O/OH in several mineral species (Zhang *et al.*, 2007) the temperature dependence of the principal modes is different from that of multi-phonon bands (Fig. 7a and c open squares).

Continuous heating experiments were performed on (001) oriented BM 96512 cordierite slabs. Two fragments were double-polished at 60 µm and 19 µm, respectively and broke up into four pieces each. Four fragments of the same 60 µm thick section were heated to 850, 900, 950 and 1000 °C (heating rate 100°C/min) and kept at the target *T* for two hours. Polarized spectra were collected using conventional light with both E//*a* and E//*b* at *RT* before the experiment, and at the target *T*, every 5 minutes for the first hour and every 10 minutes for the second hour of isothermal heating. Additional four fragments of the same

19 µm thick BM 96512 slab were heated to 825, 850, 900 and 1000 °C (heating rate 100°C/min) at different annealing times. For this second set of samples, spectra were collected using synchrotron light exclusively along the *a* crystallographic direction at *RT* and at the target T every 5 minutes. This experimental layout was necessary to get a better S/N because the reduced thickness of the samples coupled with the strong beam absorbance caused by the stage windows, sample holder and polarizers affected significantly the transmitted signal.

Figure 8 shows the CO_2 loss curves expressed as $A_{t\%} = 100 \cdot A_t/A_0$ where A_t is the A_i at time = t and A_0 is A_i at time = 0, *i.e.* just after the sample reached the target temperature; data obtained with E//*a* for the ν_3 mode at 2348 cm^{-1} for the 60 µm thick BM96512 and the 19 µm thick BM96512 (001) sections are displayed.

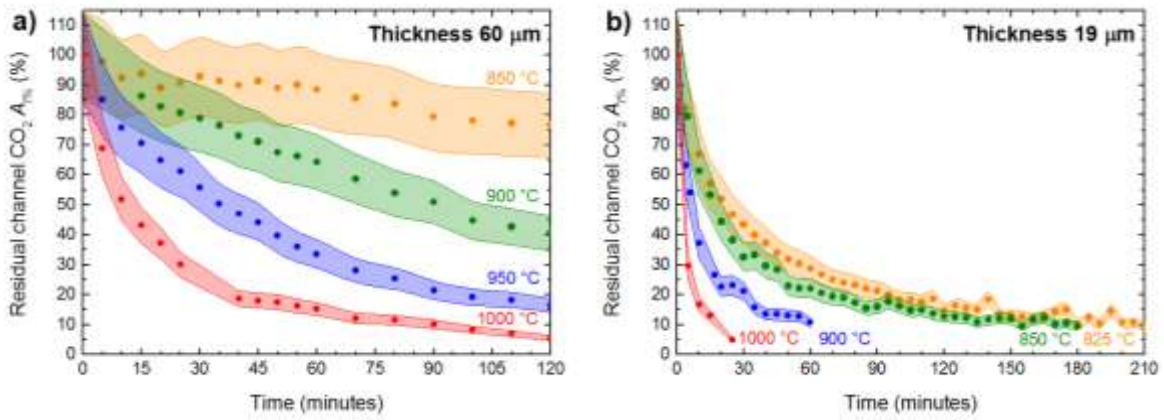

Figure 8 – Isothermal plots of residual CO_2 within the cordierite channels ($A_{t\%} = 100 \cdot A_t/A_0$ of the 2348 cm^{-1} band) as a function of time; sample BM96512, (001) section for E//*a*. Shaded areas represent the estimated error on the absorption. (a) 60 µm thick section, (b) 19 µm thick section.

The curves in Figure 8 were fitted using three different approaches: the Avrami JMAK rate equation (Hancock and Sharp, 1972), the Avrami Putnis rate equation (Putnis, 1992) and the mono-dimensional plane sheet diffusion (Ingrin, 1995).

Activation energies calculated using the Avrami approaches yield four different results on the basis of the used formula and the sample thickness. However, based on different assumptions, it is possible to conclude that the most reliable activation energy for CO_2 expulsion from cordierite provided by the Avrami formalism is E_a = 138±12 kJ/mol, *i.e.* the value obtained using the Avrami Putnis equation on the thinner sample data set. This

value is very close to those obtained by previous authors for the dehydration of cordierite (Giampaolo and Putnis, 1989).

Using the mono-dimensional plane sheet diffusion approach it was possible to evaluate both the diffusion coefficient D and the activation energy E_a for CO_2 in cordierite. Results confirmed that this approach is not influenced by sample thickness variation and fitted data for both sample set yield a value of $-\log D_0 = 4.4 \pm 0.7$ m^2/sec and $E_a = 204 \pm 15$ kJ/mol.

Section III: Experimental diffusion of CO_2 in cordierite and beryl at different *PTt* conditions (Chapter 5).

In this section I examined the interaction of cordierite with a CO_2–rich fluid under different experimental *P*, *T*, *t* conditions and evaluated the diffusion coefficients within the crystals. Experiments were performed using a non-end loaded piston cylinder apparatus (QUICKpress™ design by Depths of the Earth Co. Fig. 9a). FTIR spectra were acquired using a Bruker™ Hyperion 3000 microscope (Fig. 9b) at Laboratori Nazionali di Frascati-Istituto Nazionale di Fisica Nucleare (LNF-INFN,) Frascati (Rome).

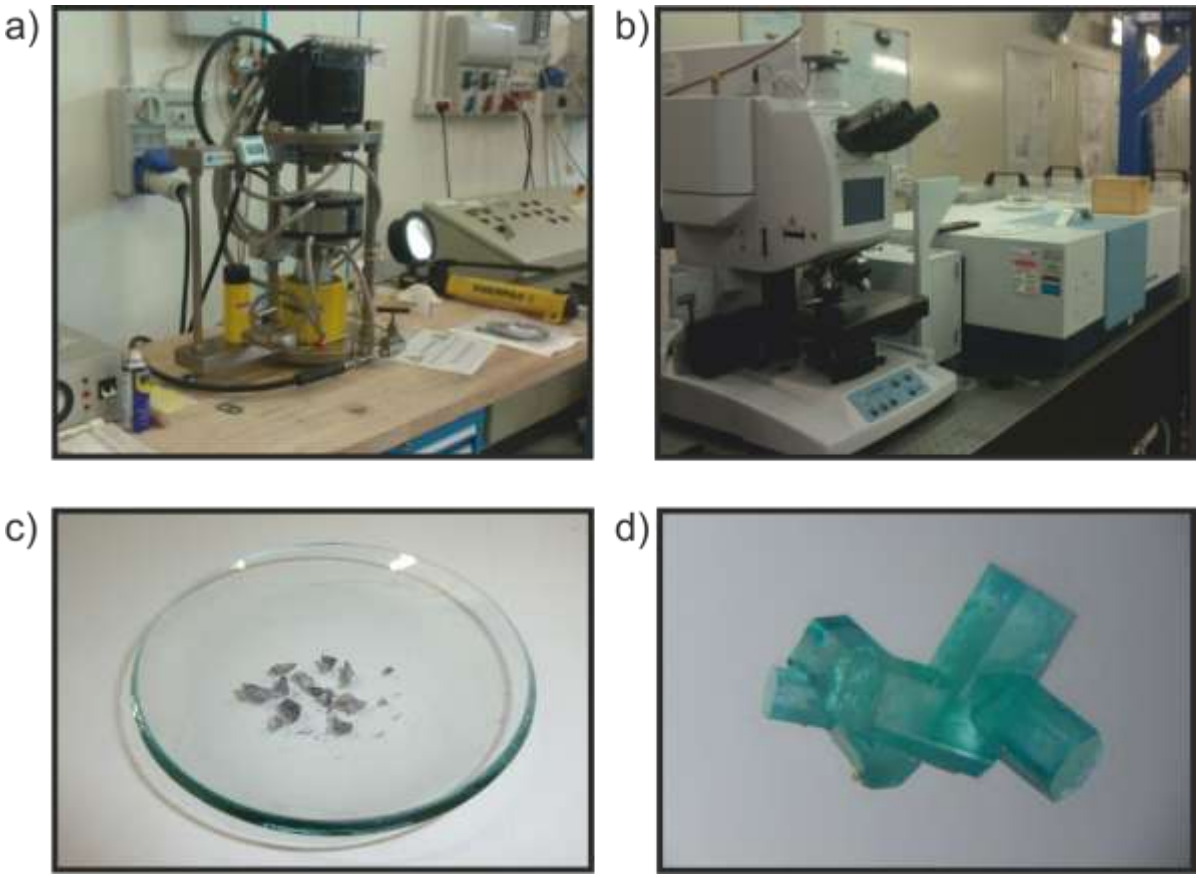

Figure 9 - (a) QUICKpress™ Non end-load Piston-cylinder Press, (b) Bruker Hyperion 3000™ FTIR microscope equipped with FPA detector. (c) Fragments of the cordierite sample RP 7344 from Karur, India and (d) a cluster of green synthetic beryls (photo courtesy of Roberto Pucci).

Several cordierite fragments (Mg-cordierite sample RP 7344 from Karur, Tamil Nadu, Chapter 1) were separated from a large single crystal (Fig. 9c). Before the experiments, the grains were pre-treated at 1250 °C for 24 hour in order to remove all H_2O and CO_2 from the sample (Chapter 5). Grains were optically clean, however cracking of larger grains occurred

during the heat-treatment. Beryl samples are from the very first flux-grown synthetic emeralds made by P.G. Hautefueille and A. Perrey in 1888 in Paris (Bellatreccia *et al.*, 2008); samples show a perfect prismatic hexagonal habitus with a maximum length of 1 mm and width of 0.5 mm (Fig. 9d).

The experiments were carried in 3 x 9 mm Pt capsules; silver carbonate was used as a CO_2 source. Al_2O_3 powder was mixed in 1 to 1 ratio by wt. with Ag_2CO_3, and added to the charge. The aluminum oxide powder was used to prevent the contact between the crystals and the capsule walls after the silver carbonate disappearance due to its decomposition. Layers of Ag_2CO_3/Al_2O_3 mix were alternated to layers of starting crystals (Fig. 10a). Each capsule contained from 4 to 7 grains of cordierite/beryl, for a total crystal weight of 2 to 10 mg. All components used to prepare the tubes were dried up at 110 °C

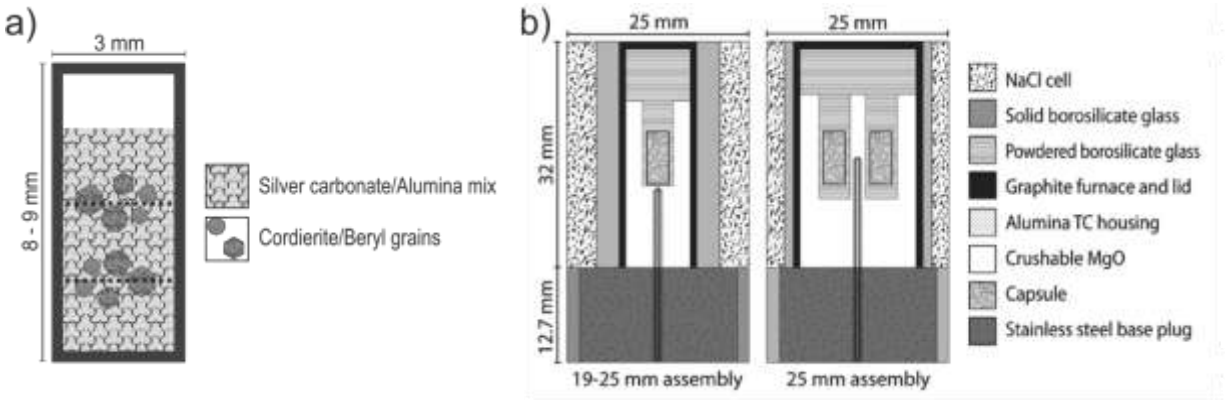

Figure 10 – (a) Schematic section of the layered crystal/filler assemblage within the capsule, (b) schematic cross section a 19-25 mm and 25 mm furnace assembly (modified after Masotta *et al.*, 2012b).

Piston cylinder experiments were conducted using two different set-ups (Fig. 10b): using a standard 19 mm assembly (Moore *et al.*, 2008), operating at P from 300 to 800 MPa and a 19-25 or 25 mm assembly (P from 150 to 300 MPa). The 25 mm assembly may accommodate up to 4 samples in a single run (Masotta *et al.,* 2012b). We used a NaCl-Pyrex-Graphite-crushable-MgO–pyrex assembly with capsule surrounded by pyrex powder instead of pyrophyllite to avoid water infiltration. Temperature was controlled using a C-type ($W_{95}Re_5$ – $W_{74}Re_{26}$) thermocouple with a ±5 °C uncertainty (Holtz *et al.*, 2001). Heating rates were set to 100 °C/min; the isobaric quenching rate ranged from 50 °C/s (25 mm assembly) to 100 °C/s (19 mm and 19-25 mm assembly) in the first 5 seconds (Masotta *et al.,* 2012b). Experiments were performed in the pressure range 200 – 700 MPa, temperature range 700 – 900 °C; run duration varied from 1 to 72 hours.

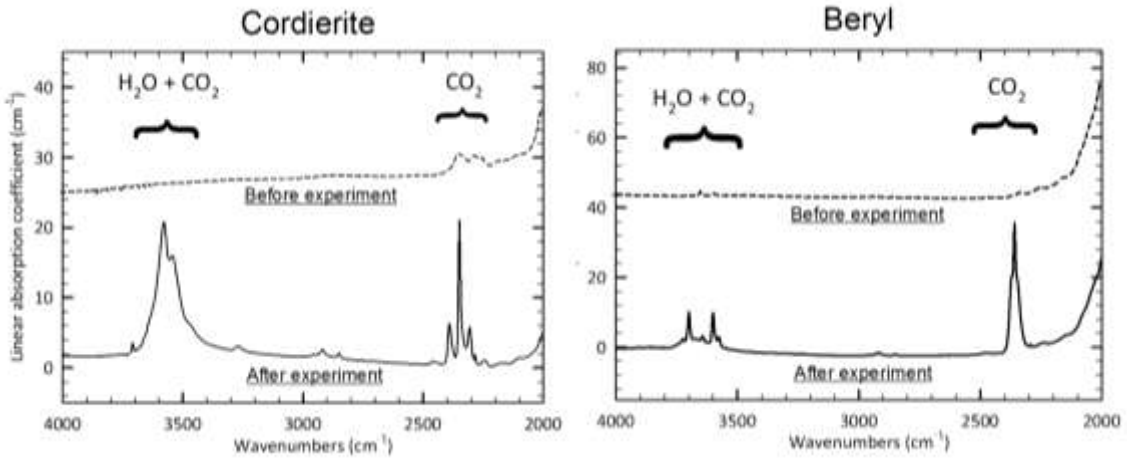

Figure 11 - (left) Unpolarized single-crystal spectra of a cordierite before and after treated at 900 °C and 500 MPa for 1 hour (CRD_Pr 15). (right) Unpolarized single-crystal spectra of a beryl before and after treated at 800 °C and 500 MPa for 10 hour (Pa_340 t).

Preliminary FTIR single spot measurements confirmed that H_2O and CO_2 had been diffused in the samples (Fig. 11), however an evident heterogeneity in carbon dioxide absorbance was observed. Therefore all samples were carefully examined by FPA to locate the area suitable for analytical spots. In particular FPA imaging revealed that the CO_2 diffusion in both cordierite and beryl proceeds exclusively along the structural channels (Fig. 12). FPA images also showed a strong enhancement of the CO_2 diffusion along cracks.

On the basis of these results we located the most suitable area for the analytical spots avoided measurements close to fractures; the beam size was kept as small as possible, usually at 20x20 μm^2 and the highest absorbance values were selected as representative of the CO_2 content of the sample.

The CO_2 contents were calculated from polarized FTIR spectra using the Beer-Lambert relationship using the procedure described in Della Ventura *et al.* (2010).

Final data shows that *T* plays only a minor role on the CO_2 diffusion for both cordierite and beryl, while pressure has a significant effect. In particular, beryl shows a steep increase in CO_2 content from 200 MPa to 500 MPa and from 500 MPa to 700 MPa. The CO_2 contents in cordierite, on the other side, show only a minor increase from 200 MPa to 500 MPa, with a significant jump from 500 MPa to 700 MPa.

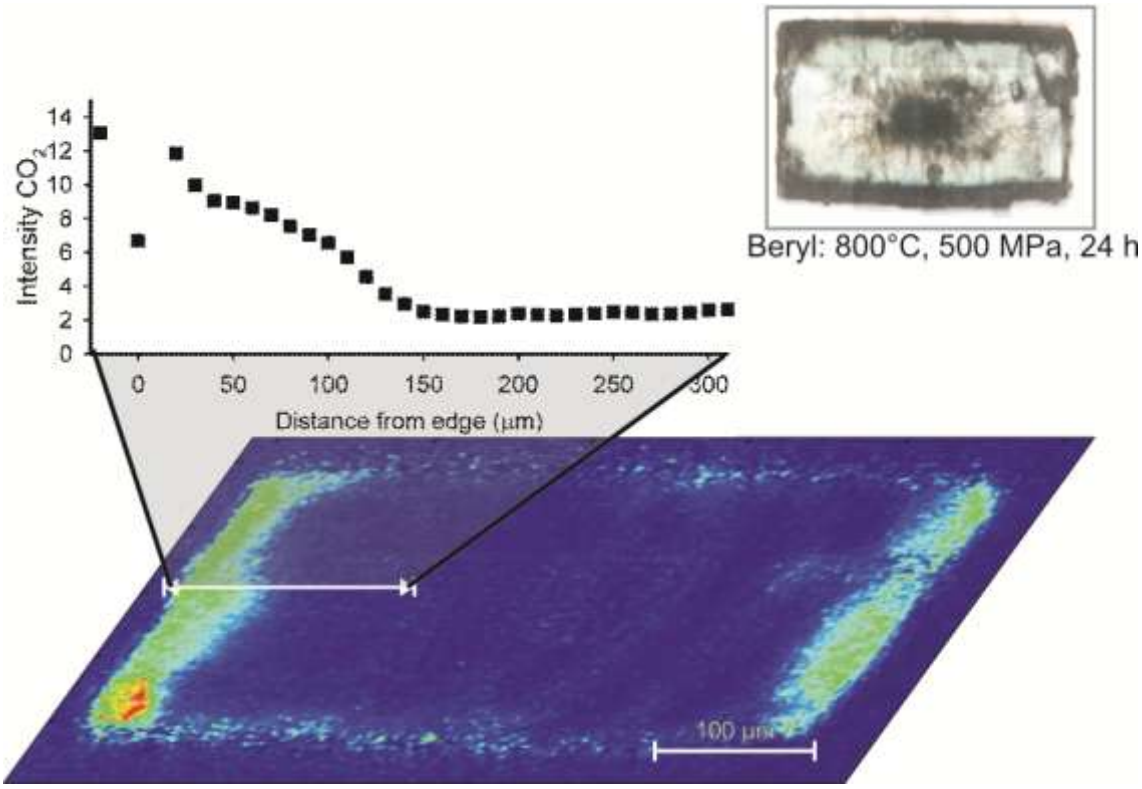

Figure 12 - FPA image and FTIR diffusion profile of beryl Pa_340 d bis treated at 800°C and 500 MPa for 24 hours.

The diffusion coefficient (*D*) for beryl was obtained by fitting the concentration profiles (Fig. 12) using a simple mono dimensional equation (Crank, 1975, Zhang and Cherniak, 2010):

$$C = C_0 \cdot erfc\left(\frac{x}{2\sqrt{Dt}}\right)$$

where *C* is the concentration at depth *x* (m) from the sample rim, C_0 is the maximum concentration, *D* is the diffusion coefficient (m^2/s), t is the time duration (s), and *erfc* is the complementary error function. Obtained D values range from 7.6E-13 to 6.3E-14 for cordierite, and 1.1E-14 to 9.5E-14 for beryl.

Activation energy (E_a) and pre-exponential factor ($-\log D_0$) were determined fitting the data on the basis of the Arrhenius equation.

$$\log(D) = \log(D_0) - E_a/R \cdot \ln(10) \cdot 1/T$$

Mean activation energy (E_a) for beryl data is 122±15 kJ/mol with a pre-exponential ($-\log D_0$) factor of 7.2±0.7.

Section IV: The diffusion of volatiles in hourglass zoned beryl, the coordination environment of H_2O in low-water samples and comments on the geological storage of CO_2 in beryl (Chapters 6, 7 and 8).

Chapters 6 and 7 deal with some particular features observed during the present Thesis, *i.e.* the role of chemical inhomogeneity in the diffusion of CO_2 in beryl, and the coordination environment of H_2O in the channels.

Some synthetic samples used for the diffusion experiments had a typical hourglass structure due to the distribution of Cr during the crystal growth (*e.g.* Bellatreccia *et al.*, 2008). After the experimental run, the FTIR-FPA imaging of these sample showed an unexpected distribution of the diffused molecules within the channels (Fig. 14): CO_2 apparently diffuses following the hourglass boundaries, while $H_2O^{[II]}$ is homogeneously distributed except along the hourglass traces.

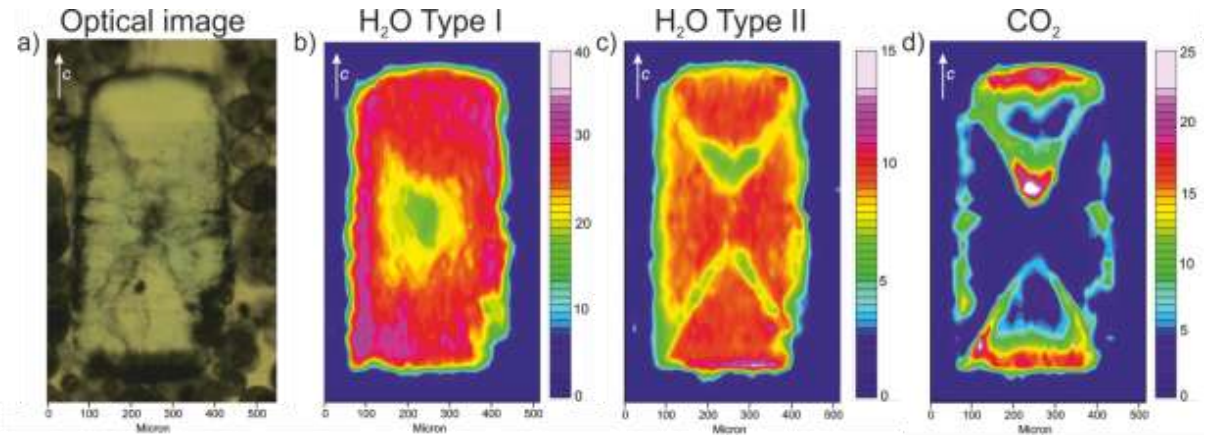

Figure 14 – Polarized light FPA images of the beryl sample treated for four days at 800°C, 500 MPa. Optical image of the grain (a), E//c FTIR-FPA map of $H_2O^{[I]}$ (b) and $H_2O^{[II]}$ (c) distribution, and (d) E⊥c FPA map of CO_2. Chromatic scale is proportional to CO_2 content.

Considering that the carbon dioxide diffusion in beryl and cordierite is significantly enhanced by the presence of fractures (chapter 5) we performed high-resolution FESEM imaging (Fig. 15) to check for the possible presence of physical discontinuities across the hourglass boundary. The results showed that indeed the hourglass structure was exclusively due to a chemical zoning, thus suggesting that the diffusion pattern of CO_2 observed in

Figure 14 must be related to a kind of defect fast-path diffusion mechanism (Zhang *et al.*, 2006).

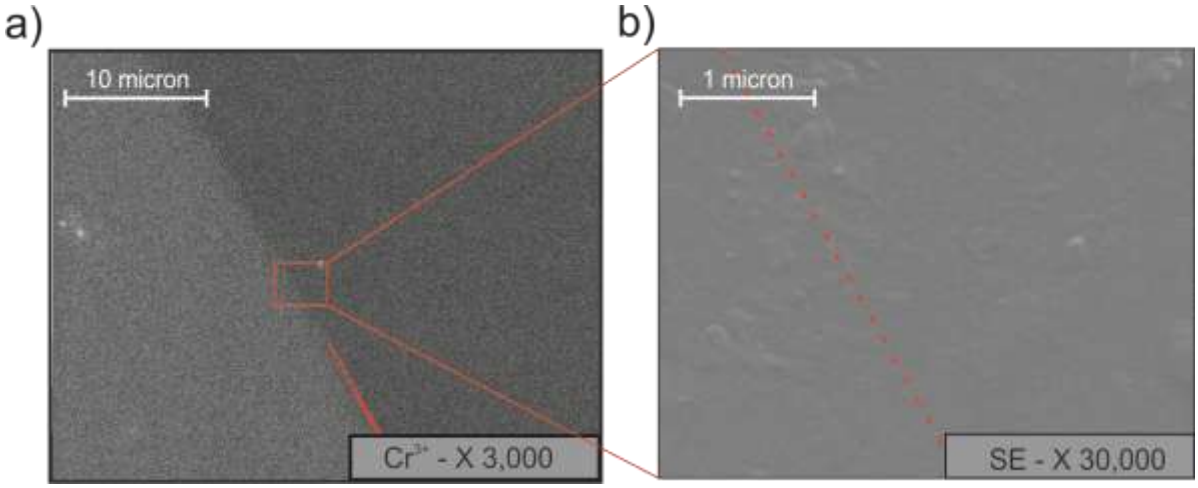

Figure 15 – Field Emission SEM pictures of the treated beryl sample in correspondence of the "hourglass" structure in a fracture free area. (a) EDS chemical mapping of Cr^{3+} zoning. (b) topological Secondary Electron (SE) images of the highlighted area. The red dashed line indicates the limit of the "hourglass" sector zoning.

TOF-SIMS chemical maps showed K is enriched along the hourglass boundary, while Na is depleted. Considering that $H_2O^{[II]}$ is preferentially associated Na^+ cations inside the channels it is reasonable to infer that $H_2O^{[II]}$ depletion along the hourglass discontinuity is the result of the increased K^+ content at the expense of Na occurring along these chemical boundary.

As explained in chapter 5, the HT/HP experiments aimed at the CO_2 diffusion across cordierite and beryl were done using a piston-cylinder apparatus, where the pressure was mechanically and not hydrothermally increased. The infrared spectra of the run products, as expected, showed the presence of significant CO_2 but also of minor H_2O; due to the experimental conditions, this water content must be related to moisture present in the starting products used for the synthesis, thus its bulk amount is very low. Single-spot spectra collected along profiles parallel to the *c* crystallographic axis show subtle changes as a function of the distance from the crystal edge; these changes can be correlated to a progressive change in the H_2O coordination environment in the channel (Fig. 16), as a response to the varying H_2O/alkali content. In particular, the data show that when $2 \cdot H_2O > Na^+$ apfu, H_2O can assume both type I and type II orientation; in the latter case, each Na cation coordinates two $H_2O^{[II]}$ molecules (doubly coordinated H_2O). If $2 \cdot H_2O < Na^+$ apfu, than

$H_2O^{[II]}$ molecules are singly coordinated to each Na cation. The same type of feature is observed and commented for the structurally related cordierite.

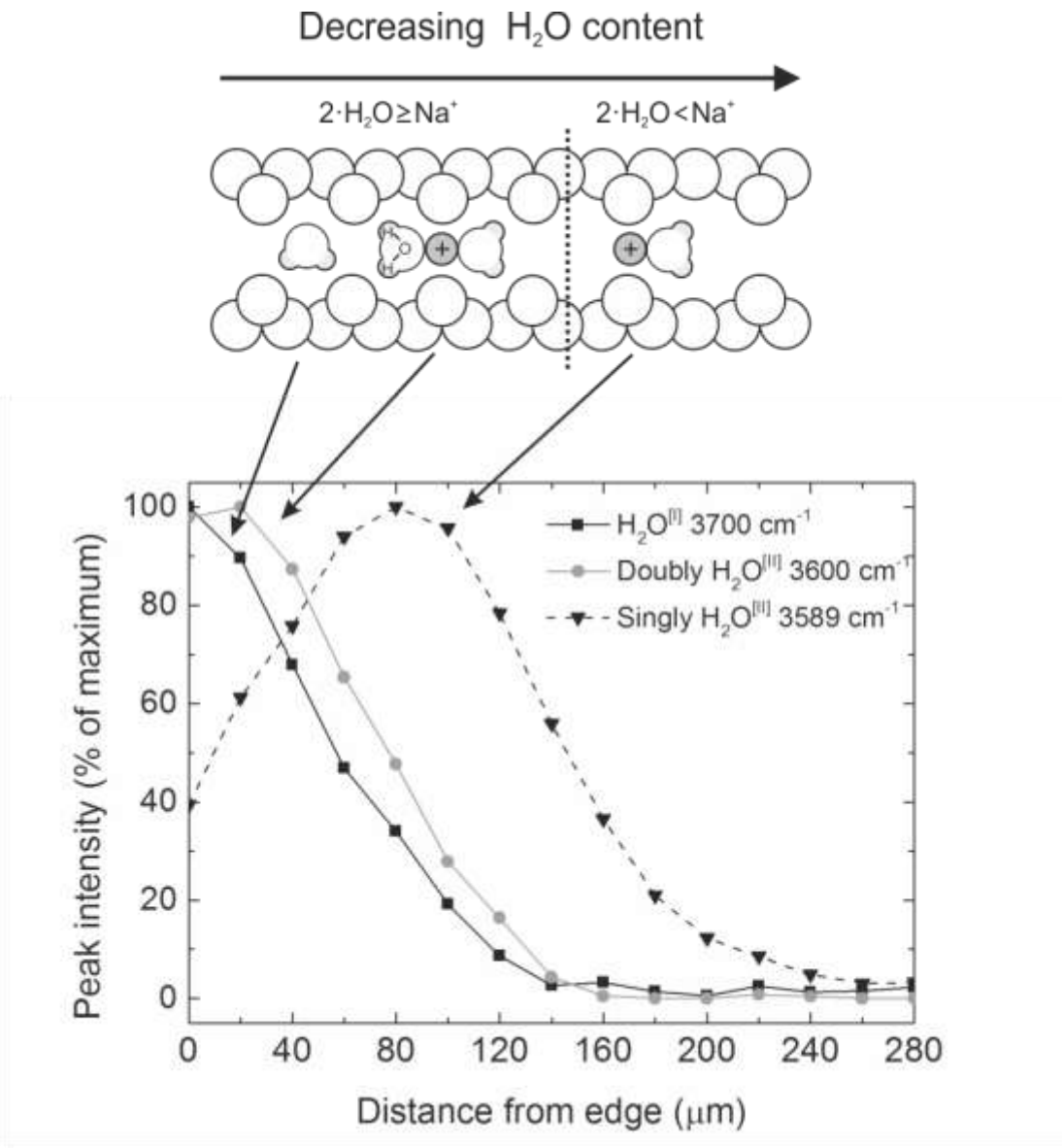

Figure 16 – Concentration trend of selected peak for sample Pa 340_o treated at 800 °C. Peak intensity were scaled to the maximum intensity. A schematic representation of the configuration of water molecules inside the structural channels of beryl, as the overall water content decreases in given above.

The implication of this finding is that H_2O in beryl and in cordierite is trapped in the structural channel following very different bonding environments, and this has a significant consequence on the diffusion rates (both inward and outward) obtained in experiments and hence on the calculation of thermodynamic properties from the observed data. For cordierite in particular, considering it is widely used in metamorphic petrology as an

indicator of the fluid system in equilibrium with the rock, the different diffusion mechanisms of water and CO_2 could affect the closing temperatures modeled on the basis of field studies.

Chapter 8 reports a short paper in press on the *Rendiconti Online della Società Geologica Italiana* discussing problems related to the permanent storage of carbon dioxide in microporous minerals.

PUBLISHED ON CONTRIBUTION TO MINERALOGY AND PETROLOGY (JULY 2012)

DOI 10.1007/s00410-012-0779-8

CHAPTER 1

QUANTITATIVE ANALYSIS OF H_2O AND CO_2 IN CORDIERITE USING POLARIZED FTIR SPECTROSCOPY

Giancarlo Della Ventura[1,2,3], Francesco Radica[1], Fabio Bellatreccia[1,2], Andrea Cavallo[3], Francesco Capitelli[4] and Simon Harley[5]

[1]Dipartimento di Scienze Geologiche, Università Roma Tre, Largo S. Leonardo Murialdo 1, I-00146 Roma, Italy

[2]LNF-INFN, Via E. Fermi 40, Frascati (Roma), Italy

[3]INGV, Via di Vigna Murata 605, Roma, Italy

[4]Institute of Crystallography, CNR, Via Salaria Km 29,300, 00016 Monterotondo, Roma (Italy)

[5]School of GeoSciences, University of Edinburgh, Kings Buildings, West Mains Road, Edinburgh EH9 3JW, Scotland, UK

Abstract

We report a FTIR (Fourier-transform infrared) study of a set of cordierite samples from different occurrence and with different H_2O/CO_2 content. The specimens were fully characterized by a combination of techniques including optical microscopy, single-crystal X-

ray diffraction, EMPA (electron micro probe analysis), SIMS (secondary ion mass spectrometry), and FTIR spectroscopy. All cordierites are orthorhombic *Ccmm*. According to the EMPA data, the Si:Al ratio is always close to 5:4; X_{Mg} ranges from 76.31 to 96.63 and additional octahedral constituents occur in very small amounts. Extraframework K and Ca are negligible, while Na reach values up to 0.84 apfu. SIMS shows H_2O up to 1.52 and CO_2 up to 1.11 wt%.

Optically transparent single-crystals were oriented using the spindle-stage and examined by FTIR micro-spectroscopy under polarized light. On the basis of the polarizing behaviour, the observed bands were assigned to water molecules in two different orientations and to CO_2 molecules in the structural channels. The IR spectra also show the presence of small amounts of CO in the samples. Refined integrated molar absorption coefficients were calibrated for the quantitative microanalysis of both H_2O and CO_2 in cordierite based on single-crystal polarized-light FTIR spectroscopy. For H_2O the integrated molar coefficients for type I and type II water molecules (ν_3 modes) were calculated separately and are $^{[I]}\varepsilon$ = 5200 ± 700 l·mol^{-1}·cm^{-2} and $^{[II]}\varepsilon$ = 13000 ± 3000 l·mol^{-1}·cm^{-2}, respectively. For CO_2 the integrated coefficient is ε_{CO2} = 19000 ± 2000 l·mol^{-1}·cm^{-2}.

Key words: cordierite, EMPA and SIMS, polarised FTIR spectroscopy, quantitative H_2O and CO_2 analysis.

1. Introduction

Cordierite, ideally $(Mg,Fe)_2Al_4Si_5O_{18}$, is a unique case of a microporous mineral stable under geological conditions spanning from the amphibolite facies to UHT metamorphism to crustal anatexis (Vry et al. 1990; Carrington and Harley 1995, 1996; Smith 1996; Kalt 2000; Harley et al. 2002; Bertoldi et al. 2004). Because of its structural channels, cordierite is able to trap H_2O and CO_2 (Schreyer and Yoder 1964; Armbruster and Bloss 1980; Kurepin 1985; Schreyer 1985; Carey 1995), but also hydrocarbons (Zimmermann 1981; Mottana et al. 1983; Khomenko and Langer 1999), CO (Khomenko and Langer 2005; Della Ventura et al. 2009), Ar (Armbruster 1985; Schreyer 1985) and N_2 (Armbruster 1985; Cesare et al. 2007). For this reason, the

analysis of the volatile constituents of cordierite can be a very useful tool to define the composition of coexisting fluids during its formation (e.g. Vry et al. 1990; Visser et al. 1994; Carrington and Harley 1996; Kalt 2000; Harley et al. 2002). Moreover, H_2O and CO_2 contents may significantly affect the stability of cordierite (e.g. Schreyer 1985; Carey 1995; Harley et al. 2002), therefore the quantitative evaluation of the channel constituents is crucial in petrologic studies.

The microanalysis of light elements like hydrogen and carbon is still extremely complex (e.g. Rossman, 2006); due to their low atomic number these elements cannot be easily studied by electron microprobe; moreover H and C are very poor X-rays scatterers hence they cannot be studied with conventional X-rays diffraction methods.

On the other hand, infrared spectroscopy is an efficient technique to detect the volatile components within the structural pores of cordierite (Farrell and Newnham 1967; Goldman et al. 1977; Aines and Rossman 1984; Le Breton 1989; Kolesov and Geiger 2000; Khomenko and Langer 2005; Rigby et al. 2008, Della Ventura et al. 2009); coupled with well-tested methods for volatile quantification like secondary ion mass spectroscopy (e.g. Thompson et al. 2001), it can be a simple yet powerful tool for sample volatile quantification (Della Ventura et al. 2009). In addition, IR has the distinguishing advantage of providing information on the closest structural environment of the target element, its molecular arrangement (for example OH *vs* H_2O, CO_2 *vs* CO_3) and the orientation of the molecules within the structure. Moreover, by using the modern techniques of FTIR imaging with the bi-dimensional focal plane array of detectors (FPA), enables detection of the zoning of volatile species across the studied sample.

Despite the large number of studies, a calibration for unambiguous infrared quantitative analysis of H_2O and CO_2 in cordierite is still lacking. The quantitative determination of an absorber (c, concentration) in a mineral is based on the Beer-Lambert law: $c = A_i / (t \cdot \varepsilon_i)$, where A_i (cm^{-1}) = integrated absorbance, t (cm) = sample thickness and ε_i (cm^{-2} per mol H_2O/L) = integrated molar absorption coefficient. A_i and t are measured, but the ε_i coefficient must be calibrated for any mineral matrix by combining an independent method. Libowitzky and Rossman (1996) definitively showed that for quantitative purposes the measurement of the absorbance in anisotropic minerals must be obtained summing-up the integrated absorbance along the three principal optical directions. For orthorhombic cordierite thus $A_i = A_x + A_y + A_z$.

For H_2O, the only molar absorption coefficient available for cordierite has been calibrated by Goldman et al. (1977) using linear (peak height) intensity data, while the only coefficient available for CO_2 has been recently calibrated by Della Ventura et al. (2009) on one cordierite crystal from a partially melted graphite-bearing granulitic enclave within the dacitic lava dome of El Hoyazo (SE Spain). According to Della Ventura et al. (2009) several problems are involved in the analysis of cordierite, primarily the possible zoning of H_2O/CO_2 in the sample and the widespread presence of inclusions or alteration products even in apparently gemmy crystals.

We address in this paper the calibration for a reliable analysis in cordierite by studying a set of samples from different occurrences.

2. Samples and analytical methods

Eight different cordierite samples (Table 1) from different localities and geological occurrences were chosen for this work such as to cover a wide range in the H_2O/CO_2 ratio. The crystals used for the spectroscopic data collection were previously fully characterized using a multidisciplinary approach.

Table 1- Sample labels and occurrence of the studied samples.

Sample	Occurrence
BM 96512	Cabo de Gata, Almaria Region, Spain
8/90	Serre Massiff, Calabria, Italy
RIG	Unknown
BB3a	Brattstrand Bluffs, Prydz Bay, Antarctica
Rp 7344	Karur, Tamil Nadu, India
Rp 5578	Tsihombe, Madagascar
Rp 3237	Kragero, Arendal, Norway
Rp 7045	Region de Bekily, Madagascar

Single-crystal X-ray diffraction data were collected on optically clean grains free from inclusions and alteration products at CNR Istituto di Cristallografia (Bari) with a Nonius Kappa CCD area detector diffractometer, using Mo-K radiation (= 0.71073 Å). Cell refinement and data reduction was performed via EvalCCD (Duisenberg et al. 2003) and absorption correction via

SADABS (Sheldrick 1996).

The structures were solved through the Direct Methods procedure of SIR2008 (Burla et al. 2007), within the orthorombic space group *Cccm*, and refined by a full-matrix least-square techniques based on F^2 using SHELX-97 (Sheldrick 1997).

The electron microprobe analyses (EMPA) were done using a Joel JXA 8200 WD-ED at the Istituto Nazionale di Geofisica e Vulcanologia (INGV), Roma. Working conditions were 15 kV accelerating voltage, 7 nA sample current, 5 µm beam diameter, counting times: 10 seconds on the peak and 5 seconds on the background on both sides of the peak. The standards, spectral lines and crystals used were: albite (Na*Kα*, TAP), pargasite (Ca*Kα*, PET), wollastonite (Si*Kα*, PET), k-feldspar (K*Kα*, PET), kyanite (Al*Kα*, TAP), pargasite (Mg*Kα*, TAP), augite (Fe*Kα*, LIF), titan oxyde (Ti*Kα*, LIF) and spessartine (Mn*Kα*, LIF). Data correction was performed using the ZAF method. Sample homogeneity was verified collecting several spots per crystal.

The H_2O and CO_2 contents were quantified by SIMS (secondary-ion-mass-spectrometry) using a Cameca IMS4f ion microprobe at EMMAC, the University of Edinburgh. Procedures follow those described in previous cordierite studies from the Edinburgh laboratory (Harley and Carrington 2001; Thompson et al. 2001; Harley et al. 2002). A 2.58 cm diameter analysis block incorporating the studied samples, and two standard cordierite grains (ANMH with X_{Mg} = 0.89; H_2O = 1.54 wt%; and CO_2 = 0.7 wt% and 8/90 with X_{Mg} = 0.75; H_2O = 0.81 %; and CO_2 = 1.31 wt%: Thompson et al. 2001) was prepared, coated with gold, and inserted into the IMS4f sample change chamber for overnight pump-down prior to in-situ SIMS analysis. Negative secondary ions ^{1}H, ^{12}C and ^{28}Si were measured at an energy offset of 75 V and energy window of 19 eV, under operating conditions of 4500 V secondary beam voltage and 8 nA and 10 kV for the primary beam of O^- ions. Under these conditions the primary ion beam sputters an elliptical analysis pit with long diameter 25-30 µm and maximum depth of 3 µm. All analyses involved a 3 minute burn-in time followed by 20 cycles of 5 second counts for each isotope. The mean isotope ratios of $^{1}H/^{28}Si$ and $^{12}C/^{28}Si$ for the last 10 cycles in each analysis has been taken as the final results, thereby avoiding surface contamination. Analyses expressed as isotopic ratios of $^{1}H/^{28}Si$ and $^{12}C/^{28}Si$ were converted to wt% H_2O or CO_2 by comparison with the calibration lines produced from fitting two standards analysed several times throughout the same analytical session.

FTIR spectra were acquired with a Nicolet Magna 760 spectrophotometer, equipped with a NicPlan Microscope, a KBr beamsplitter and a liquid nitrogen-cooled MCT detector at University Roma Tre. Polarized spectra were collected using a gold-wire grid polarizer on a ZnSe substrate. The nominal resolution was 4 cm^{-1} and 128 scans were averaged for both spectrum and background. Several fragments from each specimen were oriented using a spindle stage (Bloss 1981) fitted on a polarizing microscope following the procedure of Gunter et al. (2004). The fragments were transferred on glass slides and doubly polished to thickness variable from 20 to 190 µm. Sample thickness was measured with a Leica DCM 3D optical profilometer, at LIME (Laboratorio Interdipartimentale di Microscopia Elettronica), Università Roma Tre; vertical resolution was < 15 nm in confocal mode (20X lens, NA = 0.50) and < 4 nm in interferometric mode (50X lens, NA = 0.50); final thickness was averaged for the whole surface of the sample. FTIR maps were collected at INFN (Istituto Nazionale di Fisica Nucleare) of Frascati (Roma) using a Bruker® Hyperion 3000 IR microscope equipped with a computer-controlled, motorized sample stage and an MCT detector. Single spot spectra were collected using a beam size varying from 50 to 200 µm, on a grid up to several mm^2. FTIR images for some selected areas were acquired using a 64×64 pixel focal plane array (FPA) of detectors. By using a 15X objective each image covers an area of 170 × 170 μm^2 with a spatial resolution of ~ 5 µm (Della Ventura et al. 2010). For both maps and images the nominal resolution was set at 8 cm^{-1}, and 128 scans were averaged for each spectrum and background.

3. X-ray diffraction, optical properties and microchemistry

Single-crystal X-ray diffraction showed all samples to be orthorhombic *Cccm*; refined cell parameters are listed in Table 2.

Table 2 also give selected microchemical data, where all oxides are from EMPA, except H_2O and CO_2 which are from SIMS; the resulting crystal-chemical formulae were calculated on the basis of 18 oxygen atoms. For all samples the Si:Al ratio is always close to the stoichiometric 5:4 value (Table 2) thus excluding additional cations, such as Be and Li (Schreyer et al. 1979, Sokol et al. 2010) at the four-fold coordinated sites. Fe has been considered as Fe^{2+} (Goldman et al. 1977, Geiger et al. 2000); Mg and Fe are the main

octahedral occupants, with the X_{Mg} (= Mg/Mg+Fe) ranging from 76.31 to 96.63. Additional elements occur in very low amounts; Ti and Mn are always < 0.01 apfu, except in sample BM96512 where Mn ≈ 0.03 apfu. K and Ca occur in very minor amounts (< 0.01 apfu) while Na may reach values as high as 0.84 apfu (sample Rp7344, Table 2). SIMS shows that the studied samples contain variable H_2O and CO_2. H_2O, in particular, is extremely low in sample BB3a from Antarctica (Fitzsimons 1996; Thompson et al. 2001) and is > 0.50 apfu in sample RP7344 from Tamil Nadu (Bertoldi et al. 2004; Lal et al. 1984) (Table 2). This latter sample shows also the lowest content in carbon dioxide, while the highest CO_2 content is recorded in specimen 8/90 from the high-grade metamorphic rocks of Calabria (Italy). As expected, no relationship between H_2O and CO_2 contents is observed.

Table 2 - Microchemical analysis, crystal-chemical formula, cell parameters, density and optical properties for the studied cordierites.

Sample	BM 96512	8/90	RIG	BB3a	RP 7344	RP 5578	RP 3237	RP 7045
Chemical analysis (wt.%)								
SiO_2	49.10	48.33	49.61	48.27	49.65	49.43	49.55	49.19
Al_2O_3	33.10	32.83	33.50	32.91	33.11	32.78	33.01	33.33
MgO	10.04	9.48	12.94	8.45	13.20	11.94	12.49	10.79
FeO	5.21	6.35	0.75	8.33	1.06	2.52	1.86	4.49
TiO_2	0.03	0.04	0.05	0.04	0.02	0.00	0.00	0.06
MnO	0.34	0.05	0.03	0.06	0.01	0.05	0.02	0.12
CaO	0.04	0.01	0.01	0.01	0.02	0.02	0.00	0.01
Na_2O	0.15	0.10	0.19	0.03	0.43	0.17	0.24	0.05
K_2O	0.03	0.00	0.02	0.12	0.01	0.00	0.00	0.01
H_2O	0.62	0.81*	n.a.	0.175	1.52	0.91	0.9	0.37
CO_2	0.51	1.3*	n.a.	0.74	0.22	1.11	1.01	0.69
Total	99.16	99.31	97.10	99.14	99.25	98.94	99.06	99.11
Crystal chemical formula (apfu)								
Si	5.005	4.990	4.998	4.979	4.996	5.028	5.014	4.991
Al	3.977	3.994	3.977	4.000	3.926	3.930	3.937	3.986
Σ Tetrahedra	8.982	8.984	8.975	8.979	8.922	8.958	8.951	8.976
Mg	1.525	1.459	1.944	1.300	1.979	1.811	1.884	1.632
Fe	0.444	0.548	0.063	0.718	0.089	0.215	0.157	0.381
Ti	0.002	0.003	0.004	0.003	0.002	0.000	0.000	0.005
Mn	0.029	0.004	0.002	0.005	0.001	0.004	0.001	0.011
Σ Octahedra	2.001	2.015	2.013	2.026	2.071	2.030	2.042	2.028
Ca	0.004	0.001	0.001	0.002	0.003	0.002	0.000	0.001
Na	0.029	0.021	0.036	0.007	0.084	0.033	0.047	0.011
K	0.004	0.001	0.003	0.015	0.001	0.000	0.000	0.001
Σ Channels	0.037	0.022	0.040	0.024	0.087	0.035	0.047	0.013
n(H_2O)	0.211	0.277	n.a.	0.060	0.510	0.309	0.305	0.124
m(CO_2)	0.070	0.184	n.a.	0.105	0.031	0.154	0.139	0.096
Σ Volatiles	0.282	0.461	n.a.	0.165	0.541	0.463	0.444	0.220
$^{**}H_2O^{[II]}$	0.138	0.234	n.a.	0.013	0.335	0.238	0.210	0.097
$^{**}H_2O^{[I]}$	0.073	0.043	n.a.	0.047	0.175	0.071	0.095	0.027
$X_{crd}CO_2$	0.25	0.40	n.a.	0.63	0.06	0.33	0.31	0.44

Cell parameters (Å)								
a	17.135(7)	17.118(1)	17.103(1)	17.170(1)	17.020(1)	17.033(3)	17.085(2)	17.132(2)
b	9.781(5)	9.764(3)	9.759(1)	9.766(2)	9.751(1)	9.734(1)	9.721(1)	9.758(1)
c	9.343(7)	9.408(1)	9.451(4)	9.339(1)	9.380(1)	9.368(1)	9.353(1)	9.380(1)
Densitiy (g/cm^3)	2.602(4)	2.612(6)	2.5752(4)	2.630(8)	2.577(1)	2.584(1)	2.58(3)	2.597(2)
Optic sign	Positive	Positive	Positive	Positive	Negative	Positive	Positive	Positive
2Vx (°)	90(3)	102.9(9)	103.4(4)	91(1)	63.15(8)	96(1)	90.3(9)	96.3(7)

Note: H_2O and CO_2 from SIMS, all other elements from EMPA; crystal-chemical formulae in atoms per formula unit (apfu) calculated on the basis of 18 oxygen pfu. For cell parameters, densities and optical $2V_x$ angle estimated standard errors on the last digit are given in brackets. n.a.: not analyzed. ** calculated as explained in the text. * Data from Thompson et al. (2001).

Table 2 also gives the $2V_x$ optic axis angles measured using the spindle stage (e.g. Gunter et al. 2004); all samples are optically positive, except cordierite RP7344 which, having the lowest CO_2 content, is negative (Table 2a). The relationship between the $2V_x$ optical axis angle and the CO_2 content in the cordierite channel has been investigated experimentally by Armbruster and Bloss (1982) who found a linear trend between all optical parameters and the gas (both CO_2 and H_2O) content in the channels. The data reported in Table 2a are in agreement with these results of Armbruster and Bloss (1982) and show that the CO_2 content indeed has a strong effect of the physical properties of cordierite.

Table 3 - Site populations (apfu) on the basis of the X-ray single-crystal refined site scattering for selected atoms. Errors in brackets. Thermal parameters for H_2O and CO_2 were considered all isotropic (U_{iso}) and fixed at values known from the literature (e.g. Malcherek et al. 2001) to avoid refinement instability. Δ = Difference between the microchemical and X-ray derived apfu

Sample	BM96512	8/90	RIG	BB3a	RP 7344	RP 5578	RP 3237	RP 7045
Mg	1.564(8)	1.504(8)	2	1.328(8)	1.984(10)	1.858(10)	1.92(2)	1.660(8)
Fe^{2+}	0.436(8)	0.496(8)	-	0.672(8)	0.016(10)	0.142(10)	0.08(2)	0.340(8)
Na^+	0.042(8)	0.03(1)	0.04(1)	0.05(1)	0.15(1)	0.05(1)	0.05(2)	0.014(9)
O_{H2O}	0.048(8)	0.08(3)	0.09(3)	-	0.10(1)	0.06(6)	-	0.057(5)
C_{CO2}	0.09(2)	0.23(2)	0.29(2)	0.16(2)	0.11(1)	0.25(2)	0.25(3)	0.10(1)
				$\Delta = apfu_{EPMA+SIMS} - apfu_{XR\text{-}SCR}$				
ΔMg	0.039	0.045	0.056	0.028	0.005	0.047	0.04	0.028
ΔFe^{2+}	-0.008	-0.052	-	-0.046	-0.073	-0.073	-0.08	-0.041
ΔNa^+	0.013	0.01	0.004	0.04	0.07	0.02	0.003	0.003
ΔO_{H2O}	-0.163	-0.20	-	-	-0.41	-0.25	-	-0.067
ΔC_{CO2}	0.02	0.05	-	0.06	0.08	0.10	0.11	0.004

Site occupancy refinements (Table 3) were performed from X-ray single-crystal data considering Mg and Fe at the same crystallographic site 8g (total site occupancy factor, s.o.f = 1), Ow (the water oxygens) at the 4a site, C at the 4a site with the carbon-dioxide oxygens at the 8g site (constraining their s.o.f. to be equal), and channel Na at the 4c site (Armbruster 1985;

Malcherek et al. 2001). Comparison of EMP+SIMS values with site occupancies refined from XRD shows an excellent agreement between the two sets of data: Mg^{2+} contents obtained from XRD are slightly overestimated by 0,056 apfu, while Fe^{2+} is underestimated by roughly the same amount and Na^{+} contents are similar within esds. Interestingly, the XRD-refined CO_2 contents are slightly overestimated (Table 3) but still in excellent agreement with SIMS data. On the other side, the agreement for water is rather poor, with H_2O underestimated by as much as 0.41 molecules pfu (Table 3).

4. Single-crystal FTIR spectroscopy

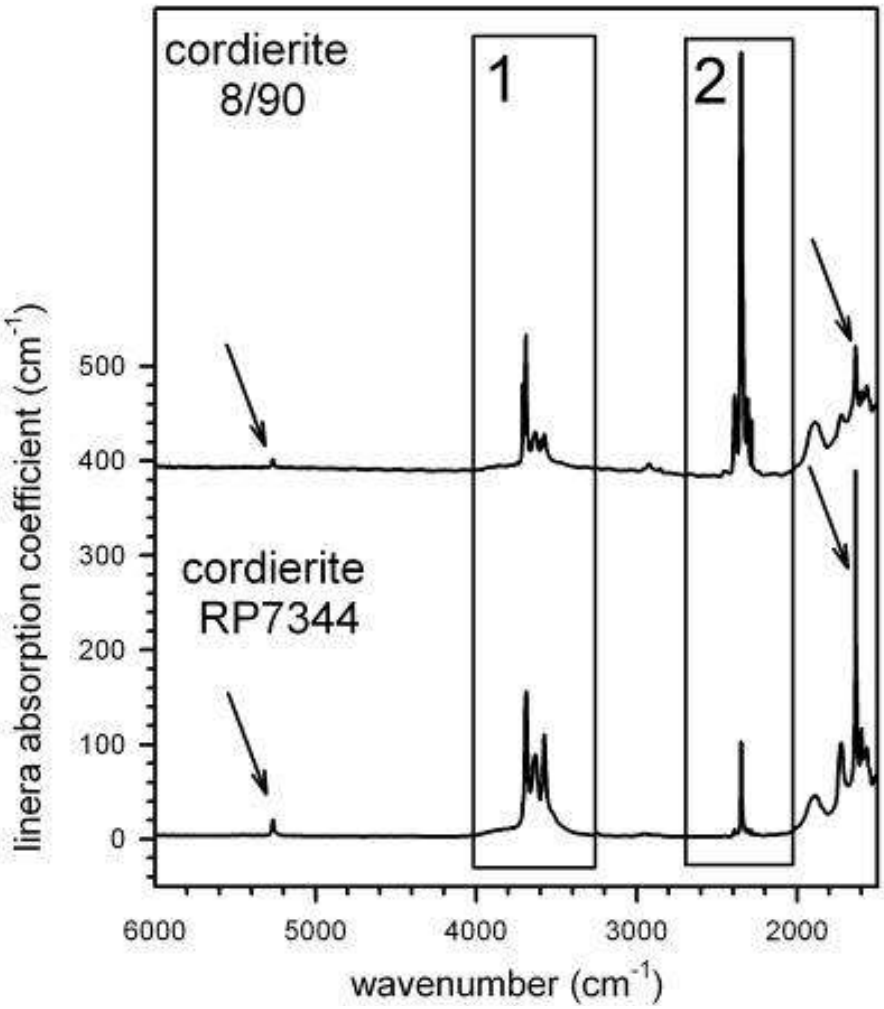

Figure 1 - Non-polarized single-crystal FTIR spectra of samples 8/90 (top) and RP7344 (bottom). Regions 1 and 2 (see text) are highlighted; bending and combination modes at 1635 and 5270 cm^{-1}, respectively, are arrowed. The linear absorption coefficient is defined as linear absorbance / thickness (A/t).

Figure 1 shows two typical unpolarized-light spectra collected on a doubly-polished fragment. The pattern consists of several bands which have been grouped for simplicity in

two regions, from 3900-3300 cm^{-1} (region 1) and 2600-2000 cm^{-1} (region 2), respectively. In both regions intense and relatively sharp peaks are present. Additional peaks relevant to the present discussion occur around 1635 cm^{-1} and in the 4000-6000 cm^{-1} range. As it will be discussed below, these bands are related, respectively, to the bending mode and to the combination of the stretching and the bending modes of the H_2O molecule(s). Furthermore a cursory examination of the unpolarized spectra of Figure 1 shows that the single-crystal FTIR spectrum provides an immediate picture of the relative volatile content for samples with different H_2O/CO_2 contents (RP7344, bottom: high-water and low CO_2; 8/90, top: rich in both H_2O and CO_2).

The polarized-light spectra collected for cordierite RP5578 are displayed in Figure 2. In region 1 (Fig. 2a, left) the most intense peaks are observed for **E** // ***c***, centred at 3689 and 3575 cm^{-1}. A broad and relatively intense band is present at 3630 cm^{-1} in the **E** // ***b*** spectrum, while the main features present in the **E** // ***a*** spectrum are the very sharp peak at 3708 cm^{-1} and a sharp and weak band at 3595 cm^{-1}.

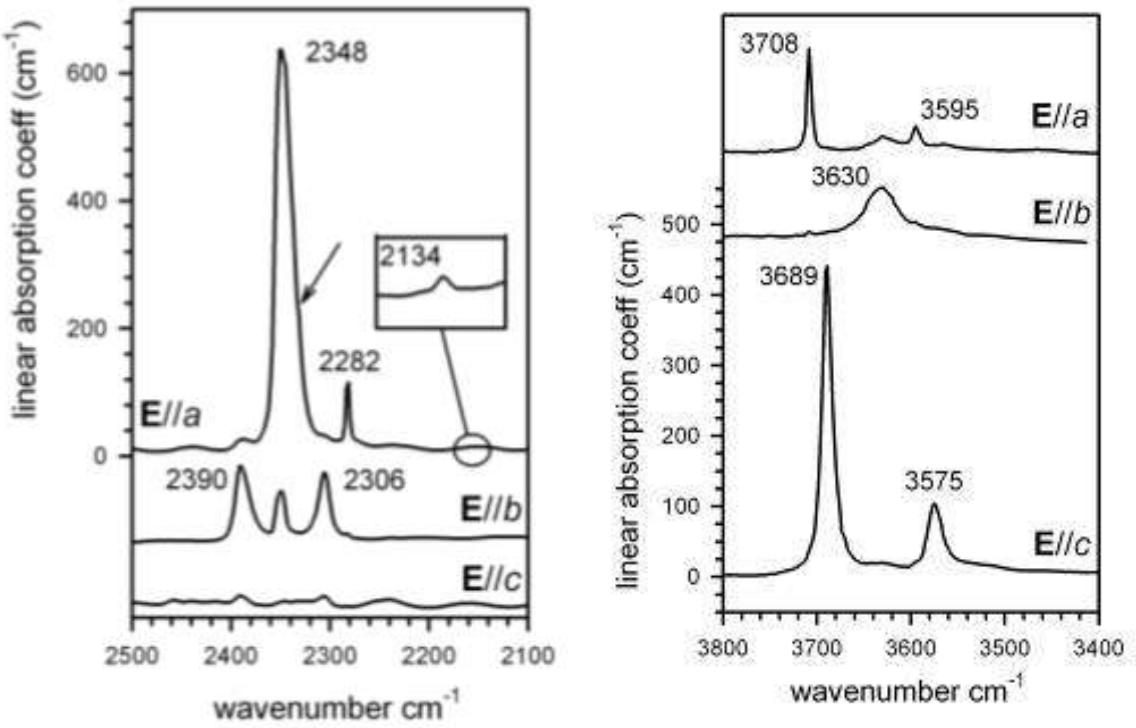

Figure 2A - Single-crystal polarized-light FTIR spectra of cordierite RP 5578 collected on oriented (010), 33 µm thick and (100), 34 µm thick, sections; left = region 1 and right = region 2. Spectra scaled to thickness and vertically displaced for clarity. The weak band at 2134 cm^{-1} (inset) is from sample RP 7045, 72 µm thick section; the linear absorption coefficient of the band is 2 cm^{-1}.

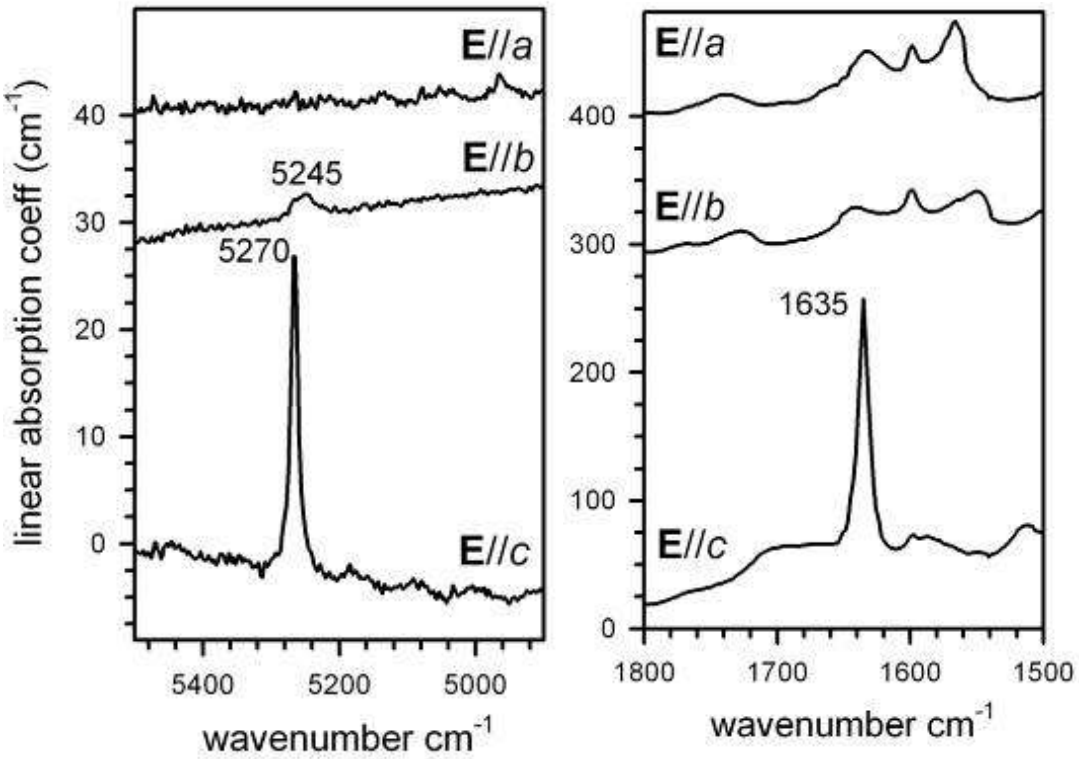

Figure 2B - Left: single-crystal polarized-light FTIR spectra of cordierite RP 3237 collected in the combination region on oriented (010), 20 µm thick and (100), 88 µm thick sections. Right: single-crystal polarized-light FTIR spectra of cordierite RP 5578 in the H_2O bending region, same sections as in Figure 2a. Spectra scaled to thickness and vertically displaced for clarity.

In region 2 (Figure 2a, right) the **E** // ***a*** spectrum shows a very sharp and intense absorption at 2348 cm^{-1}, with a weak shoulder at 2332 cm^{-1} on the low-frequency side (arrowed; see also Fig. 1 of Della Ventura et al. 2009). A minor band is observed at 2282 cm^{-1}, while a very weak peak is resolved, for some samples, at 2134 cm^{-1} (see inset in Fig. 2a and Fig. 1 of Della Ventura et al. 2009). The **E** // ***c*** spectrum is featureless, while the **E** // ***b*** spectrum shows a minor band at 2348 cm^{-1} with two side bands at 2390 and 2306 cm^{-1}, respectively.

In the NIR (near infrared) 4500-5500 cm^{-1} region (Figure 2b, left) the **E** // ***c*** spectrum shows a sharp and relatively intense (note that the absorption coefficients in this range are one order of magnitude lower than those in Figure 2a) absorption at 5270 cm^{-1}; the **E** // ***b*** spectrum shows a broad and minor band centred at 5245 cm^{-1}, while the **E** // ***a*** spectrum is featureless. In the H_2O bending region (1500-1800 cm^{-1}, Figure 2b, right) there is a very sharp peak at 1635 cm^{-1} for **E** // ***c***; this peak disappears for both **E** // ***b*** and **E** // ***a***.

5. Interpretation of polarized FTIR spectra

The correct assignment of the bands observed in the spectra of cordierite is a critical point when attempting to use the absorbance data for quantitative purposes. This issue has been addressed by Della Ventura et al. (2009) who critically revised the existing literature on the interpretation of the IR spectra of cordierite. Their conclusions will be used as a guide in the following text, and will be augmented with the analysis of the entire wavenumber range extending from 6000 cm^{-1} (NIR) to 1500 cm^{-1} (MIR).

The structural environment of the H_2O and CO_2 molecules in cordierite is shown in Figure 3. Based on all previous spectroscopic and crystal-structural studies (see Della Ventura et al. 2009 for a list of references) the H_2O molecules may be oriented in two different ways within the structural channels: (I) with their H-H direction parallel to the ***c***-axis (Figure 3 left); these are termed "type I" (nomenclature introduced by Goldman and Rossman 1977) water molecules (hereafter $H_2O^{[I]}$). (II) with their H-H direction perpendicular to the ***c***-axis; these are termed "type II" water molecules (hereafter $H_2O^{[II]}$). This second type is invariably associated with alkali cations (e.g. Goldman and Rossman 1977; Vry et al. 1990) in the channel (Figure 3 center). The carbon dioxide molecule is oriented perpendicular to the ***c***-axis (Figure 3 right), dominantly parallel to the ***a***-axis (Armbruster and Bloss 1982).

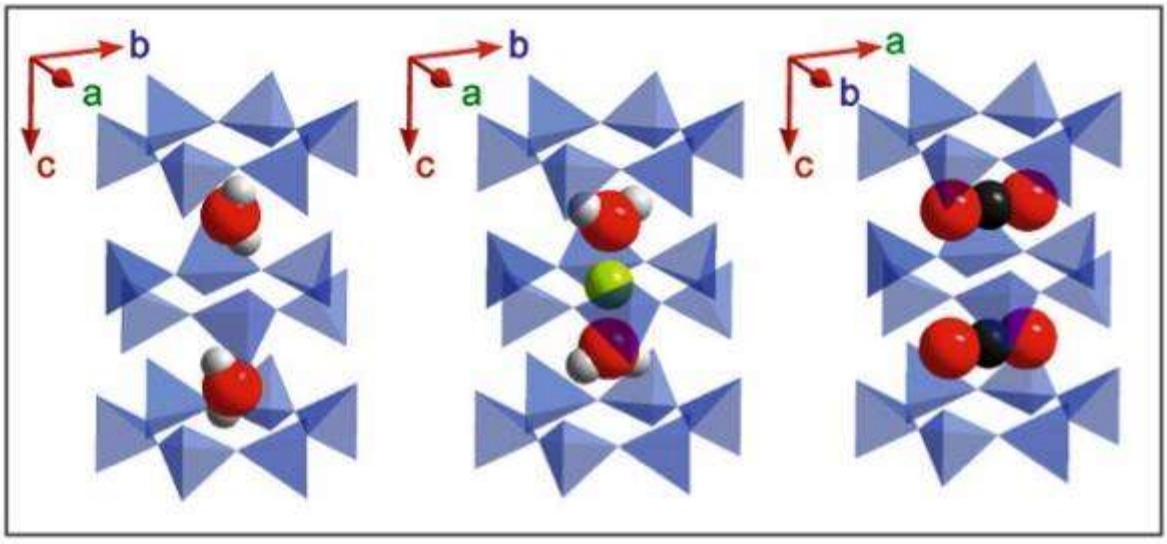

Figure 3 - The structural environment of the channel constituents in cordierite: (left) type I water, (center) type II water, (right) CO_2.

The polarization behaviour of the fundamental modes of the water molecules in cordierite is a function of the orientation of the molecule with respect the crystallographic axis. As shown by Goldman et al. (1977), the ν_3 antisymmetric stretching is polarized along the H...H direction, while ν_1 and ν_2 (symmetric stretching and bending, respectively) are polarized along the molecular two-fold axis; combining both information we may obtain the orientation of the molecular plane. The reference point for the interpretation of the spectra of Figure 2 is the powder spectrum of CO_2 and alkali-free synthetic Mg-cordierite (Paukov et al. 2007), which consists of two bands: a very intense peak at 3689 cm^{-1}, and a minor peak at 3595 cm^{-1}. Given the controlled chemistry of the sample, the former can be unambiguously assigned to the ν_3 mode of $H_2O^{[I]}$, while the latter can be assigned to the ν_1 mode of the same $H_2O^{[I]}$ molecule. The splitting between these two components [$\Delta(\nu_3 - \nu_1) = 94$ cm^{-1}] suggests that $H_2O^{[I]}$ occurs in cordierite as a relatively free, unbound molecule (Geiger and Kolesov 2002). In Figure 2a, the intense peak at 3689 cm^{-1} for **E** // ***c*** is thus assigned to the ν_3 vibration of $H_2O^{[I]}$. The ν_1 mode of the same $H_2O^{[I]}$ molecule at 3595 cm^{-1} is observed as a very weak absorption in the **E** // ***b*** spectrum. A weak component at ~ 3595 cm^{-1} is also present in the **E** // ***a*** spectrum (Figure 2). Following Della Ventura et al. (2009) this is assigned to a combination mode of CO_2.

Based on the data available in the literature (e.g. Goldman et al. 1977; Kolesov and Geiger 2000), $H_2O^{[II]}$ is characterized by a ν_3 antisymmetric stretching at ~ 3630 cm^{-1} associated with a ν_1 symmetric stretching at ~ 3575 cm^{-1}. Hence, the broad absorption at 3630 cm^{-1} for **E** // ***b*** (Figure 2a) is assigned to the ν_3 mode of $H_2O^{[II]}$, while the well defined peak at 3575 cm^{-1} for **E** // ***c*** is assigned to the ν_1 mode of the same $H_2O^{[II]}$ molecule. The splitting between these two bands [$\Delta(\nu_3 - \nu_1) = 55$ cm^{-1}] is lower than that observed for $H_2O^{[I]}$ suggesting that $H_2O^{[II]}$ is involved in some sort of bonding with the closest atoms.

In the combination region, the most intense peak at 5270 cm^{-1} is polarized for **E** // ***c*** hence it is assigned to the ($\nu_3 + \nu_2$) combination mode of $H_2O^{[I]}$, while the minor but resolvable band centred at 5245 cm^{-1}, polarized for **E** // ***b***, is assigned to the ($\nu_3 + \nu_2$) combination mode of $H_2O^{[II]}$ (see also Goldman et al. 1977). In accordance with this interpretation, the integrated intensity of the 3689 cm^{-1} is linearly correlated with the intensity of the 5270 cm^{-1} band (Figure 4a), while the integrated intensity of the 3630 cm^{-1} is linearly correlated with the intensity of the 5245 cm^{-1} band (Figure 4b).

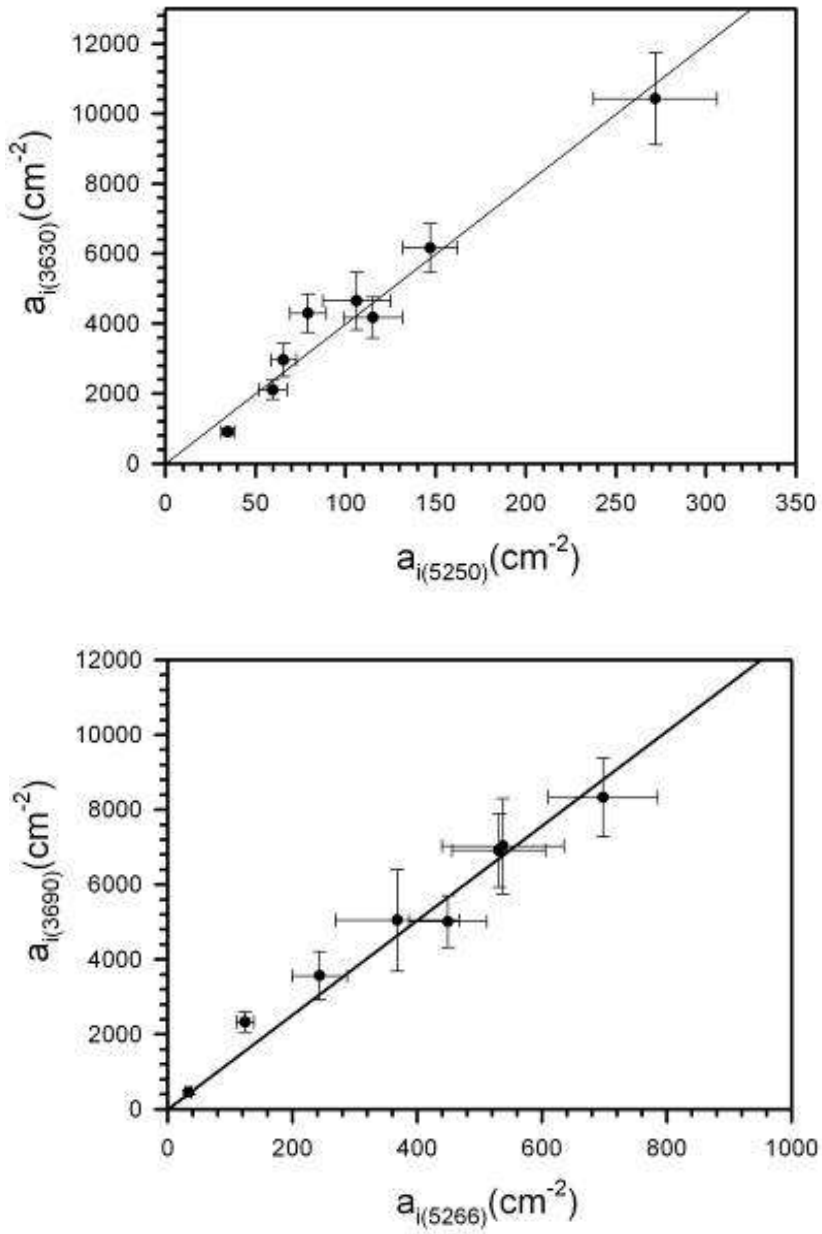

Figure 4 - Relationship between the integrated absorbance of the 5250 cm^{-1} band versus the 3630 cm^{-1} band (bottom), and the integrated absorbance of the 5266 cm^{-1} band versus the 3690 cm^{-1} band (top).

One important conclusion of the above discussion is that the very sharp and relatively intense peak at 3708 cm^{-1} is not related to water molecules, but, as suggested by Geiger and Kolesov (2002) and later established by Della Ventura et al. (2009), must be instead assigned to a combination ($\nu_3 + \nu_1$) mode of CO_2. In addition, Della Ventura et al. (2009) in their study of a CO_2-bearing, but H_2O-free cordierite from El Hoyazo (Spain) showed that the weak component at 3595 cm^{-1} in the **E** // ***a*** spectrum must also be related to a combination ($\nu_3 + 2\ \nu_2$) mode of CO_2. This band occurs at a frequency coincident with the frequency of the ν_1 mode of type I water (see above). This observation is particularly important in this context,

because all studies dealing with the spectroscopic H_2O/CO_2 determination in cordierite, particularly those done using powder data (e.g. Vry et al. 1990; Kalt 2000; Rigby et al. 2008 and references therein), have been based on the Goldman et al. (1977) model, whereby all bands in the 3900-3300 cm^{-1} range were assigned to H_2O.

In the 2600-2000 cm^{-1} region (Figure 2a, right), the most intense band at 2348 cm^{-1} is assigned to the ν_3 antisymmetric stretching mode of the $^{12}C^{16}O_2$ molecule (Khomenko and Langer 2005). The minor bands at 2282 and 2134 cm^{-1}, which are observed in single-crystal and powder spectra of CO_2-rich cordierites (e.g. Le Breton 1989), have the same polarisation behaviour as the main band at 2348 cm^{-1}. Their interpretation has been discussed recently by Khomenko and Langer (2005) who concluded that the former band can be assigned to the vibration of a $^{13}C^{16}O_2$ carbon dioxide molecule, while the latter can be assigned to the vibration of a $^{12}C^{16}O$ carbon monoxide molecule, also aligned along the ***a*** crystallographic axis. Thus the IR spectrum of cordierite potentially provides information on both the composition and the isotopic signature of molecular carbon entrapped into the structural channels. Assignment of the two side bands at 2390 and 2306 cm^{-1} observed in the **E** // ***b*** spectrum is still unclear; according to Aines and Rossman (1984), these bands may be related to librational, sum and difference motions of the CO_2 molecule on the (001) plane. Final band assignments are summarized in Table 4.

Table 4 - Position, assignment and polarization for various peaks in the cordierite spectra.

Wavelength (cm^{-1})	Molecule	Mode	Polarization
1635	$H_2O^{[II]}$	bending ν_2	*c*
2134	$^{12}C^{16}O$	stretch ν_3	*a*
2282	$^{13}C^{16}O_2$	antisym stretch ν_3	*a*
2348	$^{12}C^{16}O_2$	antisym stretch ν_3	*a*
3575	$H_2O^{[II]}$	sym stretch ν_1	*c*
3595	$H_2O^{[I]}$	sym stretch ν_1	*b*
3595	$^{12}C^{16}O_2$	combination $\nu_3 + 2\nu_2$	*a*
3630	$H_2O^{[II]}$	antisym stretch ν_3	*b*
3689	$H_2O^{[I]}$	antisym stretch ν_3	*c*
3708	$^{12}C^{16}O_2$	combination $\nu_3 + \nu_1$	*a*
5245	$H_2O^{[II]}$	combination $\nu_3 + \nu_2$	*b*
5270	$H_2O^{[I]}$	combination $\nu_3 + \nu_2$	*c*

6. The distribution of H_2O and CO_2 in the studied samples

Recent work done on several microporous materials such as leucite (Della Ventura et al. 2008) or minerals of the haüyine-sodalite group (Bellatreccia et al. 2009) has shown that water, but also carbon dioxide, can be zoned across the crystal. For cordierite in particular Della Ventura et al. (2009) have shown that the distribution of water may be complicated by the diffuse presence of alteration products or by fractures and cracks due to the geological history after the mineral formation, even in samples which are apparently optically clean. The possible inhomogeneous distribution of H_2O and CO_2 across the samples is obviously an important issue in quantitative micro-analytical work, therefore as a preliminary step we collected several FTIR maps and FPA images to test for the homogeneity of the crystals used for single-spot quantitative analyses. As discussed by Della Ventura et al. (2010), there are essentially two experimental set-ups in spectroscopic imaging: (1) FTIR *mapping* which is performed by integrating the signal from successive locations of the specimen surface; in this case a large number of single-spot spectra are collected by displacing the sample step-by-step using a motorized stage. The final resolution of the map depends on the single-spot size, which cannot be reduced below few tenths of μm^2 in conventional (globar) light (typically 20-50 μm^2), and on the grid-size. The advantage of this technique is that one can obtain maps of large areas (several mm^2) with a very good signal/noise ratio. The major disadvantage, besides the relatively poor lateral resolution (the single-spot size), is the large time needed to collect a map (up to hours for mm-sized maps). (2) FTIR *imaging*. In this case the whole image is obtained in a single data collection by using a bi-dimensional array of detectors (FPA). The number of pixels (the detectors) and their effective size will depend on the FPA type and the microscope objective. Typical arrays range from the 64×64 channels, providing 4096 individual spectra to 256×256 or 1024×1024 formats. Such arrays are coupled with 15X or 36X objectives, thus the physical dimensions of a single pixel is in the range 2.5 to 5 μm^2. The area covered in each data collection is in the order of 200-400 μm^2. Using this technique a resolution close to the diffraction limit can be attained, and the time needed to collect an image may scale down to few minutes (Della Ventura et al. 2010).

Prior to the quantitative analyses, we studied all samples by FTIR mapping; when needed, some key locations were examined using the FPA detector for higher resolution. Some crystals, for example cordierite BM96512 appeared homogeneous, while other specimens displayed an evident zoning. Cordierite RP5578 (Figure 5), for example, while being homogeneous with respect to CO_2, shows areas with different H_2O contents. A peculiar example is that of cordierite BB3a from Antarctica. Optically, the crystals show a weak chromatic zoning, consisting of light-blue to yellowish zones. The FTIR maps obtained by integrating the 3700-3400 cm^{-1} region show that the yellowish part (top in Figure 6) is extremely enriched in H_2O with respect the light-blue, lower side of the grain. Interestingly, the opposite is observed for CO_2, which is extremely enriched in the top side of the grain. Single FTIR spectra, collected with a reduced beam size in the yellowish, water-richer side, show a very broad convolute band extending from 3700-3100 cm^{-1} suggesting that this area contains dispersed very fine crystals of alteration products (Della Ventura et al. 2009) which account for the increased absorbance in the H_2O region.

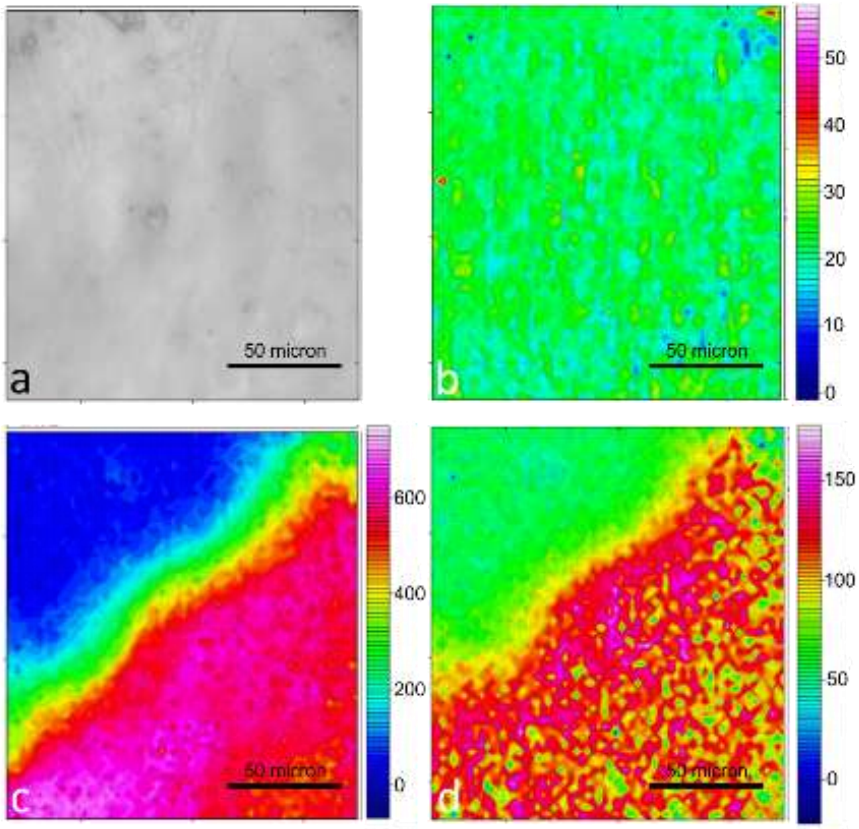

Figure 5 - Sample RP 5578: (a) Optical image of the analyzed sample area, (b) FPA image of CO_2 distribution, (c) image of the total signal from 3800 to 2800 cm^{-1} and (d) image of the 3689 cm^{-1} band ($H_2O^{[I]}$) intensity.

To define with a better resolution the transition between the yellowish and the light-blue zones, we collected for the same section some FTIR images using a multi-channel FPA detector, under the conditions explained above. Figure 6d shows that there is a sharp transition between the region where secondary alteration products are present and account for the extremely intense absorption in the water-stretching region; in addition, strong intensity of the H_2O signal is also associated with micro-fractures (arrowed) within the sample.

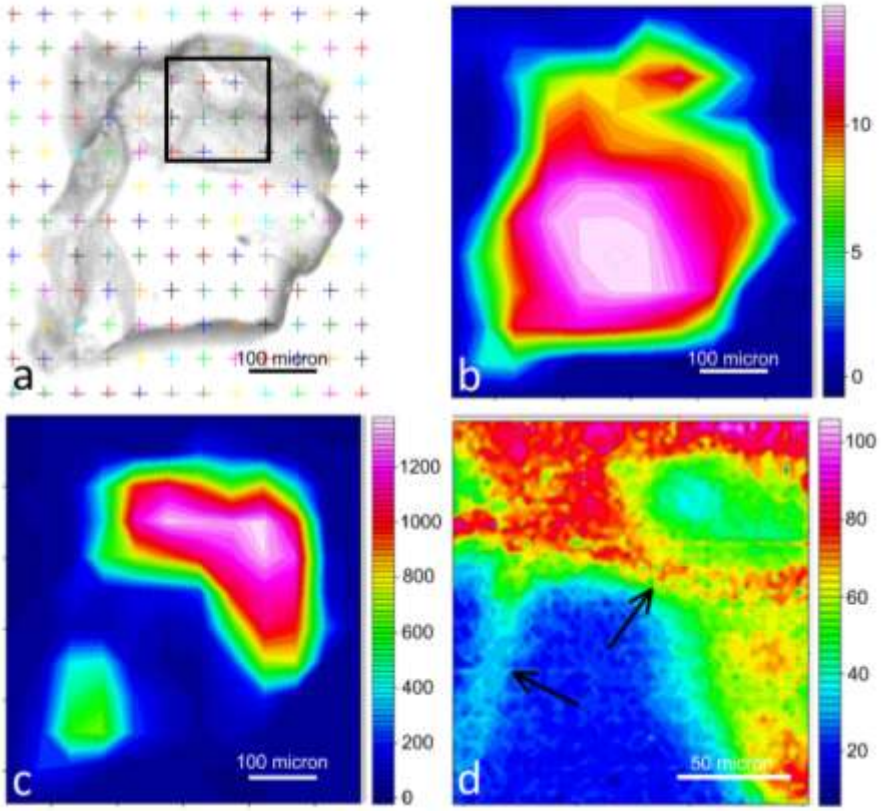

Figure 6 - Sample BB3a: (a) Optical image of the section with location of the single spots. The black box indicates the location of the FPA image in (d); (b) and (c) distribution of the CO_2 and H_2O band intensity, respectively. (d) FPA image of H_2O distribution on a 170x170 μm^2 area.

7. Calibration of a molar absorption coefficient to quantify H_2O and CO_2 in cordierite using FTIR spectroscopy

As explained above, the main problem in the quantitative spectroscopic analysis of H and C in cordierite is the lack of reliable integrated absorption coefficients to be used in the Beer-Lambert relationship $c\ (wt.\%) = A_i / (t \cdot \varepsilon_i)$. Rearranging this equation as $\varepsilon = A \cdot m / c \cdot t \cdot D$, we can calibrate both ε_{H2O} and ε_{CO2} substituting the concentrations obtained from SIMS. The

m factor in this formula is needed for the conversion of the concentration from wt% to mol l^{-1}; for H_2O m = 1.8 (Beran et al. 1993), for CO_2 m = 4.401 (Della Ventura et al. 2009). The density D (in g/cm^3, Table 2a) was calculated as $0.0036X^2 + 0.00394X + 2.573$ (Goldman et al. 1977) where X = (total Fe in wt% from Table 2a), while A_i was obtained by summing up the single absorbances measured along the three optical directions (Libowitzky and Rossman, 1996).

For H_2O, one difficulty arises from the fact that SIMS provides the total water content in the sample, while FTIR (see above) provides two different H_2O signals due to the two water types, which are resolved at different frequency (3689 *vs* 3630 cm^{-1}). According to Libowitzky and Rossman (1997), ε_{H2O} is a function of the wavenumber, thus two ε_{H2O} are expected for the two water types. To solve this problem, we calculated for each sample the relative amounts of $H_2O^{[I]}$ and $H_2O^{[II]}$ assuming that each alkali cation located within the structural channels is locally associated with two $H_2O^{[II]}$ molecules. This relationship has been proposed by several authors (e.g. Goldman and Rossman 1977; Vry et al. 1990) and is also verified in this study, as it is apparent in Figure 7, where there is a well-defined linear trend connecting the total alkali content (Na+K+Ca) from EMPA, and the integrated absorbance of the 3630 cm^{-1} band assigned to $H_2O^{[II]}$. Therefore, $H_2O^{[II]}$ was set to be $H_2O^{[II]} = 2\cdot(Na,K,Ca)^{ch}$ and $H_2O^{[I]} = H_2O_{tot} - H_2O^{[II]}$ (Table 2a). ε_{H2O} coefficients were finally calculated for both water types, independently (Table 5).

Table 5 - Integrated and linear molar absorption coefficients and errors calibrated for different modes of cordierite

	Integrated ($l\cdot mol^{-1}\cdot cm^{-2}$)		Linear ($l\cdot mol^{-1}\cdot cm^{-1}$)	
Mode	ε_i	$\sigma_{\varepsilon i}$	ε_l	$\sigma_{\varepsilon l}$
ν_3 ($H_2O^{[I]}$)	5200	700	400	100
ν_3 ($H_2O^{[II]}$)	13000	3000	240	50
ν_3 ($H_2O^{[I]}$ + $H_2O^{[II]}$)	6700	600	260	20
$\nu_3 + \nu_2$ ($H_2O^{[I]}$)	420	60	22	7
$\nu_3 + \nu_2$ ($H_2O^{[II]}$)	340	80	8	2
ν_3 (CO_2)	19000	2000	1000	100

For CO_2, again SIMS provides the total carbon content only, while FTIR spectra show (Figure 2a) that some of the examined cordierites contain also some carbon monoxide; from the intensity of the CO band (2134 cm^{-1}), its amount can, however, be estimated to be so small that the error introduced in the calculation of the molar absorption coefficient can be

considered as negligible. One point which is worth to be mentioned here is that for samples with higher CO_2 contents, the main band at 2348 cm^{-1} is extremely intense, and when this is the case there is the need to reduce the thickness of the analysed slab. This feature is evident, for instance, for sample RP 5578 which has the highest CO_2 content within the studied specimens (CO_2 = 1.11 wt%, Table 2), and its CO_2 peak is at the limits of detector saturation, even for a thickness as low as 34 μm (Fig. 2a). We faced similar problems with other CO_2-rich samples, and the only way to handle it was to reduce the sample thickness in such a way to keep the main peak absorbance below 2.0. It is obvious that, given the sharpness of the 2348 cm^{-1} band, the problem of peak truncation is relatively minor when using integrated intensities, while being much more significant if linear intensities are used for quantification purposes. An alternative way to handle this problem is by using the combination or overtone bands which have intensities much lower compared to the principal stretching bands. For CO_2 we tested the feasibility of using the 3595 cm^{-1} band assigned to the ($\nu_3 + 2\,\nu_2$) combination (Table 4) and obtained an excellent linear relationship as a function of the SIMS measured CO_2 content in the sample (not shown). However, this band, as well as the 3708 cm^{-1} peak assigned to the ($\nu_3 + \nu_1$) combination of CO_2 (Table 4), overlap strongly with the water bands and thus cannot be measured with certainty. This approach gave better results for H_2O (see below).

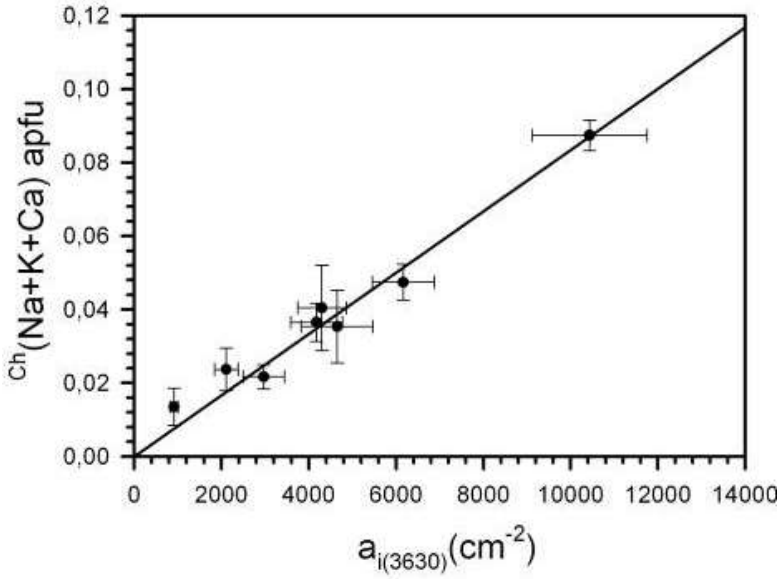

Figure 7 - Relationship between the integrated absorption coefficient (defined as the integrated absorbance / thickness, cm^{-2}) of the band at 3630 cm^{-1} assigned to the ν_3 mode of type II H_2O and the total alkali content (apfu) in the channels.

For H_2O we calculated the absorption coefficients for the principal ν_3 stretching and the combination bands. In addition to the integrated coefficient, we also calculated, for all bands, the linear molar absorption coefficient, which makes use of the linear intensity instead of the peak area. In some paper, particularly in earlier works, the linear intensity (A_l) was in fact used in the Beer-Lambert equation for quantitative purposes.

Figure 8 shows the relationship between the integrated intensity of the bands at 3689, 3630 and 2348 cm^{-1} assigned to $H_2O^{[I]}$, $H_2O^{[II]}$ and CO_2, respectively against the relative SIMS amounts (wt%). Specific molar absorption coefficients (ε) for each sample were obtained on the basis of the Beer-Lambert relationship; the error σ associated with each measurement was calculated using the classical statistics of error propagation (e.g., Bellatreccia et al. 2005) considering that the uncertainty on A is ~ 10% (Libowitzky and Rossman 1997), on the sample thickness (t) is < 2 μm, the standard deviation of the density (D) is 2% and the accuracy of SIMS analysis is better than 10%. Average final coefficients and errors for the different bands are summarized in Table 5. Note that in Table 5 we list also the molar absorption coefficients for the combination ($\nu_3 + 2\,\nu_2$) bands of type I and II H_2O which can be resolved in the NIR region for thicker sample slabs.

8. Conclusions

We provide in this paper the first integrated molar absorption coefficient for H_2O in cordierite based on polarized measurements on oriented crystal sections. Those provided by Goldman et al. (1977) were calibrated using linear (peak height) intensity data. They found very similar values for type I (ε = 204 $l \cdot mol^{-1} \cdot cm^{-1}$) and type II (ε = 269 $l \cdot mol^{-1} \cdot cm^{-1}$) H_2O, and concluded that, considering the analytical error, both types of H_2O molecules have the same molar absorption coefficient. We show here that the two water molecules are characterized by significantly different ε coefficients, and this difference is particularly evident when dealing with integrated absorbance (Table 5). In this latter case, even considering the error in the measurement, the ε_i coefficient for type II H_2O is more than double than that obtained for type I H_2O. The logical consequence of this feature is that careful quantification of H_2O in cordierite by FTIR spectroscopy requires measuring the different bands due to the different

types of channel water. In Table 5 we also give the value of the ε coefficient calculated on the basis of the total $H_2O^{[I]}$ + $H_2O^{[I]}$ band intensity versus the total $^{SIMS}H_2O$ content. This value can be used for a simplified spectroscopic quantification of the total H_2O content in the examined cordierite sample.

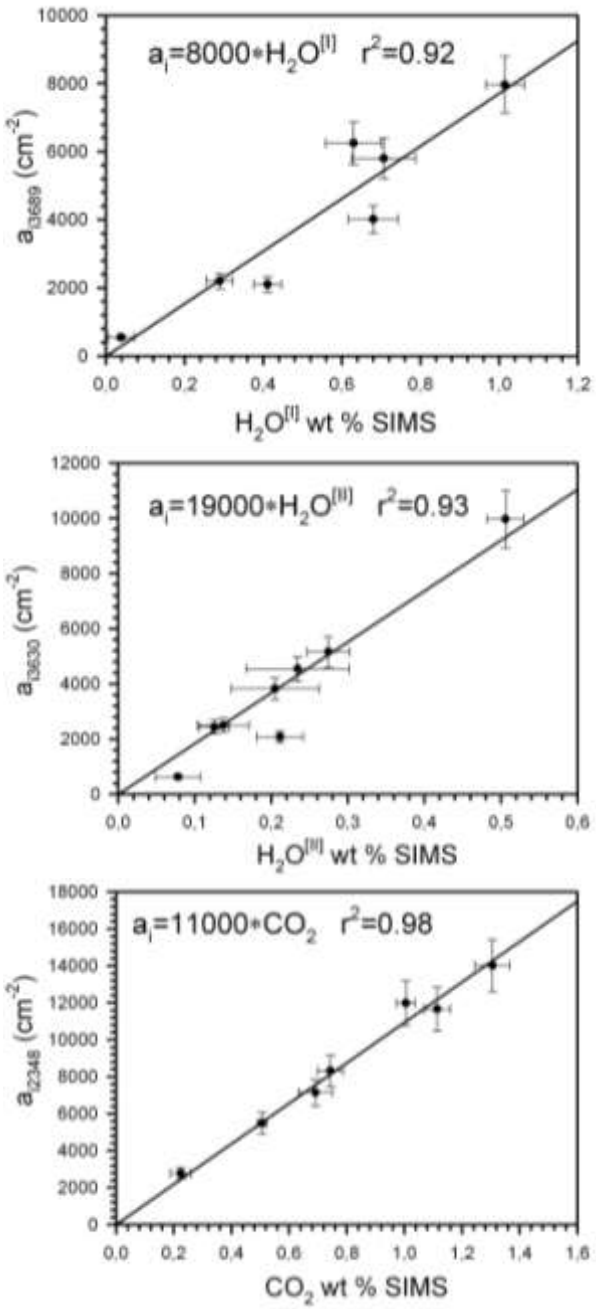

Figure 8 - Relationship between the integrated absorption coefficient (defined as the integrated absorbance/thickness, $a_i = A_i/t$ in cm^{-2}) of the band at 3689 cm^{-1} (top), at 3630 cm^{-1} (medium) and 2348 cm^{-1} (bottom) versus the $H_2O^{[I]}$, $H_2O^{[II]}$ and CO_2 contents (apfu) obtained by SIMS, respectively.

For CO_2, the ε_{CO2} calibrated in this work [19000 l/(mol cm^2)] is significantly different from that obtained recently [~ 11000 l/(mol cm^2)] by Della Ventura et al. (2009). The value obtained here however is an average of measurements done on 8 samples spanning a relatively large CO_2 variation, while the value presented by Della Ventura et al. (2009) was obtained on a single sample only. For this reason, we consider our data to be more reliable.

Powder infrared spectroscopy has been widely used in petrological studies as an analytical method for H_2O and CO_2 in cordierite (e.g. Vry et al. 1990). However, as discussed by Libowitzky and Rossman (1996) such a procedure cannot provide the absolute quantitative determination of water and/or carbon dioxide. The calibration presented in this study, on the other side, allows a high level of accuracy in the determination of both molecules.

The use of novel techniques in FTIR imaging clearly shows that at the □m-scale the distribution of H and C in this mineral may be significantly inhomogeneous, and this feature must be taken into account when collecting analytical data for petrological purposes. This feature is probably less important for carbon molecules than it is for H_2O, whose distribution within the crystal can be strongly affected by the geological history of the mineral after its formation.

Acknowledgements

Financial support was provided by COFIN 2009 to GDV. Thanks are due to V. Mangione (Lime, Roma) for assisting with optical profilometer measurements. H. Keppler (Bayreuth) and an anonymous referee helped in clarifying some aspects of the text.

PUBLISHED ON MINERALOGICAL MAGAZINE (JUNE 2013)

DOI: 10.1180/minmag.2013.07 7.4.08

CHAPTER 2

SPECTROSCOPY AND X-RAY STRUCTURE REFINEMENT OF SEKANINAITE FROM DOLNÌ BORY (CZECH REP.)

Francesco Radica[1], Francesco Capitelli[2], Fabio Bellatreccia[1,3], Giancarlo Della Ventura[1,3,4], Andrea Cavallo[4], Massimo Piccinini[5] and Frank C. Hawthorne[6]

[1]Dipartimento di Scienze Geologiche, Università degli Studi Roma Tre, Largo S. Leonardo Murialdo 1, 00146 Roma, Italy

[2]Istituto di Cristallografia, Consiglio Nazionale delle Ricerche (CNR), Via Salaria Km 29,300, 00016 Monterotondo, Rome, Italy

[3]Laboratori Nazionali di Frascati - Istituto Nazionale di Fisica Nucleare (LNF – INFN), Via E. Fermi 40, 00044 Frascati (Rome), Italy

[4]Istituto Nazionale di Geofisica e Vulcanologia (INGV), Via di Vigna Murata 605, 00143 Roma, Italy

[5]Porto Conte Ricerche s.r.l., Strada Provinciale 55 Km 8,400, 07041 Alghero (Sassari), Italy

[6]Department of Geological Sciences, University of Manitoba, Winnipeg, Manitoba R3T 2N2, Canada

Abstract

The crystal chemistry of sekaninaite from Dolnì Bory, Czech Republic, was characterized by a multi-methodological approach. Particular emphasis was put on the characterization of the channel constituents (i.e. H_2O and CO_2). Electron-micro-probe analysis shows the sample to be close to the Fe end-member [X_{Fe} = Fe/(Fe+Mg) = 94%) with significant Mn (1.48 wt.%) present; laser ablation mass-spectrometry showed the presence of 0.42 wt.% Li_2O. H_2O and CO_2 contents (1.48 and 0.17 wt.%, respectively) were determined via secondary-ion mass-spectrometry (SIMS). Sample homogeneity was checked by FTIR imaging using a microscope equipped with an FPA detector. Single-crystal FTIR spectroscopy confirmed the presence of two types of H_2O groups in different orientations (with prevalence of the type II orientation), and that CO_2 is oriented preferentially normal to the crystallographic **c** axis. Using the Beer-Lambert relation, integrated molar coefficients ε_i were calculated for both types of H_2O (ε_i $H_2O^{[I]}$ = 6000±2000; ε_i $H_2O^{[II]}$ = 13000±1000) and for CO_2 (ε_i CO_2 = 2000±1000).

Key words: sekaninaite, crystal-structure refinement, EMPA + SIMP analysis, FTIR spectroscopy

1. Introduction

Sekaninaite is the Fe^{2+} dominant member of the cordierite group (Černý *et al.*, 1997). The first occurrence of this mineral was reported by Sekanina (1928) in the pegmatites of Dolnì Bory; however, it was definitively described as a new mineral species by Staněk and Miškovský (1964, 1975). Cordierites are framework alumino-silicates with the ideal formula $(\square,Na)(Mg,Fe)_2Al_4Si_5O_{18}(\square,H_2O,CO_2) = XM_2T_9O_{18}Y$ and form a continuous solid solution between the Mg^{2+} end-member (cordierite s.s.) and the Fe^{2+} end-member (sekaninaite). The main structural feature of these minerals is the presence of 6-fold rings of tetrahedra stacked along the **c** crystallographic axis. These rings form cavities that can accommodate large cations such as Na^+, K^+ and molecules such as H_2O and CO_2. The sekaninaite framework can be described as a stacking of pseudo-hexagonal Si/Al layers of tetrahedra and mixed

layers of tetrahedra and octahedra (Fig. 1). Alkali cations, H_2O and CO_2 fill the resulting pseudo-hexagonal channel, occupying sites on the **c** axis at (0, 0, 0) for Na, and (0, 0, ¼) for H_2O and CO_2 (Hochella *et al.*, 1979; Malcherek *et al.*, 2001; Yakubovich *et al.*, 2004). The chemical composition of the framework has the ideal formula 4 Al apfu and 5 Si apfu. Due to the high concentration of alkali cations within the channels (Cěrný *et al.*, 1997; Yacobuvich *et al.*, 2004), charge balance may be restored by Be^{2+} substitution at the tetrahedrally coordinated sites (Armbruster and Irouschek, 1983; Yacobuvich *et al.*, 2004) or Li^{+} at the octahedrally coordinated sites (Cěrný *et al.*, 1997; Gottesmann and Förster, 2004). Unlike cordierite, sekaninaite is not a widespread mineral, and usually occurs in the albite zone of pegmatitic rocks (Staněk and Miškovský, 1964, Orlandi and Pezzotta, 1994; Guastoni el al., 2004). Other occurrences of sekaninaite were reported in altered bauxitic lithomarges (Ryback *et al.*, 1988) and in Fe-rich pyrometamorphosed rocks (Sharygin *et al.*, 2009; Grapes *et al.*, 2010).

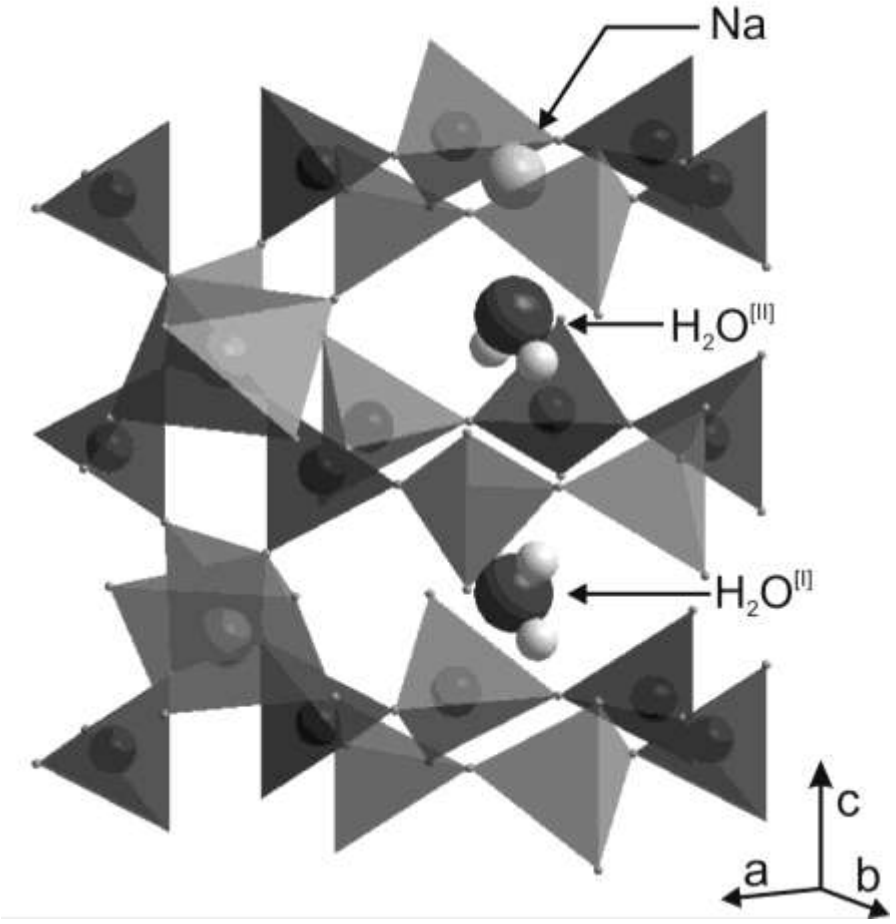

Figure - 1 Schematic view of a portion of the sekaninaite structure which includes the channel parallel along the *c* axis. Si-containing tetrahedra are shown in dark grey and Al-containing tetrahedra are shown in light grey. The structural position of Na and both orientation types of H_2O are shown in the channels.

2. Analytical methodology

Table 1 - Chemical composition (mean of 5 analyses) and chemical formula (apfu), based on 18 oxygen atoms per formula unit, for the studied sekaninaite

	Wt%	Range		apfu
SiO_2	45.41	45.65-45.16	Si	4.954
TiO_2	0.01	0.02-0.00	Al	4.054
Al_2O_3	31.53	31.84-31.27	ΣT	9.008
FeO	17.55	17.99-17.37		
MnO	1.48	1.52-1.39	Mg	0.079
MgO	0.48	0.53-0.46	Fe	1.602
CaO	0.03	0.05-0.02	Ti	0.001
Na_2O	0.90	0.96-0.86	Mn	0.137
K_2O	0.02	0.02-0.01	Li	0.186
Li_2O	0.42	0.43-0.41	ΣOct.	2.005
H_2O	1.48	1.54-1.38		
CO_2	0.17	0.23-0.11	Ca	0.004
Total	99.48		Na	0.190
			K	0.002
			ΣCh.	0.196
			H_2O	0.538
			CO_2	0.025

All data from EMP analysis except for Li_2O (Nano-LAMS), H_2O and CO_2 from SIMS (see text).

The studied sample is from the type locality of Dolnì Bory (Czec Rep.) (Staněk and Miškovský, 1964). The analyzed grains were extracted from a very clear, light blue and almost inclusion-free large crystal that gradually changes toward the rim of the sample into a greenish alteration product of clay minerals. Due to the presence of light elements (Li, H and C), the chemical composition of sekaninaite was determined using a multi-methodological approach. Elements from Si to K (Tab. 1) were analyzed using a Jeol JXA 8200 WD-ED electron micro-probe (EMP) at the Istituto Nazionale di Geofisica e Vulcanologia (INGV), Rome. Working conditions were: 15 kV accelerating voltage, 7 nA sample current, 5 µm beam diameter. Count times were 10 s on the peak and 5 s on the background on both sides of the peak. Standards, spectral lines and crystals used were: albite (Na*K*α, TAP), pargasite (Ca*K*α, PET), wollastonite (Si*K*α, PET), K-feldspar (K*K*α, PET), kyanite (Al*K*α, TAP), pargasite (Mg*K*α, TAP), augite (Fe*K*α,LiF), titanium oxide (Ti*K*α, LiF) and spessartine (Mn*K*α, LiF). Data

correction was done using the ZAF method. Sample homogeneity was verified by collecting many points per crystal. Lithium was determined by laser ablation inductively coupled plasma mass spectrometry (LA-ICP-MS) at the Department of Geological Sciences, University of Manitoba (Winnipeg), using a Merchantek New Wave UP213 laser ablation system. The data were collected from three spots with a Nd: YAG laser, beam diameter of 50 µm, 10 Hz repetition rate, about 5 J/cm^2 fluence, 30 s background acquisition and 50 s ablation time. Li was standardized against NIST SRM 610.

H_2O and CO_2 were quantified by secondary-ion mass spectrometry (SIMS) using a Cameca IMS4f ion microprobe at the Edinburgh Materials and Micro Analysis Centre, University of Edinburgh. Sputtered secondary ions ^1H, ^{12}C and ^{28}Si were measured with an energy offset of 75 V and an energy window of 19 eV, under operating conditions of 4500 V secondary-beam voltage and 8 nA and 10 kV for the primary beam of O^- ions. Under these conditions, the primary-ion beam sputters an elliptical area with long diameter 25–30 µm and maximum depth of 3 µm. All analyses involved a 3 minute burn-in time followed by 20 cycles of 5 s counts for each isotope. The mean isotope ratios $^1H/^{28}Si$ and $^{12}C/^{28}Si$ for the last 10 cycles in each analysis were taken as the final results in order to avoid surface contamination. Analyses expressed as isotopic ratios of $^1H/^{28}Si$ and $^{12}C/^{28}Si$ were converted to wt.% H_2O or CO_2 by comparison with the calibration lines produced from fitting two standards analyzed several times throughout the same analytical session. The standards used were the samples ANMH (X_{Mg} = 0.89; H_2O = 1.54 wt%; and CO_2 = 0.7 wt%, Thompson *et al.*, 2001) and 8/90 (labeled 81-90 X_{Mg} = 0.75; H_2O = 0.81 %; and CO_2 = 1.31 wt%, Thompson *et al.*, 2001).

X-ray diffraction data were collected at the Istituto di Cristallografia, Bari, with a Nonius Kappa CCD area-detector diffractometer (Tab. 2); data collection: COLLECT (Nonius, 1998); cell refinement and data reduction: EvalCCD (Duisenberg *et al.*, 2003), absorption correction: SADABS (Sheldrick, 2008).The structure was solved through the Direct Methods procedure of SIR2008 (Burla *et al.*, 2007) in the orthorhombic space group *Cccm* (n. 66), with the following unit-cell constants: *a* = 17.2340(15), *b* = 9.8457(18), *c* = 9.3463(18) Å, and refined by full-matrix least-squares based on F^2, SHELXL-97 (Sheldrick, 2008); final R indices were, for [I>2σ(I)] R_1 = 0.0178 and wR_2 =0.0490, and for all data R_1 = 0.0186 and wR_2 = 0.0499.

Table 2 - Crystal data and structure refinement data for sekaninaite from Dolnì Bory

Temperature	293(2) K
Radiation, Wavelength	Mo-*K*α, 0.71073 Å
Crystal system,	Orthorhombic
Space group	*Cccm*
Unit cell dimensions	*a* = 17.2340(15) Å
	b = 9.8457(18) Å
	c = 9.3463(18) Å
Volume	1585.9(4) $Å^3$
Z	16
Calculated density	2.726 $Mg·m^{-3}$
Absorption coefficient	2.315 mm^{-1}
F(000)	1279
Crystal size	0.25 x 0.25 x 0.12 mm
Theta range for data collection	5.25° to 27.52°
Limiting indices	$-22 \le h \le 22$, $-12 \le k \le 12$, $-12 \le l \le 10$
Reflections collected / unique	9441 / 942 [R_{int} = 0.0297]
Completeness to theta	96.6 % (theta = 27.52°)
Max. and min. transmission	0.7686 and 0.5953
Refinement method*	Full-matrix least-squares on F^2
Data / restraints / parameters	942 / 1 / 84
Goodness-of-fit on F^2	1.162
Final R indices [I>2σ(I)]	R_1 = 0.0178, wR_2 = 0.0490
R indices (all data)	R_1 = 0.0186; wR_2 = 0.0499
Extinction coefficient	0.0092(4)
Largest diff. peak and hole	0.348 and -0.416 $e·Å^{-3}$

*SHELXL-97 weighting scheme applied: $w^{-1}=[s^2(F_o^2)+(0.0179P)^2+3.4870P]$ where $P=[(F_o^2+2F_c^2)/3]$

Micro-Raman spectra were collected at Porto Conte Ricerche s.r.l., Alghero (Sassari), using a Bruker Senterra Raman microscope equipped with a 532 nm laser operated at 50 mW; 10 acquisitions of 5 s each were accumulated, with a spectral resolution set at 3 to 5 cm^{-1} (100x lens, NA = 0.9). Raw data were slightly smoothed.

FTIR spectra were acquired with a Nicolet Magna 760 spectrophotometer, equipped with a NicPlan Microscope, a KBr beamsplitter and a liquid nitrogen-cooled MCT detector at the Dipartimento di Scienze Geologiche, Università Roma Tre. The polarized spectra were collected using a gold-wire-grid polarizer on a ZnSe substrate. The nominal resolution is 4 cm^{-1} and 128 scans were averaged for both spectrum and background. The samples for polarized IR measurements were oriented using a polarizing microscope equipped with a spindle-stage; the program ExcalibrW (Bloss, 1981; Gunter *et al.*, 2005) was used to process

the extinction data and to determine the 2V values. The oriented fragments were transferred to glass slides and doubly polished to thickness below 100 µm. Sample thickness was checked with a Leica DCM 3D optical profilometer at the Laboratorio Interdipartimentale di Microscopia Elettronica (LIME), Università Roma Tre. The nominal vertical resolution was less than 15 nm in confocal mode (20X lens, NA = 0.50) and less than 4 nm in interferometric mode (50X lens, NA = 0.50); sample thickness was averaged for the whole surface of the slab.

FTIR images were collected at the Laboratori Nazionali di Frascati-Istituto Nazionale di Fisica Nucleare (LNF-INFN,) Frascati (Rome) using a Bruker® Hyperion 3000 IR microscope equipped with a 64×64-pixel focal-plane array (FPA) of liquid nitrogen-cooled MCT detectors. Using a 15X objective, each image covers an area of 170 X 170 μm^2 with a nominal spatial resolution of ~5 µm (Della Ventura *et al.*, 2010). The nominal resolution was set at 4 cm^{-1} and 64 scans were averaged for each spectrum and background.

Refractive indexes were determined by the double-variation method (Su *et al.*, 1987, Gunter *et al.*, 2004) using standard Cargille liquids as reference.

3. Chemical composition

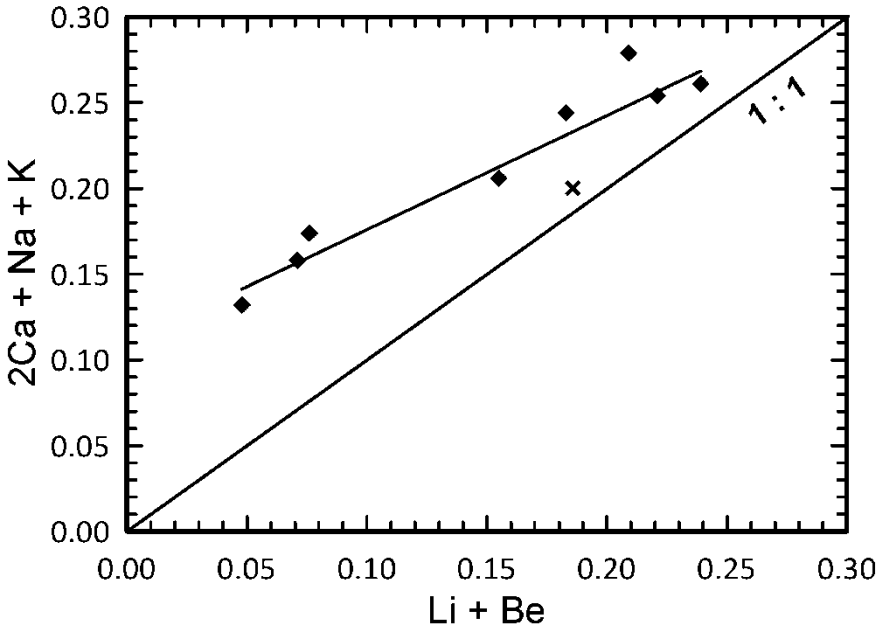

Figure 2 - Sum of channel cation charges versus Be + Li charges. Cross: this work, diamonds: samples from Dolnì Bory (Černý *et al.*, 1997); the regression line for these latter samples is reported.

Selected micro-chemical data for the studied sample are reported in Table 1. Fe_{tot} was considered as Fe^{2+}. The chemical formula, based on 18 oxygen atoms pfu, is $Na_{0.19}(Mg_{0.08}Fe_{1.60}Mn_{0.14}Li_{0.19})Al_{4.05}Si_{4.95}O_{18}\bullet 0.54H_2O\bullet 0.03CO_2$. The chemical composition of the analyzed sample is close to those reported for other samples from the same area (Stanek and Miskovsky, 1964, Hochella *et al.,* 1979, Černý *et al*. 1997). Sekaninate from Dolnì Bory, like in other pegmatite assemblages, has relatively high contents of Mn, Na and Li, on the opposite it has low concentration in Ti, Mg and K, elements usually abundant in paralava assemblages (Sharygin *et al.*, 2009; Grapes *et al.*, 2010). The Al/Si ratio is almost stoichiometric (4/5) and thus additional tetrahedrally coordinated cations are unlikely to be present. Although we do not have any information on the Fe oxidation state, we can reasonably consider all iron to be divalent, following Černý *et al*. (1997), who determined via Mössbauer spectroscopy that the $Fe^{3+}/\Sigma Fe$ is 0.5% or less for sekaninaites from the same area. Fe^{2+} is the main constituent at the octahedrally coordinated *M* site. Significant quantities of Li^+ (0.186 apfu) and Mn^{2+} (0.137 apfu) are also present, whereas Mg^{2+} and Ti^{4+} concentrations are very low. Charge imbalance due to Na^+ in the channels is compensated by Li^+ at the *M* site. If we consider the sum of channel-cation charges $(\Sigma_{Channel})/(Li + Be)$ ratio, we clearly see that our sample is located much closer to the 1 : 1 line compared to the samples analyzed by Černý *et al*. (1997) (Fig. 2). SIMS data show that the sample is almost CO_2-free and significantly enriched in H_2O, as reported by previous authors (Yakubovich *et al.*, 2004, Malcherek *et al.* 2001, Salkress and Bloss, 1980).

4. Single-crystal X-ray results

X-ray structure-refinement data are reported in Table 2, atom coordinates and equivalent isotropic-displacement parameters are reported in Table 3; bond lengths are reported in Table 4. The *a* and *b* parameters (Tab. 2) are in line with those reported for samples from the same locality (Hochella *et al.*, 1979; Selkregg and Bloss,1980; Malcherek *et al.*, 2001) and with those of synthetic iron-cordierite (Borbeski and Schreyer, 1990; Bulbak and Shvedenkova, 2011), whereas the *c* parameter (and consequently the cell volume) is at least 0.03 Å greater, a value that is more typical of Mg-cordierite. Parameters that, in our case, may increase the *c* parameter are the absence of Be at the T-sites (see below)

(Yakubovich *et al.*, 2004) and the presence of H_2O and CO_2 (Tab. 1) in the channels (Armbruster and Bloss, 1982).

Table 3 - Wyckoff site, atom coordinates, equivalent-displacement parameters ($Å^2$), and site- occupancy factors (SOF) of sekaninaite from Dolnì Bory.

Site	Wyckoff symbol	*x/a*	*y/b*	*z/c*	U(eq)	s.o.f.
*T*1	*4b*	0	1/2	1/4	0.0136(2)	
*T*2	*8l*	0.18999(4)	0.07921(7)	0	0.01273(17)	
*T*3	*8l*	0.13471(4)	0.76594(7)	0	0.01270(17)	
*T*4	*8k*	1/4	1/4	0.25011(8)	0.01421(18)	
*T*5	*8l*	0.04972(4)	0.30757(7)	0	0.01298(18)	
M	*8g*	0.33688(2)	0	1/4	0.01448(18)	0.873(5) Fe + 0.035(5) Mg + 0.09 Li*
O1	*16m*	0.24402(7)	0.89508(12)	0.35809(13)	0.0166(3)	
O2	*16m*	0.06074(7)	0.58523(13)	0.34885(14)	0.0165(3)	
O3	*16m*	0.82705(7)	0.69477(12)	0.35782(14)	0.0167(3)	
O4	*8l*	0.04328(10)	0.7543(2)	0	0.0210(4)	
O5	*8l*	0.11931(10)	0.18336(19)	0	0.0209(4)	
O6	*8l*	0.16213(10)	-0.07670(18)	0	0.0204(4)	
O7	*8g*	0.0580(6)	0	1/4	0.069	0.03*
O8w	*4a*	0	0	1/4	0.101(6)	0.62(3) O + 0.03* C
Na	*4c*	0	0	0	0.035(4)	0.203(10)

Equivalent isotropic U is defined as 1/3 of the trace of the orthogonalised U_{ij} tensor.
Na and O8w refined with isotropic displacement parameters.
C and O7 isotropic displacement parameters fixed at Malcherek *et al.* (2001) values.
*s.o.f. fixed for Li at nano-LAMS (Tab. 1) and for CO_2 at SIMS (Tab. 1) values.

In sekaninaite, the framework consists of five *T* tetrahedra (Cohen *et al.*, 1977; Armbruster, 1986). Three *T*-sites (*T*2, *T*3 and *T*5) form the six-membered pseudo-hexagonal ring and the remaining two *T*-sites (*T*1 and *T*4) connect the rings into a chain which extends parallel to the **c** crystallographic axis. Al occupies the *T*4 and *T*5 site (two of the six tetrahedra of the ring are occupied by Al) and the remaining sites (*T*1, *T*2 and *T*3) are occupied by Si (Fig. 1). Be, if present, usually occurs at the *T*4 site, according to the substitution $Na^+ + Be^{2+} \rightarrow Al^{3+}$. This substitution leads to a decrease of the mean *T*4-O distance (Tab. 4) as observed by Armbruster (1986). On the other hand, substitution of Mg for Fe leads to shortening of the *T*4-O distance (Malcherek *et al.* 2001). Figure 3 shows the *T*4-O distances from various refinements in the literature as a function of X_{Mg} (Fig. 3a) and Be at the *T*4 site (wt%) (Fig. 3b); samples with more than 1% Be at the *T*4 site (corresponding to ~ 0.02 apfu) are represented by circles. As we may observe from Figure 3a, samples with

high Be at *T*4 tend to deviate from the trend described by the $Fe^{2+} \rightarrow Mg^{2+}$ substitution, leading to a decrease in the *T*4 – O bond length; this trend is evident in Figure 3b. The *T*4 – O bond length for our sample is reported in Figure 3b as a dashed line; we may reasonably infer that Be in the sample is lower than 0.02 apfu. This conclusion is also corroborated by Figure 2.

Table 4 - Selected bond lengths (Å) for sekaninaite from Dolnì Bory.

*T*1-O2	1.6289(12)	*M*-O1^{1}	2.1561(12)
*T*1-O2^{10}	1.6289(12)	*M*-O1^{2}	2.1561(12)
*T*1-O2^{1}	1.6289(12)	*M*-O2^{3}	2.1613(12)
*T*1-O2^{11}	1.6289(12)	*M*-O2^{4}	2.1613(12)
<*T*1-O>	1.6289	*M*-O3^{5}	2.1729(13)
*T*2-O5	1.5923(18)	*M*-O3^{6}	2.1729(13)
*T*2-O6	1.6084(19)	<M-O>	2.1635
*T*2-O1^{1}	1.6402(13)		
*T*2-O1^{9}	1.6402(13)	*Na*-O8w^{16}	2.3366(5)
<*T*2-O>	1.6203	*Na*-O8w	2.3366(5)
*T*3-O4	1.5799(18)	*Na*-O4^{8}	2.532(2)
*T*3-O6^{12}	1.6198(19)	*Na*-O4^{2}	2.532(2)
*T*3-O3^{13}	1.6404(13)	*Na*-O7^{16}	2.541(4)
*T*3-O3^{14}	1.6404(13)	*Na*-O7^{15}	2.541(4)
<*T*3-O>	1.6201	*Na*-O7^{17}	2.541(4)
*T*4-O3^{7}	1.7528(13)	*Na*-O5^{16}	2.7363(19)
*T*4-O3^{5}	1.7528(13)	<*Na*-O>	2.512
*T*4-O1^{3}	1.7532(13)		
*T*4-O1^{1}	1.7532(13)	C-O7^{15}	0.999(10)
<*T*4-O>	1.7530	C-O7	0.999(10)
*T*5-O5	1.7128(19)	*Na*-C1^{16}	2.3366(5)
*T*5-O4^{8}	1.7146(18)	O7-O8w	0.999(10)
*T*5O2^{1}	1.7736(13)		
*T*5-O2^{9}	1.7736(13)		
<*T*5-O>	1.7437		

Symmetry operators: #1 x,-y+1,-z+1/2; #2 x,y-1,z; #3 -x+1/2,y-1/2,-z+1/2; #4 -x+1/2,-y+1/2,z; #5 x-1/2,y-1/2,z; #6 x-1/2,-y+1/2,-z+1/2; #7 x+1/2,y-1/2,z; #8 x,-y,-z+1/2; #9 -x+1,-y+1,z; #10 -x,-y+1,-z; #11 x,-y+1,z-1/2; #12 -x,y,-z+1/2; #13 -x,-y+1,z; #14 x-1/2,y+1/2,z; #15 x,y+1,z; #16 -x+1,y,z-1/2; #17 -x+1,y,-z+1/2.

All atoms were refined with anisotropic-displacement parameters, with the exception of Na and O8w which were refined with isotropic-displacement parameters, and of C and O7 (for CO_2) whose isotropic-displacement parameters were fixed at values compatible for ferromagnesian cordierite (Malcherek *et al.*, 2001); the site-occupancy factor (s.o.f.) for Li at the *M* site was fixed at the nano-LAMS value for Li (Tab. 1); Fe and Mg were refined, constraining the sum of their occupancies to be equal to (1 – Li); s.o.f. were refined for Na and H_2O in the channels, and the CO_2 occupancy was fixed at the SIMS value. As previously stated, the lack of monovalent charge at the *M* site due to the presence of Li^{+}, is counter-

balanced by the presence of Na^+ in the channel; H atoms of the H_2O group could not be detected due to the low concentration of H_2O in the sample (Tab. 1); Fe s.o.f. value is slightly over estimated due to the contribute of Mn. Further details of the crystal structure refinements can be obtained from the Fachinformationszentrum Karlsruhe, 76344 Eggenstein-Leopoldshafen, Germany, (fax: +49 7247-808-666; e-mail: crysdata@fiz-karlsruhe.de) on quoting the depository number CSD-425930. The list of F_o/F_c data is available from the author up to one year after the publication has appeared.

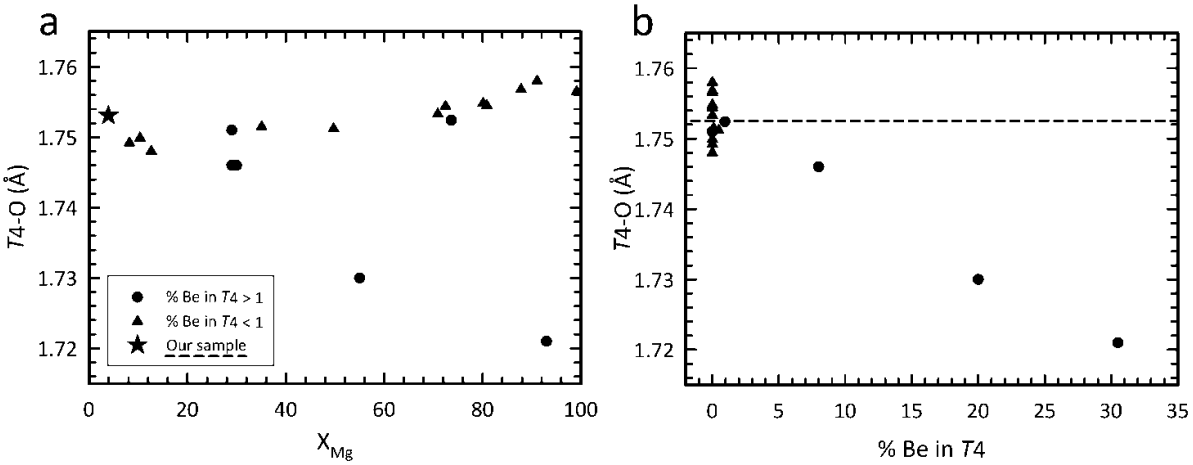

Figure 3 - *T*4-O bond lengths for various cordierite samples *vs* (a) the magnesium number (X_{Mg}) and (b) the % Be at the *T*4 site. Triangles indicate the samples with % Be in *T*4 > 1; the star and the dashed line represents our sample. Data from Hochella *et al.* 1979; Armbruster *et al.* 1986; Malcherek *et al.* 2001, Yakubovich *et al.* 2004.

5. Optical properties

The studied sekaninaite is biaxial negative. The measured $2V_X$ value is 64±2°, refractive indexes are α = 1.5640(4), β = 1.5740(4) and γ = 1.5784(4). These values are slightly lower (by 0.004) than those reported by Salkregg and Bloss (1980), probably due to a higher H_2O and Fe contents in the latter.

6. FTIR spectroscopy

The single-crystal unpolarized infrared spectrum of sekaninaite (Fig. 4) can be divided into two main regions: (I) 3900 – 3300 cm^{-1} where absorption bands are due to H_2O

stretching modes (Goldman *et al.*, 1977), and (II) 2600 – 2000 cm^{-1} where absorption bands are related to the antisymmetric stretching mode of CO_2. As shown by Geiger and Kolesov (2002) and Della Ventura *et al.* (2009, 2012) for CO_2-rich samples, the combination modes of CO_2 are also observed, overlapping with H_2O bands in region I. Additional peaks due H_2O modes also occur around 1600 cm^{-1} (bending) and 5250 cm^{-1} (combination) (Della Ventura *et al.*, 2012).

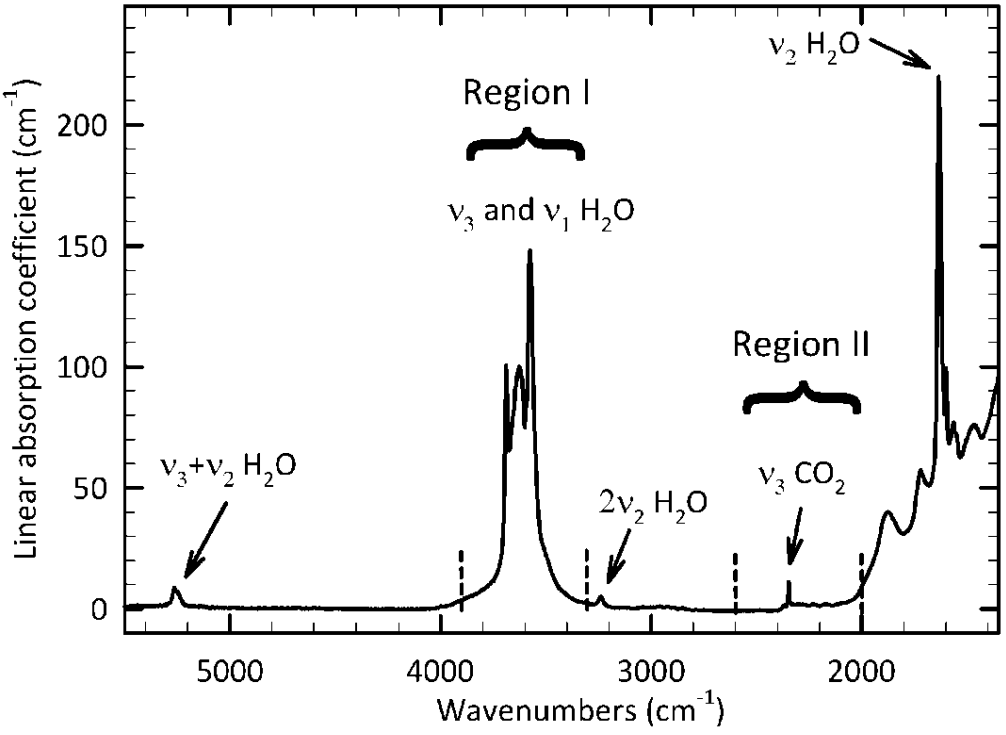

Figure 4 - Single-crystal unpolarized-light infrared spectrum of sekaninaite. The two regions from 3900 to 3300 cm^{-1} and from 2600 to 2000 cm^{-1} are highlighted. H_2O bending mode at 1635 cm^{-1}, H_2O bending first overtone mode at 3241 $cm^{-1}$and H_2O combination mode about 5260 cm^{-1} are arrowed.

The polarized spectra in the 4000 – 3200 cm^{-1} range are given in Figure 5a (right). Where the electric vector **E** is parallel to the crystallographic axis **c** (**E**||**c**), two sharp peaks are observed, the more intense centered at 3575 cm^{-1}, and the weaker at 3689 cm^{-1}. The **E**||**b** spectrum has a very broad peak at about 3630 cm^{-1} with a pronounced shoulder at 3575 cm^{-1}. The **E**||**a** spectrum shows a broad and very weak multi-component absorption with maxima at 3630 cm^{-1} and 3595 cm^{-1}.

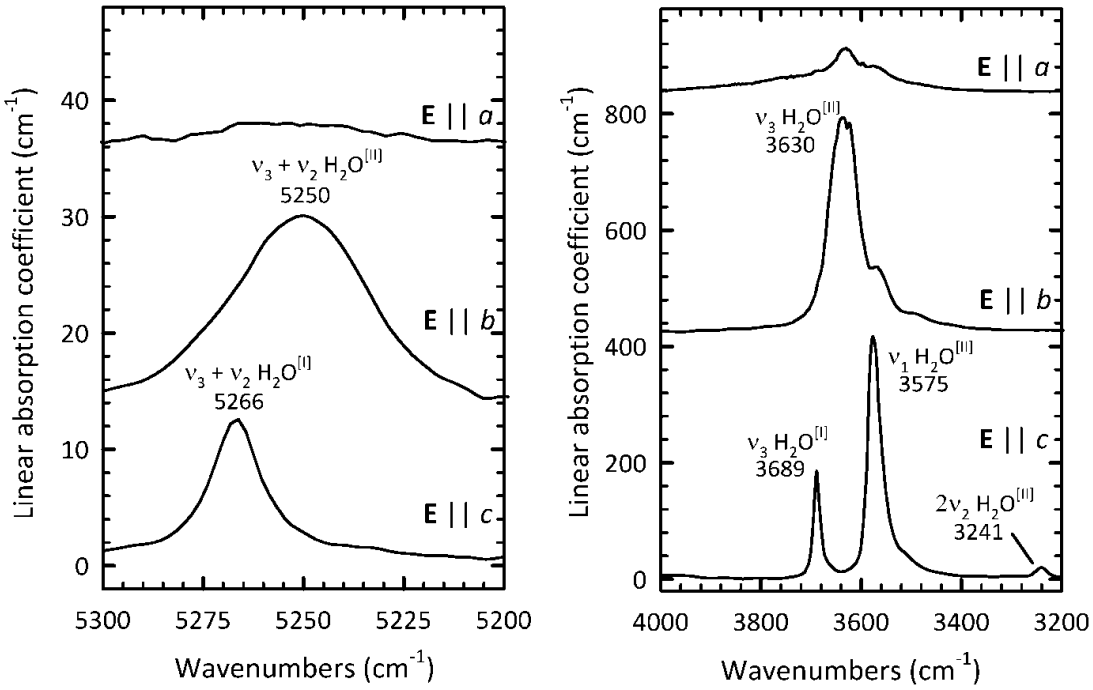

Figure 5a - Single-crystal polarized-light infrared spectra of sekaninaite in the ranges 5300-5200 cm^{-1} (left) and 4000-3200 cm^{-1} (right). Spectra were collected on (010) 43 µm thick and (100) 47 µm thick oriented slabs.

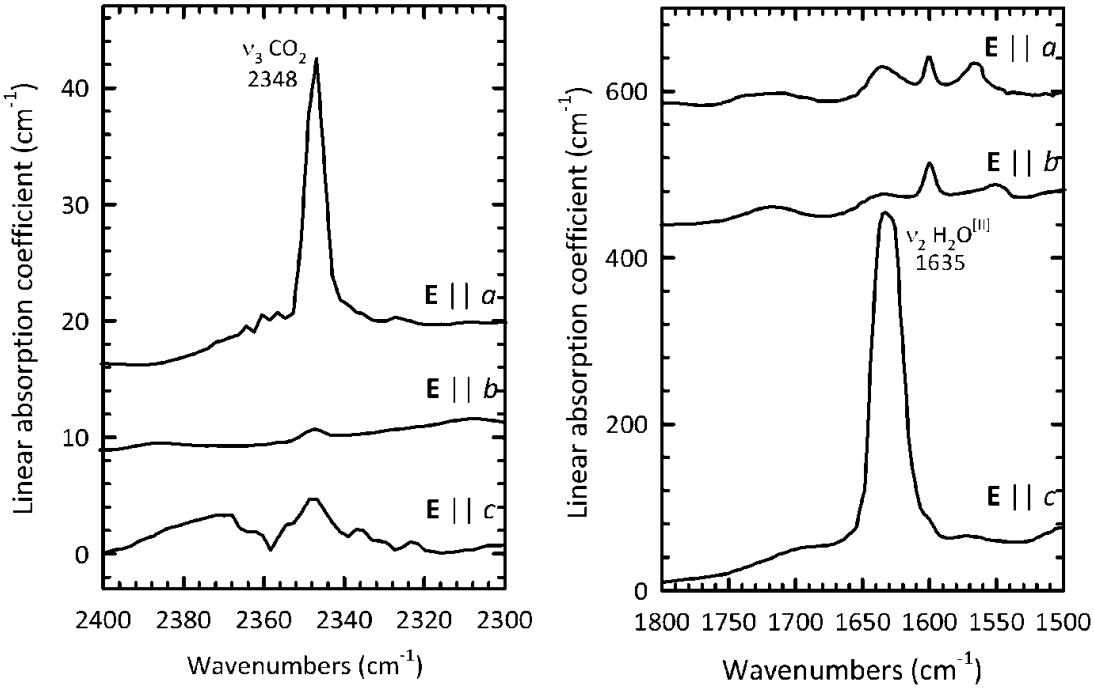

Figure 5b - Single-crystal polarized-light infrared spectra of sekaninaite in the CO_2 antisymmetric stretching mode region (left) and $H_2O^{[II]}$ bending mode (right). Spectra were collected on the same slabs of Fig. 3b except for the E ||**b** spectrum, which was collected from a (001) 168 µm thick slab.

The polarized spectra in the 5300 - 5200 cm^{-1} range (Fig. 5a, left) show a fairly sharp peak at 5266 cm^{-1} for **E**||**c**, and a broader peak about 5250 cm^{-1} for **E**||**b**. The **E**||**a** spectrum is featureless.

In region II of the spectrum (Fig. 5b left), only a weak peak at 2348 cm^{-1} is observed for **E**||**a**. Outside these ranges, additional relevant peaks are observed in **E**||*c* at 3241 cm^{-1} (Fig. 5a right) and 1635 cm^{-1} (Fig. 5b right). A triplet of very weak components is finally observed at 1552, 1600, and 1635 cm^{-1} polarized for **E**||**a** and **E**||**b**. Note that the peak at 1635 cm^{-1} is very likely offscale due to detector saturation, even for a slab thickness < 50 µm.

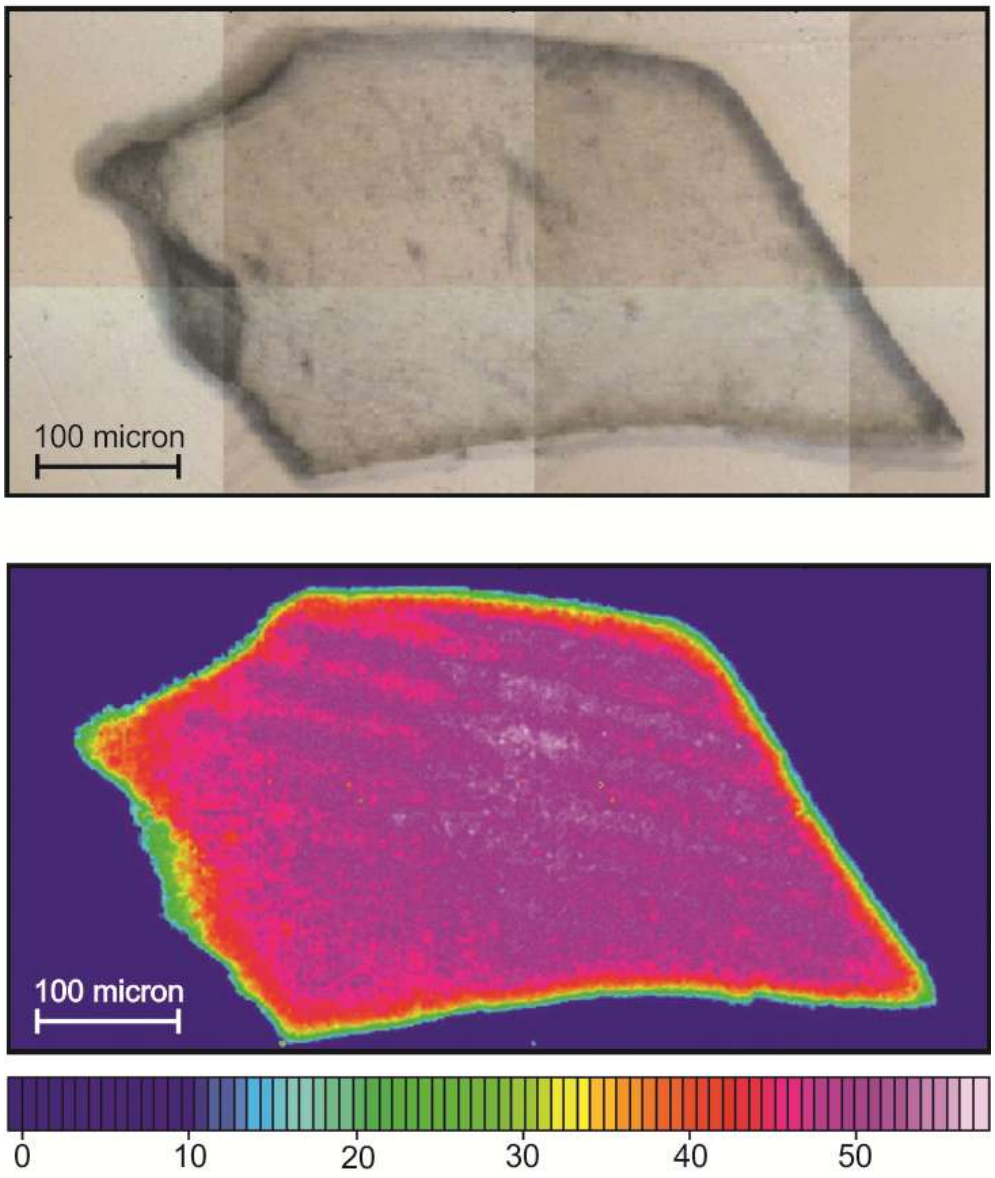

Figure 6 - FTIR image of the (100) section, 47 µm thick slab of sekaninaite. Above: video image of the sample. Below: FPA image of the same sample; integration of the H_2O stretching bands in the range 3500-3700 cm^{-1}. The chromatic scale is proportional to volatile contents, units are arbitrary.

FPA images of selected sample areas were collected to check for possible inhomogeneity in the volatile distribution across the studied crystals (Della Ventura *et al.*, 2012). Figure 6 shows that there is no significant variation in the H_2O contents for the whole sample. Imaging of CO_2 distribution was not possible because the CO_2 anti-symmetric stretching peak could not be distinguished from the noise in the FPA data due to the low concentration of CO_2. However CO_2 homogeneity was checked by collecting several random spots on the slab, and the results always gave the same value within esd.

7. FTIR band assignment

Although there are several spectroscopic (FTIR + Raman) works on the channel volatile constituents of Mg-rich cordierite in the literature (Goldman *et al.*, 1977, Geiger and Kolesov, 2002, Della Ventura *et al*., 2009, 2012), polarized data for Fe-rich cordierite are rare (Kolesov and Geiger, 2000). According to these works, it is now well-established that extra-framework H_2O groups occur in the structural channels of cordierite with the molecular plane parallel to (100). However, H_2O can be oriented in two different ways: type I H_2O (hereafter $H_2O^{[I]}$) has its H–H vector oriented parallel to the **c** axis, and type II H_2O ($H_2O^{[II]}$) has its H–H vector parallel to the **b** axis. H_2O groups of the latter type are bonded to locally associated channel Na cations as in beryl (Hawthorne and Černý, 1977, Sherriff *et al.*, 1991). The linear CO_2 molecules are oriented parallel to the crystallographic **a** axis (Khomenko and Langer, 2005, Aines and Rossman, 1984).

The band assignment given below follows the criteria proposed by Goldman *et al.* (1977), Geiger and Kolesov (2002) and Della Ventura *et al*., (2009), based on single-crystal infrared polarized-light determination on oriented slabs of Mg-rich cordierite. However, as we will see from the band positions and polarization behavior, these criteria are also suitable for sekaninaite.

The peak at 3689 cm^{-1} (Fig. 5a right), polarized for E||**c**, is assigned to the anti-symmetric stretching mode ν_3 of $H_2O^{[I]}$; the corresponding symmetric stretching mode (ν_1) in Mg-cordierite is observed at 3595 cm^{-1} (Paukov *et al.*, 2006) and is polarized for E||**b**. In the spectra collected for sekaninaite studied here, this component cannot be resolved due to the very high intensity of the 3630 cm^{-1} peak (Fig. 5a). The broad band at 3630 cm^{-1} polarized in **E**||**b** is assigned to the antisymmetric stretching mode ν_3 of $H_2O^{[II]}$. The corresponding

symmetric stretching band ν_1 occurs at 3575 cm^{-1} in **E**||**c**. The weak absorptions at 3575 cm^{-1} in **E**||**b** and 3630 cm^{-1} in **E**||**a** (Fig. 5a) can be due to slight tilting during sample preparation; the latter could be also ascribed to a very small amount of H_2O with its H–H vector parallel to **a** (Kolesov and Geiger, 2000). A peak at 3595 cm^{-1} observed in **E**||**a** was assigned by Della Ventura *et al.* (2009, 2012) to the $\nu_3 + 2\nu_2$ combination mode of CO_2. In the present case, because of the very small concentration of CO_2, the assignment must be different; the band is probably due to minor tilting of the slab.

The bending mode ν_2 of $H_2O^{[II]}$ is observed at 1635 cm^{-1} (Fig. 5b, right) and is polarized parallel to the **c** axis (Goldman *et al.*, 1977, Della Ventura *et al.*, 2009); the same behavior is observed for its first overtone mode (Fig. 5a, right) at 3241 cm^{-1} (Herzberg, 1956). On the opposite the bending mode ν_2 of $H_2O^{[I]}$ is much less intense and occurs as three features centered at 1552, 1600, and 1635 cm^{-1} as already observed Goldman *et al.*, (1977). The assignment of these features to H_2O modes is supported by the fact that they are absent in samples with low water contents (Della Ventura *et al.*, 2012) and by the fact that they disappear with the other fundamental modes after dehydration ,(Goldman *et al.*, 1977). The bending mode of $H_2O^{[I]}$ is expected to be polarized for **E**||**b** however they also appear for **E**||**a** (see also Goldman *et al.*, 1977).

In the near-infrared (NIR) region (Fig. 5a, left), the ($\nu_3 + \nu_2$) combination modes at 5266 cm^{-1} (for $H_2O^{[I]}$) and at 5250 cm^{-1} (for $H_2O^{[II]}$) are polarized with **E**||*c* and **E**||**b**, respectively, as is also observed for Mg-cordierite (Goldmann *et al.*, 1977, Della Ventura *et al.*, 2012).

The ν_3 anti-symmetric stretching vibration mode of CO_2 (Fig. 5b, left) at 2348 cm^{-1} is fully polarized for **E**||**a** .

8. Unpolarized Raman spectroscopy

In region I (Fig. 7), two absorptions are observed: one sharp peak at 3598 cm^{-1} and a second broader peak at about 3580 cm^{-1}; the former is related to the symmetric stretching mode ν_1 of $H_2O^{[I]}$ and the latter to the ν_1 mode of $H_2O^{[II]}$ (Kolesov and Geiger, 2000). No bands are present in the Raman spectrum at 1383 cm^{-1} where the CO_2 symmetric stretching should be located (Kolesov and Geiger, 2000), in accord with the very small amount of CO_2 in the studied crystal; however, two weak absorptions are resolved at 2329 cm^{-1}, indicating the

presence of N_2 and at 2916 cm^{-1}, indicating the presence of CH_4 (Cesare *et al.*, 2007) in the sample.

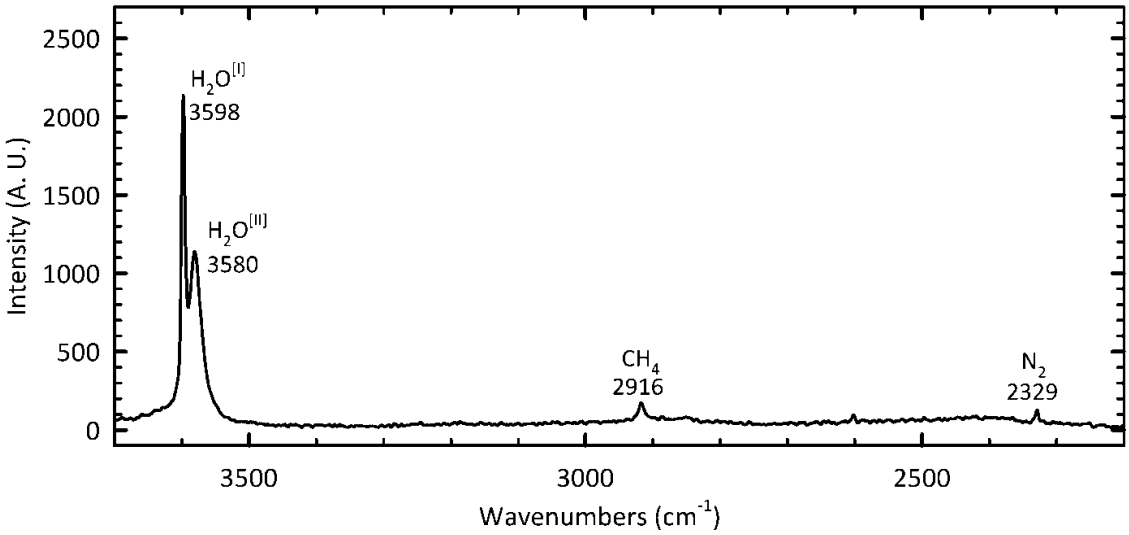

Figure 7 - Background-corrected Raman spectrum of sekaninaite. The symmetric stretching modes for both types of H_2O are indicated; intensity in arbitrary units.

9. Calibration of a molar absorption coefficients of H_2O and CO_2 in sekaninaite

The Beer-Lambert law, $C = A / (t \cdot \varepsilon)$, can be used to quantify H_2O and CO_2 from polarized FTIR spectroscopy in cordierite (Della Ventura *et al.*, 2009, 2012). In this relation, the molar absorption coefficient ε is matrix specific and must be calibrated by combining the spectroscopic measurements with a second independent analytical method. Rearranging the above equation, $\varepsilon = (A \cdot k) / (t \cdot D \cdot C)$, where *C(wt.%)* is the concentration of the target molecule, *A* is the infrared absorbance, *t* is the slab thickness in cm, *D* is the value of the sample density (g/cm^3) and *k* is a conversion factor needed to convert from wt% to mol·l^{-1}; for H_2O, k = 1.8 (Beran *et al.*, 1993) and for CO_2, k = 4.401 (Della Ventura *et al.*, 2009). *C(wt.%)* was determined using SIMS, and the absorbance *A* was calculated as the total integrated absorbance A_i (cm^{-1}) = $A_x + A_y + A_z$, where A_x, A_y and A_z are the integrated absorptions in each polarization direction (Libowitzky and Rossman, 1996). The peak areas were obtained for each component using the data calculation routine built in the spectrometer software; the background was modeled as linear. Using this method, it is possible to quantify up to a few ppm of H_2O or CO_2 in the sekaninaite channels, but also

distinguish the two different types of H_2O groups ($H_2O^{[I]}$ and $H_2O^{[II]}$) in a reliable way (Della Ventura *et al.*, 2012). Integrated molar coefficients for both types of H_2O were calculated using the method described in Della Ventura *et al.* (2012), calculating the concentration of $H2O^{[II]}$ = 2•(Na,K,Ca)ch from the chemical analysis of Table 1 and deriving $H_2O^{[I]} = H_2O^{tot} - H_2O^{[II]}$. Molar absorption values were thus obtained for both the principal and combination modes (Tab. 5). It is worth recalling here that the use of the combination modes, where applicable, is very useful as these absorptions can be measured on thicker (and thus easy to prepare) crystal slabs. The error σ_ε associated with ε was obtained using the classical statistics of error propagation (Bellatreccia *et al.*, 2006); the error on *A* is ~ 10% (Libowitzky and Rossman, 1997), the sample thickness uncertainty was set to 2 μm, the standard deviation of the density (D) is 2% and the accuracy of the SIMS analysis is better than 10%. Final values are $\varepsilon_{i\ H2O[I]}$ = 6000±2000; $\varepsilon_{i\ H2O[II]}$ = 13000±1000 and $\varepsilon_{i\ CO2}$ = 2000±1000). Used in the Beer-Lambert relation, these coefficients allow us to quantify H_2O and CO_2 in Fe-rich cordierite from polarized FTIR measurements.

Table 5 - Integrated (ε_i) and linear (ε_l) absorption coefficients of H_2O and CO_2 for sekaninaite from Dolnì Bory.

		ε_i (l/mol·cm^2)	ε_l (l/mol·cm)
ν_3	$H_2O^{[I]}$ (3689 cm^{-1})+ $H_2O^{[II]}$ (3630 cm^{-1})	11000±1000	230±20
	$H_2O^{[I]}$ (3689 cm^{-1})	6000±2000	400±100
	$H_2O^{[II]}$ (3630 cm^{-1})	13000±1000	190±20
$\nu_3 + \nu_2$	$H_2O^{[I]}$ (5266cm^{-1})+ $H_2O^{[II]}$ (5250 cm^{-1})	360±40	11±1
	$H_2O^{[I]}$ (5266cm^{-1})	500±200	25±9
	$H_2O^{[II]}$ (5250 cm^{-1})	300±30	7.1±0.8
ν_3	CO_2 (2348 cm^{-1})	2000±1000	300±200

10. Conclusions

Polarized FTIR spectroscopy show the presence of two types of H_2O groups in the structural channels; in particular, due to the relatively high concentration of extraframework alkali cations, $H_2O^{[II]}$ is dominant over $H_2O^{[I]}$. FPA images of several samples show that the

sample from Dolnì Bory has an homogeneous H_2O distribution, unlike most cordierites where many different factors such as fractures, inclusions and secondary alteration may cause very strong inhomogeneity in H_2O concentration across a crystal (Della Ventura *et al.*, 2012). Sekaninaite from Dolnì Bory contains small amounts of CO_2 and, as shown by Raman spectra, trace amounts of N_2 and CH_4.

The integrated molar absorption coefficients ε for H_2O are very close to those reported for Mg-rich cordierite by Della Ventura *et al.* (2012). On the other hand, the values of $\square_{i\ CO2}$ obtained here cannot be considered very reliable because of the uncertainty of the SIMS value (which is more than the 50%). However, this value is close to that obtained by Della Ventura *et al.* (2006) from a CO_2-poor cordierite. This suggests that the molar coefficient of CO_2 may be dependent on bulk concentration; however, this point needs additional experimental evidence for absolute confirmation.

Acknowledgements

We thank Mr. Renato Pagano for providing the studied sample, Vincenzo Mangione for the help with the optical profilometer, Giuseppe Chita (IC-CNR, Bari) for X-ray data collection and Simon Harley (University of Edinburgh) for providing the SIMS data for H and C.

CHAPTER 3

HT-FTIR MICRO-SPECTROSCOPY OF CORDIERITE. I: THE CO_2 ABSORBANCE AS A FUNCTION OF *T* FROM *IN SITU* AND QUENCHED EXPERIMENTS

Abstract

In this work we address the evolution of the intensity of the CO_2 bands in cordierite, by comparing data obtained from *in situ vs.* quenching measurements. A natural well characterized cordierite from Kragero (Arendal region, Norway) was studied up to 1200 °C using a heating stage fitted on a FTIR microscope. Two different oriented sections (001) and (010), respectively, were examined in order to check the effect of the channel orientation on the CO_2 release from the matrix. Spectra collected *in-situ* show that increasing temperatures induces an increase of peak width for all CO_2-related bands. The effects on the integrated absorbance A_i are different for the different bands. Most notably, the integrated intensity A_i of the anti-symmetric stretching mode (ν_3) increase up to 800 °C, then progressively decreases to 1000/1200°C, depending on the orientation of the channels respect to the slab surface. Data obtained on quenched sample reveals that there is no variation in the band intensity for $T < 900$ °C. Because CO_2 is not expected to change its molecular configuration during heating, the absorbance increase during *in situ* measurements may be related to an increase in the molar absorption coefficient ε.

Combined *In situ* and quenched FTIR data revealed that the CO_2 loss from the cordierite matrix starts around 800 °C and is strongly dependent to the thickness and shape of the examined samples. In more details, it is favored for small and tabular shaped grains; while for large and prismatic shaped grains the volatile loss is greatly reduced. Fracturing along direction normal to [001] direction multiplies the diffusion interfaces and enhances the CO_2 loss.

1. Introduction

Microporous minerals are important materials from both a geological and a technological point of view because their structure may permanently host or exchange, under certain circumstances, both useful or hazardous molecular species (Ferraris and Merlino, 2005). Changes in the environmental conditions, such as temperature, pressure f_{H2O}, f_{CO2} or f_{O2}, may deeply affect both the structural parameters of the matrix and the stability of trapped molecules. In this context, cordierite plays a key role since it represents the only case of a relatively common microporous mineral able to trap significant amounts of molecular H_2O and CO_2 (Armbruster and Bloss, 1982) under extreme geological conditions, spanning from the amphibolite facies to ultra-high temperature metamorphism to crustal anatexis (Vry *et al.*, 1990). The analysis of volatiles in cordierite can be a very useful tool to define the composition of coexisting fluids during its formation and/or subsequent metasomatism and alteration, thus a deeper knowledge of their diffusion mechanism through the structure is crucial in petrologic studies (Carrington and Harley, 1996). Moreover, a better definition of the ability of cordierite to exchange molecules with coexisting fluids may have implications for technological applications in environmental studies, such as in CO_2 sequestration processes.

Cordierite, with an ideal crystal-chemical formula $(Mg,Fe)_2Al_4Si_5O_{18}{\cdot}nH_2O,mCO_2$, can be regarded as a framework silicate (Gibbs, 1966) whose structure consists of 6-fold pseudo-hexagonal Si/Al tetrahedral rings stacked perpendicular the *c*-crystallogaphic axis. These ring are held together vertically by tetrahedral Si/Al chain (Gibbs, 1966, Yakubovich *et al.*, 2004). The resulting structure has a very low thermal expansion coefficient (Hocella and Brown, 1986; Bruno and Vogel, 2008) and, because of this, cordierite has important applications in ceramic industry. Mg end-member compositions shows no polymorphic changes up to about

1400° C; for higher T, cordierite reverts to the hexagonal form indialite (Kitamura and Hiroi, 1982) by a first-order displacive transition. The framework arrangement creates a series of interconnected cages or channels, running along the *c* crystallographic axis; inside these channels alkali cations and/or volatile molecules, notably CO_2 and H_2O, are typically allotted (Gibbs, 1966, Goldmann *et al.*, 1977, Della Ventura *et al.*, 2010, 2012). Based on polarized-light infrared spectroscopy, previous authors showed that the linear CO_2 molecule is oriented orthogonally to the *c* crystallographic axis and parallel to the *a* axis (Armbruster and Bloss, 1982). H_2O molecules may occur in two different orientations, *i.e.* with their H-H direction parallel to the *c* axis (type I water, $H_2O^{[I]}$) or parallel to the *b* axis (type II water, $H_2O^{[II]}$) (Wood and Nassau, 1968, Goldmann *et al.*, 1977), the latter type being associated to alkali cations inside the structural channels (Della Ventura *et al.*, 2012).

Several studies pointed out that the content of volatile constituents within the cordierite channels is strongly dependent on the composition of coexisting fluids during crystal growth (Vry *et al.*, 1990; Carrington and Harley, 1996; Harley *et al.*,2002; Kurepin, 2010), thus making this mineral an important tool to model the geological process of formation; in addition, H_2O and CO_2 contents may also affect the stability of cordierite itself (Schreyer 1985; Carey 1995; Harley *et al.*, 2002). Therefore the qualitative evaluation of kinetic behavior of channel constituents is crucial in petrologic studies. Several authors in the past have examined the thermodynamic properties of cordierite during dehydration (Giampaolo and Putnis, 1989; Carey, 1993; Carey, 1995; Paukov *et al.*, 2007; Dachs and Geiger, 2008), however no data are known so far for the possible processes of CO_2 desorption, *i.e.* the extraction of CO_2 from the structure as a function of *T*.
In this context, micro FTIR spectroscopy not only may provide quantitative information on the behavior of H and C during heat treatments, but may be a valuable tool to study the kinetics of the process, as it has been proven to be the case in a wide variety of minerals like sulfates (Putnis *et al.*, 1990, Carbone *et al.*, 2008), zeolites (Bish and Carey, 2001), and micas (Tokiwai and Nakashima, 2010a).

Quantitative FTIR spectroscopy is based on the Beer-Lambert relationship which, in its simplified form, is: $A = \varepsilon \cdot t \cdot C$. This equation relates the absorbance of a molecule (A) in the FTIR transmission spectra to its concentration (C) in a sample of thickness (t) *via* a constant known as the molar absorption coefficient, ε. The absorption coefficient is matrix dependent (Libowitzky and Rossman, 1996) and must be calibrated for any mineral and type of bands

or, alternatively, evaluated using empirical curves (Paterson, 1982, Libowitzky and Rossman, 1996). However, several authors (*e.g.* Keppler and Bagdassorov, 1993; Yamagishi *et al.*, 1997; Zhang *et al.*, 2007; Tokiwai and Nakashima, 2010b) revised recently the absorbance changes in minerals and glasses during *HT*-FTIR experiments and showed that the absorption coefficients measured during *in situ* data collection change with *T*. In addition, Zhang *et al.* (2007) observed recently that, in a variety of minerals, *in situ* absorbance trends of the same molecular species obtained using *HT*-FTIR spectroscopy may differ for the different modes (*i.e.* stretching *vs* bending or multiphonon bands). The implication of these studies is that one cannot extract quantitative information from *in situ* HT-FTIR spectra without an accurate preliminary study of the absorbance variation with temperature (Tokiwai and Nakashima, 2010b). In fact, the reason for the change in the molar absorption coefficient ε as a function of *T* is still not completely understood.

Although the behavior of H_2O has attracted significant attention, no studies have so far addressed this problem for CO_2 although carbon dioxide is an important constituent of silicate melts (Watson *et al.*, 1982; Watson, 1991; Behrens *et al.*, 2009), and minerals such as beryl (*e.g.* Wood and Nassau, 1968), cordierite (*e.g.* Khomenko and Langer, 2005, Della Ventura *et al.*, 2012), feldspathoids (Della Ventura *et al.*, 2006, 2008, Bellatreccia *et al.*, 2009) or various forms of silica (Kolesov and Geiger, 2003). In this work we address the behavior of carbon dioxide absorption in the MIR range for cordierite as a function of temperature and sample orientation. We address in particular the temperature dependence of the CO_2 bands by comparing the intensities obtained during *in situ* and quenching experiments, to investigate the effects of temperature on the molar absorption coefficient ε.

2. Studied samples

Clear and inclusion-free fragments, with a pale blue-violet color were extracted from a large crystal of cordierite Rp 3237 from Kragero (Arendal region, Norway). Chemical composition, crystal-chemical formula, cell parameters, density and optical properties of this sample are given in Della Ventura *et. al.* (2012); for sake of simplicity, a summary of data is reported in Table 1; full explanation of the analytical methods can be found in Della Ventura *et. al.* (2012). This sample was chosen because it is very poor in Fe and has an octahedral composition very close to that of a Mg-end member (Tab. 1).

Table 1 - Microchemical analysis, crystal-chemical formula, cell parameters, density and optical properties for cordierite RP 3237. Data from Della Ventura *et. al.* (2012). Crystal-chemical formula based on 18 oxygen atoms p.f.u.

oxides (wt.%)		**St. Dev.**	**formula**	
SiO_2	49.55	0.19	Si	5.01
Al_2O_3	33.01	0.10	Al	3.94
MgO	12.49	0.12	Σ Tetrahedra	8.95
FeO	1.86	0.14	Mg	1.88
TiO_2	0.00	0.00	Fe	0.16
MnO	0.02	0.02	Ti	0.00
CaO	0.00	0.00	Mn	0.00
Na_2O	0.24	0.03	Σ Octahedra	2.00
K_2O	0.00	0.01	Ca	0.00
H_2O	0.904	0.04	Na	0.05
CO_2	1.005	0.01	K	0.00
Total	99.06		Σ Channels	0.05
			n(H_2O)	0.31
			m(CO_2)	0.14
			Σ Volatiles	0.45
			**$H_2O^{[II]}$	0.10
			**$H_2O^{[I]}$	0.21
			$X_{crd}CO_2$	0.31
Cell parameters (Å)				
a	17.085			
b	9.721 (1)			
c	9.353 (1)			
Densitiy (g/cm^3)	2.58 (3)			
Optic sign	Positive			
2Vx (°)	90.3 (9)			

The H_2O and CO_2 contents were quantified by SIMS (secondary-ion-mass-spectrometry) using a Cameca IMS4f ion microprobe at EMMAC, the University of Edinburgh. Procedures follow those described in previous cordierite studies from the Edinburgh laboratory (Harley and Carrington, 2001; Thompson *et al.*, 2001; Harley *et al.*, 2002, Della Ventura *et. al.*, 2012). The crystal-chemical formula, based on 18 oxygen atoms pfu is $Na_{0.05}(Mg_{1.89}Fe_{0.16})Al_{3.97}Si_5O_{18}\cdot 0.31H_2O\cdot 0.14CO_2$. Fe^{tot} was considered as Fe^{2+}.

Preliminary FTIR imaging confirmed an homogeneous distribution of H_2O and CO_2 across the sample (Della Ventura *et. al.*, 2012).

Selected crystal fragments were oriented on (001) and (010) using a polarizing microscope equipped with a spindle-stage; the extinction data were processed using the program ExcalibrW (Bloss, 1981; Gunter *et al.*, 2005). Crystallographic orientation was based on the optical orientation *a* = Z, *b* = Y and *c* = X (Deer *et al.*, 2004). The fragments were transferred from the spindle-stage to glass slides and doubly polished. Table 2 gives the final thickness together miscellaneous information for both slabs used in this work; sample thickness was measured using an electronic micrometer with ±5 μm uncertainty and checked using the interference fringes in the FTIR spectra, using the formula $t = 1/[2 \cdot n \cdot (v_1 - v_2)]$ where *t* is sample thickness in cm, *n* = 1.535 is the refractive index and $(v_1 - v_2)$ is the distance between two adjacent fringes in cm^{-1} (Pistorius and DeGrip, 2006).

Table 2 – Miscellaneous data for the studied sections.

label	Thickness (μm)	Approximate lateral dimensions (μm)	Crystallographic orientation	Optical directions on plane
RP 3237_11	77	300 x 250	(001)	Y Z
RP 3237_14	39	500 x 250	(010)	X Z

3. Experimental methods

HT-FTIR measurements up to 1200 °C were performed using a Linkam TS 1400 XY heating stage. The cordierite slabs were oriented on the horizontal plane using a polarizing microscope and then carefully transferred on a quartz sample holder, which allows good transparency for the MIR domain down to 2070 cm^{-1}. The sample holder was inserted into a 17 mm ceramic crucible for the heating runs. Temperature was measured using a type S Pt-10% Rh/Pt thermocouple placed close to the sample; the accuracy was ±1°C according to the manufacturer. Heating ramps were set using a digital controller.

HT-FTIR spectra were acquired using a Bruker™ Hyperion 3000 microscope equipped with a KBr-broadband beamsplitter, a 15 X objective and a liquid nitrogen-cooled MCT detector at Laboratori Nazionali di Frascati-Istituto Nazionale di Fisica Nucleare (LNF-INFN, Frascati, Rome). The nominal resolution was set at 4 cm^{-1} and 128 scans were averaged for

both spectrum and background, for a total collecting time of about 30 seconds. FTIR images were collected using a 64 x 64 pixel focal-plane array (FPA); the nominal resolution was set at 4 cm^{-1} and 64 scans were averaged for each spectrum and background. With this set up each image covers an area of 170 µm x 170 µm with a nominal spatial resolution of ~5 µm (Della Ventura *et al.*, 2010, 2014).

Two different types of step-heating measurement were performed. In the first series of experiments, the (001) section was heated up to 1000 °C with a rate of 20 °C/min; FTIR spectra were collected for every step. At the end of the run, the sample was allowed to cool down to *RT* and a spectrum was measured, than was heated up to 1100 °C (rate 100 °C/min) and then cooled down again at RT; spectra were collected at 1100 °C and at RT. Background spectra were collected at the beginning of the experiment and at *RT*. The second series of experiments was performed heating up the (010) section with a rate of 100 °C/min up to 600 °C; measurements were performed every 100°C during the ramp. Then the sample was cooled down to *RT* and heated up again up to 600 °C with a rate of 100 °C/min. The same procedure was repeated at 800, 900, 1000, 1100 and 1200 °C. FTIR spectra were collected at *RT* and every 50 °C during the ramp. In any case, cooling rates were about 200°C/minute down to 200 °C, additional 5 minutes were necessary to cool down from 200 °C to *RT*. Background spectra were collected before each measurement. After each experiment FPA-FTIR images were collected in order to check the homogeneity of residual CO_2 distribution. We stress that all FTIR spectra on each slab were collected in the same point. A relatively large spot size (~150 µm) was preferred in order to obtain a better average of the CO_2 content. Indeed, as we will see later, major variations may in fact occur at a smaller scale.

4. FTIR spectra of the studied cordierite sections: preliminary considerations on the H_2O and CO_2 bands

Figure 2 compares the unpolarized-light FTIR spectra of cordierite Rp 3237 collected for both (001) and (010) sections; spectra are scaled to thickness (for peak assignment refer to Tab. 3). Notably, even under unpolarized light, the spectra are significantly different, and partly reflect the polarizing behavior of the respective orientations. For instance, the (001)

spectrum contains all absorption that are expected to be most intense for E//a and E//b, while absorptions that are expected to be strongly polarized per E//c, *i.e.* the v_3 mode of $H_2O^{[I]}$ at 3689 cm^{-1} (*e.g.* Della Ventura et al., 2010) are very weak. Moreover in the (010) section, the librational bands of CO_2 at 2391 and 2306 cm^{-1}, which are expected to be polarized for E//b (Tab. 3), are completely absent.

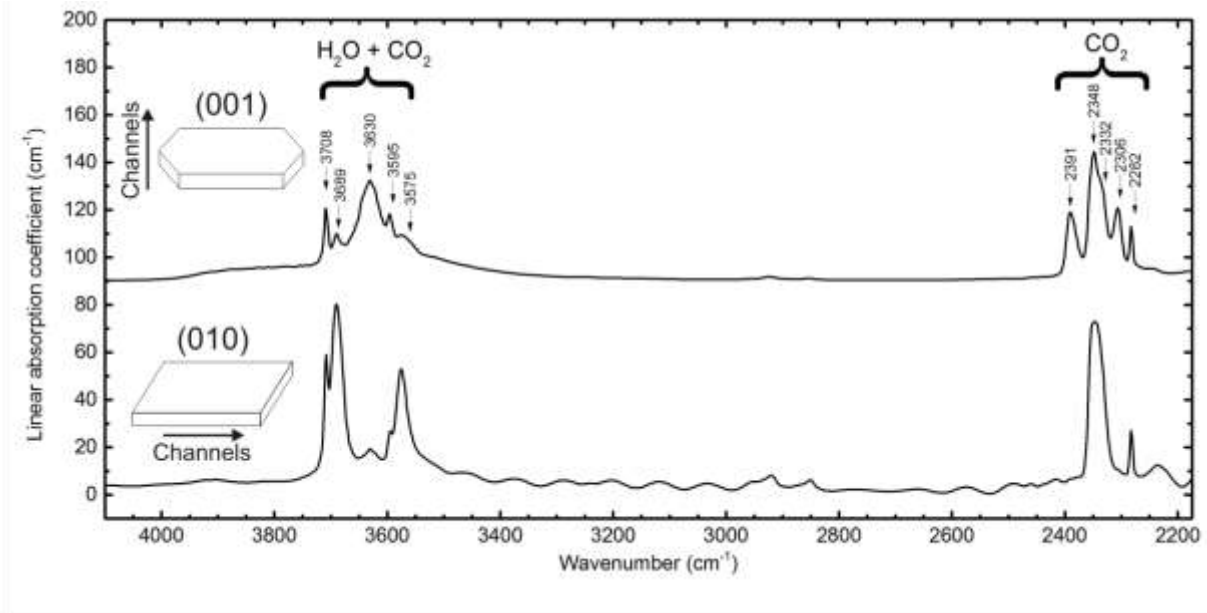

Figure 2 – Unpolarized light *RT* FTIR spectra of cordierite Rp 3237; top (001) section, and bottom (010) section. H_2O and CO_2 peak positions are reported (for peak assignment see Tab. 3); spectra scaled to thickness. A schematic representation of the channel orientation for each slab is reported.

These two sections were chosen such as to check for the effect of the channel orientation on the CO_2 release from the matrix; as a matter of fact, as schematically shown in Figure 2, the preferential escape path for the evolving gas, which is expected parallel to the structural channels (Fukuda and Shinoda, 2011) is oriented on the shorter (001) or longer (010) dimension of the sample, respectively.

Assignment of the several bands present on the spectra of cordierite can be based on a large number of unpolarized and polarized-light FTIR studies, see in particular Geiger and Kolesov (2002), Khomenko and Langer (2005), Della Ventura *et al.* (2009, 2012) and Radica *et al.* (2013).

To help following the discussion below, Table 3 gives a summary of the most relevant H_2O and CO_2 absorptions in the MIR (medium infrared) range, and their polarization directions.

Table 3 – Position, assignment and polarization direction of H_2O and CO_2 bands of cordierite; note that CO_2 antisymmetric stretching ν_3 mode presents residual absorptions per E//b. For explanations and references see text.

Molecule	Mode	Peak position (cm^{-1})	Polarization direction
$^{12}C^{16}O_2$	Antisym stretch ν_3	2348	E//a
	Antisym stretch ν_3 + lib	2391	E//b
	Antisym stretch ν_3 - lib	2306	E//b
	combination $\nu_3 + \nu_1$	3708	E//a
	combination $\nu_3 + 2\nu_2$	3595	E//a
$^{13}C^{16}O_2$	Antisym stretch ν_3	2282	E//a
$^{12}C^{16}O^{18}O$	Antisym stretch ν_3	2332	E//a
$H_2O^{[I]}$	bending ν_2	1635, 1600, 1560	E//a, E//b
	sym stretch ν_1	3689	E//c
	Antisymm stretch ν_3	3595	E//b
$H_2O^{[II]}$	bending ν_2	1634	E//c
	sym stretch ν_1	3575	E//c
	Antisym stretch ν_3	3630	E//b

5. Experimental Results

5.1 *In situ HT*-FTIR measurements: the (001) section

Figure 3 shows selected unpolarized-light *HT*-FTIR spectra collected *in situ* on the (001), 77 μm thick, section. In this orientation the structural channels are directed normal to the sample surface (Fig. 2). At room *T*, five peaks are observed in the principal CO_2 stretching region (Fig. 3b): three of these are related to the anti-symmetric stretching mode of CO_2 and its isotopes (2348 cm^{-1}: $^{12}C^{16}O_2$, 2332 cm^{-1}: $^{12}C^{16}O^{18}O$, and 2282 cm^{-1}: $^{13}C^{16}O_2$, Khomenko and Langer, 2005, Della Ventura *et al.*, 2009) and two are assigned to librational sideband peaks at 2391 and 2306 cm^{-1} and are symmetrically sited at ±43 cm^{-1} from the principal ν_3 anti-symmetric stretching peak at 2348 cm^{-1}. The temperature increase induces a general broadening of all five bands and an increase in band area (A_i). At higher temperatures the 2391 and 2306 cm^{-1} bands shift respectively to lower and to higher energies, converging toward the principal 2348 cm^{-1} band. At 400 °C we observe a doublet with maxima at 2358 cm^{-1} and at 2317 cm^{-1}, caused by overlapping of the former 2348-2391 and 2332-2306 cm^{-1} components. The 2282 cm^{-1} peak due to the isotope $^{13}C^{16}O_2$ is still resolved on the lower frequency side of this broad band. For $T > 900$ °C there is a sudden decrease in intensity of the absorption which is virtually zero at 1000°C.

Figure 3a displays selected spectra collected in the 3750-3650 cm^{-1} region. In this range we can follow the behavior of the relatively intense and sharp peak at 3708 cm^{-1} which is assigned to the CO_2 ($\nu_3 + \nu_1$) combination mode (Table 3, see also Della Ventura *et al.*, 2009, 2012), as a function of increasing *T*. Inspection of Figure 3a shows that this peak shifts to higher frequency and broadens considerable for increasing *T*; for *T* > 800°C it is barely appreciable and at *T* = 1000°C it disappears. The peak parameters of the 3708 cm^{-1} band as a function of *T* could be easily measured because this band is well isolated from the H_2O absorption at 3689 cm^{-1}. Spectra were treated with the OriginPro 9™ software using a Lorentzian peak shape function and a linear background; the absorbance contribution due to the 3689 cm^{-1} band could be easily subtracted. The obtained results, i.e. the evolution of the absorbance (both linear and integrated), position and FWHM are displayed in Figure 4.

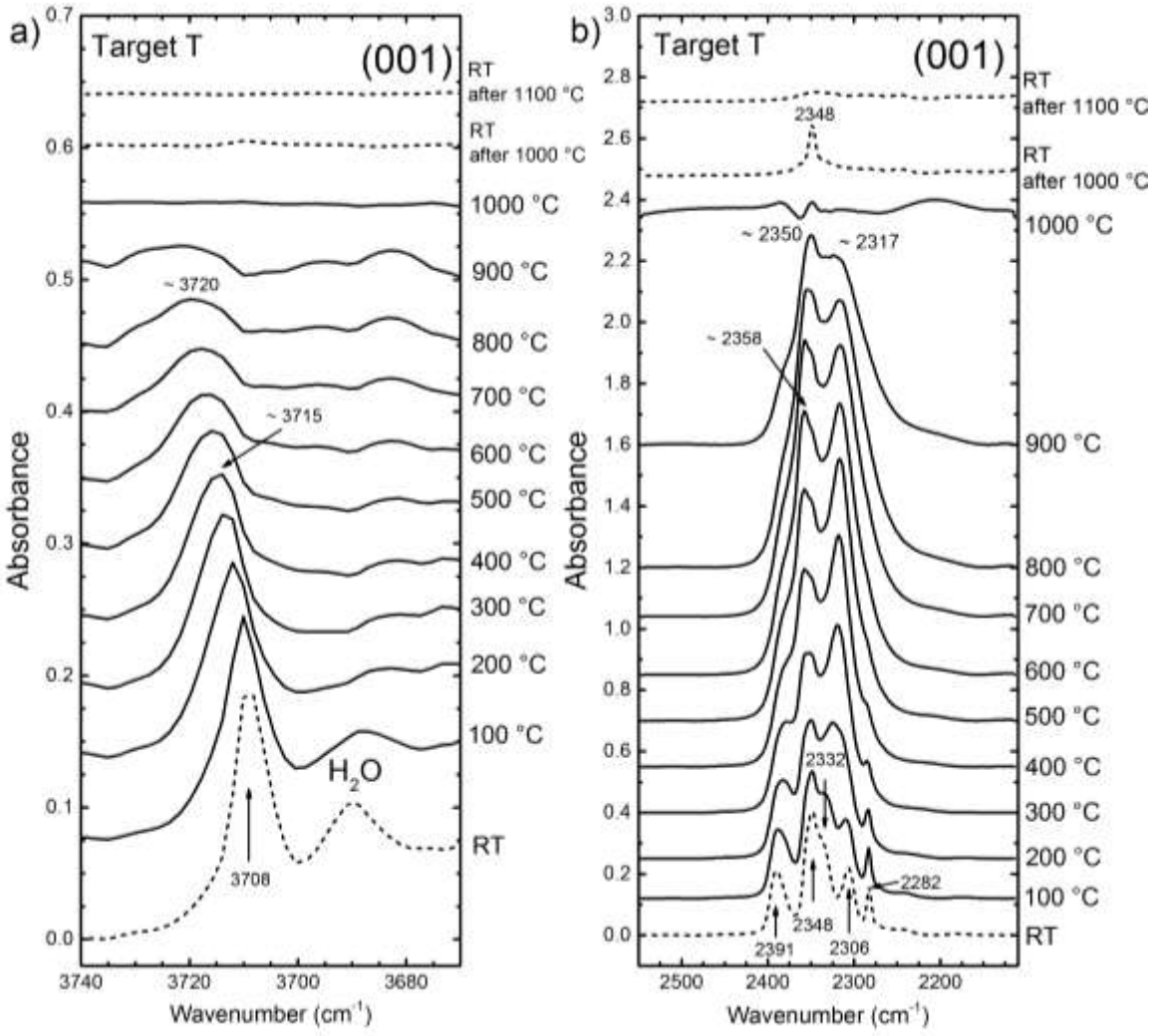

Figure 3 – *In situ* FTIR spectra for cordierite Rp 3237, 77 µm thick (001) section, at selected temperatures in the CO_2 ($\nu_3 + \nu_1$) combination region (a) and ν_3 anti-symmetric stretching region (b). For peak assignment see Table 3.

The integrated absorbance (A_i) (Fig. 4a) is almost constant up to about 450 °C, then decrease up to 850 °C. For higher *T* the intensity decreases with a much faster rate; the band disappears at 950°C. This trend is the result of a decreasing peak height (Fig. 4c) and a simultaneous increasing peak broadening (Fig 4d): the FWHM in fact increases from 6 cm^{-1} to about 18 cm^{-1} and finally decreases for *T* > 850°C. The peak position (Fig. 3 and Fig. 4b) shifts almost linearly to higher energies, from 3708 cm^{-1} at *RT* to 3715 cm^{-1} at 400 °C, up to about 3720 cm^{-1} at 850 °C. Note that for this section the H_2O ν_3 peak at 3689 cm^{-1} (Fig. 2, top curve) is no longer resolved from the background for *T* > 200 °C because of extreme peak broadening (Fig. 3a). The evolution of the 3595 cm^{-1} peak cannot be followed in the unpolarized spectra because of its very weak intensity. As already stated, at 1000 °C no CO_2 bands are observed in the higher frequency range, however, after quenching the sample to *RT* (Fig. 3b), a weak CO_2 band at 2348 cm^{-1} shows up, suggesting that at 1000°C weak amounts of carbon dioxide are still present in the sample. This band definitively disappears from the spectrum collected on the quenched sample only for *T* > 1100° C (Fig. 3b top dashed curves).

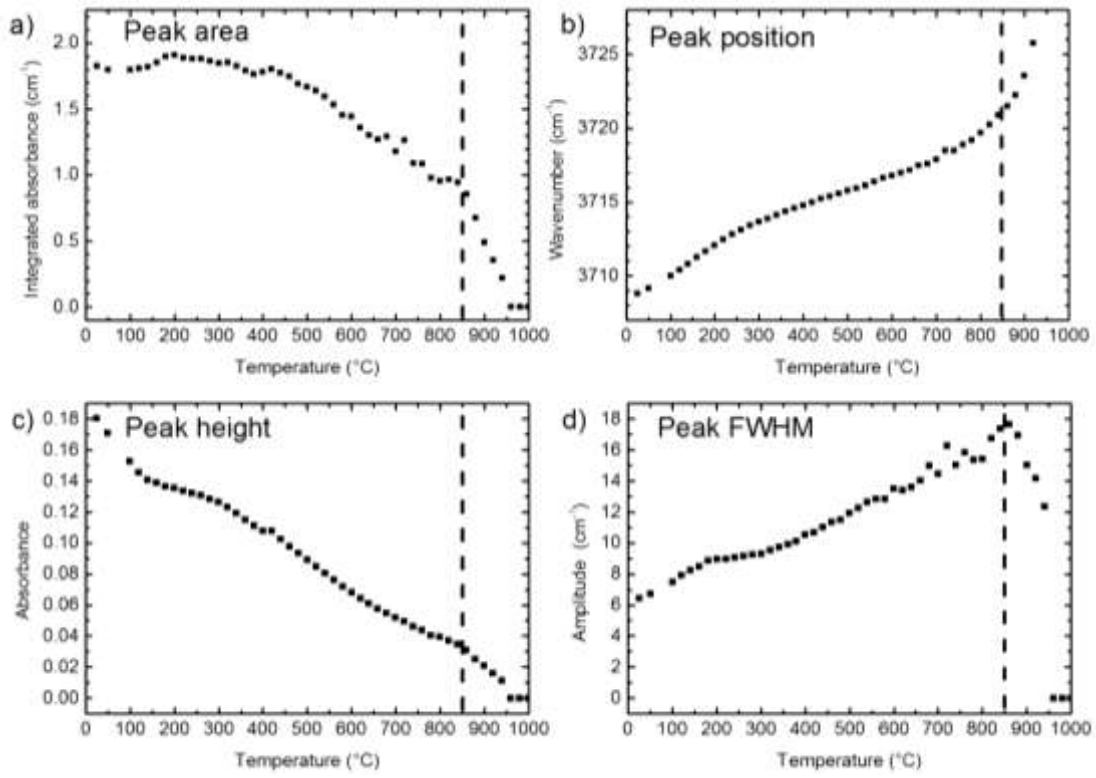

Figure 4 – Integrated absorbance (a), peak position (b), peak height (c) and peak FWHM (d) for the 3708 cm^{-1} CO_2 combination mode for cordierite Rp 3237, measured on the (001) oriented section. The dashed line at 850 °C is a guide for the eye and denotes the temperature at which the CO_2 band starts to decrease drastically.

5.2 *In situ HT*-FTIR measurements: the (010) section

As expected, trends similar to those described for the (001) section are observed for the (010) section cut out from the same cordierite crystal (Fig. 5). In the H_2O stretching region (Fig. 5 left) the 3708 cm^{-1} combination mode of CO_2 decreases in intensity, broadens and shifts to higher frequency, up to 3717 cm^{-1} at 900°C. The 3595 cm^{-1} CO_2 combination mode, which has a weak intensity and is strongly overlapped with the H_2O bands may be resolved exclusively at the lower temperatures (Fig. 2, lower curve).

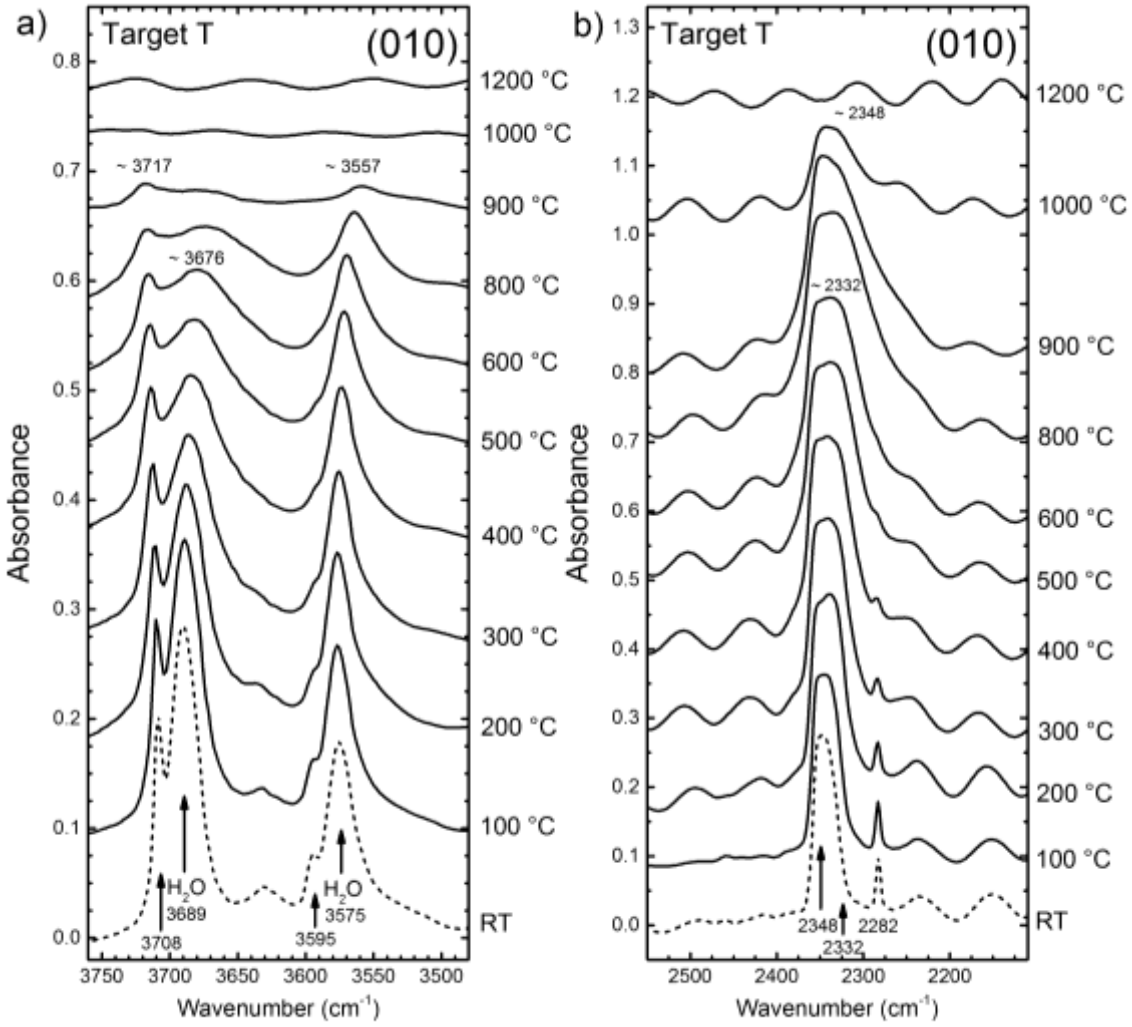

Figure 5 – Selected unpolarized light *in situ HT*-FTIR spectra collected on the (010) section of cordierite Rp 3237 in the CO_2 $\nu_3 + \nu_1$ combination region (a) and CO_2 stretching region (b). Note that interference fringes are present in the spectra of the CO_2 stretching region. For peak assignment see Table 3 and text.

A linear intensity decrease and peak broadening are also observed for the type II H_2O band at 3689 cm^{-1} (ν_3) and 3575 cm^{-1} (ν_1) however in this case both peaks shift to lower

frequencies (Fig. 5a). Because the CO_2 stretching region for this section is much better resolved due to the absence in the spectra of the librational modes (see above), the peak parameters (intensity, position and FWHM) of the principal 2348 cm^{-1} band (Fig. 5b) could be easily obtained and monitored as a function of T, using the data calculation routine built in the spectrometer software. Figure 6 shows that the integrated absorbance (A_i) of the 2348 cm^{-1} peak increases up to 850 °C (Fig. 6a) as a result of the simultaneous and significant linear increase of the peak FWHM (Fig. 6d); on the other side, the peak height is constant up to 900 °C (Fig. 6c). For T > 850 °C all parameters show a sudden drop (Fig. 6). The peak position does not show any clear behavior; around 400 °C the tip of the peak flattens (Fig. 5) and the peak position cannot be properly measured (Fig. 6b). The CO_2 absorptions disappears completely at 1200 °C.

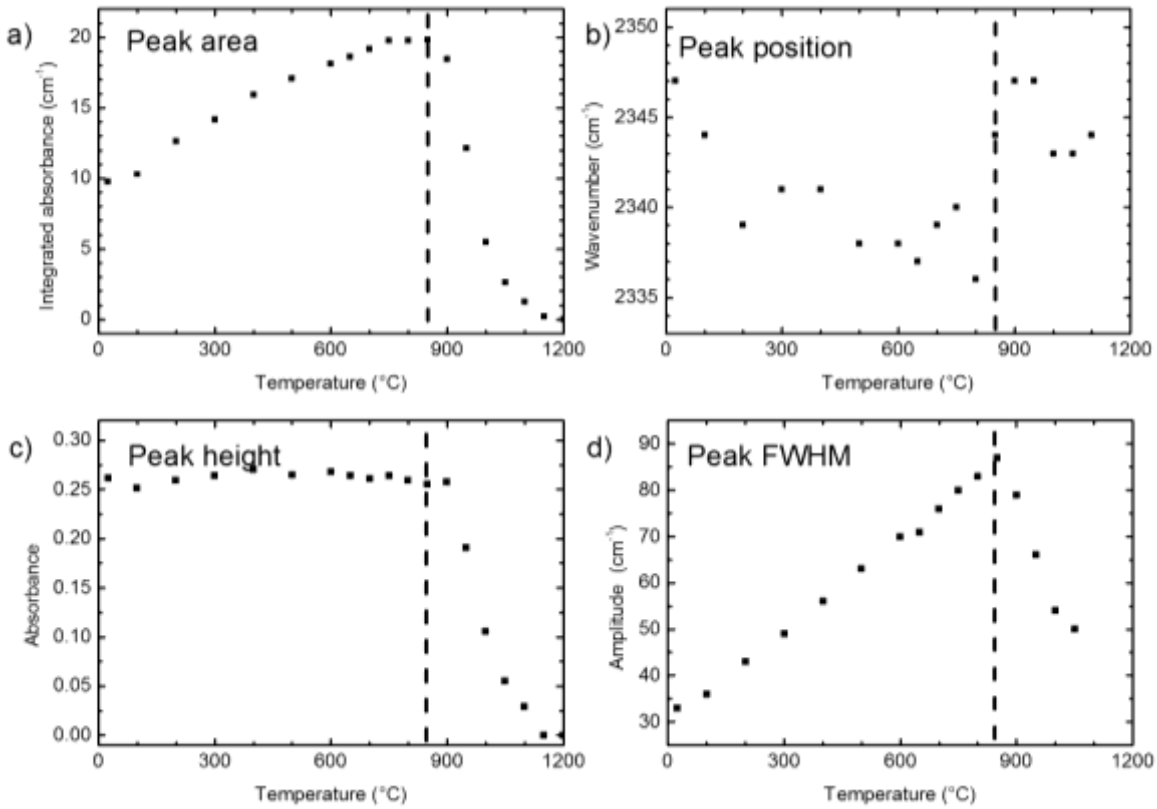

Figure 6 – Integrated absorbance (a), peak position (b), peak height (c) and peak FWHM (d) for the 2348 cm^{-1} CO_2 anti-symmetric stretching mode collected on the (010) section for cordierite Rp 3237. The dashed line at 850 °C is a guide for the eye and denotes the temperature at which the CO_2 band starts to vanish drastically.

5.3 Measurements at *RT* on quenched samples

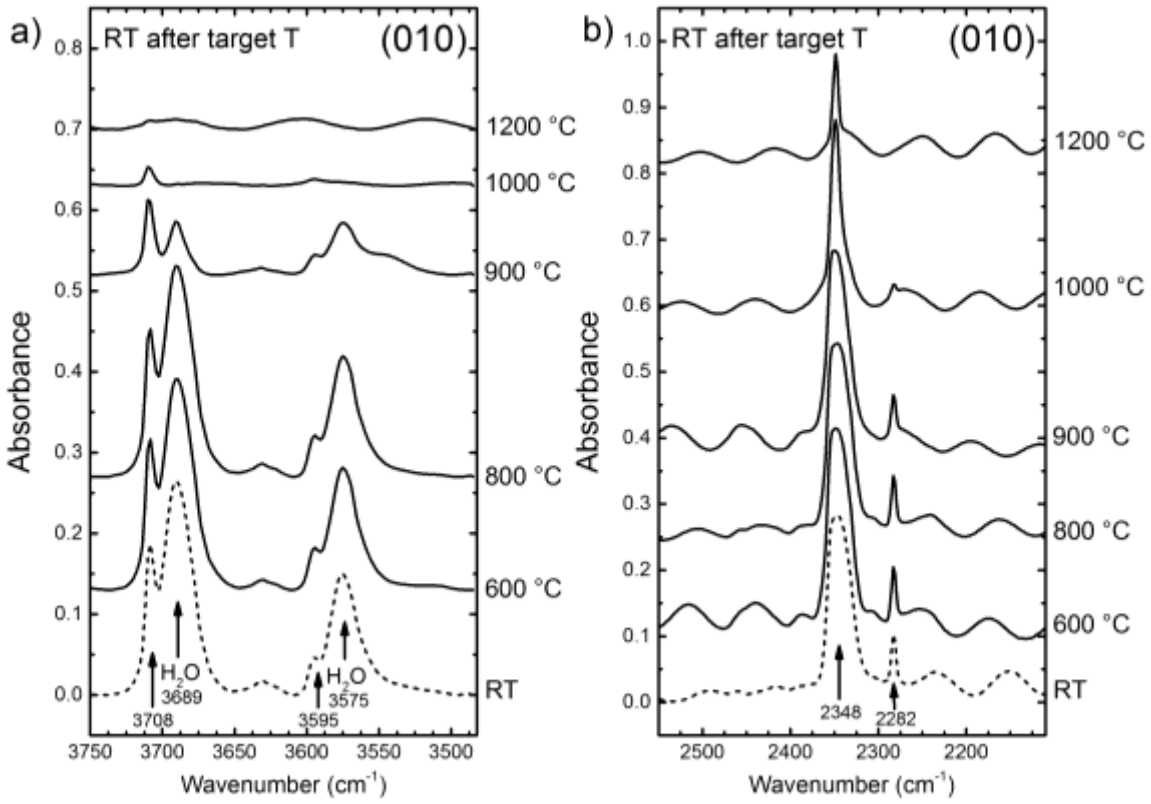

Figure 7–FTIR spectra of cordierite Rp 3237, (010) section, collected at *RT* after heating the sample at the target temperature, in the CO_2 $\nu_3 + \nu_1$ combination region (a) and CO_2 stretching region (b), respectively. Interference fringes are observed for of the CO_2 stretching region. For peak assignment see Table 3 and text.

The FTIR spectra collected on the same sections after quenching the sample reveal a totally different situation from that described above. In Figure 7 the FTIR spectra collected on the (010) section in the same spectral range displayed in Figure 5 are displayed. Comparison on these Figures reveals that (1) no band shift or band broadening are retained after cooling the sample at RT; (2) the intensity of the CO_2 bands is constant up to 900°C, and, more importantly (3) some CO_2 (as it is well visible in the 2500-2400 cm^{-1} region) is still present in the sample heated up to 1200 °C (Fig. 7b). A point to note is that the CO_2 peak measured at *RT* after the sample has been heated a $T > 900$°C is sharper that the same peak measure on the untreated crystal. In fact, a closer inspection of the spectra suggests that, for $T > 900$°C, a second component at lower frequency, which is unresolved at *RT*, preferentially disappears. This point is presently still not completely understood; one reasonable hypothesis is that at higher concentrations, the CO_2 molecules interact to give (at least) two different local coordination environments, characterized by a slightly different vibrational frequency. For lower CO_2 concentrations, at T > 900°C, this interaction is removed, and only

one component persists in the spectrum. This being the case, however, the proportionality between the absorption area and the CO_2 concentration will be still valid.

5.4 The intensity variation of *in situ vs* quenched data

Figure 8 displays the relative changes in band area $A_{RT\%}$, expressed as the ratio of the integrated absorbance measured at a target temperature (A_{iTT}) and the absorbance measured at *RT* (A_{iRT}) before the beginning of the heating experiment ($A_{RT\%} = 100 \cdot A_{iTT}/A_{iRT}$).

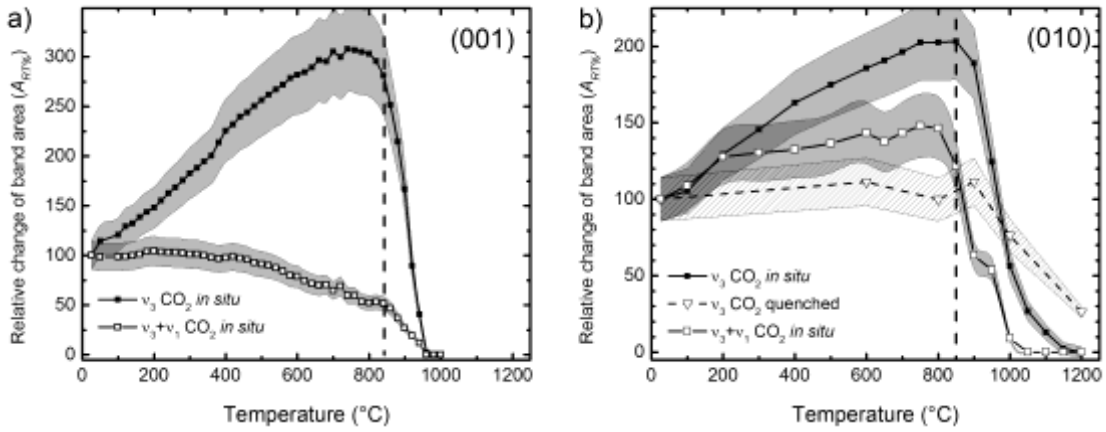

Figure 8 – Relative change in band area ($A_{RT\%}$ %) of CO_2 bands (filled squares, stretching band at 2343 cm^{-1} and open squares combination band at 3708 cm^{-1}) for cordierite Rp 3237 (a) (001) section, (b) (010) section; the relative change in 2343 cm^{-1} band area measured on quenched samples is also shown (open triangles) for comparison. The shaded areas represent the estimated error on $A_{RT\%}$ (see txt).

The shaded region (Fig. 8) represents the estimated error on the ratio calculated using the classic statistic of error propagation, considering that the error on A_i is about ±10 % (*e.g.* Libowitzky and Rossman, 1997, Bellatreccia *et al.*, 2005). Inspection of Figure 8 clearly shows that the evolution of the absorbance as a function of *T* is extremely different when we consider the *in situ* measurement *vs.* the data collected at *RT* after quenching the sample. For the former case, in the 25°C - 750/800 °C range there is a significant increase in the integrated intensity of CO_2. A difference in the absolute values is observed for the different slab orientations, however the general trend is the same. It is worth to note that the 3708 cm^{-1} CO_2 combination mode (Fig. 8a and b) has a behavior extremely different from that of the ν_3 mode, and shows only a minor variation up to 850°C. The different behavior of the principal *vs* multiphonon bands has been recently described for several minerals by Zhang *et al.* (2007) who observed differences in the rate of absorbance variation for different

matrices, and also different trends for the same molecular species in different spectral regions. For *T* > 850 °C there is, for all CO_2 modes, a drastic drop in the intensity.

The trend observed for the spectra collected at *RT* on quenched samples is displayed as a dashed black line in Figure 8b. The data show that in this case there is no significant intensity variation up to 900 °C, followed by a drop of the intensity in the 900-1200° temperature range. It is also important to note that at 1200°C minor but significant amounts of CO_2 (~ 25%) are still retained in the structure. The sudden drop in intensity observed between 800 and 900 °C for the *in situ* experiments cannot be explained as a sudden change of the molar absorption coefficient ε_i (Tokiwai and Nakashima, 2010b), but must be exclusively ascribed to progressive loss of CO_2 from the channels, as testified by *RT* measurements in Figures 7b and 8b.

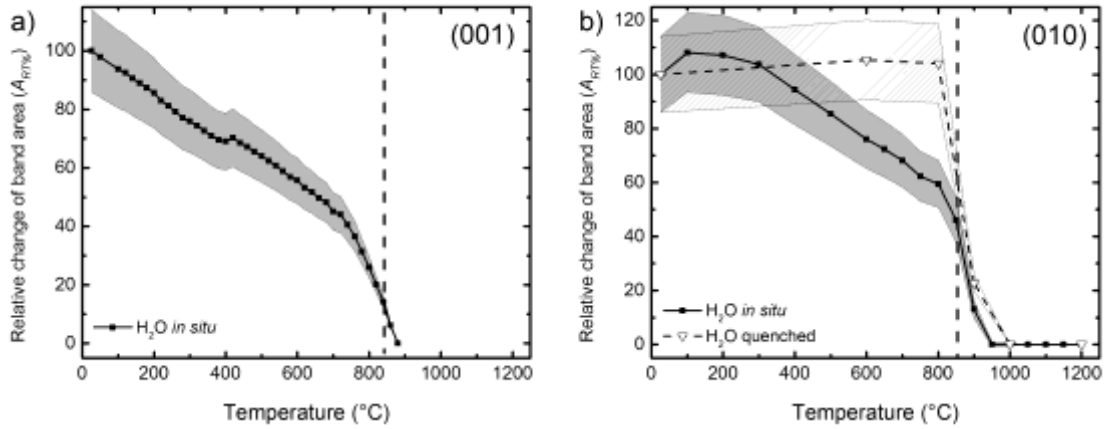

Figure 9 – (a) Sample Rp 3237 section (001), relative change in H_2O band area ($A_{RT\%}$ in %), integration range 3800 to 3400 cm^{-1}. (b) sample Rp 3237 (010) section, relative change in band area ($A_{RT\%}$ in %) of H_2O related absorptions *in situ* (filled squares) and at *RT* after quenching (open triangles). The shaded areas represent the estimated error on $A_{RT\%}$ (see text).

Although the present work was not intended to study the behavior of H_2O in cordierite at *HT* (this will be the argument of a forthcoming paper), it is interesting to note that the evolution of the H_2O absorbance as a function of increasing *T* is extremely different to that of CO_2 (Fig. 9). Due to severe band overlap, for the (001) section we integrated the whole range between 3800 and 3400 cm^{-1} (Fig. 9a); for the (010) section we could measure independently the intensity variation of the 3689 cm^{-1} + 3575 cm^{-1} components, both *in situ* and at *RT* after quenching (Fig. 9b). Contrary to CO_2 (Fig. 8) the trends for H_2O show in both cases a linear and constant decrease of ~50% of the intensity up to 800°C; in the 800°-900°C range there is a sudden drop and at 950°C the sample is completely anhydrous. Similarly to

what observed for CO_2, the data collected on quenched samples show a different scenario: the integrated H_2O absorbance (proportional to the amount of water in the sample) is constant up to 800°C and suddenly drops in the 800-900°C range. At 1000° the sample is completely anhydrous.

6. Discussion

6.1 The thermal behavior of CO_2 bands

6.1.1 Temperature dependence of peak position and width

Figure 4a shows a significant frequency shift of both ν_3 (3689 cm^{-1}) and ν_1 (3575 cm^{-1}) type I H_2O peaks of about 15 cm^{-1}; this result is consistent with previous studies and has been assigned to a temperature dependence of the H_2O vibrational constants (Kolesov, 2008; Fukuda and Shinoda, 2008 and 2011). On the other side, no systematic shift with temperature is observed for the CO_2 absorptions at 2348 or 2332 cm^{-1}, from -200 °C (Khomenko and Langer, 2005) to 1000 °C (this work, Fig. 5b and Fig. 6b). This issue was studied by Olijnyk *et al.* (1988) who observed that the principal vibrational modes in solid CO_2 do not show any shift with *T*, but are strongly influenced by pressure changes (see also Hanson and Jones, 1981). Our data, however, show a significant shift, from 3708 to 3720 cm^{-1}, for the ($\nu_3 + \nu_1$) combination mode (Fig. 4 and 5).

We also observed a significant peak broadening of all CO_2-related bands upon heating (Fig. 4 and 6), in particular of the 2332 cm^{-1} peak which is well resolved only below -200 °C, where its FWHM is just 5-6 cm^{-1} (Khomenko and Langer, 2005).

6.1.2 Temperature dependence of integrated absorbance (A_i)

In the introduction we mentioned the change in the molar absorption coefficients ε with temperature for the OH molecular species, that has been recently addressed by several authors (Zhang *et al.*, 2007, Fukuda and Shinoda, 2008 and 2011, Tokiwai and Nakashima, 2010b). Tokiwai and Nakashima (2010b), during their *in-situ* FTIR study on muscovite dehydration, identified two distinct stages of intensity decrease: at lower temperatures, they observed a progressive and linear decrease in the A_i; at higher temperatures the A_i decrease

was steeper and non-linear. The authors imputed the decrease of A_i at low *T* exclusively to the effect of the change of molar absorption coefficient ε with temperature; whereas at high *T* there is an effective dehydration of the mineral. A similar trend may be easily recognized for H_2O in cordierite (Fig. 9), where it is possible to distinguish two different trends: 1) a linear (or quasi-linear) A_i decrease from *RT* to 700 °C (001 section, Fig. 9a) and 800 °C (010 section Fig. 9b), and 2) a steeper A_i decrease for higher *T*. Quenched data collected at *RT* on the (010) lamella (Fig. 9b dashed line) clearly proves that up to 800 °C there is no loss of H_2O from the sample, while for higher temperatures, the H_2O content drops drastically. Based on the Beer-Lambert relationship given above, assuming negligible change in the sample thickness across the studied *T* range, and considering no H_2O loss as evidenced by the quenched measurements, the decreasing trend of Figure 9 for the *in situ* measurements must be assigned to a decrease of ε. On the other side, the sudden and fast A_i decrease for *T* > 800°C may be imputed to the dehydration process.

Interestingly, a similar but reverse trend may be observed for the integrated absorbance of the anti-symmetric CO_2 stretching mode at low *T* (Fig. 8). From *RT* to ~ 700 °C it is possible to observe a first stage characterized by a strong linear increase of A_i, followed by an intermediate stage (~ 100 °C) with no variation of the integrated absorbance. Then there is a second stage characterized by a strong decrease of A_i up to 1200 °C. Quenched data reveal that CO_2 loss occurs exclusively above 900 °C. Thus the A_i increase in the first stage may be imputed exclusively to an increase in the molar absorption coefficient ε with temperature, while in the second stage the A_i decrease may be imputed exclusively to CO_2 loss. Note that during the intermediate stage both effects of ε increase and CO_2 loss may be balanced with the result of no or small A_i variation.

In previous *HT*-FTIR studies, all done on H_2O/OH spectroscopy, a decrease of the integrated absorbance A_i has been systematically observed (see Prasad *et al.*, 2005, Bonaccorsi *et al.*, 2007; Zhang *et al.*, 2006, 2007; Tokiwai and Nakashima, 2010, among the others), whereas for CO_2 we obtain a completely opposite trend, *i. e.* an increase of A_i with temperature. Such behavior has been so far observed (Zhang *et al.*, 2007) only for the overtone modes of some phyllosicates, although, as they discussed in their work, multi-phonon processes cannot be directly compared to single phonon processes.

At present we have no explanation for the odd behavior of CO_2 related absorbance trends, however examination of Figure 8 suggests that: 1) the apparent increase of CO_2

absorbance up to ~ 800 °C is due to an increase with temperature of ε; 2) CO_2 loss begins around 750/800 °C depending on the investigated slab; and 3) as already observed for H_2O/OH in several mineral species (Zhang *et al.*, 2007) the temperature dependence of the principal modes is different from that of multi-phonon bands (Fig. 9a).

6.2 The effect of channel orientation on volatile loss

There are two points to consider when modeling H_2O and CO_2 devolatilization in cordierite: (1) as shown by Fukuda *et al.* (2009) and by Radica *et al.* (this Thesis) for beryl, the volatile diffusion occurs much faster along the structural channels along the [001] crystallographic direction, and (2) as shown by Aines and Rossmann (1984), CO_2 does not change its molecular configuration during heating, suggesting that the CO_2 loss can be considered as a simple diffusion, although with a much slower rate than H_2O (chapter 4). Considering these points, we may infer that in cordierite (and beryl) the CO_2 loss must be strongly affected by both particle size and the shape of the studied sample, *i.e.* the length of the escape path. To check for these issues, we used for our experiments two different crystallographic orientations: the (001), 77 μm thick slab, to simulate the diffusion mechanism for small or tabular shaped grains (although cordierite does not occur as tabular crystals, see for example Deer *et al.*, 2004), where the maximum diffusion pathway is 34 μm, *i.e.* half slab thickness. On the opposite, the (010) slab, was used to model the case of large or prismatic grains (typical growth habit of cordierite, Deer *et al.*, 2004), where the mean diffusion pathway is about 120 μm, corresponding to half the mean slab dimension along the *c* axis.

The differences between the two orientations may be observed comparing the *in-situ* intensities in Figures 8a and 8b. In both samples we observe an inversion in the absorption trends starting at 750/800 °C (Fig. 8). For the (001) slab (Fig. 8a) a sudden decrease of the absorbance occurs between 820 and 950 °C; at 950-1000°C A_i is zero. On the other hand, in the (010) slab the CO_2 decrease occurs only for $T > 900$ °C; at 1000°C there is still a significant intensity in the spectra, and the absorbance disappears only at 1200 °C. Note that the experimental duration between the two *HT* treatments are comparable. Small differences related to slab orientation may be observed also for sample dehydration (Fig. 9). In addition, the dehydration temperatures observed in this work are at least 100 °C, for the (001) slab,

and 200 °C, for the (010) slab, higher than those reported by Aines and Rossman (1984) (600 °C), or by Lepezin and Melenevsky (1977), who gave a range for the beginning of dehydration of 500 - 700 °C.

Quenched data show that only for the (001) slab all CO_2 is lost at 1100 °C (Fig. 3b top dashed curve), while for the (010) slab the average CO_2 content of the grain decreases rather slowly and, at 1200°C, the sample still retains 26% of the starting CO_2 (Fig. 8b dashed line). The H_2O content, on the other hand, drops drastically down to the 20 % between 800 and 900 °C (Fig. 9b dashed line).

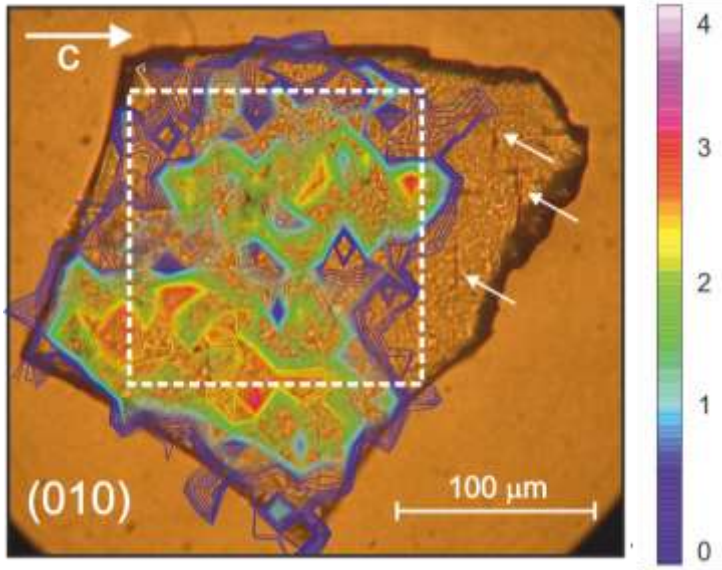

Figure 10 – Parallel polars light (PPL) optical microscope image and superimposed FPA image of the residual distribution of CO_2 in the (010) cordierite section after the heating experiment; CO_2 poor areas presented diffuse fracturing. Chromatic scale (in cm^{-1}) is proportional to CO_2 content. The dashed square indicates the spot for FTIR in-situ measurements. White arrows indicate fractures developed during the heating.

To sum up, in the (001) oriented lamella or in thin and tabular cordierite grains both CO_2 and H_2O desorption proceeds smoothly even when *T* increases with a very fast rate; on the other side, for thicker or prismatic cordierite grains, as simulated by the (010) lamella, both CO_2 desorption and dehydration occur at higher temperatures, at least 50/100 °C higher than in the (001) sample. In other words, the difference in diffusion path length has a significant effect on the temperatures of CO_2 and H_2O desorption. Because volatile molecules are known to diffuse faster along the channel direction, it follows that longer heating times are necessary to extract all volatile molecules from the core of the grain (see also Chapter 4). With this respect, we also noticed that additional diffusion interfaces, such as cracks or fractures, may significantly promote outward diffusion. In Figure 10 we display

the FTIR-FPA contour map of residual CO_2 in the (010) oriented lamella after the heating experiment. As opposite to single spot measurements that are specifically designed to probe a great portion of the heat-treated slab (dashed square in Figure 10), the higher spatial resolution of FPA image revealed an extremely inhomogeneous distribution of residual CO_2. Optical analysis revealed the presence of several 20 μm long fractures oriented normal to the *c* direction (arrowed in Figure 10). Notably the fractured area did not show any residual CO_2, suggesting a strong role of the fractures in enhancing the loss of carbon dioxide from the matrix.

7. Conclusions

FTIR spectroscopy is one of the most effective methods in Earth and material Science to study *in-situ* the effects of high pressures and temperatures for elements like H and C (Koch-Müller *et al.*, 2003, Iezzi *et al.*, 2006, 2009, Keppler and Smyth, 2006; Hawthorne *et al.*, 2007, Welch *et al.*, 2007, Della Ventura *et al.*, 2010, 2014), however increasing evidence shows that quantitative studies using *in-situ* HT-FTIR spectroscopy are complicated by several factors. First of all, similarly to previous studies done for H_2O/OH (Yamagishi *et al.*, 1997, Zhang *et al.*, 2006, 2007; Tokiwai and Nakashima, 2010), the present work shows that the molar absorption coefficient ε for CO_2 in cordierite is strongly dependent on T. In addition, the temperature dependence of the principal modes may be strongly different compared to the multi-phonon modes.

In-situ FTIR spectra also revealed that CO_2 desorption is strongly dependent on the grain size, thickness of the sample and orientation of the studied section. We observed that volatile loss is favored for small and tabular grains (below 100 μm in thickness); on the opposite, because volatile flux in cordierite occurs preferentially along the structural channel parallel to the *c* crystallographic axis and through the crystal interfaces normal to [001], volatile loss is hindered for large sized and prismatic crystals. In this type of grains H_2O and CO_2 may be retained inside the sample for higher temperatures. Because of these reasons the process of CO_2 desorption from cordierite cannot be ascribed to a first order reaction, where the decrease rate of CO_2 is proportional exclusively to CO_2 concentration, but, because long distance transport is involved, CO_2 desorption must be described as a diffusion

process (see also Chapter 4). Additionally sample fracturing along the direction normal to the *c* axis may multiply the diffusion interfaces thus favoring both H_2O and CO_2 loss.

Comparing H_2O and CO_2 loss curves it is also possible to infer that from a qualitative point of view H_2O diffuses faster than CO_2 inside cordierite structural channels.

We wonder if combination of the size/orientation effect, the different diffusion rates, and the role of crystal fracturing may be responsible for the scatter of dehydroxylation data observed in the literature.

CHAPTER 4

HT-FTIR MICRO-SPECTROSCOPY OF CORDIERITE.

II: THE DIFFUSION KINETICS OF CO_2

Abstract

In-situ high temperature FTIR micro-spectroscopy is a powerful tool to study the kinetic processes of minerals at extreme environmental conditions. In recent years additional techniques were implemented in order to improve spectral quality and resolution, in particular synchrotron light (SR-FTIR) sources may provide high S/N (signal-to-noise) data allowing to extract reliable quantitative information. In this work we performed several isothermal heating experiments on (001) oriented sections of a CO_2-rich natural cordierite, a mineral with a great geological and technological relevance. The slices were heat-treated up to 1000 °C using a Linkam TS 1400XY heating stage. Single-crystal were heated to the target temperature; the intensity of the v_3 anti-symmetric stretching mode of CO_2 at 2348 cm^{-1} was monitored as a function of heating time. The resulting curves of residual CO_2 were modeled using different approaches to evaluate the kinetic process of CO_2 desorption and diffusion coefficients. In particular, two different versions of the Avrami equations were found to be significantly sensitive to the sample thickness. On the other side, the mono-dimensional plane sheet diffusion approach was found to be more suitable to deal with the examined

purely diffusive process. Fitting of the diffusion coefficients in the Arrhenius space yielded – logD_0 = 4.4±0.7 m^2/sec and E_a = 204±15 kJ/mol.

1. Introduction:

Cordierite, ideally $(Mg,Fe)_2Al_4Si_5O_{18}$, consists structurally of pseudo-hexagonal rings of Si/Al tetrahedra stacked along the *c* crystallographic axis. These rings are linked both laterally and vertically by corner-sharing four-membered tetrahedral chain to give a framework of tetrahedra (Gibbs, 1966). Within this framework there are sites for (Mg, Fe^{2+}) ions in octahedral coordination that share two edges with one Al, and one edge with a Si tetrahedron. The stacking generates a channel-like open structure running parallel to the *c* crystallographic axis, where narrower "bottlenecks" (about 2.5 Å in diameter) alternates to large "cages" (about 5.4 Å along *b* and 6.0 Å parallel to *a*) (Armbruster and Bloss, 1982). Alkaline cations (like Na^+, K^+ and Ca^{++}) and molecular groups (H_2O and CO_2) may be present in significant amounts within the cordierite structural channels. The highest value so far reported for H_2O in the literature is about 2.4 wt.% (Deer *et al.*, 2004), which is very close to the maximum theoretical value of 1 molecule per formula unit in the channel. The highest observed CO_2 content is about 2.2 wt.% corresponding to about 0.3 molecules per formula unit. Most notably, water and carbon dioxide are located in the wider parts of the structural channels. Hydrocarbons (Zimmermann, 1981; Mottana *et al.*, 1983; Khomenko and Langer, 1999), CO (Khomenko and Langer 2005; Della Ventura *et al.*, 2009), Ar (Armbruster, 1985; Schreyer, 1985), N_2 (Armbruster, 1985; Cesare *et al.*, 2007), Cs (Hawthorne and Černý, 1977, Daniels, 1992) and Fe (Goldmann *et al.*, 1977) were also reported inside the structural channels. The linear CO_2 molecules are oriented orthogonally to the *c* axis, parallel to the *a* crystallographic axis (Aines and Rossman, 1984; Khomenko and Langer, 2005). Extra-framework H_2O groups occur in the structural channels with the molecular plane parallel to (100). However, H_2O may occur in two different orientations: in type I H_2O (hereafter $H_2O^{[I]}$) the H–H vector is oriented parallel to the *c* axis, in type II H_2O ($H_2O^{[II]}$) the H–H vector is rotated by 90°, parallel to the *b* axis (Goldmann *et al.*, 1977). H_2O molecules of the latter orientation are bonded locally to channel alkali cations in a 2:1 ratio (Goldmann *et al.*, 1977).

The potential use of cordierite as a water and carbon dioxide fugacity indicator in rocks has generated much interest in the thermodynamics and structural properties of the gases contained in its channels (Vry *et al.*, 1990; Carrington and Harley, 1996). While there are several studies concerning the thermodynamic parameters of cordierite dehydration (Giampaolo and Putnis, 1989; Carey, 1993; Carey, 1995; Paukov *et al.*, 2007; Dachs and Geiger, 2008), almost no experimental works were devoted to the kinetics of CO_2 expulsion from cordierite and/or cordierite-like structures (Radica *et al.*, chapter 3), partly due to the higher temperatures involved in this process. However several authors pointed out that the CO_2 content in the system not only has a significant influence on the cordierite crystallization (Harley *et al.*,2002; Kurepin, 2010), but it also affects the H_2O diffusivity out of the structural channels because, for size reason, CO_2 act as a plug in the larger cages (Aines and Rossman, 1984; Vry *et al.*, 1990; Radica *et al.*, this Thesis)

Cordierite is also of interest as a model for extremely small channel zeolite-like minerals (McCrusker, 2005) and for the behavior of water and carbon dioxide trapped in small cavities (Aines and Rossman, 1984).

2. Studied sample

In-situ isothermal heating experiments were performed on fragments of a natural cordierite BM 96512 from Cabo de Gata (Almaria region, Spain). The fragments were clear and inclusion-free, with a violet to dark blue color. Chemical composition, crystal-chemical formula, cell parameters, density and optical properties are given in Della Ventura *et. al.* (2012); for sake of simplicity, a summary of data is reported in Table 1. In particular, the H_2O and CO_2 contents were quantified by SIMS (secondary-ion-mass-spectrometry) using a Cameca IMS4f ion microprobe at EMMAC, the University of Edinburgh. Procedures follow those described in previous cordierite studies from the Edinburgh laboratory (Harley and Carrington, 2001; Thompson *et al.*, 2001; Harley *et al.*, 2002; Della Ventura *et al.*, 2012). Fe^{tot} was considered as Fe^{2+}. The crystal-chemical formula, based on 18 oxygen atoms p.f.u. is $Na_{0.03}(Mg_{1.52}Fe_{0.44})Al_{3.98}Si_5O_{18}\cdot 0.21H_2O\cdot 0.07CO_2$. Preliminary FTIR imaging confirmed an homogeneous distribution of H_2O and CO_2 across the sample (Della Ventura *et. al.*, 2012).

Table 1 - Microchemical analysis, crystal-chemical formula, cell parameters, density and optical properties for cordierite studied here. Data from Della Ventura *et. al.* (2012). Crystal-chemical formula is based on 18 oxygen atoms p.f.u.

	BM 96512	St. Dev.
Chemical analysis (wt.%)		
SiO_2	49.10	0.31
Al_2O_3	33.10	0.25
MgO	10.04	0.13
FeO	5.21	0.12
TiO_2	0.03	0.04
MnO	0.34	0.07
CaO	0.04	0.02
Na_2O	0.15	0.02
K_2O	0.03	0.01
H_2O	0.62	0.08
CO_2	0.51	0.08
Total	99.17	
Crystal chemical formula (apfu)		
Si	5.01	
Al	3.98	
Σ Tetrahedra	8.98	
Mg	1.53	
Fe	0.44	
Ti	0.00	
Mn	0.03	
Σ Octahedra	2.00	
Ca	0.00	
Na	0.03	
K	0.00	
Σ Channels	0.04	
n(H_2O)	0.21	
m(CO_2)	0.07	
Σ Volatiles	0.28	
$**H_2O^{[II]}$	0.08	
$**H_2O^{[I]}$	0.13	
$X_{crd}CO_2$	0.25	
Cell parameters (Å)		
a	17.135 (7)	
b	9.781 (5)	
c	9.343 (7)	
Densitiy (g/cm^3)	2.602 (4)	
Optic sign	Positive	
2Vx (°)	90 (3)	

3. Experimental methods

In-situ heating experiments were performed on cordierite fragments using a high temperature Linkam TS 1400 XY heating stage. Selected crystal fragments were oriented using a polarizing microscope equipped with a spindle-stage; the extinction data were processed using the program ExcalibrW (Bloss, 1981; Gunter *et al.*, 2005). Crystallographic orientation was based on the optical orientation *a* = Z, *b* = Y and *c* = X (Deer *et al.*, 2004). The fragments were transferred from the spindle-stage to glass slides and doubly polished.

Sample thickness was measured using an electronic micrometer with ±5 μm uncertainty and checked using the interference fringes in the FTIR spectra, using the formula $t = 1/[2 \cdot n \cdot (v_1 - v_2)]$ where t is sample thickness in cm, n is the refractive index and $(v_1 - v_2)$ is the distance between two adjacent fringes in cm^{-1} (Pistorius and DeGrip, 2006). Doubly polished fragments were oriented on the horizontal plane using a polarizing microscope and carefully transferred on a quartz sample holder (FTIR frequency cut below 2070 cm^{-1}). The sample holder was inserted into a 17 mm ceramic crucible for the heating runs. Temperature was measured using a calibrated type S Pt-10% Rh/Pt thermocouple placed close to the sample; the accuracy was ±1°C according to the manufacturer. Heating ramps were programmed using a digital controller.

Conventional light HT-FTIR spectra were acquired using a Bruker™ Hyperion 3000 microscope equipped with a KBr-broadband beamsplitter and a liquid nitrogen-cooled MCT detector at Laboratori Nazionali di Frascati-Istituto Nazionale di Fisica Nucleare (LNF-INFN) Frascati (Rome). Synchrotron light HT FTIR spectra were collected at beamline B22, Diamond Light Source laboratory Oxford (UK). Polarized spectra were collected using a gold-wire-grid polarizer on a ZnSe substrate. A spot size of 50 μm using a 15 X objective was used for data collection in conventional light, while a spot size close to 20 μm with a 20 X objective was used in synchrotron light; the nominal resolution was 4 cm^{-1} and 128 scans were averaged for both spectrum and background, for a total collecting time of about 30 seconds. FTIR images were collected using a 64 x 64 pixel focal-plane array (FPA), using a 15 X objective; the nominal resolution was set at 4 cm^{-1} and 64 scans were averaged for each spectrum and background. With this set up each image covers an area of 170 μm x 170 μm with a nominal spatial resolution of ~5 μm (Della Ventura *et al.*, 2010, 2014).

3.1 FTIR polarized-light isothermal heating experiments

In order to study the kinetic of CO_2 diffusion within cordierite at high T, two sets of experiments were performed on (001) slabs. This orientation was chosen to ensures a homogenous outward diffusion of CO_2 across the entire slab surface considering that CO_2 diffuses much faster along the structural channels oriented parallel to the c crystallographic direction (Fig. 1, see Chapter 3). Diffusion through the prismatic faces can be neglected because, as it has already been verified for the structurally related beryl, it is at least two

orders of magnitude lower, as observed by Fukuda *et al.* (2009) for beryl, and shown for cordierite in the previous chapters.

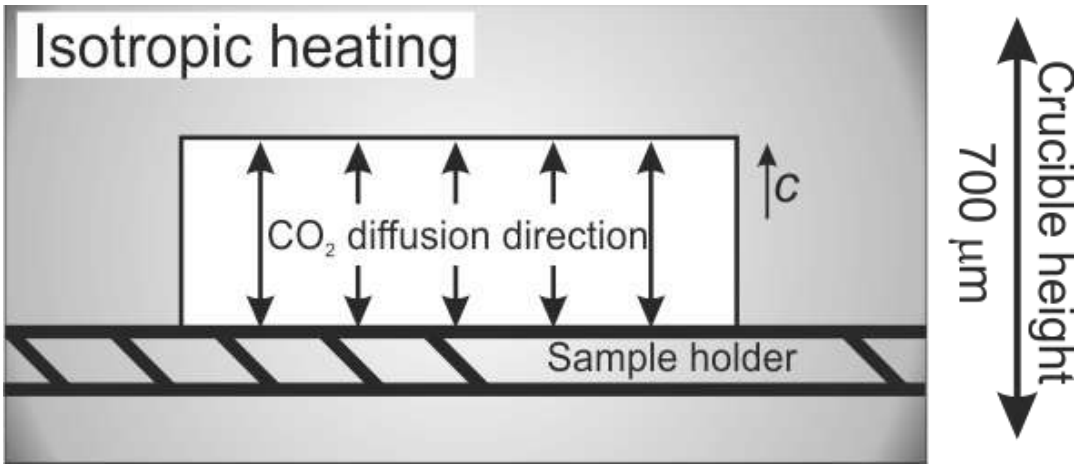

Figure 1 – Schematic set up (not in scale) of the CO_2 diffusion across the sample (white) inside the heating stage during the isothermal kinetic heating experiments. Considering that the ceramic tube heater completely encases the sample in a uniform T controlled environment, and the reduced sample thickness, we assume that there is no T gradient across the grain. Diffusion directions parallel to the *c* crystallographic axis are indicated as arrows, the diffusion perpendicular to the *c* direction is negligible (see text for explanation).

Two oriented fragments were double-polished at 60 µm and 19 µm, respectively and broke up into four pieces each. Four fragments of the same 60 µm thick section were heated to 850, 900, 950 and 1000 °C (heating rate 100°C/min) and kept at the target *T* for two hours (Tab. 3). Polarized spectra were collected using conventional light with both E//*a* and E//*b* at RT before the experiment, and at the target *T*, every 5 minutes for the first hour and every 10 minutes for the second hour of isothermal heating. Four fragments of the same 19 µm thick slab were heated to 825, 850, 900 and 1000 °C (heating rate 100°C/min) at different annealing times (Tab. 3). For this second set of samples, spectra were collected using synchrotron light exclusively along the *a* crystallographic direction at *RT* and at the target *T* every 5 minutes. This experimental layout was necessary to get a better S/N because the reduced thickness of the samples coupled with the strong beam absorbance caused by the stage windows, sample holder and polarizers, affected significantly the transmitted signal. The spectra collected for this second set of fragments showed unexpected interference fringes, thus a background correction was needed to extract the intensity data. Heating temperatures were selected on the basis of previous work (Radica *et al.* chapter 3) which

showed a strong decrease in channel CO_2 content around 850 °C. In all cases the lateral dimension of the sample was significantly larger than the beam size.

Table 3 – Isothermal kinetic heating experiments details.

Sample slab (orientation 001)	Thickness (µm)	Annealing temperature (°C)	Annealing time (min)	Light source
BM 96512_T 850	60	850	120	Conventional
BM 96512_T 900	60	900	120	Conventional
BM 96512_T 950	60	950	120	Conventional
BM 96512_T 1000	60	1000	120	Conventional
BM 96512_T3 825	19	825	210	Synchrotron
BM 96512_T3 850	19	850	180	Synchrotron
BM 96512_T3 900	19	900	60	Synchrotron
BM 96512_T3 1000	19	1000	30	Synchrotron

4. Polarized-light FTIR spectroscopy of cordierite and band assignment

The correct assignment of the absorption peaks in cordierite spectra is a crucial point when using the absorbance data for quantitative purposes (Della Ventura *et al.*, 2012, Radica *et al.*, 2013). In Figure 2 we display the single-crystal polarized infrared spectra of sample BM 96512 collected at RT. H_2O and CO_2 absorptions are present in 4 different regions of the spectrum: (a) the H_2O combination region around 5250 cm^{-1} (Della Ventura *et al.*, 2012) (b) the 3900 – 3300 cm^{-1} region where the H_2O stretching modes (Goldman *et al.*, 1977) and the combination modes of CO_2 are observed (Geiger and Kolesov, 2002); Della Ventura *et al.,* 2009, 2012); (c) the antisymmetric stretching (2600 – 2000 cm^{-1}) region of CO_2 (Geiger and Kolesov, 2002) and (d) the H_2O bending region around 1600 cm^{-1} (Della Ventura *et al.*, 2012).

Selected polarized spectra in the 3800 – 3200 cm^{-1} range are given in Figure 2b. When the electric vector E is parallel to the crystallographic axis *c* (E//*c*), two sharp peaks are observed, one centered at 3575 cm^{-1}, and the other at 3689 cm^{-1}; a third weaker peak is observed at 3242 cm^{-1}. The E//*b* spectrum features a very broad peak centered about 3630 cm^{-1} with a shoulder around 3595 cm^{-1}. The E//*a* spectrum shows a broad and weak multi-component absorption with maxima at 3630 cm^{-1} and 3575 cm^{-1}; two sharper peaks are present at 3708 and 3595 cm^{-1}. The polarized spectra in the 5300 - 5200 cm^{-1} range (Fig. 2a) features a fairly sharp peak at 5266 cm^{-1} for E//*c*, and a very broad peak about 5250 cm^{-1} for E//*b*. The E//*a* spectrum is featureless. In Figure 2c the E//a spectrum in the CO_2 region

consists of a very sharp and intense absorption centered at 2348 cm^{-1}, with a weak shoulder at 2332 cm^{-1} on the low-frequency side. A minor band is observed at 2282 cm^{-1}. The E//*c* spectrum is featureless, while the E//*b* spectrum shows a minor band at 2348 cm^{-1} with two side bands at 2391 and 2306 cm^{-1}, respectively. In the H_2O bending region relevant peaks are observed in E//*c* at 1634 cm^{-1} (Fig. 2d). At 1560, 1600, and 1635 cm^{-1} polarized for E//*a* and E//*b* a triplet of weak components may be observed.

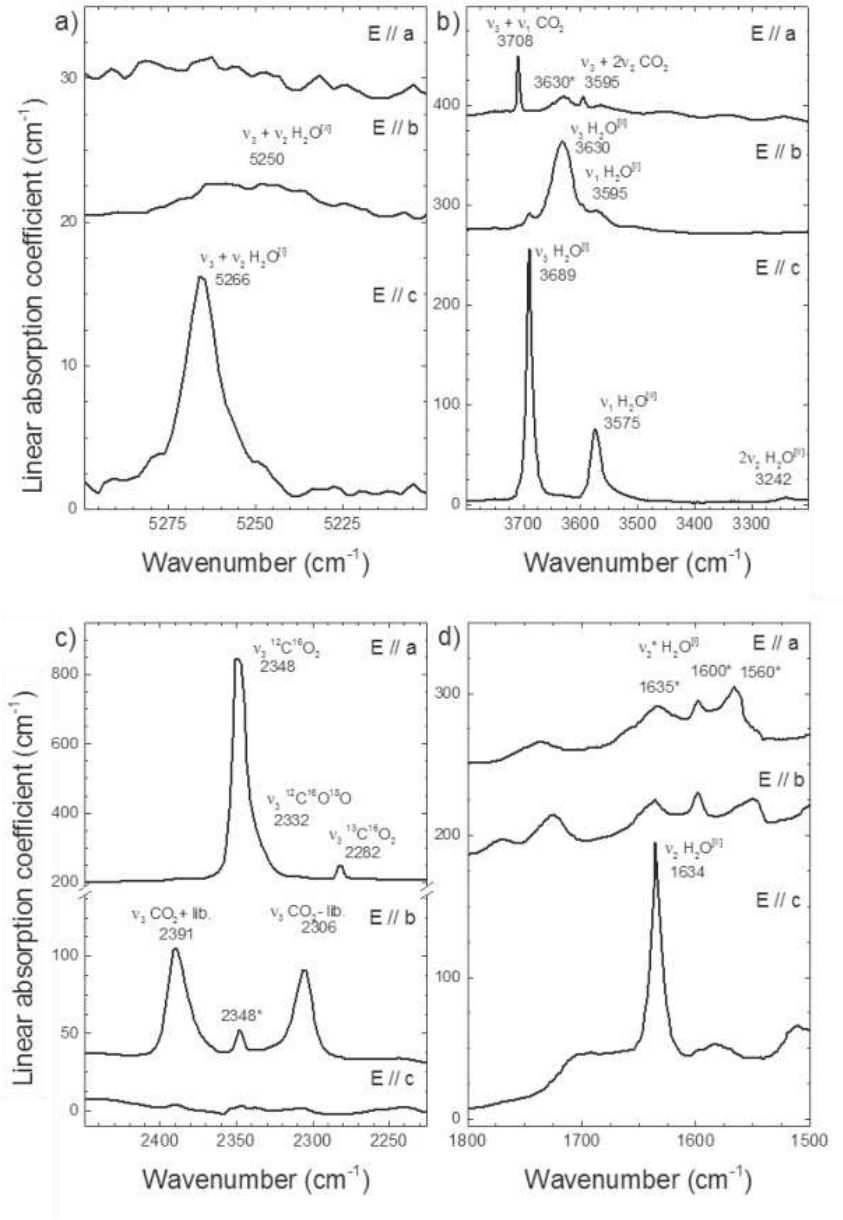

Figure 2 - Single-crystal polarized-light infrared spectra of BM 96512 cordierite collected at *RT* in the ranges 5300-5200 cm^{-1} (a), 3800-3200 cm^{-1} (b), in the CO_2 antisymmetric stretching mode region (c) and H_2O bending mode (d). Spectra were collected on (010) oriented 33 µm thick (E//*a* and E//*c*) and (100) oriented 50 µm thick (E//*b*) oriented slabs. Spectra are scaled to thickness. Band assignment is reported, *=see description in the text.

The vibrational (FTIR and Raman) spectrum is well characterized due to the many spectroscopic works published in the literature (*e.g.* Goldman *et al.*, 1977, Geiger and Kolesov, 2002, Khomenko and Langer, 2005, Della Ventura *et al.* 2009, 2012 and references therein). For the band assignment used in this work we follow the work of Della Ventura *et al.* (2009, 2012), who critically revised the existing literature on the interpretation of the IR spectra of cordierite, and also extending the spectrum analysis to the entire wavenumbers range from 6000 cm^{-1} (NIR) to 1500 cm^{-1} (MIR).

Accordingly, the peak at 3689 cm^{-1} (Fig. 2b), polarized for E//*c*, is assigned to the anti-symmetric stretching mode v_3 of $H_2O^{[I]}$; the corresponding symmetric stretching mode (v_1) in Mg-cordierite is observed at 3595 cm^{-1} (Paukov *et al.*, 2007) and is polarized for E//*b* (Fig. 2b) The splitting between these two components [$\Delta(v_3 - v_1)$=94 cm^{-1}] suggests that $H_2O^{[I]}$ occurs in cordierite as a relatively free, unbound molecule (Geiger and Kolesov, 2002). The broad band at 3630 cm^{-1} polarized in E//*b* is assigned to the antisymmetric stretching mode v_3 of $H2O^{[II]}$. The corresponding symmetric stretching band v_1 occurs at 3575 cm^{-1} in E//c. The absorptions at 3575 cm^{-1} for E//*b* and 3630 cm^{-1} for E//*a* (Fig. 2b) may be the result of slight tilting during sample preparation; the latter could be also ascribed to a very small amount of H_2O with its H–H vector parallel to the *a* crystallographic axis (Kolesov and Geiger, 2000). The peaks at 3708 and 3595 cm^{-1}, observed for E//*a*, are assigned respectively to the $v_3 + v_1$ and $v_3 + 2v_2$ combination mode of CO_2 (Della Ventura *et al.*, 2009, 2012).

The 1634 cm^{-1} peak (Fig. 2d) polarized parallel to the *c* axis is assigned to the bending mode (v_2) of $H_2O^{[II]}$ (Goldman *et al.*, 1977, Della Ventura *et al.*, 2009); the same polarization behavior is observed for its first overtone (Fig. 2b) at 3242 cm^{-1} (Herzberg, 1956). On the opposite, the bending mode v_2 of type I H_2O is much less intense and occurs as three features centered at 1560, 1600, and 1635 cm^{-1} (Radica *et al.*, 2013). The assignment of these features to H_2O modes is supported by the fact that they are absent in samples with low water contents (Della Ventura *et al.*, 2009) and by the fact that they disappear with the other fundamental modes after dehydration (Goldman *et al.*, 1977). The bending modes of $H_2O^{[I]}$ are expected to be polarized for E//*b*, however they also appear for E//*a* (see also Goldman *et al.*, 1977).

In the NIR region (Fig. 2a), the 5266 cm^{-1} peak polarized for E//*c* and the 5250 cm^{-1} polarized for E//*b* are assigned to the ($v_3 + v_2$) combination modes respectively of $H_2O^{[I]}$ and $H_2O^{[II]}$ (Della Ventura *et al.*, 2012).

In the 2600–2000 cm^{-1} region (Fig.2c), the most intense band at 2348 cm^{-1} is assigned to the v_3 antisymmetric stretching mode of the $^{12}C^{16}O_2$ molecule (Khomenko and Langer, 2005). The minor bands at 2282 and the shoulder at 2332 cm^{-1}, which are observed in single-crystal and powder spectra of CO_2-rich cordierites (*e.g.* Le Breton, 1989), have the same polarization behavior as the main band at 2348 cm^{-1}. These bands are respectively interpreted as the v_3 antisymmetric stretching mode of the $^{13}C^{16}O_2$ and $^{12}C^{16}O^{18}O$ isotope molecules (Khomenko and Langer, 2005). Assignment of the 2348 cm^{-1} band for E//*b* is unclear; due to position, shape and polarization it could be related to the v_3 mode of CO_2 molecules oriented parallel to the *b* axis, however there are no further evidence supporting this assumption. The two symmetric bands at 2390 and 2306 cm^{-1} observed for E//*b* are related to librational, sum and difference motions of the CO_2 molecule on the (001) plane (Aines and Rossman, 1984). Final assignment and respective polarization directions are reported in Table 4 for all bands.

Table 4 – Position, assignment and polarization of H_2O and CO_2 related peak observed in beryl. *=see description in the text, [1]=residual absorptions.

Molecule	Mode	Wavenumber (cm^{-1})	Polarization
$H_2O^{[I]}$	Bending v_2	1635*, 1600*, 1560*	E//a, E//b
	Stretch v_1	3689	E//c
	Antisymm Stretch v_3	3595	E//b
	Comb $v_3 + v_2$	5266	E//c
$H_2O^{[II]}$	Bending v_2	1634	E//c
	Bending $2v_2$	3242	E//c
	Stretch v_1	3575	E//c, E//a[1]
	Antisymm Stretch v_3	3630	E//b, E//a[1]
	Comb $v_3 + v_2$	5250	E//b
$^{12}C^{16}O_2$	Antisymm Stretch v_3	2348	E//a, E//b[1]
	Antisymm Stretch v_3 + lib	2391	E//b
	Antisymm Stretch v_3 - lib	2306	E//b
	Comb $v_3 + v_1$	3708	E//a
	Comb $v_3 + 2v_2$	3595	E//a
$^{13}C^{16}O_2$	Antisymm Stretch v_3	2282	E//a
$^{12}C^{16}O^{18}O$	Antisymm Stretch v_3	2332	E//a

5. Results

5.1 Isothermal heating experiments

Figures 3 and 4 show selected polarized light spectra collected on the (001) 60 µm thick section in the CO_2 combination region (3750-3550 cm^{-1}) for E//*a* (a), and in the CO_2 anti-symmetric stretching region (2450-2200 cm^{-1}) for E//*a* (b) and E//*b* (c). In particular, the

spectra displayed in Figure 3 are those collected at room *T* before the experiments, (dashed lines) and *in situ* just after reaching the target *T* indicated on the figure (solid lines). High temperature polarized measurements confirms the trends observed in Radica *et al.* (chapter 3): the $\nu_3 + \nu_1$ combination peak clearly broadens and shifts to higher frequency, at about 3720 cm^{-1}, while, for T > 850°C, the $\nu_3 + 2\nu_2$ combination peak of CO_2 at 3595 cm^{-1} and the H_2O absorptions at 3630 and 3575 cm^{-1} disappear. A weak shoulder can be observed around 3680 cm^{-1} (Fig. 3a). In the 2450-2200 cm^{-1} region, the 2348 cm^{-1} and the 2332 cm^{-1} components broadens without shifting. Note that at high *T*, the 2332 cm^{-1} peak intensity is almost comparable with that of the 2348 cm^{-1} peak. The 2282 cm^{-1} peak is hidden under the low-frequency tail of the broadened 2348-2332 cm^{-1} band (Fig. 3b). For E//*b* the high temperature behavior of the CO_2 sidebands is observed. In particular we observe the convergence of both components at 2391 and 2306 cm^{-1} toward the central 2348 cm^{-1} band, with a major shift (30 cm^{-1}) observed for the 2391 cm^{-1} band, due to a ν_3 + libration mode (Aines and Rossman, 1984) with respect the 2306 cm^{-1} (ν_3 – libration mode), whose shift is 9 cm^{-1} (Fig. 3c).

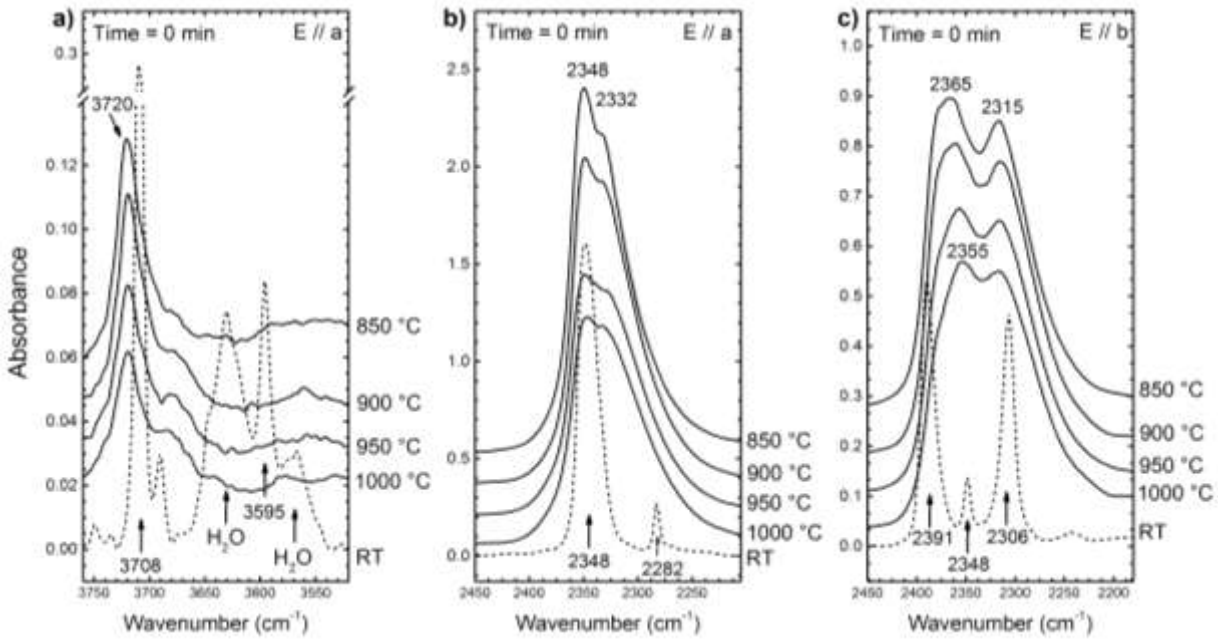

Figure 3 – Conventional light polarized FTIR spectra in (a) the CO_2 combination region for E//*a*, and anti-symmetric stretching region for (b) E//*a*, and (c) E//*b*; sample BM96512, 60 µm thick (001) section. Dashed line: *RT* spectrum before the heating experiments. HT spectra collected in situ just after reaching the target *T* (time = 0 min). Peak position at *RT* and at selected *T* are indicated. For peak assignments see Table 4 and text.

Figure 4 compares the spectra collected at *RT* before the experiments (dashed line) and the *RT* spectra collected on the quenched sample after 120 min annealing at the same temperatures as in Figure 3. Inspection of Figure 4 confirms a decrease in the integrated absorption of all CO_2 related peaks; the magnitude in decrease is directly proportional to the temperature, with the only exception of the 2348 cm^{-1} absorption polarized parallel to the *b* crystallographic axis, which presents a constant A_i of about 40 % of the starting intensity. A similar behavior was observed by Fukuda and Shinoda (2011). It is worth of note that after the heat-treatment no H_2O related absorption are present in the spectra, even at the lowest 850°C temperature (Fig. 4a). In addition, no peak shifts are observed.

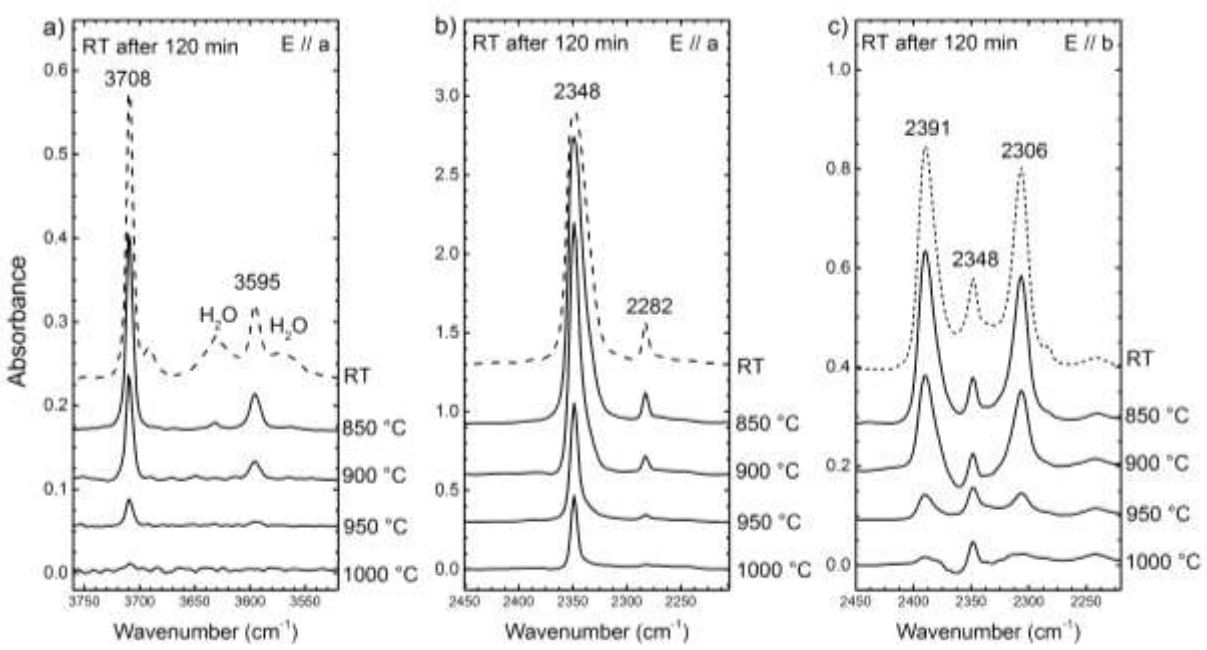

Figure 4 – Room T polarized light FTIR spectra, sample BM96512 60 µm thick collected before the experiment (dashed curves) and after 2 hours at the indicated temperatures (solid curves). Spectra in the CO_2 combination region for E//*a* (a), and anti-symmetric stretching region of with E//*a* (b) and E//*b* (c).

Figure 5 shows the CO_2 loss curves expressed as $A_{t\%} = 100 \cdot A_t/A_0$ where A_t is the A_i at time = t and A_0 is A_i at time = 0, *i.e.* just after the sample reached the target temperature; data obtained with E//*a* for the ν_3 mode at 2348 cm^{-1} for the 60 µm thick BM96512 and the 19 µm thick BM96512 (001) sections are displayed. Errors on the CO_2 loss curves are accounted as ±10% of the integrated absorbances A_i (Libowitzky and Rossman, 1997), hence, following the error propagation rules, the estimated error is expressed as $\sigma A_{t\%} = A_{t\%} \cdot 0.1 \cdot \sqrt{2}$.

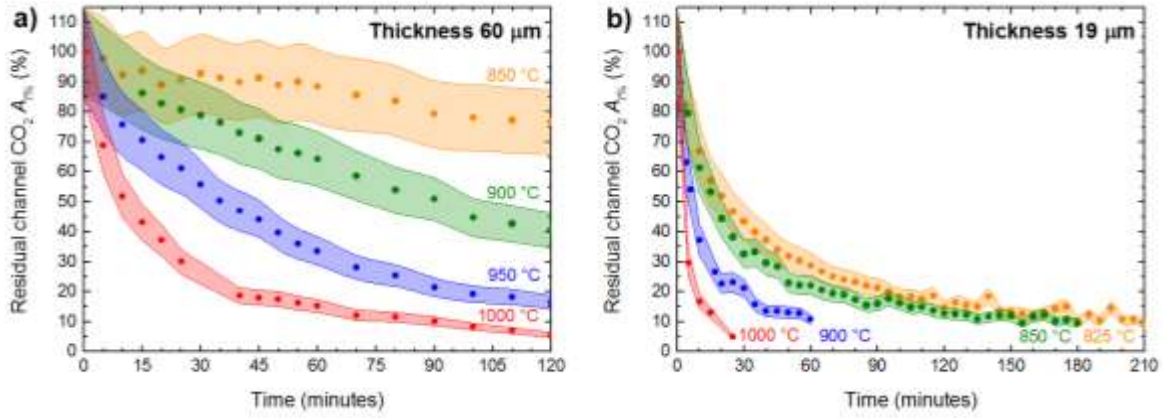

Figure 5 – Isothermal plots of residual CO_2 within the cordierite channels ($A_{t\%} = 100 \cdot A_t/A_0$ of the 2348 cm^{-1} band) as a function of time; sample BM96512, (001) section with E//*a*. Shaded areas represent the estimated error on the absorption. (a) 60 µm thick section, (b) 19 µm thick section.

5.2 Reaction kinetics

5.2.1 Avrami rate equations

Figure 5 shows that for $T > 800°C$ the CO_2 content decreases significantly as a function of time. As a first step, we modeled the results of Figure 5 by using the same formalism employed by previous authors for their dehydration experiments (Hancock and Sharp, 1972; Giampaolo and Putnis, 1989), *i.e.* by assuming that CO_2 loss from cordierite may be described as a first order reaction. In such a case, the rate is exclusively proportional to the concentration of CO_2, because no chemical reactions are involved during CO_2 loss other than simple desorption. A first order reaction follows the general Avrami formula (Avrami, 1939, 1940, 1941) of exponential decay:

$$y = 1 - \exp\big(-f(t)\big) \text{ or } A_t = A_0 \cdot \exp\big(-f(t)\big) \quad (1)$$

where $y = 1 - A_t/A_0$ is the fraction of CO_2 lost at time = t (min), A_t is the integrated absorbance (A_i) at time = t, A_0 is A_i at time = 0 and f(t) is a time dependent exponential function. f(t) is usually described by two parameters k and m. The coefficient k, the rate constant, describes the way the decrease depends on the concentration of the reactant. The exponential factor m is an empirical factor used to model the reaction mechanism. Curves with the same value of m are isokinetic and indicate that the reaction type does not change within the examined range of temperature or fraction loss. The kinetic parameter k may be

used, *via* the Arrhenius equation, to calculate the activation energy E_a (kJ/mol) of the process leading to CO_2 loss from the structural channels:

$$k = A \cdot \exp\left(-\frac{E_a}{RT}\right) \tag{2a}$$

Linearized:

$$\ln k = \ln \alpha - E_a/RT \tag{2b}$$

where R is the universal gas constant (kJ/mol K), T is the temperature in K and α is the frequency factor.

Because various equations can fit the same data set equally well, very different values of the empirical activation energy can be derived from the same experiments. Thus the activation energy is only meaningful in terms of the rate equation used to fit the data. In order to test for the best model to describe the CO_2 loss form cordierite, we fitted our data (Fig. 6) with two of the most commonly used equations in kinetic studies for minerals:

$$A_t = A_0 \cdot \exp(-k \cdot t^m) \tag{3a}$$

Hereafter referred as Avrami JMAK (Avrami, 1939, 1940, 1941; Hancock and Sharp, 1972; Carbone *et al.*, 2008), and:

$$A_t = A_0 \cdot \exp[-(k \cdot t)^m] \tag{3b}$$

referred as Avrami Putnis (Giampaolo and Putnis, 1989, Putnis *et al.*, 1990, Putnis, 1992). It is important to note that in the latter formula the rate constant k has always the dimension of t^{-1}, while in the former case the dimension of k is t^{-m} and thus depends on the fitted curve.

Figure 6 shows the results of fitting the above equations to the experimental data for the v_3 anti-symmetric stretching mode of CO_2 for both sections 60 µm and 19 µm thick, respectively; fitted parameters are compared in Table 5. Figure 7 shows the values of the fitted parameters in the Arrhenius space. The activation energies E_a calculated from the

Arrhenius equation (equation 2b above) for each of the aforementioned datasets are reported in Table 6.

Table 5 – Avrami JMAK and Avrami Putnis fitted values and its associated errors (σ). ln*k* and R^2 are also reported.

	Avrami JMAK							Avrami Putnis						
	BM 96512 60 µm thick													
Temp (°C)	***m***	**σ *m***	***k***	**σ k**	**ln*k***	**σ ln*k***	**R^2**	***m***	**σ *m***	***k***	**σ k**	**ln*k***	**σ ln*k***	**R^2**
1000	0.54	0.03	2.14E-01	3.00E-02	-1.54	0.14	0.984	0.54	0.03	5.78E-02	7.50E-03	-2.85	0.13	0.976
950	0.80	0.03	4.13E-02	6.40E-02	-3.19	0.15	0.995	0.80	0.03	1.84E-02	7.60E-04	-4.00	0.04	0.995
900	0.97	0.04	8.68E-03	1.91E-03	-4.75	0.22	0.995	0.96	0.05	7.60E-03	1.50E-04	-4.88	0.02	0.994
850	1.17	0.40	8.80E-04	2.10E-03	-7.04	2.39	0.661	1.18	0.22	2.47E-03	5.70E-04	-6.00	0.23	0.917
	BM 96512 19 µm thick													
Temp (°C)	***m***	**σ *m***	***k***	**σ k**	**ln*k***	**σ ln*k***	**R^2**	***m***	**σ *m***	***k***	**σ k**	**ln*k***	**σ ln*k***	**R^2**
1000	0.58	0.07	4.55E-01	1.10E-01	-0.79	0.24	0.971	0.58	0.07	2.60E-01	6.50E-02	-1.35	0.25	0.971
900	0.46	0.05	3.50E-01	7.30E-02	-1.05	0.21	0.950	0.46	0.05	1.00E-01	2.00E-02	-2.30	0.20	0.951
850	0.42	0.05	2.80E-01	4.50E-02	-1.27	0.16	0.953	0.42	0.03	5.00E-02	1.00E-02	-3.00	0.20	0.956
825	0.51	0.06	1.55E-01	5.80E-02	-1.86	0.37	0.958	0.51	0.02	3.00E-02	9.00E-03	-3.51	0.30	0.960

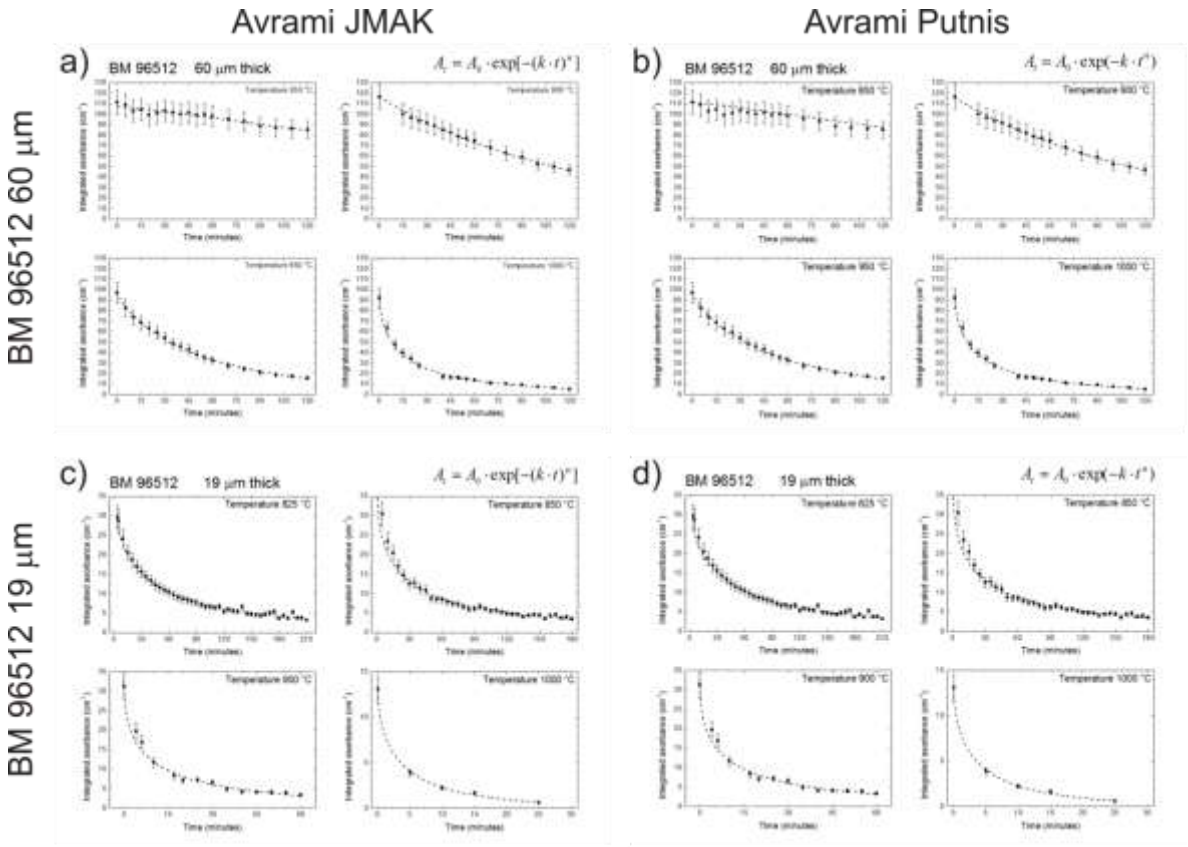

Figure 6 – Evolution of integrated CO_2 absorbance (v_3 anti-symmetric stretching mode) as a function of time for the experimental data set collected for the BM 96512 60 µm thick (a, b) and 19 µm thick (c, d). Curves are fitted by Avrami JMAK equation (left column) and Avrami Putnis (right column) for each temperature.

Table 6 – Arrhenius equation parameters and activation energies *Ea* for each of the dataset obtained *via* Avrami JMAK and Avrami Putnis equation.

	Avrami JMAK	Avrami Putnis
	BM 96512 60 µm	
ln *A*	36.5±1.2	18.1±1.4
***E*$_a$/R**	48.5±1.5	26.9±1.7
E*$_a$ *(kJ/mol)	403±12	224±14
	BM 96512 19 µm	
ln *A*	3.9±1.9	11.8±1.2
***E*$_a$/R**	5.9±2.2	16.6±1.4
E*$_a$ *(kJ/mol)	49±16	138±12

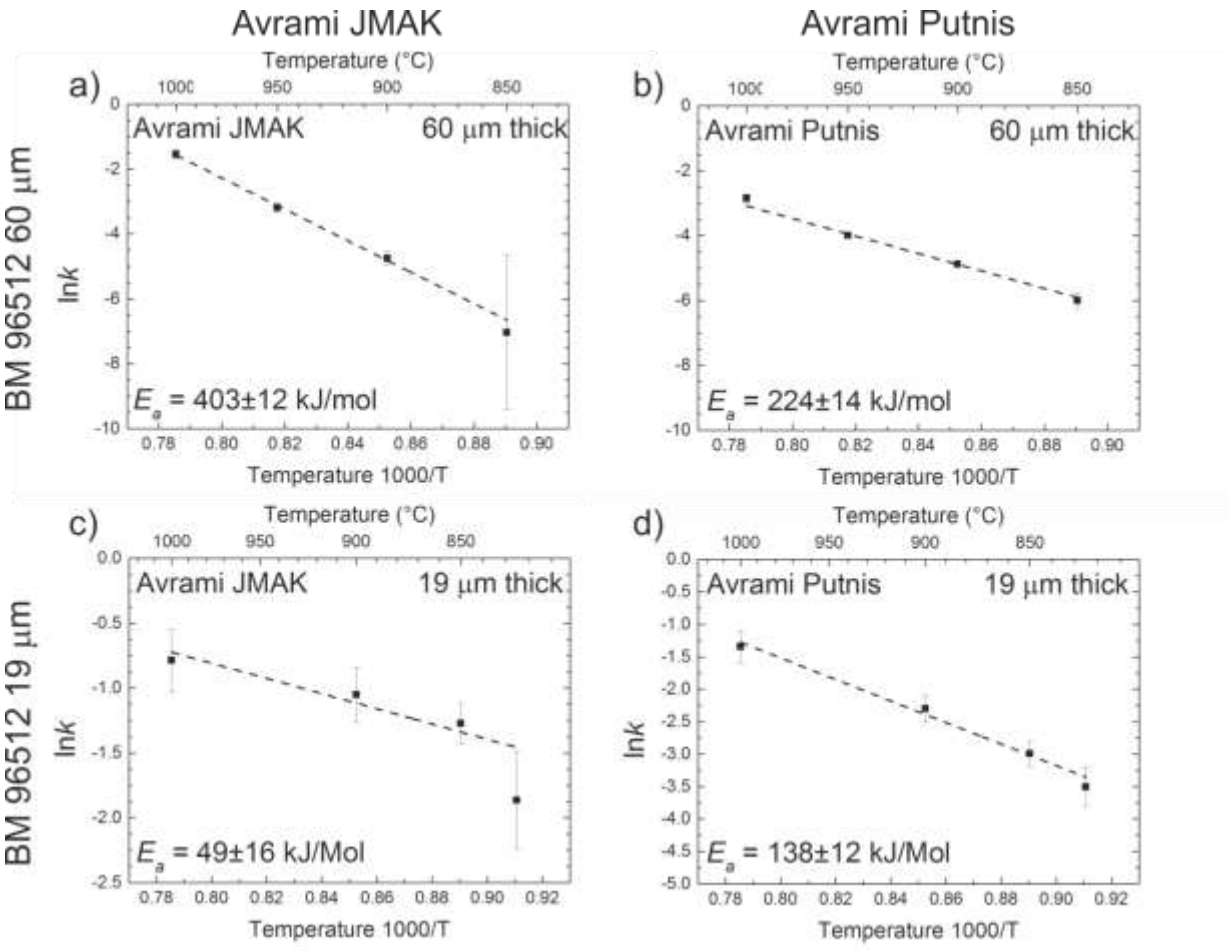

Figure 7 – Arrhenius plots for cordierite BM 96512, 60 µm thick (a, b) and 19 µm thick (c, d).

Examination of Table 6 shows that two different sets of results are obtained when using the two (JMAK *vs* Putnis) equations, suggesting that the Avrami formalism is not suitable to describe the CO_2 desorption along the structural channels. This point will be discussed in more details below.

5.2.2 Mono-dimensional plane sheet diffusion

In the previous paragraph, we showed that the process of CO_2 loss in cordierite is not related exclusively to the starting CO_2 content, but depends strongly on the shape and size of the examined sample. Therefore, we modeled the data on the basis of a mono-dimensional diffusion from a plane sheet of finite thickness (Fig. 8), using the equation (Carlslaw and Jeager, 1959; Crank, 1975; Ingrin, 1995; Tokiwai and Nakashima, 2010a):

$$A_t = A_0 \cdot \sum_{n=0}^{\infty} \left\{ \frac{8}{(2n+1)^2 \pi^2} \right\} \cdot \exp \left\{ \frac{-D(2n+1)^2 \pi^2 t}{L^2} \right\} \quad (4)$$

where A_t is the A_i at time = t, A_0 is A_i at time = 0, D is the diffusion coefficient in m^2/sec, t is the time in sec and L is sample thickness in m, n is the index of summation.

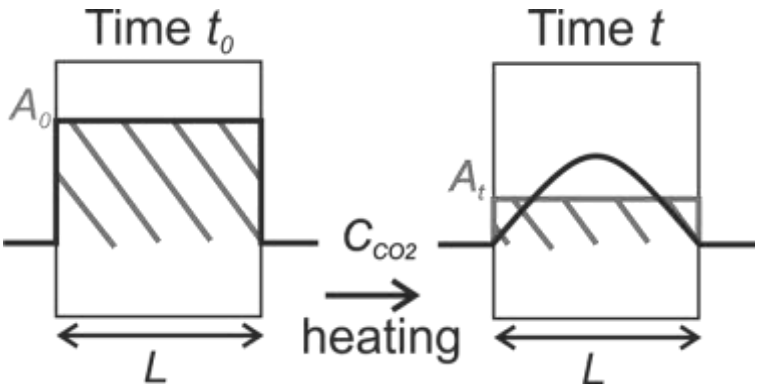

Figure 8 – Schematic diagram of a mono-dimensional diffusion from a plane sheet with thickness of L and initial concentration of A_0. After time t, CO_2 integrated absorbance decrease to A_t due to surface diffusion. The actual CO_2 distribution inside the sample is described by the black line. Modified after Ingrin *et al.* (1995).

In order to apply equation (4) the following consideration were done: 1) the CO_2 concentration C may be replaced by the integrated absorbances A_i, because the CO_2 content and its absorbance in the FTIR spectrum are related by the Beer-Lambert equation; 2) any CO_2 at the crystal surface was removed using a gentle flow of N_2 in the microscope chamber; 3) the diffusion normal to the slab surface is homogeneous, because the CO_2 diffusion occurs exclusively along the *c* crystallographic direction (Fukuda *et al.*, 2009; Radica *et al.* Chap. 3); moreover FPA images collected after the experiments on the 60 µm thick section, confirmed an homogenous distribution of residual CO_2 (Fig. 9).

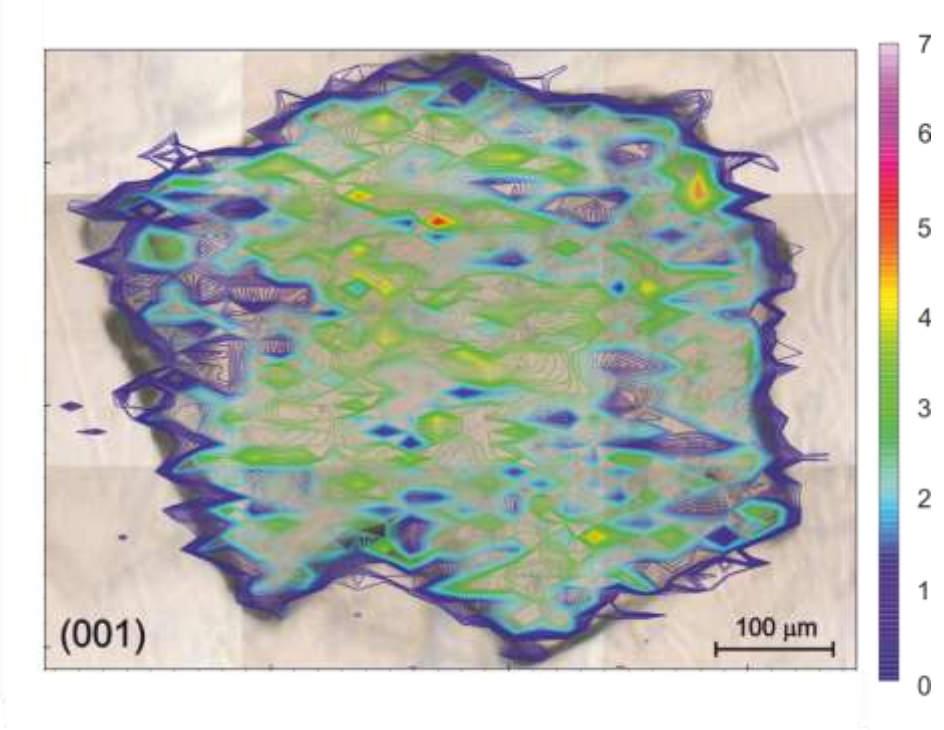

Figure 9 - Optical picture and FPA image of the residual distribution of CO_2 in the 60 µm thick (001) oriented cordierite lamella heat-treated at 1000° C for 2 hour. Chromatic scale (in cm^{-1}) is proportional to CO_2 content.

The diffusivity of a given species in a particular medium is described by the Arrhenius equation in the form:

$$D = D_0 \cdot \exp\left(-\frac{E_a}{RT}\right) \tag{5}$$

with *D* is the diffusion coefficient, D_0 the pre-exponential factor, E_a the activation energy, which is the amount of energy required for a particle to pass the potential barrier between its equilibrium position and an adjacent one. *R* is the ideal gas constant, and *T* the absolute temperature in K. The parameters E_a and D_0 are obtained from the Arrhenius plot -log*D* vs. 1/*T*, where the diffusion coefficients plot in a straight line:

$$\log D = \log D_0 - E_a/R \cdot \ln 10 \cdot 1/T \tag{6}$$

Hence, the activation energy E_a is derived from the slope of the line and D_0 is the intercept; ln10 is needed to convert from log units (diffusion coefficients) to ln units (Arrhenius equation).

Figure 10 shows the results obtained by fitting the equation (4) to the experimental data for the CO_2 ν_3 mode in the spectra of both 60 µm and 19 µm thick sections, while Table 7 lists the diffusion coefficients *D* obtained from the calculations. Figure 11 displays the data in the Arrhenius space. E_a values calculated from equation (6) are listed in Table 8.

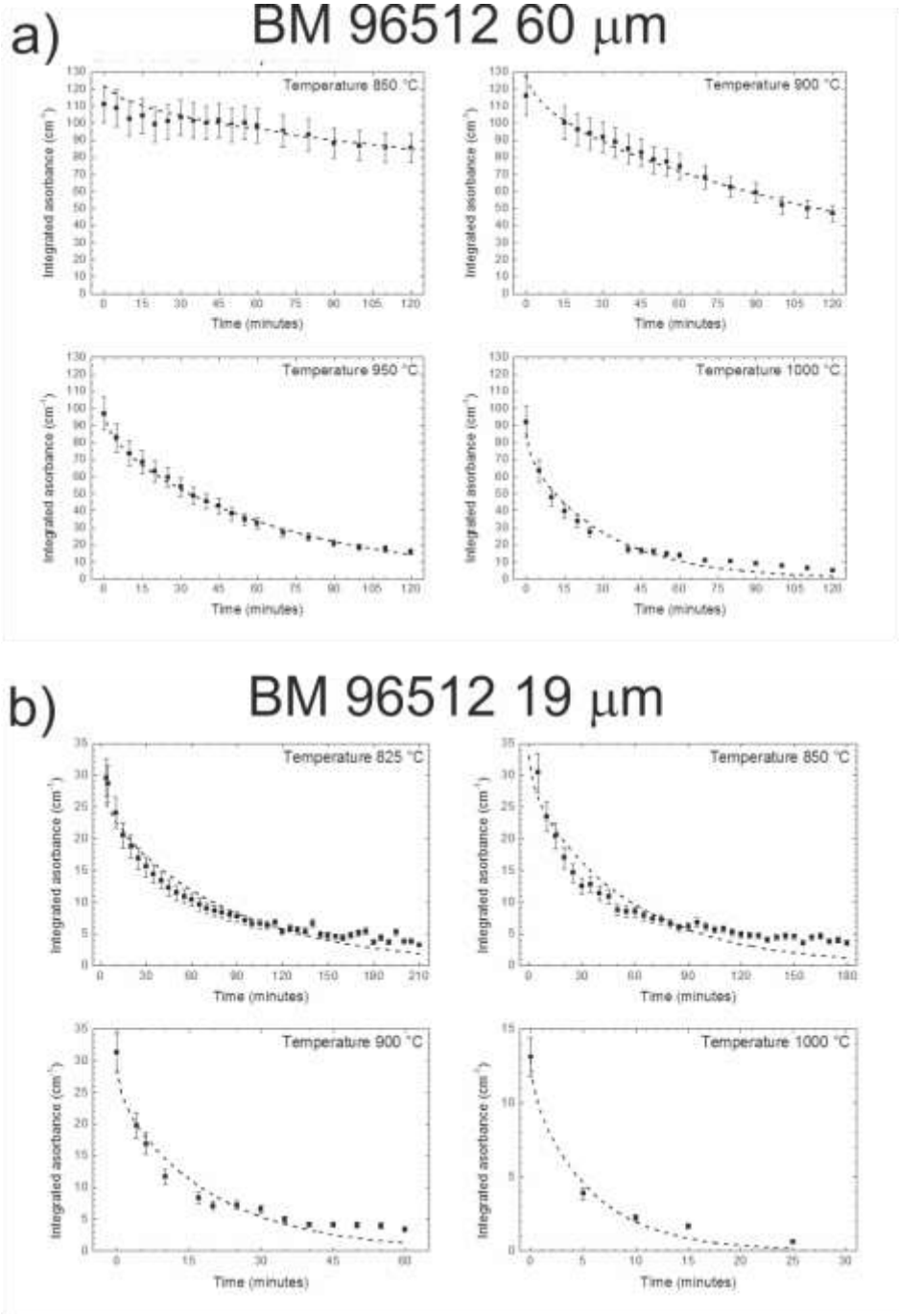

Figure 10 – Evolution of CO_2 integrated absorbance (as a function of time) of the ν_3 anti-symmetric stretching mode for the experimental data sets obtained for the 60 µm (a) and 19 µm thick (b) sections. Curves are fitted using the mono-dimensional plane sheet diffusion equation (4).

Table 7 – Values obtained using the mono-dimensional plane sheet diffusion model and associated errors. -log*D* and R^2 are also reported.

BM 96512 60 µm						
Temp (°C)	**10^3/T**	***D***	**σ *D***	**-log*D***	**σ -log*D***	**R^2**
1000	0.79	1.94E-13	1.37E-14	12.71	0.07	0.984
950	0.82	8.84E-14	1.94E-15	13.05	0.02	0.995
900	0.85	4.04E-14	1.72E-15	13.39	0.04	0.979
850	0.89	1.01E-14	1.02E-15	14.00	0.10	0.949
BM 96512 19 µm						
Temp (°C)	**10^3/T**	***D***	**σ *D***	**-log*D***	**σ -log*D***	**R^2**
1000	0.79	1.04E-13	1.43E-14	12.98	0.14	0.979
900	0.85	3.02E-14	2.99E-15	13.52	0.10	0.944
850	0.89	1.07E-14	7.20E-16	13.97	0.07	0.914
825	0.91	7.45E-15	1.27E-15	14.13	0.17	0.939

Table 8 – Arrhenius equation parameters (5) and activation energies E_a for each of the dataset obtained *via* mono-dimensional plane sheet diffusion equation (4).

	-logD_0	**E_a/(R ln10)**	**E_a (kJ/mol)**
BM 96512 60 µm	4.0±0.9	11.1±1.1	213±21
BM 96512 19 µm	5.4±0.7	9.6±0.8	183±15
All points	4.4±0.7	10.7±0.8	204±15

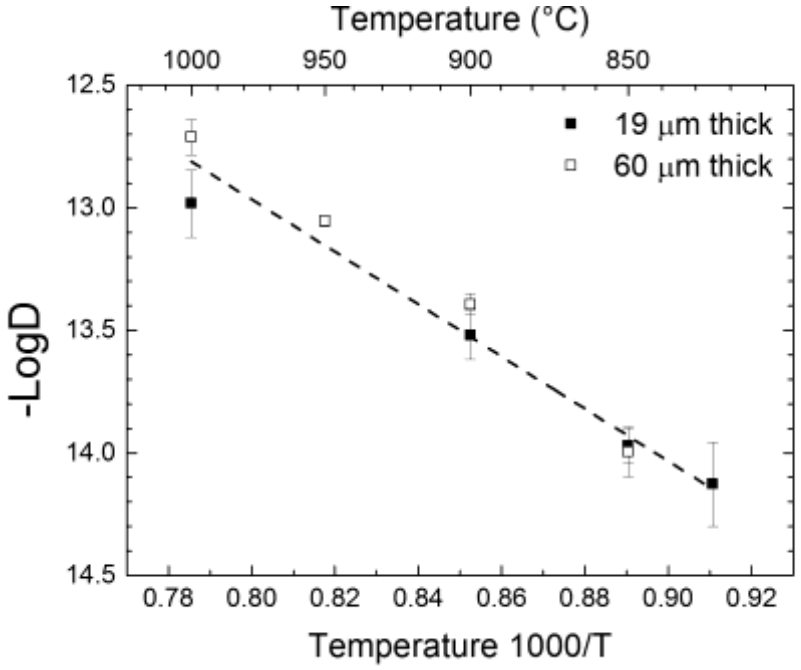

Figure 11 – Arrhenius plot using values of the diffusion coefficient *D* obtained fitting the equations (4) for the ν_3 anti-symmetric stretching mode for both 60 µm and 19 µm thick sections. The combined diffusion law is reported, line parameters are reported in Tab. 8.

6. Discussions: Kinetic of CO_2 extraction

The kinetic of CO_2 expulsion from cordierite channels in the temperature range from 825 °C to 1000 °C was calculated using the integrated absorbance (A_i) changes in the MIR region. Isothermal heating experiments were performed on oriented cordierite slabs doubly polished along the direction normal to the *c* crystallographic axis; FTIR spectra were collected *in situ*. Hereafter we discuss the differences on the calculated activation energies (E_a) of CO_2 expulsion on the basis of the used analytical approach or the effects of the sample thickness.

1) From Table 6 we observe that, when using the Avrami approach, calculation of the activation energies E_a on the basis of two different equations (JMAK and Putnis), yields very different values, spanning from 403 kJ/Mol to 49 kJ/Mol. The differences are not only related to the different analytical approach, but mostly to the different sample thickness. The value calculated with the Avrami JMAK equation are in fact reduced by almost one order of magnitude for the thinner sample with respect the thicker one, while those calculated using the Avrami Putnis equation are only halved.
2) Data reported in Table 8 suggest that when using the mono-dimensional diffusion model, the thickness has no effect on the resulting D_0 or E_a values, thus confirming that, unlike to what observed for H_2O in muscovite (Tokiwai and Nakashima, 2010a) the CO_2 diffusion in cordierite can be well described by this formalism.
3) In the previous section we mentioned that the *m* parameter in the Avrami equation is dependent of the reaction mechanism (Putnis *et al.*, 1990). Examination of Figure 12 shows two distinct trends between the *m* values obtained for the different sections: the values fitted for the 60 µm thick sample in fact decrease progressively as a function of *T*, suggesting a progressive change of the expulsion mechanism. On the other hand, those fitted using the data collected on the 19 µm thick sample are constant in the whole *T* range considered. Considering that the two experimental sets of data differ just for the thickness of the studied crystal slab, and that in this temperature range no significant change in CO_2 expulsion mechanism are expected (also see point 2 above), we may conclude that the *m* values in the Avrami approach are sensitive to the sample thickness. In addition, because the *m* values are constant

exclusively for thinner 19 µm we may conclude that Avrami formalism could be suitable to describe the behavior of very small, possibly powdered, samples.

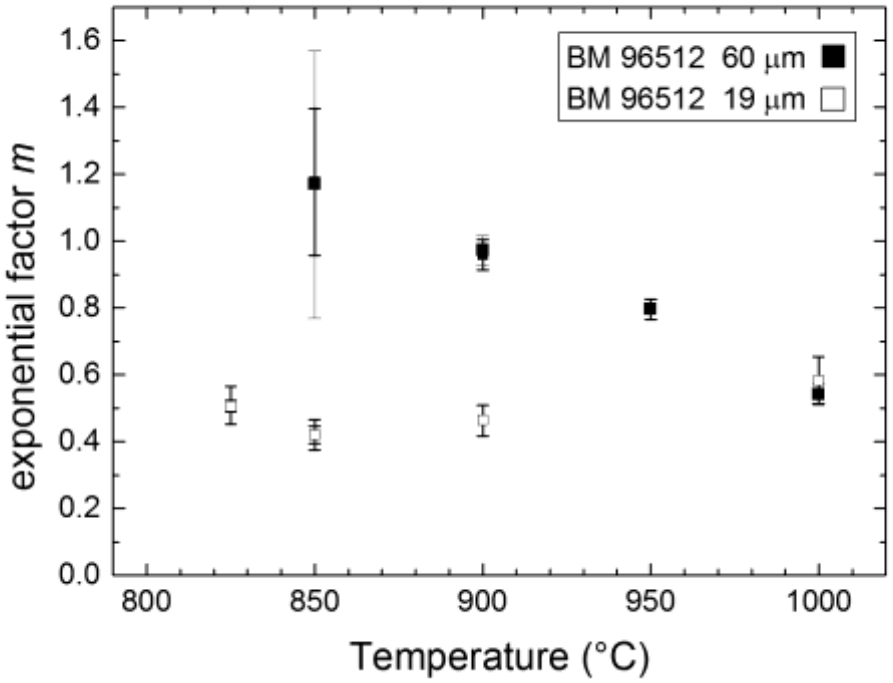

Figure 12 – Fitted exponential *m* factors for each experimental temperature of sample BM 96512 60 µm (black squares) and BM 96512 19 µm (open squares).

4) The same procedures were adopted to model the absorbance trends for CO_2 sidebands polarized per E//*b* (Fig. 3c) in the 60 µm sample data set. In Table 9 we compare the calculated activation energies E_a, ln*A* and –logD_0 obtained for each different approach. Only small differences are observed with the E_a calculated using the ν_3 mode collected for E//*a*; in particular, the Avrami Putnis and the mono-dimensional plane sheet diffusion method yield very similar E_a values (see also Tab. 6 and 8).

Table 9 – Arrhenius equation parameters and activation energies *Ea* for the sidebands in sample BM 96512 60 µm *via* Avrami JMAK, Avrami Putnis and mono-dimensional plane sheet diffusion equations.

	Avrami JMAK	**Avrami Putnis**	**1D diffusion**	
ln *A*	31.4±1.2	18.0±1.5	**-logD_0**	5.4±0.4
E_a (kJ/mol)	348±13	222±14	**E_a (kJ/mol)**	180±10

Scattering of the E_a values confirms that the Avrami approach cannot be used to evaluate the kinetic parameters of CO_2 extraction. However, based on the above assumptions, it is possible to infer that the most reliable activation energy for CO_2 expulsion from cordierite provided by the Avrami formalism is E_a = 138±12 kJ/mol, *i.e.* the value obtained using the Avrami Putnis equation on the thinner sample data set. Note that this value is very close to those obtained by previous authors for the dehydration of cordierite (Giampaolo and Putnis, 1989; Lepezin and Melenevsky, 1977; Zimmermann, 1981).

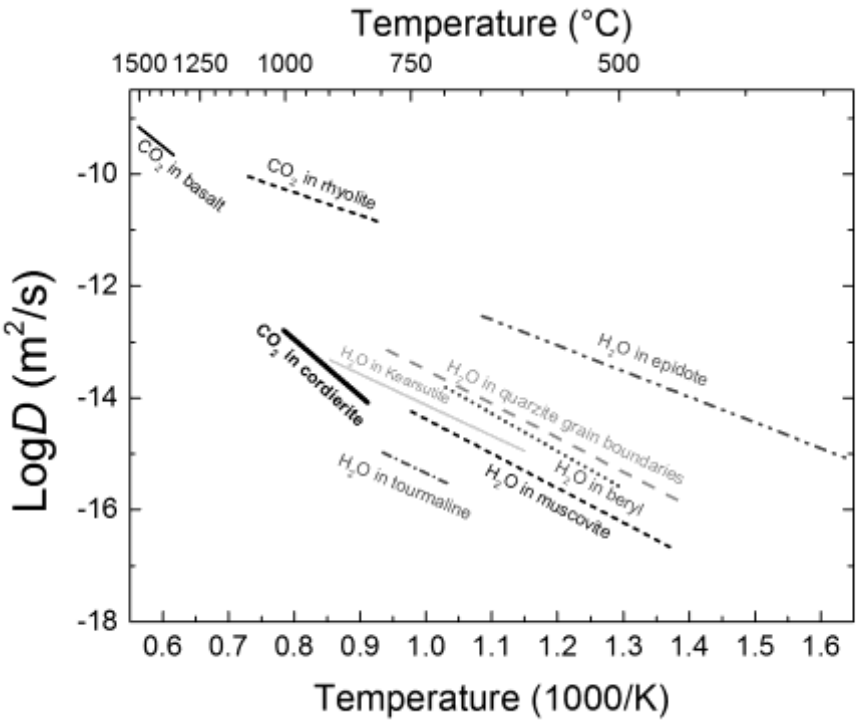

Figure 13 – Arrhenius diagram of various diffusion coefficients *D* for different silicates or silicate melts for H_2O and CO_2. Numerical values and references in Tab. 10.

We calculated also the diffusion coefficient *D* and E_a for CO_2 in cordierite using the mono-dimensional plane-sheet diffusion approach (Crank, 1995). We discussed in the previous paragraph how CO_2 likely diffuses across cordierite through a simple diffusion mechanism for temperatures between 825 and 1000 °C. Diffusion coefficients of volatile molecular species in silicates are expected to be tightly related to the molecule dimension and the diffusing structure. It is also widely accepted that for more compact silicate structures and/or larger molecules diffusing rates are smaller and activation energies larger. As we may observe from Figure 13 the diffusing rates calculated for CO_2 in cordierite (this

work) are almost one order of magnitude lower then H_2O diffusion coefficients calculated in the isotructural beryl (Fukuda *et al.*, 2009).

It is difficult to draw a direct comparison between our data and the diffusion coefficients available in the literature for minerals; the reason is that, beryl and cordierite behave as microporous structures trapping H and C as H_2O and CO_2 molecules, while the vast majority of the existing data have been collected on minerals where H is present as an OH^- group. Moreover no data are available for CO_2 diffusion in minerals (excluding C diffusion in carbonates, *e. g.* Anderson, 1972; Labotka *et al.*, 2000). Thus in the next paragraph we are forced to compare our data with those derived for basically different processes.

Figure 18 and Table 6 give selected examples of diffusion rates for the most common hydrous minerals. In Figure 18 we may observe that the diffusion coefficients measured for CO_2 in beryl are close to the OH^- diffusion coefficients obtained in other ring silicates like tourmaline (Desbois and Ingrin, 2007), layer silicates like muscovite (Graham, 1981), amphiboles like kaersutite (Ingrin and Blanchard 2000), or in disilicates like epidote (Graham, 1981). However, it is important to note that structural OH^- probably diffuses inside these structures in the form of H^+ (Zhang *et al.*, 2010) thus the diffusing species is much smaller compared to molecular CO_2 and H_2O.

Our data suggest that the structural channels of cordierite and beryl act more likely as fast paths for the mobility of large molecular groups compared to similar silicate structures, and for this reason the diffusing behavior is more similar (in terms of diffusion coefficients, not in the mechanism) to the one typically observed for grain boundary diffusion, such as, for example, H_2O in quartzite (Farver and Yund, 1991) or to the behavior of CO_2 in non-crystalline materials, like silicate melts (Watson *et al.*, 1982; Watson, 1991).

Table 10 – Comparison of the experimental data for H_2O and CO_2 diffusion in various silicate minerals and melts found in the literature.

Mineral	Diffusing molecule	T (°C)	P (MPa)	E_a (kJ/mol)	logD_0 (m^2/s)	Reference
Rhyolite	CO_2	800-1100	1000	75	-7.2	Watson, 1991
Basalt	CO_2	1350-1500	1500	195	-3.4	Watson *et al.*, 1982
Muscovite	D/H_2O, D_2O	450-750	200 or 400	121	-8.0	Graham, 1981
Epidote	D/H_2O, D_2O	250-650	200 or 400	90	-7.4	Graham, 1981 in Ingrin and Blanchard, 2006
Kearsutite	D/D_2	600-900	0.1	104±12	-8.7	Ingrin and blanchard, 2000
Tourmaline (par *c*)	D/Ar, D_2	700-800	0.1	106.3±36.8	-9.8	Desbois and ingrin, 2007
Quarzite	H_2O	450 -800	100	113	-7.6	Farver and Yund, 1991
Beryl	H_2O	500 -700	50 -150	133	-6.6	Fukuda *et al.*, 2009

7. Conclusions

In this work we evaluate the kinetic parameters and diffusion rates of CO_2 along the structural channels of cordierite for increasing thermal conditions. High-quality polarized-light *in-situ HT*-FTIR data up to 1000 °C could be obtained for very thin samples thanks to the increased brilliance of a synchrotron radiation light source (SR-FTIR, Della Ventura *et al.*, 2014), compensating for the degradation of the IR signal resulting from the use of a polarizer and the heating stage.

Isothermal heating experiments were performed on (001) oriented cordierite slabs that ensure a homogeneous CO_2 desorption out from the slab surface (Radica *et al.* chapter 3). Inspection of the spectra collected at high-*T* shows a significant peak broadening of all CO_2 peaks, while no peak shift were observed for the ν_3 mode at 2348 cm^{-1}. Polarized spectra collected at RT after the heating experiments for the 60 μm thick sample confirms a decrease in the integrated absorption of all CO_2 peaks; the magnitude of decrease is directly proportional to the temperature. No H_2O bands are present in the spectra after the heat-treatments, indicating that, differently from CO_2, for $T > 850$°C H_2O is totally lost from the cordierite matrix.

Because no changes in CO_2 speciation occur during desorption, CO_2 loss can be described as a simple diffusion mechanism. The mono-dimensional plane-sheet diffusion approach is not influenced by thickness; calculated activation energies are larger, about 204±15 kJ/mol. Measured diffusion coefficients (*D*) for CO_2 along the structural channels are almost two order of magnitude lower than those for H_2O in the isostructural beryl, and very close to those of H^+ in hydrated minerals or CO_2 in silicate melts.

CHAPTER 5

KINETICS OF INCORPORATION OF CO_2 IN CORDIERITE AND BERYL: AN FTIR-FPA SPECTROSCOPY STUDY

Abstract

In this work, we address experimentally the diffusion of CO_2 into cordierite and beryl, two isostructural microporous rock-forming minerals, using FTIR spectroscopy coupled with FPA (focal-plane-array of detectors) imaging. Fragments of a natural, almost Mg end-member cordierite and CO_2-free synthetic beryl were used as starting materials; the cordierite crystallites were degassed before the experiments. Starting crystals were treated in a CO_2-saturated atmosphere at different pressure, temperature and time conditions, using a non end-loaded piston-cylinder apparatus. Ag-carbonate was used as the source for carbon dioxide. After the high pressure experiments, the recovered crystals were oriented using a spindle stage, cut and doubly polished, and analyzed using polarized micro-FTIR spectroscopy to study the distribution of CO_2 across the sample and quantify its concentration. The IR data show that pressure plays a major role on the incorporation of gaseous CO_2 in both cordierite and beryl, whereas the effect of temperature is limited. The spectroscopic data show that the diffusion of CO_2 occurs preferentially along the structural channels parallel the c-axis direction. Diffusion coefficients (D) for beryl were calculated using the monodimensional diffusion equations; obtained values are in the order of 10^{-14} m^2/s between 700 – 900°C. Fitting of the diffusion coefficients in the Arrhenius plot yielded – $\log D_0$ = 7.2±0.7 m^2/sec and an activation energy E_a = 122±15 kJ/mol. Sample cracks formed

during the high pressure experiments were found to enhance significantly the gas diffusion within the samples.

1. Introduction

Microporous and mesoporous minerals are important from both a geological and a technological viewpoint. Initially these attributes were only referred to zeolites, however in the last decade the IUPAC nomenclature was extended to non-zeolitic minerals (McCusker *et al.*, 2001; McCusker, 2005). Among these phases, cordierite plays a key role because it represents the only case of a widespread microporous mineral (pore size under 2 nm, Rouquérol *et al.*, 1994; McCusker *et al.*, 2001) that is able to trap significant amounts of molecular H_2O and CO_2 (Schreyer and Yoder 1964; Mirwald *et al.*, 1979; Newton and Wood, 1979; Armbruster and Bloss 1982; Kurepin 1985) under extreme geological (P, T) conditions. Cordierite stability extends from the amphibolite facies to ultra-high temperature metamorphism to crustal anatexis conditions (Mirwald and Schreyer, 1977; Vry *et al.*,1990; Carrington and Harley, 1996; Smith 1996; Kalt 2000; Harley *et al.*, 2002; Bertoldi *et al.*, 2004; Sarkar *et al.*, 2010). The analysis of the volatile constituents of cordierite can used to determine the composition of the fluid pahse during crystallization (Vry *et al.*, 1990; Carrington and Harley, 1996; Harley *et al.*,2002; Kurepin, 2010). H_2O and CO_2 contents affect the stability of cordierite (Schreyer 1985; Carey 1995; Harley *et al.*, 2002). Therefore, a quantitative determination of its channel constituents is crucial in petrologic studies.

Among the wide range of cordierite occurrences, the most investigated is the ultra high-temperature metamorphism of pelitic rocks. Dehydration melting of biotite-bearing pelites with moderate to high X_{Mg} variations (X_{Mg}/X_{Mg+Fe} >0.5) is often controlled by cordierite-forming reactions in migmatites and leuco-granites at 200–700 MPa and 700–900° C (Fitzsimons, 1996; Harley *et al.*, 2002). Thus understanding the role of cordierite as an H_2O and CO_2 bearing phase is essential for understanding melting processes and for thermodynamic calculation of fluid activities during these events (Harley and Thompson, 2004). Kurepin (2010) made calculations of the dependence of H_2O and CO_2 contents in cordierite as a function of *P, T* and fluid composition for the aforementioned P-T conditions, and his thermodynamic model showed a non-ideality of thermodynamic behavior of H_2O

and CO_2 mixing. In addition evaluation of the H_2O and CO_2 activities showed that cordierites in high temperature and pressure assemblages were formed under fluid-saturated conditions over a wide range of H_2O/CO_2 ratios (Vry *et al.*, 1990; Kurepin, 2010).
In order to understand these mechanisms, several experimental studies on the solubility of volatile components in cordierite have been performed, in particular H_2O (Schreyer and Yoder 1964; Mirwald *et al.*, 1979, Harley and Carrington, 2001 among the others), CO_2 (Armbruster and Bloss, 1982, Armbruster, 1985; Le Breton and Schreyer, 1993), and mixed H_2O – CO_2 (Johannes and Schreyer 1981; Thompson *et al.*, 2001).

As a result of these studies, there is agreement that pressure exerts a stronger influence on the solubility of both H_2O and CO_2 than does temperature. Both H_2O and CO_2 contents slightly decrease with increasing temperature, while increasing pressure favors higher concentrations (*e.g.* Fig. 1, modified after Harley and Thompson, 2004). It is important to note that the maximum H_2O content obtained at 700 MPa is about 2.4 wt.%, which is close to the maximum theoretical value of 2.9 wt.% or 1 molecule per formula unit in the channel (Deer *et al.*, 2004). The maximum calculated value for CO_2 is about 2.2 wt.% (Deer *et al.*, 2004) corresponding to about 0.3 molecules per formula unit.

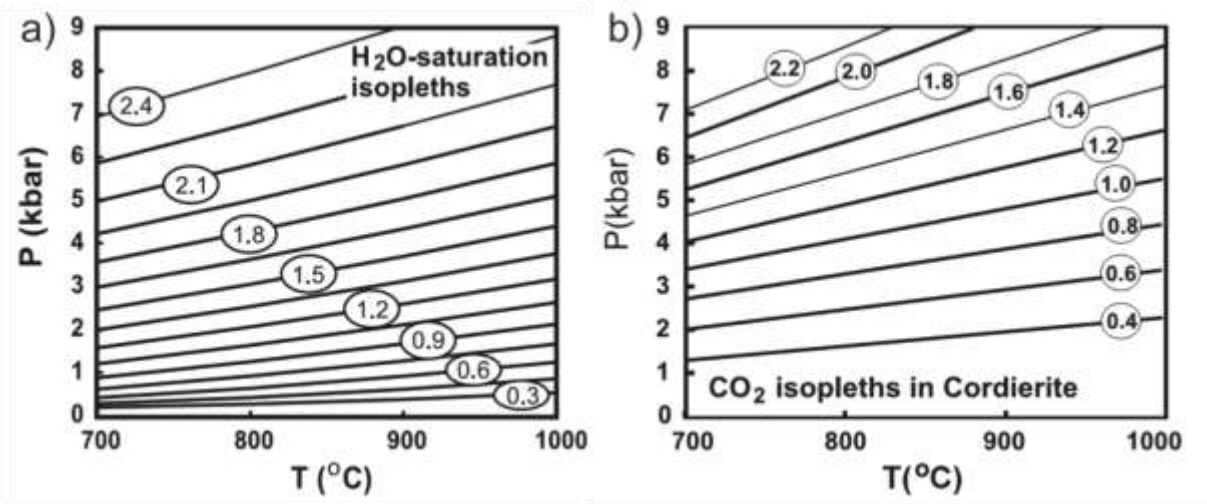

Figure 1 – (a) Pressure – temperature phase diagram of the isopleths of H_2O (expressed in wt.%) for X_{Mg} = 0.75 cordierite coexisting with pure H_2O fluid, as calculated by Harley and Carrington (2001); (b) isopleths of CO_2 (expressed in wt.%) for X_{Mg} = 0.80 cordierite in a pure fluid after Thompson *et al.*, (2001) and Harley *et al.*, (2002).

Studies on X_{CO2}, where $X_{CO2} = CO_2/(CO_2+H_2O)$, partitioning between melt and cordierite have shown that H_2O tends to be incorporated preferentially into the cordierite structure, while CO_2 preferentially remains in the melt (Fig. 2b and Johannes and Schreyer,

1981). This behavior is only slightly changed at higher temperatures (Harley and Carrington, 2001), while X_{CO2} increases with increasing pressure, facilitating CO_2 uptake (Johannes and Schreyer, 1981). Moreover, increasing X_{CO2} decreases significantly the amount of H_2O+CO_2 diffused into the mineral. In particular, there is a decrease of H_2O (Fig. 2a) probably because the presence of CO_2 obstructs its diffusion to the channel ways. This behavior, which is observed also in natural samples (Vry *et al.*, 1990), can be explained by the configuration of the CO_2 molecule inside the channels. Another factor that decreases the total amount of diffused fluids is the alkali content within the structural channels (Johannes and Schreyer, 1981; Vry *et al.*, 1990). There is evidence suggesting that CO_2 (and possibly alkali cations) may act as plugs in the channel ways obstructing inward and outward molecule diffusion, drastically slowing down the time of degassing and re-equilibration in case of pressure drop (Johannes and Schreyer, 1981; Kalt, 2000). This behavior complicates the possibility to predict the diffused molecules coexisting with mixed H_2O and CO_2 fluids, although a theoretical approach has been attempted by Kurepin (2010).

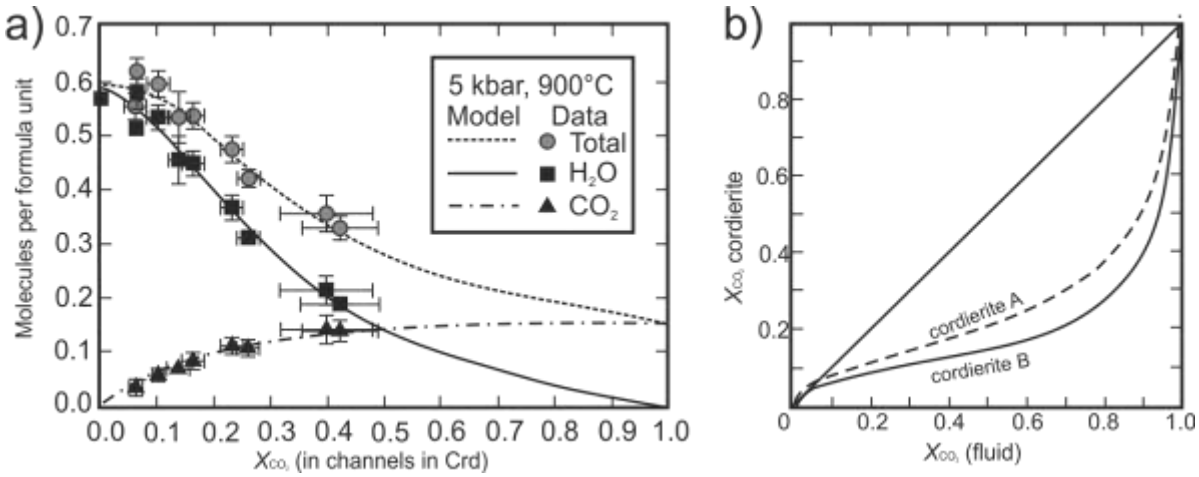

Figure 2 (a) variation of the volatile composition in cordierite (X_{Mg} = 0.68) channels with fluid-saturated, intermediate H_2O - CO_2 fluid composition. The lines show the calculated values at Thompson *et al.* (2001). Squares = H_2O, triangles = CO_2, circles = total number of molecules per formula unit (modified after Thompson *et al.*, 2001). (b) partition curves showing X_{CO2} fractioning between cordierite and coexisting fluid at 500 MPa and 600°C fort two different synthetic cordierites A and B (modified after Johannes and Schreyer, 1981).

The experiments were performed with small cordierite grains as starting materials (about 200 µm in Armbruster and Bloss, 1982 and Armbruster, 1985; 125-250 µm in Thompson *et al.*, 2001) in order to maximize the surface-to-volume ratio, and were carried out for a long duration (up to a few weeks) in order to achieve fluid/mineral equilibration. However there is still no agreement on the results, among the different authors. For

instance, Johannes and Schreyer (1981) obtained different results as a function of different starting material (Fig. 2b) or grain size of cordierite, and Le Breton and Schreyer (1993) observed a nonlinear behavior of the CO_2 contents between 15 minutes to 3 weeks experimental runs. Major problems arise with CO_2 diffusion, because its "sluggish" nature delays or even prevents sample saturation. Thus, the study of the run products cannot be addressed by conventional bulk methods, such as coulometric titration (Armbruster and Bloss, 1982; Johannes and Schreyer, 1981) or powder FTIR spectroscopy (Vry *et al.*, 1990) or single spot micro-analytical techniques, such as SIMS (secondary ion mass spectrometry) (Thompson *et al.*, 2001), which do not allow characterizing the inhomogeneous distribution of the target element.

The aim of this work is to examine the interaction of cordierite single grains with a CO_2–rich fluid under different experimental *P*, *T* and *t* conditions and to determine the diffusion behavior of CO_2 within the crystals at controlled *P*-*T* conditions. In particular, we performed several short duration experiments on relatively large samples (max dimension 2 mm across) in order to observe the diffusion behavior of CO_2 in the early stages of the experiment. Along to cordierite, we investigated the behavior of isostructural beryl that is also known to trap significant amounts of H_2O and CO_2 inside its channels (*e.g.* Wood and Nassau, 1968). Differently from the used cordierite fragments, the beryl crystals had a perfect prismatic hexagonal habit that make easier the orientation of the crystal recovered after the run, and to evaluate the anisotropy of diffusion coefficients. Based on previous literature data, we expected neither saturation nor sample homogenization with respect the CO_2 content. Therefore we made extensive use of FPA imaging to preliminarily characterize the run products and to locate the single-spot analyses for quantitative measurements. Recent works on cordierite (Della Ventura *et al.*, 2009, 2012) and other microporous minerals of the haüyine-sodalite group (Bellatreccia *et al.*, 2009) or feldspathoids such as leucite (Della Ventura *et al.*, 2008) have shown that FTIR-imaging is crucial when dealing with volatile or channel constituents which may be strongly zoned across the samples. Moreover, several experimental studies (*e.g.* Zhang *et al.*, 2006; Watson and Baxter, 2007) have shown that growth imperfections and/or stress induced deformations may lead to preferential "fast–paths" complicating the diffusion behavior across apparently homogeneous crystals.

1.1 Cordierite and beryl: structural details

Cordierite is a framework alumino silicate with the ideal formula $(\square,Na)(Mg,Fe)_2Al_4Si_5O_{18}(\square,H_2O,CO_2)$ and a continuous solid solution between the Mg^{2+} end-member and the Fe^{2+} end-member (sekaninaite) exists (e.g. Černý *et al.*, 1997, Radica *et al.*, 2013). The cordierite framework can be described as a stacking of pseudo-hexagonal Si/Al layers of tetrahedra and mixed layers of tetrahedra and octahedra (Fig. 3a). Alkali cations such as Na, K, Ca, and molecules such as H_2O and CO_2 may be allotted within the resulting pseudo-hexagonal channel, occupying sites on the c axis at the height of the narrow "bottle necks" for Na, and of the large cavities for H_2O and CO_2 (Gibbs, 1966, Hochella *et al.*, 1979; Malcherek *et al.*, 2001; Yakubovich *et al.*, 2004).

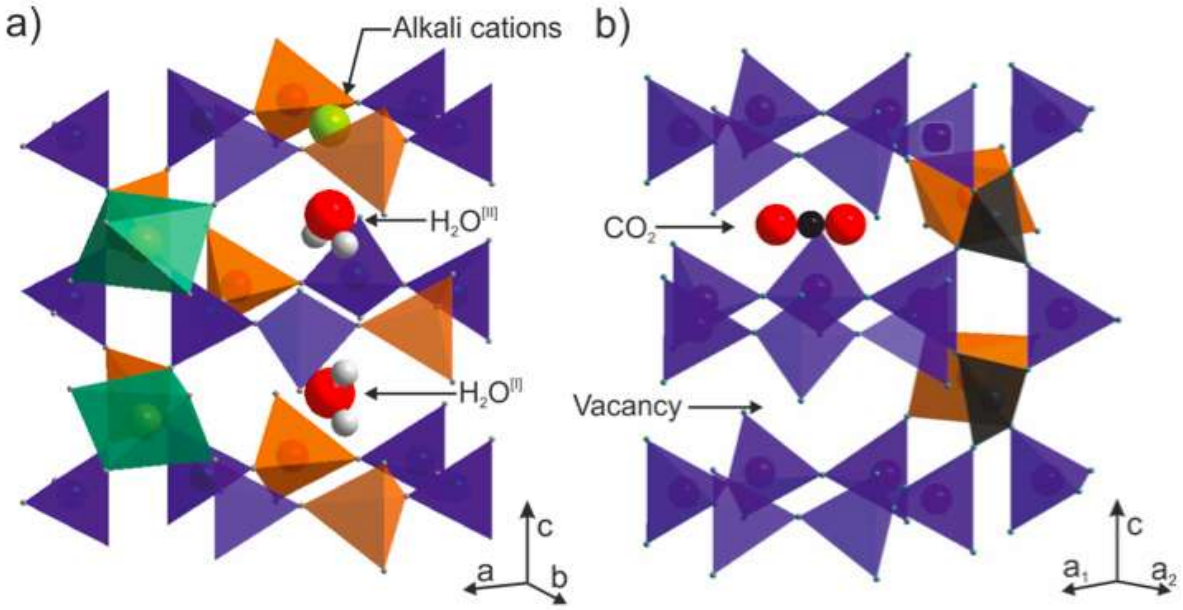

Figure 3 - Schematic view of a portion of the cordierite (a) and beryl (b) structures emphasizing the channels parallel the *c* axis. Si-containing tetrahedra are shown in blue, Al in tetrahedral and octahedral coordination is shown in orange, Be- containing distorted tetrahedra in dark gray and Mg-octahedra in dark green. The structural position of the channel alkali cations, both orientation types of H_2O and CO_2 are shown (modified after Radica *et al.*, 2013)

Beryl (ideal formula $(\square,Na)Be_3Al_2Si_6O_{18}(\square,H_2O,CO_2)$ is isostructural with cordierite (Fig. 3b). Its framework is constituted by 6-fold Si-centered tetrahedral rings stacked along the c axis. The hexagonal rings are interconnected parallel to [001] by distorted Be-centered tetrahedra. Al occupies the octahedral sites (Gibbs *et al.*, 1968). Beryl also has structural

channels running along the *c* axis that can contain alkali cations and volatile molecules (Wood and Nassau, 1968).

Extra-framework H_2O groups occur in the structural channels with the molecular plane parallel to (100). In both cordierite and beryl H_2O can be oriented in two different ways: type I H_2O (hereafter $H_2O^{[I]}$) has its H–H vector oriented parallel to the *c* axis, and type II H_2O ($H_2O^{[II]}$) has its H–H vector normal to the c axis (parallel to the *b* axis in cordierite). H_2O groups of the latter type are locally associated with channel cations (Goldmann *et al.*, 1977; Hawthorne and Černý, 1977). Winkler *et al.* (1994) proposed that $H_2O^{[I]}$ in synthetic Mg-cordierite is rotationally disordered about [001] and that a purely static description is inappropriate to describe its behavior in the channel cavity. They proposed a model whereby the H...H vector remains parallel to [001] and the H_2O molecule rotates in two different positions about its center of mass with an estimated hopping time of about 6 picoseconds at room temperature; this feature however cannot be observed by using FTIR spectroscopy. The linear CO_2 molecules are systematically oriented normal to the c axis and parallel to the crystallographic *a* axis for cordierite (Aines and Rossman, 1984;Kolesov and Geiger, 2000; Khomenko and Langer, 2005).

The molecular dimension of H_2O is 2.8 X 3.2 X 3.7 Å and CO_2 is 2.8 X 2.8 X 5.0 Å (Wood and Nassau, 1968). However the CO_2 molecule barely fits inside the cage, so once inside it tends to be wedged to the structure behaving as a “plug” (Aines and Rosmann, 1984; Vry *et al.*, 1990). On the opposite, the smaller H_2O polar molecules are bonded to the structure mainly by electrostatic interactions with the structural oxygens ($H_2O^{[I]}$) and alkali cations ($H_2O^{[II]}$).

The maximum H_2O and CO_2 content in both cordierite and beryl is constrained by the available space in the channels that corresponds roughly to 1 molecule per formula unit (about 2.5 - 2.9 wt% of H_2O or about 6.9 - 7.1 wt% of CO_2; Deer *et al.*, 2004). While the theoretical maximum water content has been observed in nature for both minerals (2.90 wt%, in a cordierite-biotite gneiss: Fediuk, 1971; 2.68 wt.% in a pegmatite beryl: Erämetsä *et al.*, 1973), the highest CO_2 contents so far recorded of only 1.97 wt. % (0.26 molecules p.f.u.) was observed for a cordierite occurring in a granulite from Cauchon Lake (Vry *et al.*, 1990). Cordierites with high CO_2 and CO are typically found in granulitic facies rocks, while in amphibolite facies H_2O specimens prevails (Zimmerman, 1981).

2. Experimental and analytical procedure

2.1 Starting materials

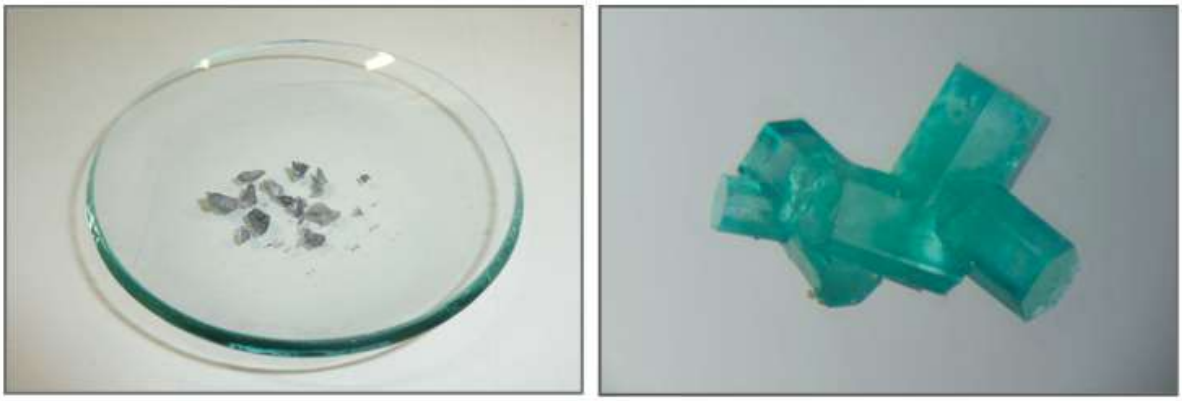

Figure 4 - (left) Fragments of the cordierite sample RP 7344 from Karur, India and (right) a cluster of green synthetic beryls (photo courtesy of Roberto Pucci).

For the experiments described here, cordierite RP 7344 (Fig. 4 left) from Karur, Tamil Nadu (India) were used as starting material; the crystals were provided by Mr. Renato Pagano. The fragments are clear and inclusion-free, with a color from pale blue-violet with yellow nuances, typical of its pleochroic nature. The sample composition, crystal-chemical formula, cell parameters, density and optical properties of this sample can be found in Della Ventura *et. al.* (2012) and are reported In Table 1 for simplicity. Chemical data collected over three analytical points.

Fe^{tot} was considered as Fe^{2+} allotted in the octahedral sites. However we remark that some Fe^{2+} can be also present in the tetrahedral site (Geiger *et al.*, 2000). The chemical formula, based on 18 oxygen atoms p.f.u. is $Na_{0.08}(Mg_{1.98}Fe_{0.09})Al_{3.93}Si_5O_{18}\cdot 0.51H_2O\cdot 0.03CO_2$; due to the very high magnesium number (X_{Mg} = 95.6%) the selected sample can be considered as a Mg end-member of the Mg-Fe cordierite series. Untreated cordierite presents significant H_2O and very low CO_2. Preliminary FTIR analysis confirmed an homogeneous distribution of H_2O and CO_2 across the sample (Della Ventura *et. al.*, 2012) and showed that water is mostly present as $H_2O^{[II]}$ because of the high Na contents in the structural channels (Della Ventura *et. al.*, 2012).

Table 1 - Microchemical analysis, crystal-chemical formula, cell parameters, density and optical properties for the cordierite (from Della Ventura *et. al.*, 2012) and beryl samples (from Bellatreccia *et al.*, 2008) used for the experiments. The beryl density was recalculated on the basis of the composition and cell parameters. Crystal-chemical formulae were recalculated based on 18 oxygen atoms p.f.u. for cordierite and 36 oxygen atoms p.f.u. for beryl.

	Cordierite	St. Dev.		Beryl	St. Dev.
Chemical analysis (wt.%)					
SiO_2	49.65	0.05	**SiO_2**	65.91	0.49
Al_2O_3	33.11	0.37	**TiO_2**	0.04	0.05
MgO	13.20	0.25	**Al_2O_3**	18.80	0.23
FeO	1.06	0.10	**Cr_2O_3**	1.77	0.44
TiO_2	0.02	0.04	**MgO**	0.02	0.02
MnO	0.01	0.00	**FeO**	0.02	0.02
CaO	0.02	0.02	**ZnO**	0.04	0.06
Na_2O	0.43	0.04	**BeO**	13.95	0.06
K_2O	0.01	0.01	**Na_2O**	0.06	0.02
H_2O	1.52	0.02	**K_2O**	0.06	0.02
CO_2	0.22	0.02	**F**	0.12	0.09
Total	99.25		**Total**	100.79	0.53
Crystal chemical formula (apfu)					
Si	4.996		**Si**	11.802	
Al	3.926		**Al^{IV}**	0.198	
Σ Tetrahedra	8.922		**Be**	6.000	
Mg	1.979		**Σ Tetrahedra**	18.000	
Fe	0.089		**Ti**	0.002	
Ti	0.002		**Al^{VI}**	3.770	
Mn	0.001		**Cr**	0.252	
Σ Octahedra	2.071		**Mg**	0.005	
Ca	0.003		**Fe**	0.003	
Na	0.084		**Zn**	0.005	
K	0.001		**Σ Octahedra**	4.037	
Σ Channels	0.087		**Na**	0.010	
n(H_2O)	0.510		**K**	0.012	
m(CO_2)	0.031		**Σ Channels**	0.022	
Σ Volatiles	0.541		**F**	0.065	
****$H_2O^{[II]}$**	0.335				
****$H_2O^{[I]}$**	0.175				
$X_{crd}CO_2$	0.06				
Cell parameters (Å)			**Cell parameters (Å)**		
a	17.020(1)		***a***	9.2264(25)	
b	9.751(1)		***c***	9.1904(2)	
c	9.380(1)		***c/a***	0.9961	
Densitiy (g/cm^3)	2.577(1)		**Densitiy (g/cm^3)**	2.657(1)	
Optic sign	Negative		**Optic sign**	Negative	
2Vx (°)	63.15(8)				

Beryl samples are part of the very first Li_2O and MoO_3 flux-grown synthetic emeralds, made by P.G. Hautefueille and A. Perrey in 1888 in Paris (Bellatreccia *et al.*, 2008) and currently kept in the mineralogical collection of the Muséum National d'Histoire Naturelle, Paris. The crystals were obtained after 15 days of growth at 800°C, because higher temperatures lead to formation of phenakite (Hautefeuille and Perrey, 1888, 1890). Beryl

crystals show a perfect prismatic hexagonal habitus with a maximum length of 1 mm and width of 0.5 mm (Bellatreccia *et al.*, 2008).

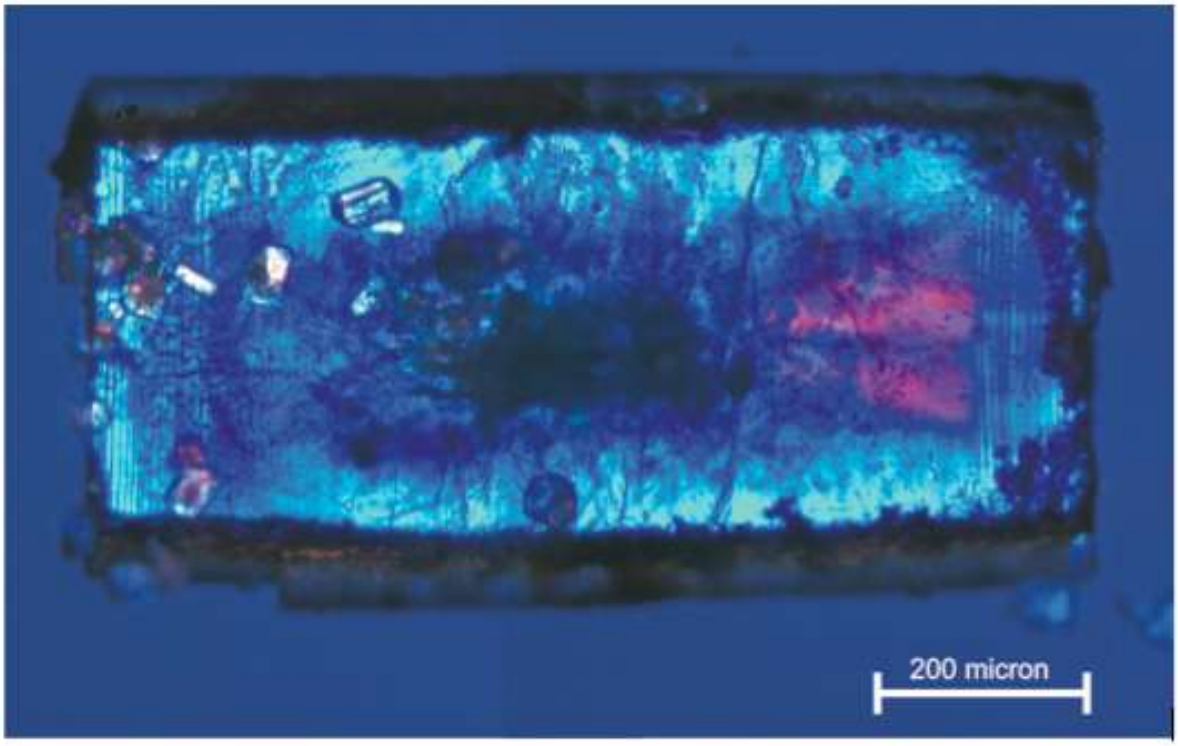

Figure 5 – Crossed polarizers optical microscope picture of a 1 mm long and 0.2 mm wide, double-polished beryl slab (Pa_340 d bis). The dark part at the center of the grain consists of molybdenum inclusions (Bellatreccia *et al.*, 2008). Tiny inclusions, remnants of the natural beryl seeds used for the synthesis are observable at the left side.

The used batch consists of fairly large (max. dimensions 1 mm X 0.5 mm) emerald-green hexagonal prismatic beryls. Close examination of these samples reveals the presence of tiny dark inclusions (EDS spectra indicates the presence of molybdenum, Bellatreccia *et al.*. 2008) and beryl seeds within the grains (Fig. 5). Cracks may occasionally be present.

A crystal-chemical study for these beryls is reported in Bellatreccia *et al.* (2008) and data are summarized in Table 1. Chemical data collected over six analytical points. The crystal-chemical formula (Be calculated by stoichiometry) based on 36 oxygen atoms p.f.u. is $Na_{0.02}K_{0.01}(Al_{3.77}Cr_{0.23})Be_6Al_{0.18}Si_{11.82}O_{36}\cdot F_{0.12}$ (Bellatreccia *et al.*, 2008). Octahedral Al was calculated as: $Al^{VI} = Al^{tot} – Al^{IV}$ where $Al^{IV} = 12 – Si$ (all elements in apfu), *i.e.* assuming that all aluminum exceeding the amount needed to fill the tetrahedral rings is allotted to the octahedral sites. The final composition is close to the stoichiometric composition except for the Cr_2O_3 content which ranges from 1.45 to 2.95 wt.%, the Cr being responsible for the characteristic emerald green color. The c/a ratio of 0.9961 (Bellatreccia *et al.*, 2008) is typical

of normal-type beryls (Aurisicchio *et al.*, 1988) characterized by the substitution of $Al^{3+} \rightarrow Me^{2+}$ at the octahedral site. Normal beryls usually compensates the charge unbalance with alkali cations inside the structural channels and may show both type of water where the $H_2O^{[II]}$/ $H_2O^{[I]}$ ratio depends on the Na in the channels (Aurisicchio *et al.*, 1994). Following the classification proposed by Hawthorne and Černý (1977), the studied synthetic beryl may be considered as "alkali-free beryl" (total alkali ≤ 0.1 Wt.%), with a composition similar to those occurring inside vugs of predominantly graphic pegmatites and schlieren and pocket-type bodies in granites.

As expected, preliminary FTIR single-crystal unpolarized spectra of untreated samples showed no CO_2 related absorptions at around 2360 cm^{-1}, however small traces of H_2O, indicated by the weak absorptions at 3643 and 3587 cm^{-1}, are present (Fig. 6).

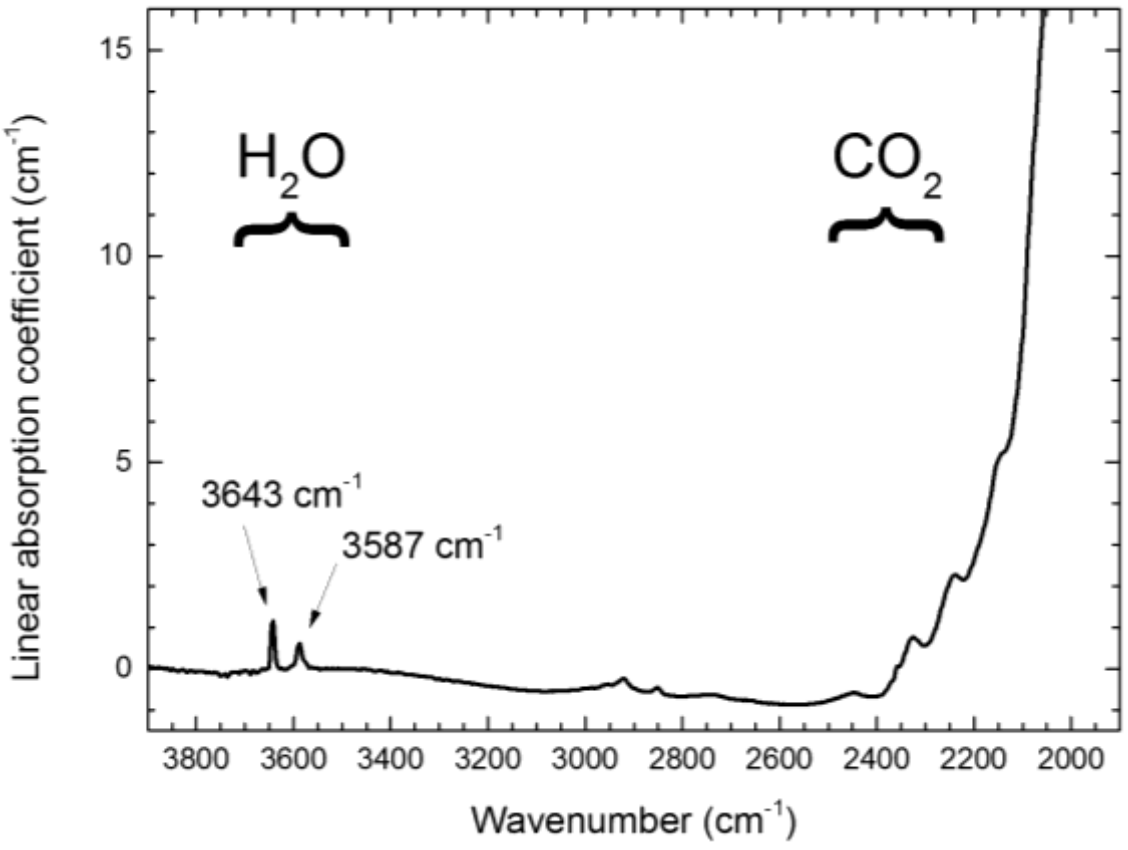

Figure 6 - Unpolarized single-crystal FTIR spectrum of untreated beryl Pa340. The regions corresponding to the stretching vibrations modes of CO_2 and H_2O are indicated in brackets. No CO_2 related absorptions at around 2360 cm^{-1} are present. Small traces of H_2O are indicated by the weak absorptions at 3643 and 3587 cm^{-1}.

2.2 Experimental procedure

Several cordierite fragments with size ranging from 1.5 to 0.2 mm were separated from a large single crystal. Before the experiments the fragments were blown through an abrasive cylinder to remove sharp edges and then the grains were pre-treated at 1250 °C for 24 hour in order to remove all H_2O and CO_2 from the sample (Chapter 3). Grains showed no evident variation in color or clarity, however cracking of larger grains occurred during the heat-treatment.

The experiments were carried in 3 x 9 mm Pt capsules; silver carbonate was used as a CO_2 source to saturate the system with carbon dioxide during HT/HP treatment. As a matter of fact Ag_2CO_3 decomposes according to the $2Ag_2CO_3 \rightarrow 2Ag_2O + 2CO_2$ reaction at 210 °C, yielding a theoretical CO_2 content ≈16 wt.%. Al_2O_3 powder (Al_2O_3 = 99.72 wt.%, SiO_2 = 0.07 wt.%, others = 0.21 wt.%) was mixed in 1 to 1 ratio by wt. with Ag_2CO_3, and added to the charge. The aluminum oxide powder was used to prevent the contact between the crystals and the capsule walls after the silver carbonate disappearance due to its decomposition. Layers of Ag_2CO_3/Al_2O_3 mix were alternated to layers of starting crystals (Fig. 7a). Explorative runs were performed to check different setups (Tab. 2, experiments QP1-12, QP1-14 and QP1-15); these trials lead to capsule failure. Capsules containing both beryl and cordierite or exclusively beryl or cordierite (Tab. 2) were prepared; each capsule contained from 4 to 7 grains, for a total crystal weight of about 2 to 10 milligram of sample. All components used to prepare the tubes were dried up at 110 °C in order to avoid water contamination. The capsules were crimped and welded on both sides. After each run the capsule, if possible, was pierced to check the presence of CO_2 in excess.

Table 2 - Experimental conditions and set up.

Code experiment	Set up	Sample	Mineral	Temperature (°C)	Pressure (MPa)	Time	Note
QP1-12	QP 25	Crd_pr 1	Cordierite	750	200	4	Al_2O_3 and Ag_2CO_3 not mixed
"	QP 25	Crd_pr 2	Cordierite	750	200	4	"
"	QP 25	Crd_pr 3	Cordierite	750	200	4	"
"	QP 25	Crd_pr 4	Cordierite	750	200	4	Ag_2CO_3 only
QP1-13	QP 19-25	Crd_pr 5	Cordierite	900	200	24	
QP1-14	QP 19-25	Crd_pr 6	Cordierite	900	200	42	Ag_2CO_3/Al_2O_3 = 2/1
QP1-15	QP 19-25	Crd_pr 7	Cordierite	900	250	4	Failed

QP1-22	QP 19-25	Crd_pr 8	Cordierite	800	150	48	
QP1-23	QP 19-25	Crd_pr 9	Cordierite	800	200	24	
QP34-50	QP 19	Crd_pr 10	Cordierite	800	500	43	
QP1-26	QP 25	Crd_pr 12	Cordierite	700	200	24	
"	QP 25	Pa_340 b	Beryl	700	200	24	
QP1-25	QP 25	Crd_pr 13	Cordierite	700	200	2	
"	QP 25	Pa_340 a	Beryl	700	200	2	
QP34-52	QP 19	Crd_pr 14	Cordierite	900	500	4<t<20	
QP34-53	QP 19	Crd_pr 15	Cordierite	900	500	1	
QP1-32	QP 19-25	Pa_340 c	Beryl	900	220	24	
QP34-55	QP 19	Crd_pr 16	Cordierite	700	500	24	
QP34-56	QP 19	Crd_pr 17	Cordierite	900	500	24	
QP34-59	QP 19	Crd_pr 18	Cordierite	800	350	24	
QP34-60	QP 19	Crd_pr 19	Cordierite	800	500	24	
QP34-57	QP 19	Pa_340 d	Beryl	700	500	24	
QP34-58	QP 19	Pa_340 e	Beryl	900	500	24	
QP1-45	QP 19-25	Pa_340 f	Beryl	900	200	72	
QP1-61	QP 19	Pa_340 g	Beryl	900	500	24	
QP1-67	QP 19	Crd_pr 20	Cordierite	800	500	48	
QP1-49	QP 25	Crd_pr 22/Pa_340 h	Cordierite/Beryl	800	200	20	Rerun
"	QP 25	Crd_pr 25/Pa_340 k	Cordierite/Beryl	800	200	20	Rerun
QP34-68	QP 19	Crd_pr 23/Pa_340 i	Cordierite/Beryl	800	500	24	
QP34-69	QP 19	Crd_pr 24/PA_340 J	Cordierite/Beryl	800	500	24	
QP34-70	QP 19	Crd_pr 29/Pa_340 o	Cordierite/Beryl	800	700	10	
QP34-71	QP 19	Crd_pr 27/Pa_340 m	Cordierite/Beryl	800	700	48	
QP1-53	QP 25	Crd_pr 26/Pa_340 l	Cordierite/Beryl	800	200	24	
"	QP 25	Crd_pr 30/Pa_340 p	Cordierite/Beryl	800	200	24	
QP1-54	QP 19-25	Crd_pr 28/Pa_340 n	Cordierite/Beryl	800	200	48	
QP34-72	QP 19	Crd_pr 31/Pa_340 q	Cordierite/Beryl	800	500	> 33	
QP34-74	QP 19	Crd_pr 32/Pa_340 r	Cordierite/Beryl	700	700	24	
QP34-75	QP 19	Crd_pr 33/Pa_340 s	Cordierite/Beryl	900	700	24	
QP34-77	QP 19	Crd_pr 34/Pa_340 t	Cordierite/Beryl	800	500	10	
QP1-78	QP 19	Crd_pr 21	Cordierite	700	500	24	
QP1-102	QP 19	Crd_pr 48/Pa_340 z	Cordierite/Beryl	800	700	24	

All experiments were performed using a non-end loaded piston cylinder apparatus (QUICKpress™ design by Depths of the Earth Co.) at the HP-HT Laboratory of Experimental Volcanology and Geophysics of Instituto Nazionale di Geofisica e Vulcanologia (INGV, Rome, Italy). Experiments were conducted using two different set-ups (Tab. 2): experiments coded QP34-xx were performed using a standard 19 mm assembly (Moore *et al.*, 2008) with an oxygen fugacity set at NNO +2 (Freda *et al.*, 2008, Masotta *et al.,* 2012a) and pressure ranging from 300 to 800 MPa. Experiments coded QP1-xx in a 19-25 and 25 mm assemblies with comparable oxygen fugacity and pressure ranging from 150 to 300 MPa; the 25 mm

assembly may accommodate up to 4 samples in a single run (Fig. 7b, modified after Masotta *et al.,* 2012b). We used a NaCl-Pyrex-Graphite-crushable-MgO–pyrex assembly with capsule surrounded by pyrex powder instead of pyrophyllite powder to avoid water infiltration. Temperature was controlled using a factory calibrated C-type ($W_{95}Re_5$ – $W_{74}Re_{26}$) thermocouple with a ±5 °C uncertainty (Holtz *et al.*, 2001). Error on pressure of ±25 MPa is associated with the piston cylinder NaCl calibration method (Baker, 2004, Masotta *et al.,* 2012b). Heating rates were set to 100 °C/min; the isobaric quenching rate ranged from 50 °C/s (25 mm assembly) to 100 °C/s (19 mm and 19-25 mm assembly) in the first 5 seconds (Masotta *et al.,* 2012b). Experiments were performed in the pressure range 200 – 700 MPa, temperature range 700 – 900 °C; run duration varied from 1 to 72 hours.

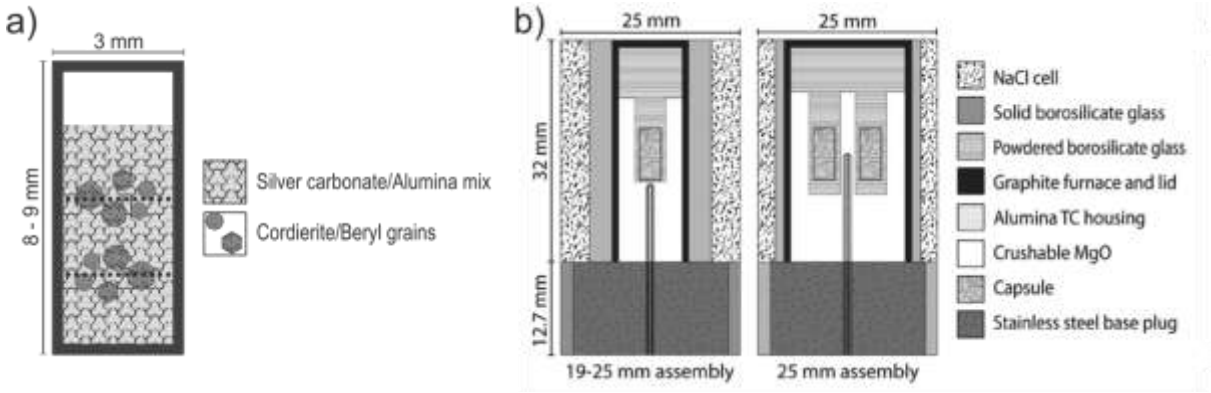

Figure 7 – (a) Schematic section of the layered crystal/filler assemblage within the capsule, (b) schematic cross section a 19-25 mm and 25 mm furnace assemblies (modified after Masotta *et al.*, 2012b).

2.3 Analytical methods

BSE-SEM images were collected at INGV using a field emission scanning electron microscope (FE-SEM) Jeol 6500F equipped with an energy-dispersive (EDS) detector. Samples were coated with Au before the analysis.

FTIR spectra were acquired using a Bruker™ Hyperion 3000 microscope equipped with a KBr-Broadband beamsplitter and a liquid nitrogen-cooled MCT detector at Laboratori Nazionali di Frascati-Istituto Nazionale di Fisica Nucleare (LNF-INFN,) Frascati (Rome). Polarized spectra were collected using a gold-wire-grid FTIR polarizer on a ZnSe substrate. The spot size was variable; a 15x objective and a conventional light source (Globar) was employed, with a nominal resolution of 4 cm^{-1} averaging 128 scans for both spectrum and background. The FTIR images were collected with the same device using a 64 x 64 pixel focal-

plane array (FPA) of liquid nitrogen-cooled MCT detectors. Using a 15x objective, each image covers an area of 170 µm x 170 µm with a nominal spatial resolution of ~5 µm (Della Ventura *et al.*, 2010, 2014). The nominal resolution was set at 4 cm^{-1} and 64 scans were averaged for each spectrum and background.

For polarized IR measurements, the cordierite samples were oriented on (010) using a polarizing microscope equipped with a spindle-stage; the program ExcalibrW (Bloss, 1981; Gunter *et al.*, 2005) was used to process the extinction data. Beryl samples were oriented (hk0) using the external hexagonal prismatic morphology. The oriented fragments were transferred to glass slides and doubly polished to thickness usually below 400 µm.

Sample thickness was checked using an electronic micrometer with ±5 µm uncertainty and double checked using the interference fringes in the FTIR spectra, based on the formula $t = 1/[2 \cdot n \cdot (\nu_1 - \nu_2)]$ where t is sample thickness in cm, n = 1.535 is the refractive index and $(\nu_1 - \nu_2)$ is the distance between two adjacent fringes in cm^{-1} (Pistorius and DeGrip, 2006). For some samples, thickness were also checked with a Leica DCM 3D optical profilometer at the Laboratorio Interdipartimentale di Microscopia Elettronica (LIME), Università Roma Tre. The nominal vertical resolution was less than 15 nm in confocal mode (20X lens, NA = 0.50) and less than 4 nm in interferometric mode (50X lens, NA = 0.50); sample thickness was averaged for the whole surface of the slab.

The CO_2 content of run samples were calculated from polarized FTIR spectra using the Beer-Lambert relationship, $C = (A \cdot k) /(t \cdot D \cdot \varepsilon)$, where ε_i (l mol^{-1} cm^{-2}) is the molar absorption coefficient, C (wt.%) is the concentration of the target molecule, A is the measured absorbance, t is the slab thickness in cm, D is the value of the sample density (g/cm^3) and *k* is a conversion factor needed to convert from wt% to $mol \cdot l^{-1}$; for CO_2, *k* = 4.401 (Della Ventura *et al.*, 2009, 2012). A was calculated as total integrated absorbance A_i (cm^{-1}) = $A_x + A_y + A_z$ for trimetric cordierite and A_i (cm^{-1}) = $2A_x + A_z$, for dimetric beryl, where A_x, A_y and A_z are the integrated absorptions along each polarization direction (Libowitzky and Rossman, 1996). The peak areas were obtained for each component using the data calculation routine built in the spectrometer software; the background was modeled as linear. Using this method, it is possible to quantify even few ppm of CO_2 in the channels (Della Ventura *et al.*, 2009). Integrated absorbance values were obtained for the principal ν_3 anti-symmetric stretching modes of CO_2 (Fig. 8) at 2348 cm^{-1} polarized for E//a for cordierite (Della Ventura *et al.*, 2009) and at 2360 cm^{-1} polarized for E⊥c for beryl (Charoy *et al.*, 1996).

The density was set at 2.577 g/cm^3 for cordierite (Sample RP 7344 in Della Ventura *et al.*, 2012) and 2.657 g/cm^3 for beryl (Tab. 1). The integrated molar absorption coefficients for cordierite, ε_{iCO2} = 19000±2000 was taken from Della Ventura *et al.* (2012), while for beryl ε_{iCO2} = 70000±7000 was recalculated after Charoy *et al.* (1996). The error σ_C associated with C was obtained using the classical statistics of error propagation (Bellatreccia *et al.*, 2005); the error on A is ~ 10% (Libowitzky and Rossman, 1997), the sample thickness uncertainty was ±5 µm, the standard deviation of the density (D) is 2%.

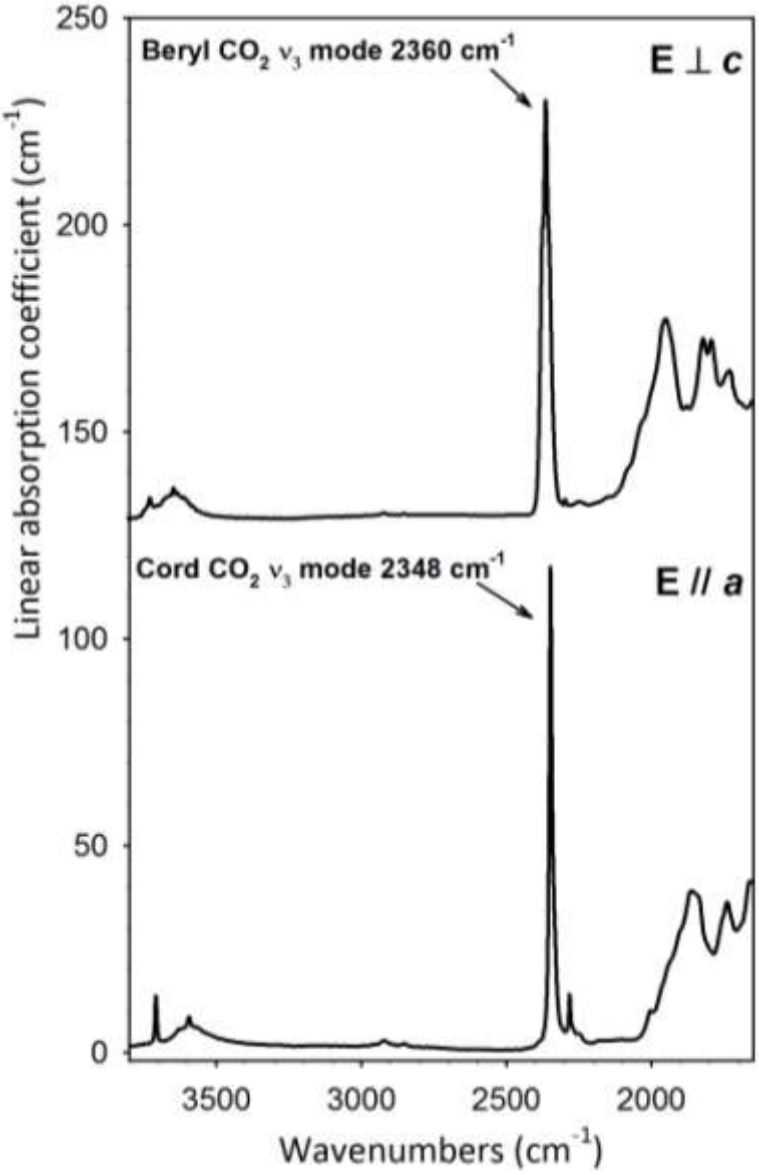

Figure 8 – FTIR polarized light spectra for E//a in a 130 µm thick cordierite slab, and E⊥c in a 153 µm thick beryl slab both treated at 700 MPa and 900 °C for 24 hour. Spectra scaled to sample thickness.

3. Results

3.1 Run products

After the run, the mineral grains were embedded in a fine white-grayish powder. XRD diffraction pattern of this powder revealed the presence of residual alumina (corundum) and metallic silver together with traces of silver carbonate/oxides.

Beryl grains usually presented a brown-red reaction/alteration coating of a few microns. This coating was not observed for shorter duration experiments. On the opposite, cordierite grains usually presented a very thin metallic coating around the edge and inside the major cracks. In Figure 9a, we present a crossed polars optical microscope image of a (010) cordierite section. Beside the very heterogonous aspect of the grain indicated by the interference colors, the sample shows several major cracks filled with a metallic material; in section the filling color ranges from a silver to a dark black tone. Two-hour treated cordierite also presented the same type of cracks, although the crack filling is incomplete (Fig. 9b). A closer examination of the slabs (especially near the edges of the grain) reveals a system of about 20 μm wide cracks oriented normally to the *c* crystallographic axis (dashed yellow square in Fig. 9c). BSE-SEM images showed in fact (top side of Fig. 9d) the presence of two systems of smaller cracks, one parallel to the larger cracks observed in optical microscopy, and a second system normal to the *c* axis. SEM-EDS spots revealed that the metallic filling is constituted mainly by Ag due to the Ag_2CO_3 added to the charge (Fig. 9e). Cordierite treated at 700° C did not show these micro-cracks at any pressure conditions and the grains were always very clear after the extraction. The beryl samples after the run presented some fracturing due to differential stress, but never presented any micro-cracking at any pressure and temperature.

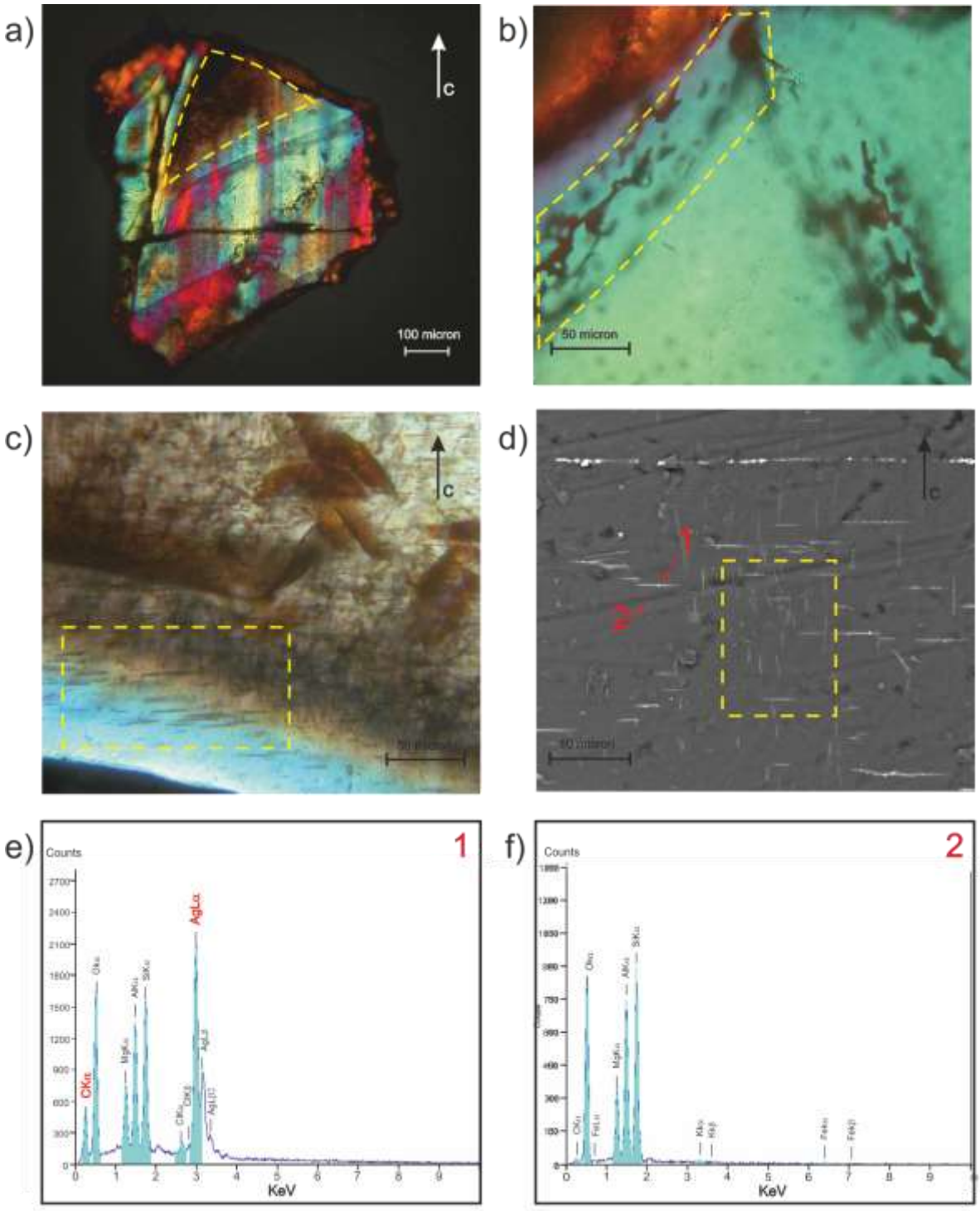

Figure 9 – (a) Crossed polars light (XPL) picture of a (010) 130 µm thick cordierite slab (Crd_pr 33, 700 Mpa, 900° C, 24 hours): in the top part of the sample there is a large brown area corresponding to a crack completely filled with silver/silver carbonate particles. (b) XPL picture of a (010) 127 µm thick cordierite slab (Crd_pr 13, 200 Mpa, 700° C, 2 hours): the highlighted area corresponds to a crack partially filled by Ag probably due to the short duration of the experiment. (c) XPL picture of a (010) 292 µm thick cordierite slab (Crd_pr 18, 350 Mpa, 800° C, 24 hours): the sample presents diffuse small cracks perpendicular to the c crystallographic direction (dashed yellow square). (d) BSE-SEM image of a (010) 110 µm thick cordierite slab (Crd_pr 5, 200 Mpa, 900° C, 24 hours showing additional systems of cracks 2 µm wide, perpendicular and parallel to the c axis, respectively (dashed yellow square). EDS spectra of (e) spot 1 (crack) and (f) spot 2 (cordierite) indicated in Figure 9d.

The formation of these systems of micro-fractures may be due to the different response of beryl and cordierite to thermal shocks. Hochella and Brown (1986) observed that, during heating, the channel structure of cordierite contracts along the *c* axis due to a twisting of the tetrahedral framework, partially driven by the octahedral site expansion along the *a* and *b* axis (see also Khosrovani and Sleight, 1999). This mechanism is enhanced for high X_{Mg}, as it is the case of the samples studied here (Tab. 1 and solid line in Fig. 10a). On the opposite, the thermal expansion of the Be tetrahedra and Al octahedra in beryl is less pronounced than in cordierite, and this prevents the shortening along the *c* axis. Indeed Morosin (1972) observed that a small degree of $Cr^{3+} \rightarrow Al^{3+}$ substitution, as in emeralds, causes expansion in both *a* and *c* axis (dashed line Fig. 10b).

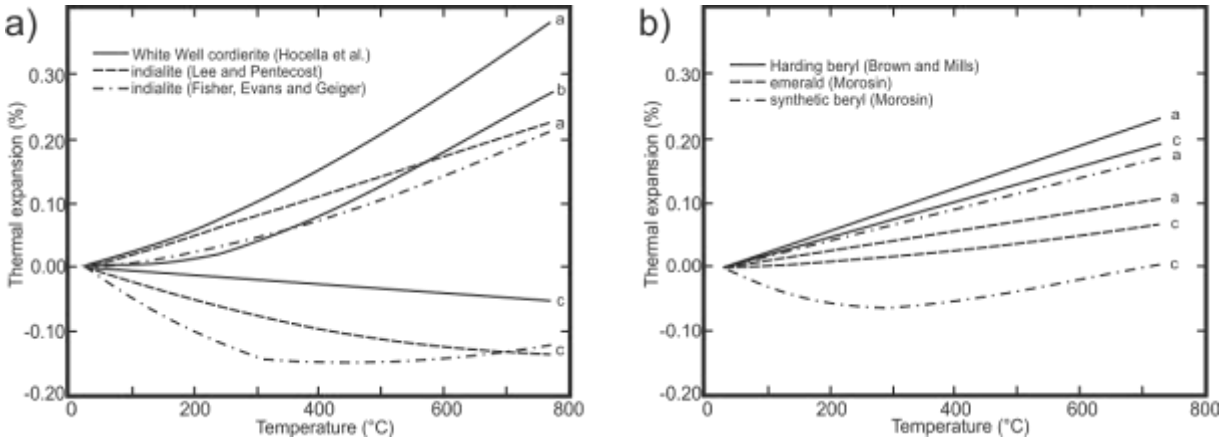

Figure 10 – Selected thermal expansion curves for cordierite and indialite (a), and for beryl and emerald (b) (from Hochella and Brown, 1986). The White Well cordierite (Fig 10a, solid lines) is a natural almost Mg end-member containing alkali cations in the channels with a composition similar to our starting sample. The gem quality beryl curve (Fig 10b, dashed lines) contains small amounts of Cr.

The set of fractures parallel to the *c* crystallographic direction along the (010) and (100) cleavage planes may be due to the thermal expansion along the *a* and *b* crystallographic directions. On the other hand, the set of micro-cracks oriented normal to the *c* crystallographic axis may be caused by the local stress caused by contraction along the *c* axis. When this stress overrides the lattice strength, probably for $T > 700$ °C, an extension fracture occurs along the (001) cleavage plain (Coulomb, 1776). The presence of cracking is random, and is not preferentially related to specific *T* or *P* conditions. This process may be favored by the fluid circulation inside the cracks; in our case, the fluid circulation is witnessed by the silver carbonate filling the voids. This is a notable point to consider: the fact that the cracks are filled by Ag indicates that they developed during the experiment, and not

as a consequence of the decompression at the end of the run. One may argue that in such a case the cracks could have provided a favorable path for the CO_2 diffusion across the sample. However, considering that the fractures are all filled by Ag, we consider this possibility as unlikely. In addition, we note that only cordierite is affected by this phenomenon, while beryl did not show any evidence of cracking. In the following, the diffusion coefficients that will be discussed were obtained mostly on the beryl samples.

3.2 CO_2 diffusion in cordierite and beryl: preliminary considerations

The main problem in experimental studies on CO_2 (as well as H_2O) diffusion in minerals is the difficulty to quantify the amount of carbon dioxide (and hydrogen) but also its distribution within the matrix. Carbon can be quantitatively analyzed only using SIMS; besides the non-easy access to this facility, few SIMS laboratories are equipped to work with this element, the analysis of which requires non-conventional cautions and standardization. In addition, as already shown by Della Ventura *et al.* (2009, 2012) and Bellatreccia *et al.* (2009) in microporous minerals, CO_2 is frequently zoned, and the lack of the zoning patterns may significantly alter the data and their interpretation. Preliminary FTIR-FPA imaging for CO_2 revealed an extreme heterogeneity in carbon dioxide concentrations across the crystals, thus each sample was carefully examined by FPA to locate the area suitable for analytical spots (Fig. 11).

Selected FPA images are given in Figure 11. The interpretation of those relative to beryl (Fig 11c, 11d) is much easier due to the well-developed morphology of the samples; it is evident that the CO_2 diffusion proceeds exclusively from the basal (001) pinacoids through the crystal, following the structural channel. A similarly observation was reported by Fukuda *et al.* (2009) for H_2O diffusion in beryl. For cordierite, due to the strongly irregular shape of the grains, the interpretation of the images given in Figures 11a and 11b is less straightforward. Considering that cordierite is isostructural with beryl, however, it is likely that also in this case the CO_2 diffusion proceeds along the channels parallel to the *c* crystallographic direction (see also Chapter 3). Figure 11b, in particular, shows the strong enhancement of the CO_2 diffusion along a cracks well evident in the center of the grain. An additional source of uncertainty, for cordierite, is the fact that, under high *T* and P_{H2O} conditions, it has the strong tendency to give reaction rims (*e.g.* Deer *et al.*, 2004) typically

consisting of clay-like products (pinite). In such a case, a possible negative effect (a kind of plug effect) on the CO_2 diffusion could result. In the system studied here, however, this problem is minimized because the experimental system was very poor in H_2O; we did not examined by EMPA the rims of the crystals after the experiments, however optical observations did not show any presence of reaction products.

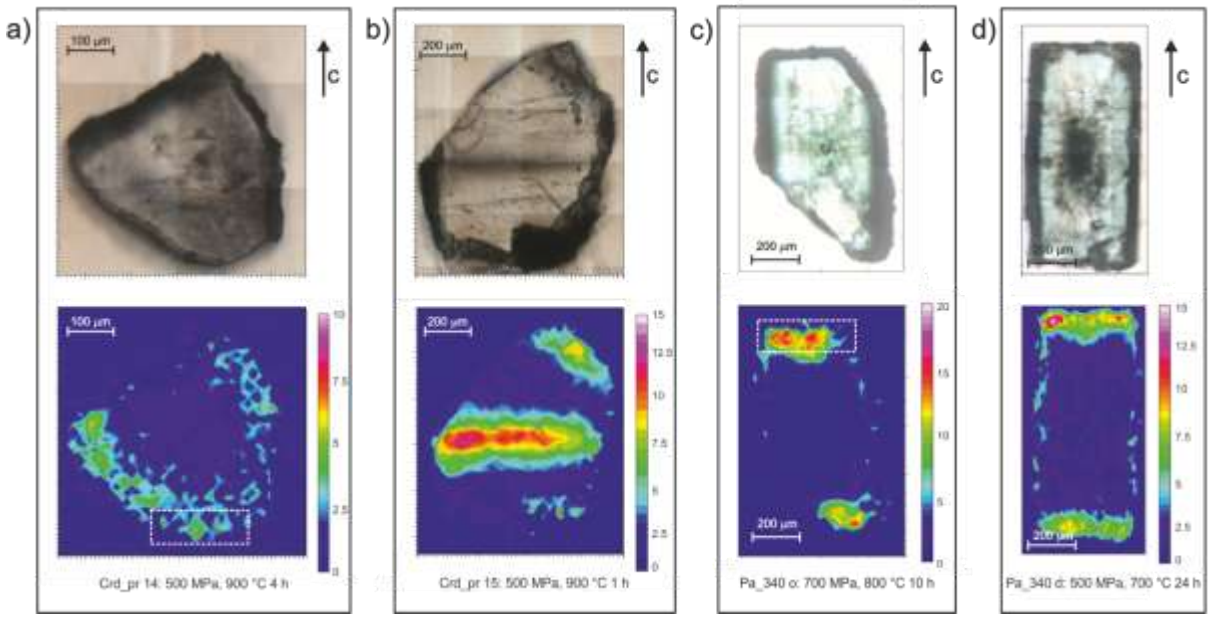

Figure 11 – Optical images and FTIR-FPA contour maps of CO_2 distribution in selected cordierite and beryl sections: (a) cordierite Crd_pr 14 (010) section, (b) cordierite Crd_pr 15 (010) section, (c) Beryl Pa_340 o (hk0) section and (d) Pa_340 d_bis (hk0) section. Experimental conditions are given. Chromatic scale is proportional to CO_2 content.

All samples recovered after the experiments were previously examined by FTIR imaging, and on the basis of the results we located the most suitable area for the analytical spot, usually on the first 20/30 µm from the edge. We carefully avoided measurements spots close to fractures (see below). In the case of controversial data, detailed IR transects were performed; the beam size was kept as small as possible, usually at 20x20 μm^2 and the highest absorbance values were selected as representative of the CO_2 content of the sample.

3.3 CO_2 contents

The maximum CO_2 contents (in ppm) measured in the experimental samples, considering the above considerations, are summarized in Table 3 for cordierite and Table 4 for beryl. Slab thickness and the experimental conditions are also given. Samples from the

same capsule prepared multiple times are indicated with brackets. Measurements indicated with F were performed on fractures in order to compare the fracture contents with those at the grain edges. The presence of brown-red coating (RC) in beryls and Ag crack filling (HF, SF) in cordierite is also reported. Failed capsule featuring pale white solid filling are indicated with WM.

Table 3 – CO_2 contents (in ppm) obtained for the studied cordierites. Integration range 2300-2400 cm^{-1}, ε_i=19000±2000. Sample thickness estimated standard error (ESE) is reported in brackets. Sample thicknesses with ESE = ±5 µm were obtained using an electronic micrometer, sample thicknesses with ESE < ±5 µm were obtained using the optical profilometer. F = analytical spot on fracture, HF = Heavy filled cracks , SF = Slightly filled cracks, WM = White solid mass, 1 = grain with diffuse fracturing, 2 = calculation performed on unpolarized FTIR spectrum.

Sample	Thickness	Pressure (MPa)	Temperature (°C)	Time (h)	Maximum measured CO_2 concentration (ppm)	σConcentration CO_2(ppm)	Note
Crd_pr 5	153 (5)	200	900	24	316	49	HF
Crd_pr 8	152 (5)	200	800	48	237	36	SF
Crd_pr 12 (F)	171 (5)	200	700	24	388	59	SF, F
Crd_pr 12	171 (5)	200	700	24	146	22	SS
Crd_pr 13	127 (5)	200	700	2	142	22	
Crd_pr 14	110 (5)	500	900	4<t<20	334	52	SF
Crd_pr 15	241 (5)	500	900	1	111	17	
Crd_pr 15 (F)	241 (5)	500	900	1	1455	221	F
Crd_pr 16	196 (5)	500	700	24	187	28	SF
Crd_pr 17	224 (1)	500	900	24	405	61	HF
Crd_pr 18 (F)	292 (2)	350	800	24	476	72	SF, F
Crd_pr 18	292 (5)	350	800	24	268	40	SF
Crd_pr 19 (F)	324 (1)	500	800	24	928	139	SF, F
Crd_pr 19	324 (1)	500	800	24	307	46	SF
Crd_pr 20	84 (5)	500	800	48	405	65	HF
Crd_pr 22 (F)	185 (5)	200	800	20	1346	205	1, WM
Crd_pr 25 (F)	237 (5)	200	800	20	1017	154	1
Crd_pr 23 (F)	140 (5)	500	800	24	936	145	HF, F
Crd_pr 23	140 (5)	500	800	24	425	66	HF
Crd_pr 24	90 (5)	500	800	24	418	67	HF
Crd_pr 29 (F)	175 (5)	700	800	10	2419	370	SF, F
Crd_pr 29	175 (5)	700	800	10	939	144	SF
Crd_pr 27	99 (5)	700	800	48	308	49	WM
Crd_pr 26	81 (5)	200	800	24	158	26	WM
Crd_pr 30	198 (5)	200	800	24	285	43	HF
Crd_pr 28	160 (5)	200	800	48	364	56	WM
Crd_pr 31 (bis)	75 (5)	500	800	> 33	4449	731	F, WM
Crd_pr 32 (bis)	53 (5)	700	700	24	1022	181	
Crd_pr 33	130 (5)	700	900	24	1622	252	HF

Crd_pr 33 (F)	130 (5)	700	900	24	2834	440	HF, F
Crd_pr 34	95 (5)	500	800	10	438	70	SF
Crd_pr 34 (F)	95 (5)	500	800	10	2102	335	SF, F
Crd_pr 48	108 (5)	700	800	24	885	139	HF
Crd_pr 48 (F)	108 (5)	700	800	24	2766	435	HF, F
Crd_pr 21	88 (5)	500	700	24	183	29	SF

Table 4 –CO_2 content (in ppm) measured for the studied beryl samples. Integration range 2300-2406 cm^{-1}, ε_i=70000±7000. Estimated standard error (ESE) on sample thickness is reported in brackets. Sample thicknesses with ESE = ±5 µm were obtained using an electronic micrometer, sample thicknesses with ESE < ±5 µm were obtained using the optical profilometer. F = analytical spot on fracture, RC = Reddish Coating, WM = White solid mass, 1 = eroded grain edge.

Sample name	Thickness (µm)	Pressure (MPa)	Temperature (°C)	Time (h)	Maximum measured CO_2 concentration (ppm)	σConcentration CO_2(ppm)	Note
Pa_340 a	243.2 (0.6)	200	700	2	65	9	
Pa_340 b	194.5 (0.7)	200	700	24	82	12	
Pa_340 c (340)	92 (2)	200	900	24	69	10	
Pa_340 c (88)	101.2 (0.4)	200	900	24	72	11	
Pa_340 c (380)	380 (5)	200	900	24	80	12	
Pa_340 d (bis)	125 (5)	500	700	24	699	106	RC
Pa_340 e (bis)	101 (1)	500	900	24	829	122	RC
Pa_340 f	252 (5)	200	900	72	89	13	
Pa_340 g (bis)	77 (5)	500	900	24	1434	211	F
Pa_340 h	240 (5)	200	800	20	nd	nd	WM
Pa_340 k	248 (5)	200	800	20	527	78	RC, F
Pa_340 i (bis)	89 (5)	500	800	24	1046	164	F
Pa_340 j	220 (5)	500	800	24	679	101	
Pa_340 o	188 (5)	700	800	10	1071	159	RC
Pa_340 m	147 (5)	700	800	48	nd	nd	WM
Pa_340 l	68 (5)	200	800	24	nd	nd	WM
Pa_340 p	241 (5)	200	800	24	176	26	RC
Pa_340 n (bis)	180 (5)	200	800	48	nd	nd	WM
Pa_340 q	180 (5)	500	800	> 33	nd	nd	WM
Pa_340 t	118 (5)	500	800	10	1320	201	F
Pa_340 t (bis)	152 (5)	500	800	10	515	77	RC
Pa_340 s	106 (5)	700	900	24	2489	383	RC, F
Pa_340 s (bis)	101 (5)	700	900	24	1531	237	RC
Pa_340 r	107 (5)	700	700	24	1795	276	
Pa_340 z	125 (5)	700	800	24	1211	184	RC

CO_2 concentration measured for the 24 hour experiment for both cordierite and beryl are plotted in Figure 12 as a function of temperature (a and c) and as a function of pressure (b and d).

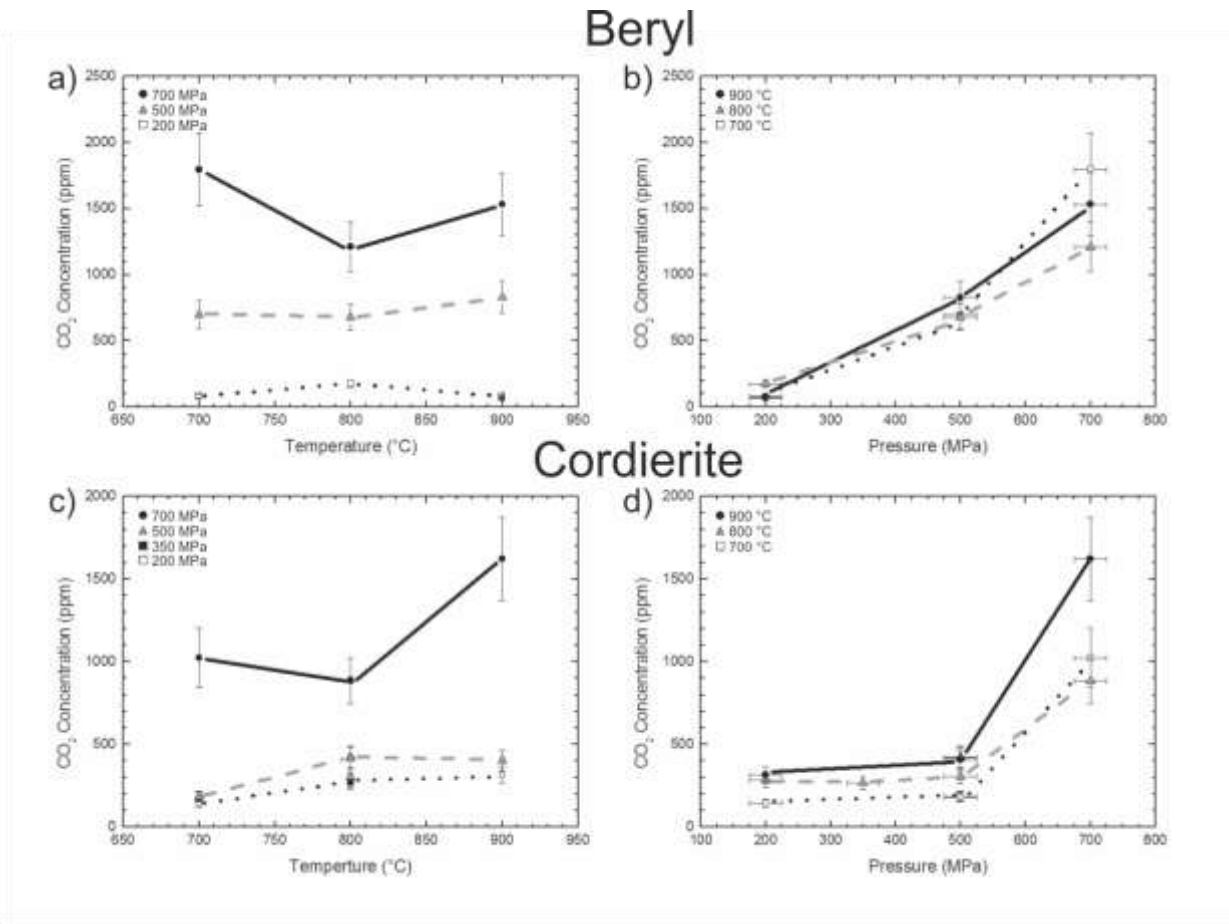

Figure 12 – CO_2 concentration for the 24 hour runs for beryl (a and b) and cordierite (c and d), plotted as a function of temperature (left) and pressure (right).

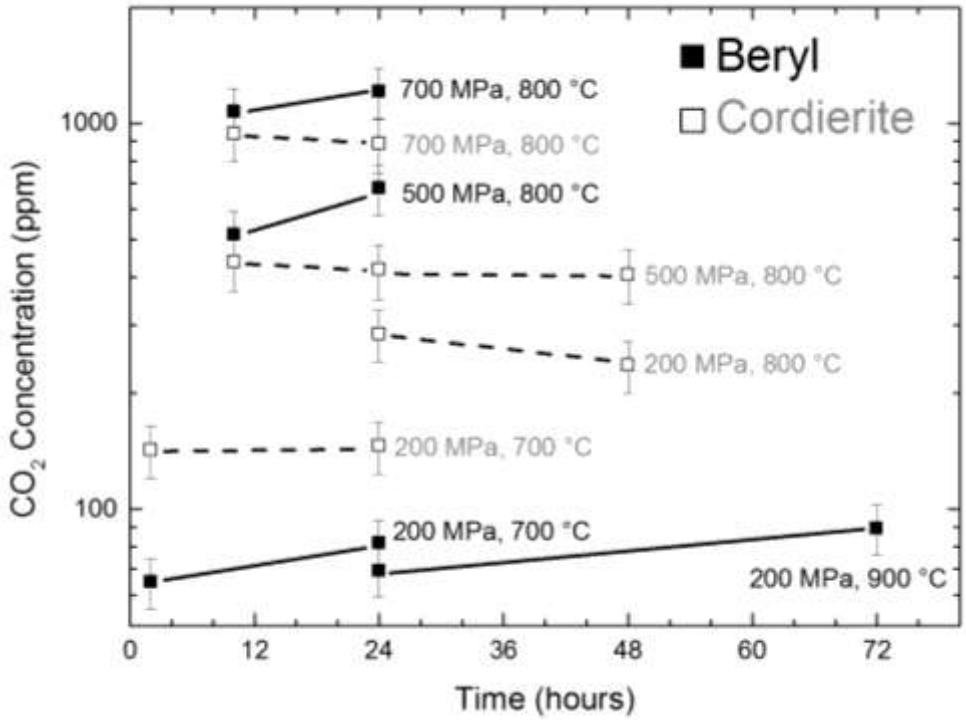

Figure 13 – CO_2 concentration measured for the same P, T annealing condition, reported on the side, and for different run times. All samples are annealed in presence of silver carbonate. Log scale was used for clarity.

Inspection of Figure 12 shows that *T* plays only a minor role on the CO_2 solubility for both cordierite and beryl. Major variations are observed with pressure. In particular, beryl shows a steep increase in CO_2 content from 200 MPa to 500 MPa and from 500 MPa to 700 MPa. The CO_2 contents in cordierite, on the other side, show only a smaller increase from 200 MPa to 500 MPa, than from 500 MPa to 700 MPa.

Figure 13, shows the effect of the annealing time on the CO_2 amount incorporated in cordierite and beryl. The logarithmic scale was chosen for clarity. Longer duration experiments had only a slight effect on the amount of CO_2. At least over the first 72 hours all samples treated with different run times present a concentration variable within the error bars.

4. Diffusion coefficients of CO_2 for cordierite and beryl

The early work on diffusive mass transport was undertaken at the end of the 19th century by the German physiologist Adolf Fick (Zhang and Cherniak, 2010), who related the diffusive mass flux (*J*) to the variation of the concentration of a component (*C*) in space (*x*) times the negative of a diffusion coefficient (*D*) (Fick's first law $J = -D(\partial C/\partial x)$). However in diffusion studies, it is often necessary to determine how a concentration profile evolves with time given the initial concentration distribution. For this purpose it is necessary to describe how the concentration is related to both space and time (*t*), i.e. the *C(x,t)* function, which is expressed by the Fick's second law of diffusion: $\partial C/\partial t = D\,\partial^2 C/\partial C^2$.

Diffusion is a temperature-dependent phenomenon, where the increased kinetic energy associated with higher temperature improves atoms mobility. In the site-jumping model, the diffusivity (*D*) is proportional to the jump frequency (Zhang and Cherniak, 2010), and varies with T^{-1} in log-linear fashion. The diffusivity of a given species in a particular medium is described by the Arrhenius equation:

$$D = D_0 \times \exp\left(-\frac{E_a}{RT}\right)$$

where *D* is the diffusion coefficient, D_0 the pre-exponential factor, E_a the activation energy, which is the amount of energy required for a particle to overcome the potential barrier

between its equilibrium position and an adjacent one. *R* is the ideal gas constant, and *T* is the absolute temperature in K. The parameters E_a and D_0 are derived from the Arrhenius plot relating log(*D*) *vs* 1/*T*, in which the diffusion coefficients plot on a straight line described by:

$$\log(D) = \log(D_0) - E_a/R \cdot \ln(10) \cdot 1/T$$

The activation energy E_a is calculated from the slope of the line and D_0 is the intercept on the ordinate axis.

As shown above, both structural considerations and our FTIR imaging clearly shows that the diffusion proceeds from the (001) crystal face into the grain. In order to obtain the diffusion coefficient (*D*), the CO_2 concentration profiles (Fig. 14) were fitted by a simple mono dimensional diffusion equation (Crank, 1975, Zhang and Cherniak, 2010):

$$C = C_0 \cdot erfc\left(\frac{x}{2\sqrt{Dt}}\right)$$

where *C* is the concentration at depth *x* (m) from the sample rim, C_0 is the maximum concentration, *D* is the diffusion coefficient (m^2/s), t is the time duration (s), and *erfc* is the complementary error function. C_0 and *D* parameters were fitted using the OriginPro 9™ software. FTIR-FPA images were collected before each FTIR diffusion profile in order to find the most suitable analytical areas. CO_2 contents in beryl were measured along traverses parallel to the *c*-axis usually from the middle of the (001) edge. Diffusion through the prismatic faces can be neglected because it is at least two order of magnitude slower (Fukuda *et al.*, 2009). Diffusion profiles in cordierite grains were also performed along traverses parallel to the *c*-axis, on grains oriented using the spindle stage as explained above. *C* and C_0 where fitted on data profiles obtained by integrating the principal ν_3 anti-symmetric stretching modes of CO_2 at 2348 cm^{-1} polarized for E//*a* for cordierite and at 2360 cm^{-1} polarized for E⊥*c* for beryl (Fig. 8). In order to reduce border effects and/or slab surface unevenness, *C* and C_0 were scaled to the 1880 cm^{-1} peak area, corresponding to a lattice overtone (Aines and Rossman, 1984), whose intensity and shape is dependent only of sample thickness and orientation. This expedient was possible because *D* is dependent on the C/C_0 ratio and not on their absolute values.

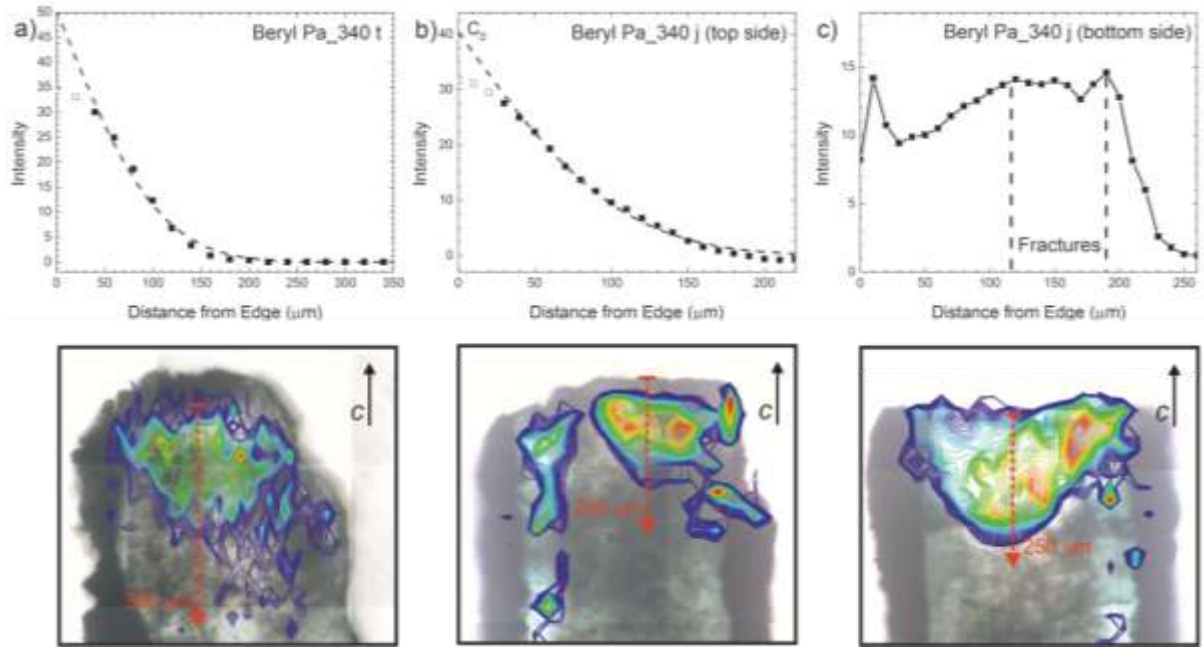

Figure 14 - (a, b) selected CO_2 diffusion profiles obtained for the antisymmetric stretching mode along the *c* crystallographic axis direction. (c) Example of a diffusion profile obtained across two fractures about 115 μm and 190 μm from the crystal edge. In (a) and (b) the dashed lines are the fitted curves; open squares in (b) are data points excluded from fitting (see text). Below each profile the corresponding FPA CO_2 image is displayed where the analytical transect is indicated by a dashed red line.

Figure 14 (a and b) shows the most common situation where, due to slight underestimation of the CO_2 content close to the crystal rim, a deviation from the ideal inverse error-function (*erfc*) trend of a component diffusing inside a matrix (Zhang and Cherniak, 2010) is typically observed. In such a case the concentration profiles were fitted excluding these points (Fig. 14b), as suggested by Fukuda *et al.* (2009). The third example (Fig. 14c) shows the case of an analytical transect across a fracture. In such a case multiple maxima located in correspondence of the fracture(s) are observed. Obviously these profiles could not be used for the *D* determination. Below each diffusion profile we reported the optical images and FPA CO_2 contour maps of the areas where the FTIR transects (dashed red line) were collected.

Table 5 – Diffusion coefficients for CO_2 along the structural channels of beryl and cordierite.

Sample	Pressure (MPa)	Temperature (°C)	Time (h)	D (m^2/sec)	1000/T (K)	Log D
Pa_340 j	500	800	24	6.2E-14	0.93	-13.21
Pa_340 d (bis)	500	700	24	2.4E-14 ÷ 1.7E-14	1.03	-13.62 ÷ -13.76
Pa_340 r	700	700	24	1.9E-14 ÷ 1.1E-14	1.03	-13.72 ÷ -13.97

Pa_340 o	700	800	10	8.9E-14 ÷ 4.9E-14	0.93	-13.05 ÷ -13.31
Pa_340 k	200	800	20	7.2E-14 ÷ 6.1E-14	0.93	-13.15 ÷ -13.21
Pa_340 t	500	800	10	9.5E-14 ÷ 7.0E-14	0.93	-13.02 ÷ -13.15

Calculated *D* coefficients are reported in Table 5; activation energy (E_a) and pre-exponential factor (-logD_0) were determined fitting the data on the basis of the Arrhenius equation. Mean activation energy (E_a) for beryl data is 122±15 kJ/mol with a pre-exponential (-logD_0) factor of 7.2±0.7. Figure 15 shows the calculated diffusion coefficients in the Arrhenius space, the solid line with errors (dashed lines) is the best fit of the Arrhenius equation for all the data points in Table 5.

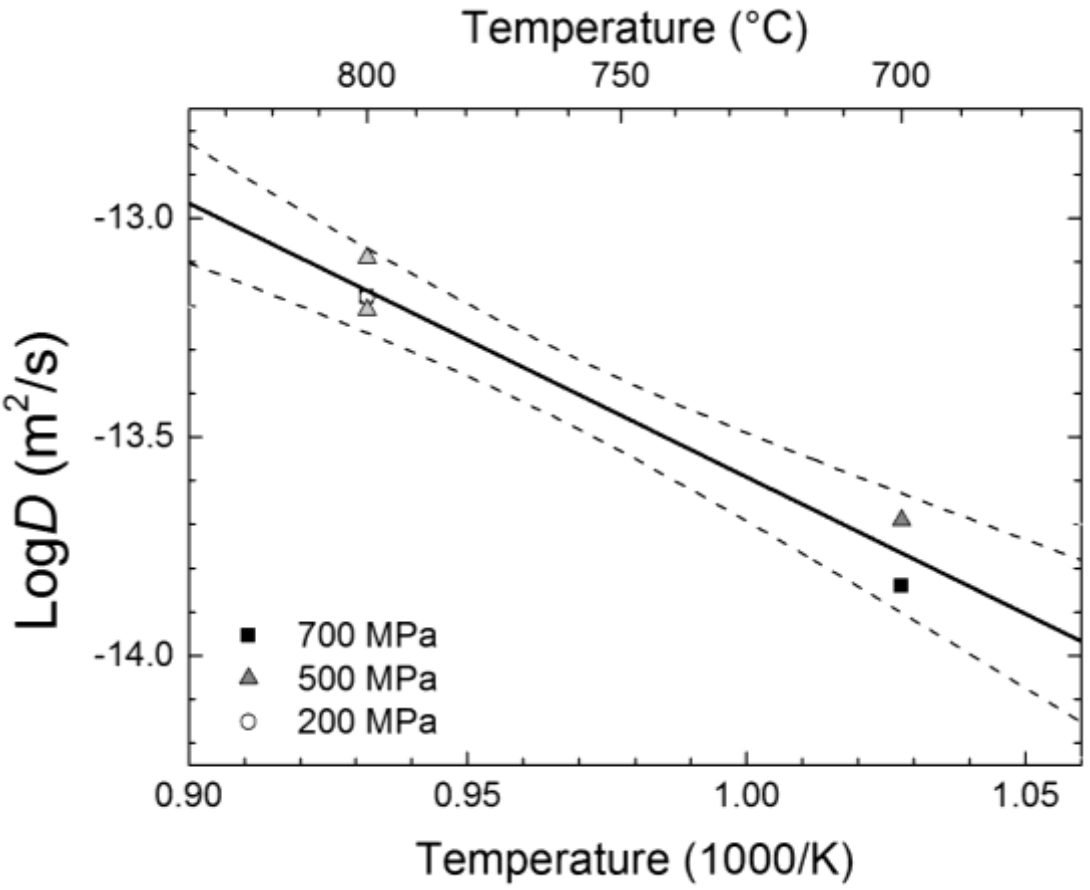

Figure 15 - Arrhenius plot for diffusion coefficients of CO_2 in beryl (black squares 700 MPa, gray triangles 500 MPa and open circles 200 MPa) from the data reported in Table 5. Solid line with errors (dashed lines) is the best fit of the Arrhenius equation for all the data points.

5. Discussion

In this chapter we address an old problem, *i.e.* the diffusion of CO_2 across minerals of geological relevance, in the present case cordierite and beryl, using a modern methodology, such as FTIR micro-spectroscopy coupled with imaging (Della Ventura *et al.*, 2014), to characterize the distribution and the amount of gas inside the sample. Because of the non-conventional procedure set up and used during this work, in this section we will discuss the problems and the advantages of this methodology by comparing the data obtained during our work with those obtained by previous authors.

5.1 The solubility of CO_2 in cordierite and beryl

Tables 3 and 4 summarize the CO_2 contents measured in the first 20 µm from the (001) edge of cordierite and beryl treated samples, inferred to represent the maximum content diffused into the phase. For cordierite, our experiments are in agreement with previous studies in showing that the CO_2 solubility within the mineral increases as a function of pressure, while temperature has only a minor effect. However while our data indicate a slightly increase in CO_2 for increasing T, previous authors (e.g. Johannes and Schreyer, 1981, Harley and Thompson, 2004) observed a slight but significant opposite trend. Figure 13 in addition shows that the CO_2 contents are not influenced by the duration of the experiment, opposite to what found by Le Breton and Schreyer (1993), at least in the range from 2 hours to 3 days. This last finding is in agreement with the work of Johannes and Schreyer (1981) who concluded that equilibration can be obtained even after just 1 hour. No literature data are available for the experimental solubility of CO_2 in beryl; however, due to the close structural similarities between the two minerals, we obtain trends similar to those observed for cordierite (Fig. 12).

A notable point is that, in comparison with the literature data, we observed a large difference in the absolute CO_2 content incorporated into cordierite, which is more than one order of magnitude lower. For instance, Johannes and Schreyer (1981) and Armbruster and Bloss (1982) reported, for cordierites treated at 500 MPa and 800°C, CO_2 contents in the 1 – 2 wt. % range, while under the same conditions we measured a CO_2 content of ~ 0.04 wt. %.

Armbruster and Bloss (1982) reported values as high as 3.13 wt% CO_2 in the White Well cordierite treated at 600°C, 600 MPa for 4 weeks. This point is extremely important, thus considering that we are comparing completely different experimental and analytical techniques, below we will discuss some factors that may explain such differences.

1) The cordierite used here as a starting material has significant amounts of alkaline cations (Tab. 1) in its structural channels; Vry *et al.* (1990) observed that in natural cordierite the total content of CO_2 + alkali cations may induce a volatile deficiency of both H_2O + CO_2 during equilibration with the surrounding fluid because of a "plug effect" affecting the diffusion rate of the relatively large CO_2 molecule from the fluid into the mineral. However, while Johannes and Schreyer (1981) used synthetic and thus alkali-free crystals as starting material for their experiments, Armbruster and Bloss (1982) used a natural cordierite from White Well containing 0.05 Na apfu, thus the alkali content alone cannot explain such a huge discrepancy.

2) One problem could be looked for in the sample handling and preparation for the analyses. Figure 9 shows that the thermal/baric treatment of the sample during the experiments induces development of a series of micro-fractures close to the edges of the cordierite crystals. These micro-fractures may induce the formation of a CO_2-rich (see above) but fragile external layer which could be removed during sample slicing and polishing for FTIR analyses. In order to test for this hypothesis, and check the effect of longer fluid-mineral interaction time, we performed some longer duration (10 days) experiments at 500 MPa, 800 °C, adding silver oxalate ($Ag_2C_2O_4$) to the charge and using a Tuttle-type H_2O cold seal pressure vessel (CSPV) at Institut für Mineralogie, Leibniz Univerität Hannover (Germany). The choice of this alternative experimental set up was due to the fact that such long duration experiments could not be performed with the used Quickpress, where the experiment duration is limited to few (1-3) days. The results are displayed in Figure 16a where we show the FPA image of CO_2 distribution in cordierite. From this image it is possible to observe that the outer zone of the grain consists of 150/200 μm thick strongly fractured layer, presenting a fairly high CO_2 content, while the core of the grain is almost CO_2 free. Because of this thick layer it was not possible to orient the grain by optical means and consequently determine the actual CO_2 content by using polarized data. However, using unpolarized data we can estimate a rough content in this layer of at least 0.42±0.09 wt.%. Figure 16b displays the FPA contour map of CO_2 in a synthetic beryl treated at the same *P*,*T*,*t*

conditions. Contrary to cordierite, synthetic emeralds did not develop significant thermally induced micro-fractures along the grain edges. Figure 16b shows that the 10 days treated beryl still presents a prismatic hexagonal habitus and no thick alteration layers were formed; CO_2 diffusion occurred, as usual, from the (001) pinacoidal face of the grain and along cracks (dashed line). This "edge effect" may thus strongly affect the CO_2 content measured for the experimentally-treated grains as well as the diffusion of CO_2 into cordierite.

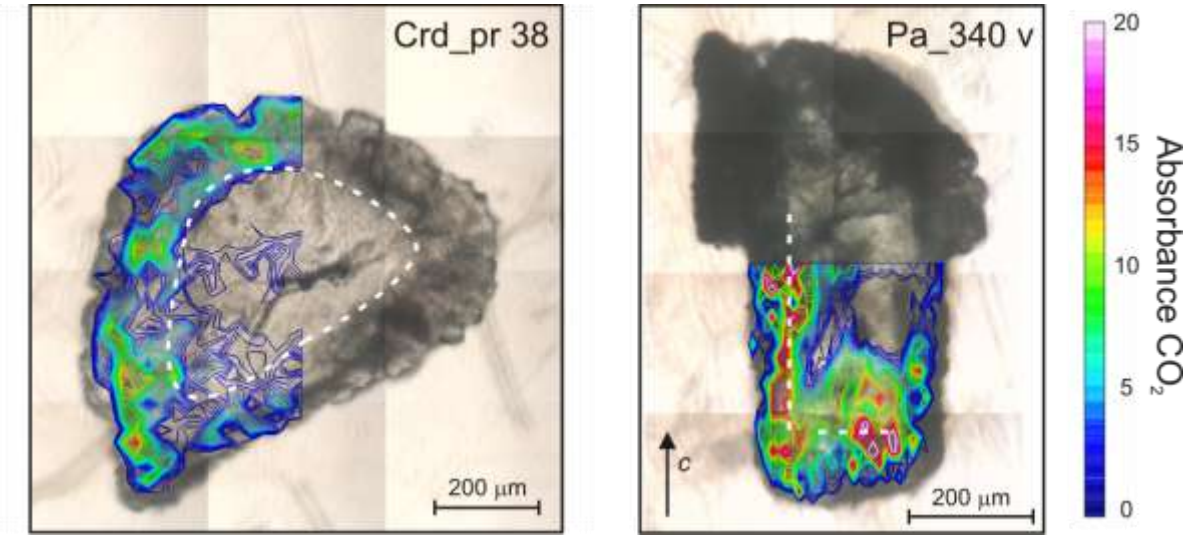

Figure 16 – FTIR – FPA image of the CO_2 distribution in cordierite Crd_pr 38 (left) and beryl Pa_340 v (right) treated with a CSPV for 10 days at 500 MPa and 800 °C. The beryl crystal is oriented parallel to c-crystallographic axis; white dashed line are cracks. The cordierite sample is randomly oriented, the white dashed line marks the boundary of the altered layer.

5.2 The effect of fractures on the CO_2 content

The second most notable feature from Tables 3 and 4 is the difference between the data measured at the edges of the grain and those measured in correspondence of fractures (labeled with "F" in the notes). CO_2 contents observed in correspondence of fractures may be several times higher than the value calculated at the edge of the grain, this effect is more pronounced in cordierite samples than in beryl samples, where the CO_2 content measured on fractures are rarely higher than the CO_2 content measured on the edges. An example is reported in Figure 17. Sample Crd_pr 25 and Crd_pr 30 were treated at the same conditions (200 MPa and 800 °C for 24 hours), however sample Crd_pr 25 was re-run after a thermal shock due to a technical problem occurred during the heating ramp; after the experiment, optical examination of the grains revealed the presence of diffuse fracturing across the

crystals. FTIR analyses showed that the amount of CO_2 in sample Crd_pr 30 was lower than in sample Crd_pr 25, indicating that the fracturing favored CO_2 solubility all across the grain, in line with the general observation that grain-boundary diffusion and diffusion along interfaces, like cracks, can be several order of magnitude faster than lattice diffusion (Zhang and Cherniak, 2010). One final point to note is that, although no water was present in the experimental tubes, the spectra of Figure 17 show the presence of minor water (3000 ppm) in the run products. This water originated from the moisture present in the chemicals used for the sample preparation.

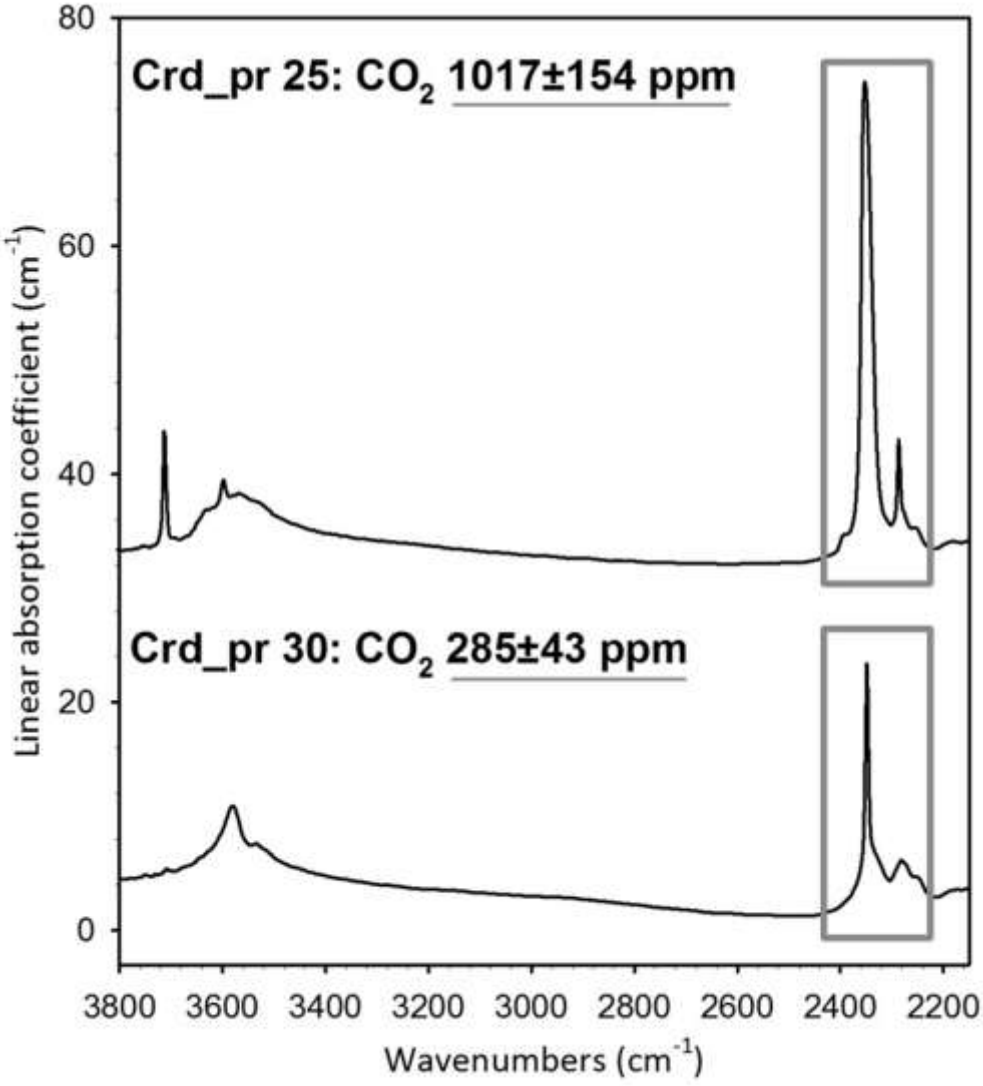

Figure 17 - Polarized FTIR spectra of Crd_pr 25 (above) and Crd_pr 30 (below) both treated at 200 MPa and 800 °C for 24 hours. The anti-symmetric stretching peaks of CO_2 are highlighted. Spectra scaled to sample thickness. Sample Crd_pr 25 presents diffuse fracturing and a much higher CO_2 content, for explanation see text.

5.3 The CO_2 diffusion in microporous structures

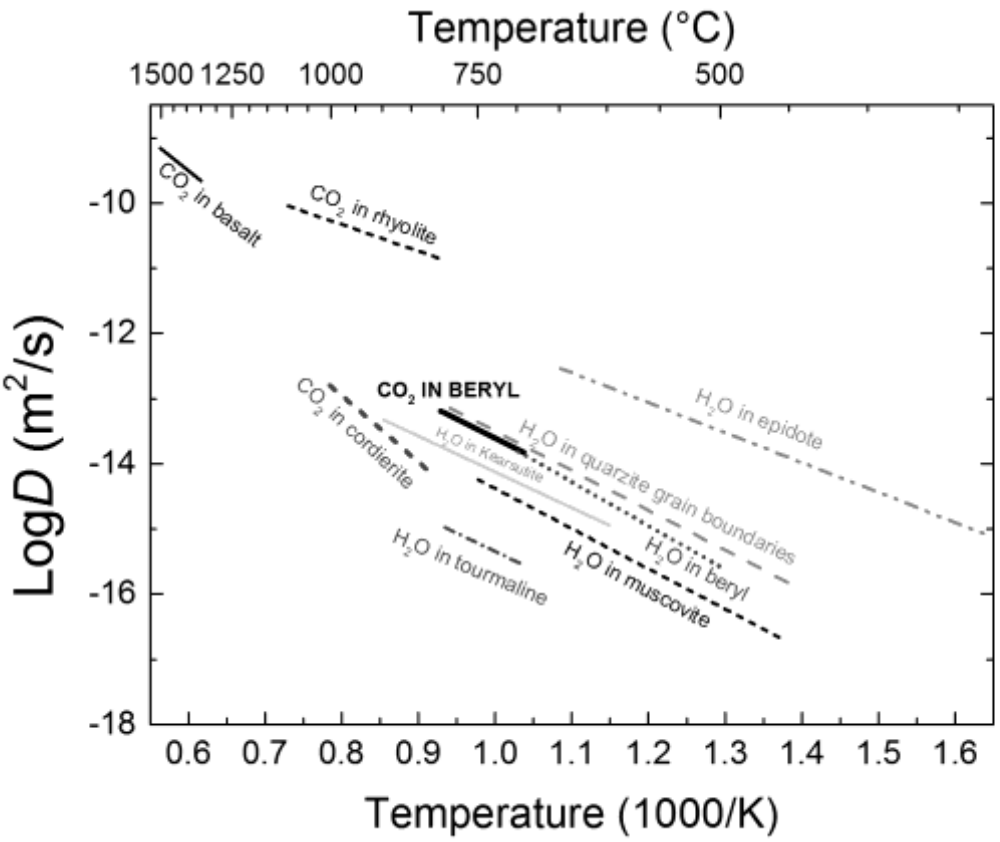

Figure 18 – Diffusion coefficients *D* for different silicates or silicate melts for H_2O and CO_2 from the literature plotted onto the Arrhenius diagram. For numerical values and references see Table 6.

Because of the well-developed hexagonal prismatic habitus, the beryl samples were excellent candidates to evaluate the diffusivity of CO_2 in these channel-like structures. In Table 5 we list the diffusion coefficients determined from different beryl samples treated at different T, P conditions, as well as the activation energy (E_a) necessary to induce the diffusion process. From Table 5 we may notice that pressure variation from 200 to 700 MPa has little effect on the diffusion coefficients. It is also interesting to note that while the overall CO_2 content inside the beryl samples is greater at higher pressure (Figure 12), the diffusing rate remains constant. On the opposite, the diffusion coefficient for cordierite was more difficult to evaluate because of the very irregular shape of the crystals.

From a general point of view, diffusion coefficients of molecular species in silicates are expected to be tightly related to the dimension of the diffusing molecule and the hosting structure. It is also widely accepted that for more compact silicate structures and/or larger molecules diffusing rates are smaller and activation energies larger. As we may observe from

Figure 18 the diffusing rates calculated for CO_2 (this work) and H_2O (Fukuda *et al.*, 2009) in beryl are very close, even though CO_2 molecule are larger than the H_2O molecule (the overall dimension of H_2O is 2.8 x 3.2 x 3.7 Å and for CO_2 is 2.8 x 2.8 x 5.0 Å: Wood and Nassau, 1968). On the other hand, the CO_2 diffusion coefficients for beryl (this work) are greater than the diffusion coefficient calculated for the outward CO_2 diffusion from the cordierite channels (chapter 4). In addition, Vry *et al.* (1990) observed that, in cordierite, the inward diffusion is quicker than outward diffusion. These authors concluded that the difference between inward and outward diffusion rates may be caused by alkali cations and CO_2 itself, that, acting as plugs in the channel, preferentially slows down the outward volatile diffusions.

It is difficult to draw a direct comparison between our data and the diffusion coefficients available in the literature for minerals; the reason is that, beryl and cordierite behave as microporous structures trapping H and C as H_2O and CO_2 molecules, while the vast majority of the existing data have been collected on minerals where H is present as an OH^- group. Moreover no data are available for CO_2 diffusion in minerals (excluding C diffusion in carbonates, *e. g.* Anderson, 1972; Labotka *et al.*, 2000). Thus in the next paragraph we are forced to compare our data with those derived for basically different processes.

Figure 18 and Table 6 give selected examples of diffusion rates for the most common hydrous minerals. In Figure 18 we may observe that the diffusion coefficients measured for CO_2 in beryl are close to the OH^- diffusion coefficients obtained in other ring silicates like tourmaline (Desbois and Ingrin, 2007), layer silicates like muscovite (Graham, 1981), amphiboles like kaersutite (Ingrin and Blanchard 2000), or in disilicates like epidote (Graham, 1981). However, it's important to note that structural OH^- probably diffuses inside these structures in the form of H^+ (Zhang *et al.*, 2010) thus the diffusing species is much smaller compared to molecular CO_2 and H_2O.

Our data suggest that the structural channels of cordierite and beryl act more likely fast paths for the mobility of large molecular groups compared to similar silicate structures, and for this reason the diffusing behavior is more similar to the one typically observed for grain boundary diffusion, such as, for example, H_2O in quartzite (Farver and Yund, 1991) or to the behavior of CO_2 in non-crystalline materials, like silicate melts (Watson *et al.*, 1982; Watson, 1991).

Table 6 – Experimental data for H_2O and CO_2 diffusion in various silicate minerals and melts found in the literature

Mineral	Diffusing molecule	T (°C)	P (MPa)	E_a (kJ/mol)	logD_0 (m^2/s)	Reference
Rhyolite	CO_2	800 - 1100	1000	75	-7.2	Watson, 1991
Basalt	CO_2	1350 - 1500	1500	195	-3.4	Watson *et al.*, 1982
Muscovite	D/H_2O, D_2O	450-750	200 or 400	121	-8.0	Graham, 1981
Epidote	D/H_2O, D_2O	250-650	200 or 400	90	-7.4	Graham, 1981 in Ingrin and Blanchard, 2006
Kearsutite	D/D_2	600-900	0.1	104±12	-8.7	Ingrin and blanchard, 2000
Tourmaline (par *c*)	D/Ar, D_2	700-800	0.1	106.3±36.8	-9.8	Desbois and ingrin, 2007
Quarzite	H_2O	450 -800	100	113	-7.6	Farver and Yund, 1991
Beryl	H_2O	500 -700	50 -150	133	-6.6	Fukuda *et al.*, 2009
Cordierite	CO_2	825 -1000	0.1	198	-4.7	Chapter 4

6. Conclusions

In this study we combined micro-FTIR spectroscopy and FPA imaging to study the carbon dioxide diffusion in cordierite and beryl. The starting crystals were treated at different pressure and temperature in a CO_2 rich atmosphere using a non end-load piston–cylinder designed for short term experiments and able of very fast heating ramps and cooling rates. Because of the relative short duration of the experiments and the slow diffusion rates of CO_2 in the structural channels we did not expect a complete homogenization of the sample, thus in this work we made extensive use of FTIR-FPA imaging as primary tool to characterize the distribution of CO_2 in the run product and locate correctly the most suitable points for FTIR analysis. The results showed that CO_2 diffusion in both minerals occurs exclusively along the structural channels parallel to the *c* crystallographic axis; FTIR micro-spectroscopy showed that the final CO_2 content is strongly influenced by pressure, while temperature has a minor effect. Surprisingly, however, the CO_2 contents introduced into cordierite were even two order of magnitude lower than expected. Cracks and fractures, produced during the thermal treatment, were found to enhance significantly the CO_2 diffusion across cordierite, while beryl was less affected by this kind of phenomenon. The calculated activation energies and diffusion coefficients for CO_2 along beryl structural channels were found to be close to values typical of grain boundary diffusion and melts, or H^+ in the most common hydrated minerals.

CHAPTER 6

THE DIFFUSION OF CO_2 AND H_2O IN A SYNTHETIC SECTOR-ZONED BERYL: A MULTI-ANALYTICAL STUDY

Abstract

In this work we investigate the strong inhomogeneous distribution of CO_2 and H_2O across a synthetic beryl characterized by a peculiar hourglass structure due to the Cr distribution during the crystal growth. The sample was treated at 800°C, 500 MPa, in a CO_2-rich atmosphere. A combination of analytical techniques and, in particular, polarized-light FPA imaging, revealed an additional pathway of carbon dioxide diffusion along the zoning discontinuity. Using high-resolution synchrotron-light mapping it was possible to distinguish between the enhancement of the CO_2 diffusion along the hourglass trace and a fracture in the grain. High-resolution FESEM images revealed that no physical discontinuities are present in the matrix, at least at the scale of tenth of nanometers. Therefore, the hourglass zone boundary may be considered as a planar defect possibly due to the mismatch induced by the different growth rates of each sector. The H_2O diffusion follows an extremely different pattern: combining TOF-SIMS and FTIR-FPA a significant depletion of $H_2O^{[II]}$ along the hourglass boundary where a significant amount of Na was replaced by K.

1. Introduction

Diffusion of hydrogen-oxygen species in minerals as a function of *T* and *P* has been addressed by numerous experimental studies (*e.g.* Ingrin and Blanchard, 2006; Watson and Baxter, 2007; Farver, 2010 and references therein) due to the extremely important consequences that this processes may have in Earth Science systems. Accordingly, diffusion may occur in three different ways: (i) intra-crystalline (volume), (ii) grain boundary (Fukuda *et al.*, 2009) and (iii) planar defects diffusion (Zhang *et al.*, 2006). Intra-crystalline diffusion is the slower mechanism, whereas grain boundary and planar defects act as fast-pathways for the travelling of ions or molecular species across the mineral (*e.g.* Zhang *et al.*, 2006). Several rock forming minerals are structurally characterized by atomic arrangements which leave free space to the molecular diffusivity in the form of connected cavities or channels: notable examples are the zeolite-type feldspathoids, and ring silicates such as beryl and cordierite. Diffusion along these connected structural cavities is typically faster than the volume diffusion. In other words there is evidence that diffusivity along structural channels can be assimilated to fast mobility diffusion. In this work we address some particular aspects of the diffusivity of CO_2 in beryl, after the more general experimental work described in chapter 5 of this Thesis. The chapter deals in particular with a peculiar diffusion pattern observed for an hourglass-zoned crystal.

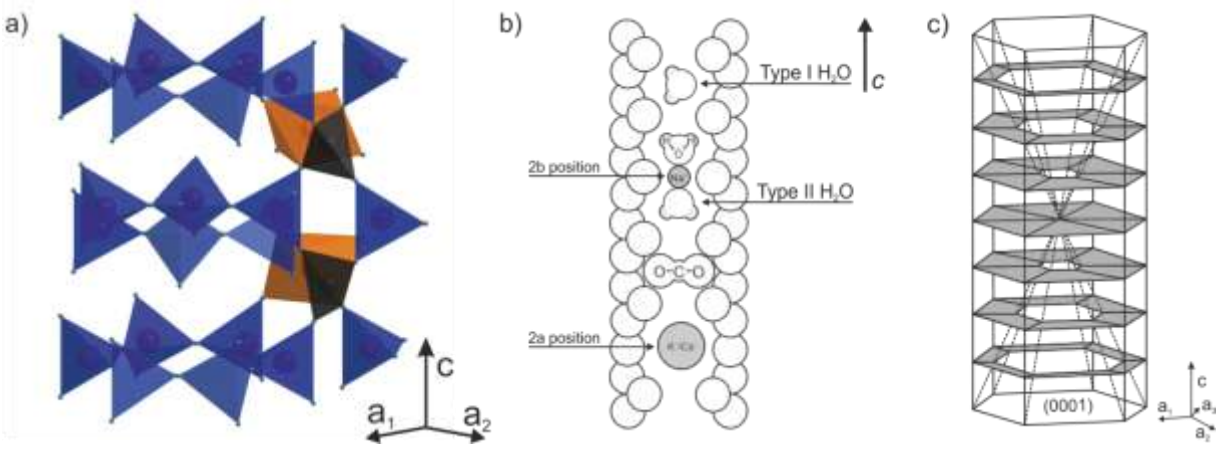

Figure 1 – a) Schematic view of beryl crystal structures parallel to the crystallographic *c* axis. Blue = Si tetrahedra; orange = Al sites and gray = Be sites. b) Schematic section of beryl channel parallel to [0001], modified after Fukuda and Shinoda (2011). c) Sketch of the hourglass zoning inside a beryl (modified after Hollister, 1970)

Beryl is a relatively rare rock-forming mineral, and is found as an accessory constituent in pegmatites, in cavities of granitic rocks and occasionally in metamorphic rocks (Deer *et al.*, 1986). A rare occurrence in a volcanic syenitic ejectum has also been reported (Della Ventura *et al.*, 2000). It is structurally a ring silicate with ideal formula $Be_3Al_2Si_6O_{18}$, consisting of six-member hexagonal rings of tetrahedra. The vertical stacking of these rings forms a succession of interconnected cages arranged along the *c* axis (Fig. 1a). The cages have a maximum diameter of about 5.0 Å and a minimum diameter of 2.8 Å (Gibbs *et al.*, 1968); channel height is about 4.7 Å (Fukuda and Shinoda, 2011).

Figure 1b shows a schematic section of the structural channel parallel to [001], where different atoms and/or molecular groups may be hosted. H_2O and CO_2 are the main constituents in beryl channels (Wood and Nassau, 1968, Aines and Rossman, 1984) and are located in the wider sites of the channels (2a position in Fig. 1b). Larger ions like Cs^+ and K^+ (Hawthorne and Černý, 1977) and possibly OH groups (Wickersheim and Buchanan, 1959, Aurisicchio *et al.*, 1994) may also be located in the 2a position, while smaller cations like Na^+ (Wood and Nassau, 1968) occur at the narrower 2b site (Fig. 1b).

Polarized FTIR data show that the linear CO_2 molecules are oriented orthogonally to the *c* axis (Wood and Nassau, 1968; Aines and Rossman, 1984). Extra-framework H_2O occur in the structural channels with the molecular plane parallel to (100) and may present two different orientations (Fig. 1b): in type I H_2O (hereafter $H_2O^{[I]}$) the H–H vector is oriented parallel to the *c* axis and in type II H_2O ($H_2O^{[II]}$) the H–H vector is rotated by 90° orthogonally to the *c* axis (Wood and Nassau, 1968, Bellatreccia *et al.*, 2008). H_2O molecules of this latter type are locally bonded to alkali cations sited in the 2b position (Goldmann *et al.*, 1977; Hawthorne and Černý, 1977).

H_2O and CO_2 diffusion in beryl has been recently studied by Fukuda *et al.* (2009) and in this thesis (chapter 5); the available data show without doubt that mobility of molecules across the mineral occurs exclusively along the structural channels.

In this work we describe the crystal-chemistry of one beryl grain recovered from one of the CO_2 diffusion experiments described in chapter 5 of this Thesis. Preliminary FTIR-FPA data showed a peculiar inhomogeneity of CO_2 and H_2O in this sample, thus the crystal has been characterized in detail using a multidisciplinary approach. The volatile distribution, in particular, has been studied by high-resolution synchrotron-radiation (SR) FTIR-FPA imaging under polarized light. The data clearly demonstrate that careful determination of the

inhomogeneous distribution of volatile species is mandatory when studying the distribution mechanisms and coefficients across mineral matrixes.

2. Materials and Methods

The single-crystal used as starting product for the diffusion experiments (sample label 103_391_c) described here, is a synthetic beryl from the very first attempt to produce Li_2O and MoO_3 flux-grown emeralds; the crystals were obtained after 15 days of annealing at 800°C, whereas higher temperatures lead to formation of phenakite (Hautefeuille and Perrey, 1888, 1890). Batches of these syntheses are currently kept in the mineralogical collection of Muséum National d'Histoire Naturelle in Paris (MNHN), and some grains were kindly donated to us to be used for scientific research. The batch consists of fairly large (~ 1.0 mm X 0.5 mm) emerald-green prismatic crystals, showing a particular sector (hourglass) zoning of Cr (Fig. 1c, see also Liedl *et al.*, 2014); this type of feature had already been mentioned by Bellatreccia *et al.* (2008) for grains from a different batch kept at the Museum of Mineralogy of University La Sapienza (Rome).

Some crystals were used for the experiments described below; one of these samples, recovered after the run, has been fully characterized by a combination of methods, and the results will be discussed in this text. One additional, untreated crystal from the same batch, was oriented using its prismatic morphology, embedded and doubly polished for EMPA-WDS chemical imaging and single spot analysis using a JEOL JXA 8200 WD-ED electron micro probe at INGV (Rome). Working conditions were 15 kV accelerating voltage, 7 nA sample current, 5 µm beam diameter, counting times: 10 seconds on the peak and 5 seconds on the background on both sides of the peak. The standards, spectral lines and crystals used were: albite (Na*Kα*, TAP), wollastonite (Si*Kα*, PET), k-feldspar (K*Kα*, PET), kyanite (Al*Kα*, TAP). Data correction was performed using the ZAF method. BeO content was calculated by stoichiometry.

Selected results are reported in Figure 2 and will be useful to compare the observed chemical inhomogeneity before and after the thermal treatment. The BSE image (Fig. 2, top) clearly shows the sector zoning mentioned above. The XRF maps reveal that the zoning visible in the BSE image is related to the distribution of Cr; this element is in fact significantly enriched in the outer sector. A slight inhomogeneity is also observed for Si that is enriched in

the inner sector, while both Al and K are slightly enriched in the outer sector. The eventual zoning of Na is unclear from these images, due to its low concentration. Selected microchemical data are given in Table 1, for the high Cr and Low Cr sectors, respectively. In line with the data presented by Bellatreccia *et al.* (2008), the Cr content is close to 2.0 wt% in the high-Cr zones, while being < 1.0 wt% in the low-Cr zones. The Na content is too low to allow conclusions on its distribution based on EMP, while the K content, although very low, is clearly slightly higher in the Cr-rich areas, as indicated by the XRF images of Figure 2.

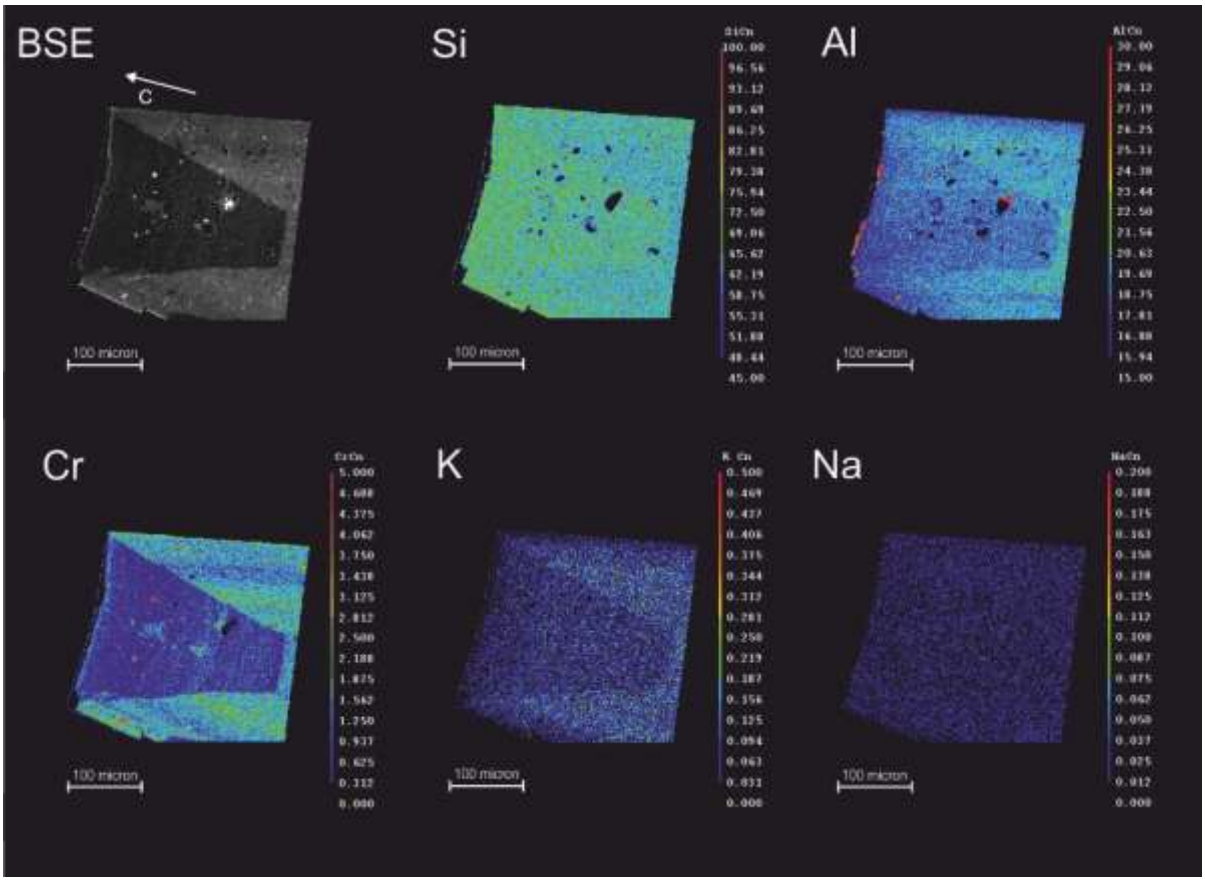

Figure 2 – EMPA-WDS chemical maps of selected elements for the untreated beryl sample; the grain was oriented parallel to [001] using its perfect prismatic morphology. The color scale is proportional to element concentration.

Differently from the crystal studied by Bellatreccia *et al.* (2008), which showed traces (~ 30 ppm) of H_2O, several single-spot spectra collected at random on the sample studied here showed the crystal to be completely anhydrous and, obviously, CO_2-free. This point is particularly important for the discussion below.

The experiments were done using 3 x 9 mm Au capsules; silver oxalate was used as a CO_2 source to saturate the system with carbon dioxide during HT/HP treatment. $Ag_2C_2O_4$

decomposes into $2Ag + 2CO_2$ at 140 °C, yielding a theoretical CO_2 content ≈29 wt.%. Al_2O_3 powder (Al_2O_3 = 99.72 wt.%, SiO_2 = 0.07 wt.%, others = 0.21 wt.%) was mixed in 1 to 1 ratio by wt with $Ag_2C_2O_4$, and added to the charge. The aluminum oxide powder was used to prevent the contact between the crystals and the capsule walls after the silver oxalate disappearance due to its decomposition, and helped to dissipate the differential stress that may arise during the experiment. All components used to prepare the tubes were dried up in oven at 110 °C in order to avoid moisture contamination, however, despite this precaution, FTIR data (see below) revealed significant H_2O in the sample after the run.

Table 1 - Microchemical analysis for the beryl in Figure 2, data points were collected in the high Cr sector (HighCr) and low Cr sector (lowCr and lowCr2). Crystal-chemical formulae were recalculated based on 18 oxygen atoms p.f.u. The tetrahedral site-population was constrained to be 9 apfu, Be was calculated by stoichiometry

	HighCr	lowCr	lowCr2
SiO_2	62.44	63.87	65.09
Al_2O_3	20.15	19.59	19.34
Cr_2O_3	1.80	0.91	0.70
BeO	13.55	13.62	13.76
Na_2O	0.01	0.02	0.00
K_2O	0.09	0.06	0.04
Total	98.04	98.06	98.92
Si	5.756	5.859	5.909
Al^{IV}	0.240	0.140	0.090
Be	3.001	3.001	3.001
Σ Tetrahedra	8.997	9.001	9.000
Al^{VI}	1.950	2.118	2.069
Cr	0.131	0.066	0.050
Σ Octahedra	2.081	2.183	2.119
Na	0.001	0.004	0.001
K	0.010	0.007	0.004
Σ Channels	0.012	0.010	0.005

The experiments were performed using an externally heated vessel at Institut für Mineralogie, Leibniz Univerität Hannover (Germany). The temperature uncertainty at the sample position is estimated to be ±10 °C and pressure was automatically controlled to be within 5 MPa (Behrens, 2010); oxygen fugacity within the vessel was close to NNO. The sample was treated at 800 °C and 500 MPa for 4 days. The X-ray diffraction pattern of the

powder added within the tube revealed the presence of residual alumina (corundum) and metallic silver, together with traces of silver oxide. The beryl sample was separated from the residual powder, oriented using its perfect prismatic morphology, embedded in epoxy resin and doubly polished to 63 µm; sample thickness was determined using an electronic micrometer with ±5 µm uncertainty.

Preliminary FTIR spectra were acquired using a Bruker™ Hyperion 3000 microscope equipped with a KBr broadband beamsplitter and a liquid nitrogen-cooled MCT detector at Laboratori Nazionali di Frascati-Istituto Nazionale di Fisica Nucleare (LNF-INFN,) Frascati (Rome). High-resolution spectra were acquired at beamline B22, Diamond Light Source Laboratory (Oxford, UK) using a similar set up except a synchrotron FTIR source instead a Globar source. The polarized spectra were collected using a gold-wire-grid polarizer on a ZnSe substrate. A 15 x objective in conventional light and 36 x objective in synchrotron light were employed; the nominal resolution was 4 cm^{-1} and 128 scans were averaged for both spectrum and background. FTIR images were collected with a 64 x 64 pixel focal-plane array (FPA) of liquid nitrogen-cooled MCT detectors. The nominal resolution was set at 4 cm^{-1} and 64 scans were averaged for each spectrum and background; each image covers an area of 170 µm x 170 µm with a nominal spatial resolution of ~ 5 µm (Della Ventura *et al.*, 2010, 2014).

Time of Flight – Secondary Ion Mass Spectroscopy (TOF – SIMS) data were collected on a ION – TOF TOF.SIMS 5™ mass-spectrometer at Dipartimento di Matematica e Fisica, University of Roma Tre, using a ToF-SIMS V instrument equipped with a 30 keV Bi liquid metal ion gun (BiLMIG). Sample surface sputtering procedure was performed before the measurements.

3. Results

3.1 TOF-SIMS mapping

Figure 3 shows the distribution of selected chemical components across the beryl extracted from the vessel after the T/P treatment, obtained by TOF-SIMS imaging. Inspection of Figure 3a shows that the crystal has a well evident hourglass growth structure, which is visible in optical microscopy under both parallel and crossed polars. Figure 3b indicates that,

as already discussed above, the hourglass zoning is essentially due to the Cr^{3+} distribution across the crystal; in particular comparing Figure 3a and Figure 3b it is possible to observe that the Cr^{3+} zoning is also the main responsible for the difference in birefringence in the different sides of the grain: higher birefringence (darker-yellow colors in Fig. 3a) is associated with higher Cr content, while a lower Cr content is associated with a lower birefringence (pale yellow/white in Fig. 3a). Such a distribution has been recently characterized in 3D by Liedl *et al.* (2014) on a crystal from the same batch and later used for microchemical analyses (see below) using μ-CT X-ray tomography.

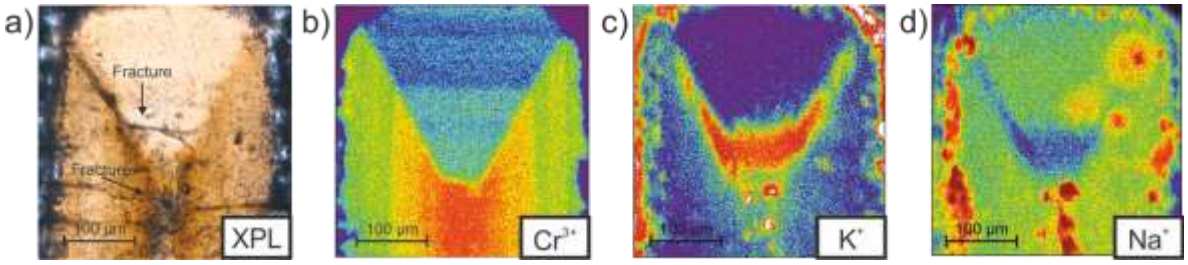

Figure 3 – XPL (a) and TOF-SIMS images (b to d) of the studied beryl sample after the experimental run. The color scale is proportional to the element contents from red (high) to blue (low).

Figure 3c and 3d show a peculiar distribution of K^+ and Na^+ which indicates that, despite these elements are present as accessory constituents inside the structural channels, their content also is inhomogeneously distributed and follows the hourglass pattern; in agreement with XRF images (Fig. 2), TOF-SIMS data show that the K content is slightly higher in the outer sector while Na seems to be inversely correlated to K (compare Fig. 3c with Fig. 3d).

3.2 Polarized-light FTIR spectra, band assignment, and volatile contents

Figure 4 shows selected single-crystal polarized-light FTIR spectra collected for the treated sample close to the (001) edge of the grain, were the maximum CO_2 (and H_2O) content is expected (this thesis, chapter 5). The single-crystal polarized infrared spectrum of beryl has been studied by several authors, after the early work of Wood and Nassau (1967, 1968) and Aines and Rossman (1984) who clearly showed that the beryl channels may in fact host H_2O in two different orientations, and CO_2 molecules. A detailed analysis of the beryl spectrum is behind the scope of the present work and will be given in chapter 7, thus we will describe briefly only those absorptions that will be used for the measurements discussed

below. In the 4000-3200 cm^{-1} range, when the electric vector E is parallel to the *c* crystallographic axis (E//c), two very sharp and intense peaks occur at 3699 cm^{-1} and 3602 cm^{-1}. Based on the literature data (Wood and Nassau, 1967, Charoy *et al.*, 1996, Kolesov and Geiger, 2000b, Gatta *et al.*, 2006, Della Ventura et al., 2007, Adamo *et al.*, 2008, Bellatreccia *et al.*, 2008) the former peak is assigned to the ν_3 mode of type I H_2O, while the latter peak is assigned to the ν_1 mode of type II H_2O. In the same range, the E⊥c spectrum consists of a very broad multi-component absorption with maxima at 3724, 3675 and 3605, with a shoulder around 3591 cm^{-1}; pertinent to the following discussion is the 3675 cm^{-1} band that is assigned to the ν_3 mode of type II H_2O.

In the 2600-2000 cm^{-1} range, the very sharp and asymmetric peak centered at 2360 cm^{-1} for E//c is assigned to the ν_3 mode of CO_2 (Wood and Nassau 1967, Charoy *et al.*, 1996); in the same range the E⊥c spectrum is featureless, in agreement with the fact that the CO_2 molecule is aligned ⊥ to the c crystallographic axis (see Fig. 1).

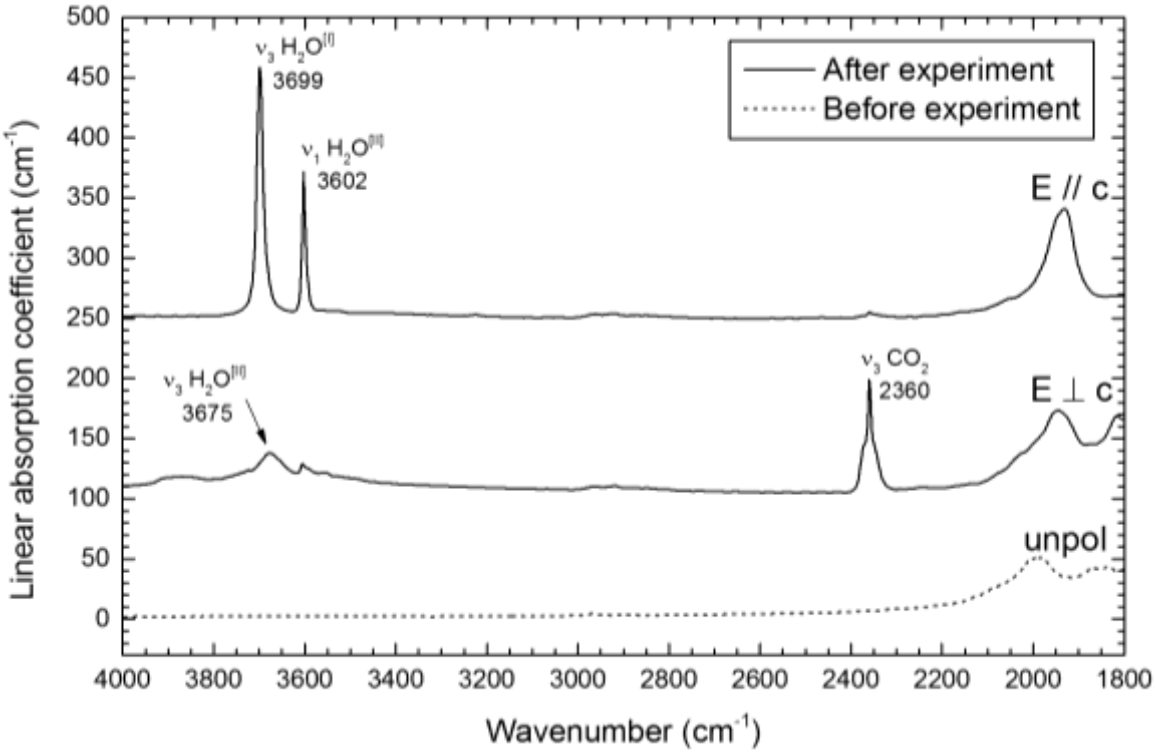

Figure 4 - Single-crystal polarized-light infrared spectra of the experimentally treated beryl (solid lines). Data collected on a 63 µm thick, (hk0) oriented slab. The single-crystal unpolarized-light FTIR spectrum (dashed line) of an untreated beryl sample from the same batch is reported for comparison. Spectra scaled to thickness.

Both the H_2O and CO_2 contents were quantified from the polarized data collected close to the sample edge, where the content of these molecules is maximum (see below).

The Lambert-Beer equation: $C = (A_{itot} \cdot k)/(\varepsilon_i \cdot D \cdot t)$, was used, where *C* is the concentration in wt%, A_{itot} is the total integral absorbance in cm^{-1} ($A_{itot} = A_i//c + 2 \cdot A_i \perp c$: Libowitzky and Rossman, 1996), D is the sample density in $g \cdot cm^{-3}$ and *t* is the sample thickness in cm. k_{H2O} = 1.8 (Beran *at al.*, 1993) and k_{CO2} = 4.401 (Della Ventura *et al.*, 2009, 2012) were used to convert H_2O and CO_2, respectively, from $mol \cdot l^{-1}$ to wt.%. The critical point in the Lambert-Beer equation is the integral molar absorption coefficient, ε, which is matrix-dependent and needs to be calibrated for the mineral under investigation; alternatively it can be derived from empirical curves such as the one proposed by Libowitzky and Rossman (1997). For beryl, ε_{H2O} values are available in the literature, however their use is complicated by the fact that H_2O occurs in two different molecular configurations, which absorb the IR beam at different wavenumbers. In addition, previous authors have used either integrated or linear absorbance data, thus it is difficult to compare results from different methods. We give in Table 2 the contents derived using both the ε_{H2O} coefficients calculated from the curve of Libowitzky and Rossman (1997) for $H_2O^{[I]}$ and $H_2O^{[II]}$, independently, and the ε_{H2O} values given by Charoy *et al.* (1996) and Goldman *et al.* (1977), as proposed by Fukuda *et al.* (2009). Table 2 gives also the CO_2 content calculated using the ε value recalculated after Charoy *et al.* (1996). The error σ_C associated with C was obtained according to Bellatreccia *et al.* (2005). For sake of comparison we also list in Table 2 the CO_2 content obtained using the ε_i calibrated by Della Ventura *et al.* (2012) for the closely (structurally) related cordierite.

Table 2 - Measured H_2O and CO_2 maximum contents for the studied beryl.

Integrated absorbance data; ε_i values calculated from Libowitzky and Rossman (1997)			
Molecule	Mode, position and polarization	ε_i ($l \cdot mol^{-1} \cdot cm^{-2}$)	C (wt.%)
Type I H_2O	ν_3 at 3699 cm^{-1}, E//c	13316	0.29±0.04
Type II H_2O	ν_3 at 3674 cm^{-1}, E⊥c	19481	0.50±0.07
Total H_2O			0.79±0.11
Linear absorbance data; ε_l values from Charoy *et al.* (1996) for type I H_2O, and from Goldman *et al.* (1977) for type II H_2O			
Molecule	Mode, position and polarization	ε_l ($l \cdot mol^{-1} \cdot cm^{-1}$)	C (wt.%)
Type I H_2O	ν_3 at 3699 cm^{-1}, E//c	197	0.94±0.13
Type II H_2O	ν_1 at 3602 cm^{-1}, E//c	256	0.44±0.06
Total H_2O			1.38±0.19
Integrated absorbance data; ε_i values recalculated after Charoy *et al.* (1996), see also Chapter 5, and Della Ventura *et al.* (2012) for cordierite			
Molecule	Mode, position and polarization	ε_i ($l \cdot mol^{-1} \cdot cm^{-2}$)	
CO_2	ν_3 at 2360 cm^{-1}, E⊥c	70000±7000	0.21 ± 0.04
CO_2	ν_3 at 2360 cm^{-1}, E⊥c	19000±2000	0.79 ± 0.13

As a general comment, it is evident from Table 2 that the choice of the absorption coefficient is crucial when quantifying the amount of H_2O and CO_2 in beryl: using the curve of

Libowitzky and Rossman (1997) the final total H_2O content is in fact halved with respect the result obtained when using the coefficients calibrated by other authors. In addition, the relative amount of type I / type II water is also reversed. Therefore, until the ε coefficients are calibrated for beryl, the values reported in Table 2 must be considered just indicative of the real H_2O and CO_2 contents. For CO_2, in particular, Della Ventura *et al.* (2012) provided recently a reliable molar absorption coefficient based on a combination of SIMS + FTIR data on a well-characterized set of samples. However, at present, it is unknown whether the ε_{CO2} coefficient calibrated for cordierite can be exported to beryl.

A second point to note is that, although the nominally dry experimental conditions, the maximum amount of water incorporated into the sample is however significantly higher than that of CO_2. As explained above, the absolute H_2O/CO_2 amounts can be affected by the use of wrong the ε_{H2O} coefficients, however, it is indisputable that the FTIR spectra of Figure 4 show significant H_2O in the examined sample. Such relatively H_2O content is probably the result of the different pressure medium used in this experiment compared to those described in Chapter 5 and 7. Indeed, the beryl described in this chapter was treated in an externally heated vessel using H_2O as a pressure medium, while the experiments described in Chapter 5 and 7 were performed in a piston-cylinder apparatus, where pressure is transmitted by NaCl.

3.2 Polarized-light FPA imaging

The distribution of $H_2O^{[I]}$, $H_2O^{[II]}$ and CO_2 across the treated beryl was studied by using polarized SR-FTIR FPA imaging; in this work, polarized light was necessary to differentiate the absorptions related to $H_2O^{[I]}$ and $H_2O^{[II]}$ (*e.g.* Della Ventura *et al.*, 2010). Contour maps were obtained by integrating the ν_3 antisymmetric stretching mode of $H_2O^{[I]}$ at 3699 cm^{-1} (Fig. 5b) for E//c, the ν_1 symmetric stretching mode of $H_2O^{[II]}$ at 3602 cm^{-1} (Fig. 5c) for E//c, and the ν_3 antisymmetric stretching mode of CO_2 at 2360 cm^{-1} (Fig. 5d) for E⊥c.

Figure 5b shows that $H_2O^{[I]}$ is distributed rather homogeneously across the sample, except close to the core of the grain, where the $H_2O^{[I]}$ content is almost 70%. $H_2O^{[II]}$ is also distributed rather homogeneously (Fig. 5c), however along the hourglass boundary its content decreases also about 70%. CO_2 on the opposite is distributed exclusively close to the (001) basal edges of the crystal, as expected, and, surprisingly, along the hourglass boundaries.

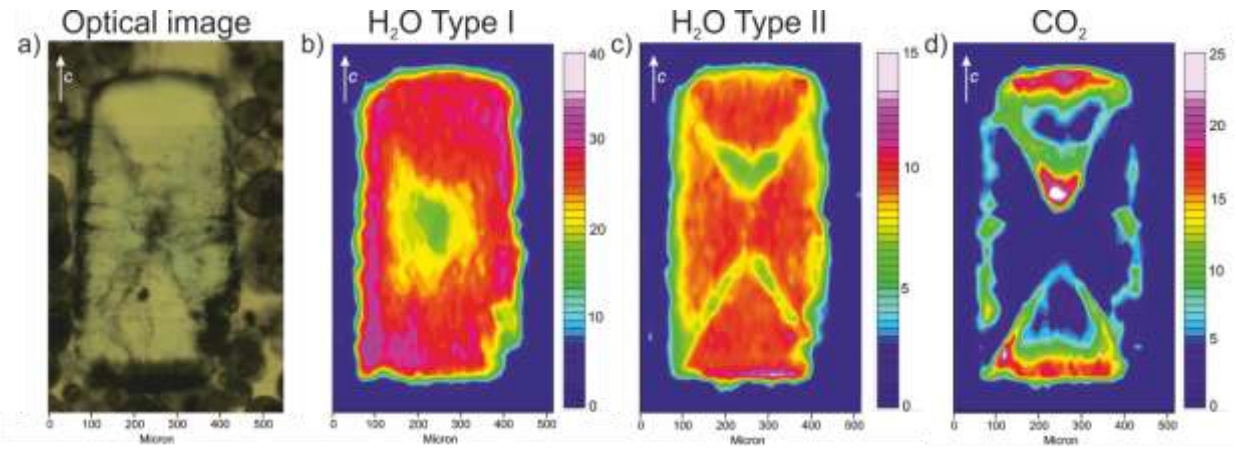

Figure 5 – Polarized light FPA images of the treated beryl sample. (a) optical image, (b) E//c FTIR-FPA contour map of $H_2O^{[I]}$ and (c) $H_2O^{[II]}$ distribution, and (d) E⊥c FTIR-FPA contour map of CO_2 distribution. Chromatic scale is proportional to H_2O/CO_2 content. Data collected under conventional FTIR light.

Figure 6b shows the diffusion profile for $H_2O^{[I]}$ (open circles), $H_2O^{[II]}$ (open triangles) and CO_2 (solid squares) along the AA' trace of Figure 6a. Single-spot SR-FTIR analyses were collected with a beam size of 20x20 µm and absorbance data were obtained by integrating the mode at 3699 cm^{-1} for $H_2O^{[I]}$, the ν_1 mode at 3602 cm^{-1} for $H_2O^{[II]}$ and the ν_3 mode at 2360 cm^{-1} for CO_2. The intensity data for each band were scaled to its maximum intensity. The diffusion profiles confirm the observations from Figure 5: the $H_2O^{[I]}$ content (open circles) is almost constant until ~200 µm from the grain edge, then progressively decrease close to the core of the grain. The $H_2O^{[II]}$ content (open triangles), on the other hand, is almost constant from rim to core; it decrease in the vicinity of the hourglass boundary crossed by the profile (Fig. 6a) and then increases again. The CO_2 absorbance (solid squares) has a trend opposite to $H_2O^{[II]}$: starting from the edge of the grain it decrease progressively until it reaches a minimum around 130 µm from the edge. The CO_2 content in addition shows two relative maxima around 200 and 280 µm from the edge, and finally goes to zero at the core of the grain. The relative maxima in CO_2 content correspond to fractures present inside the treated grain as also shown by the XPL picture (Fig. 6a).

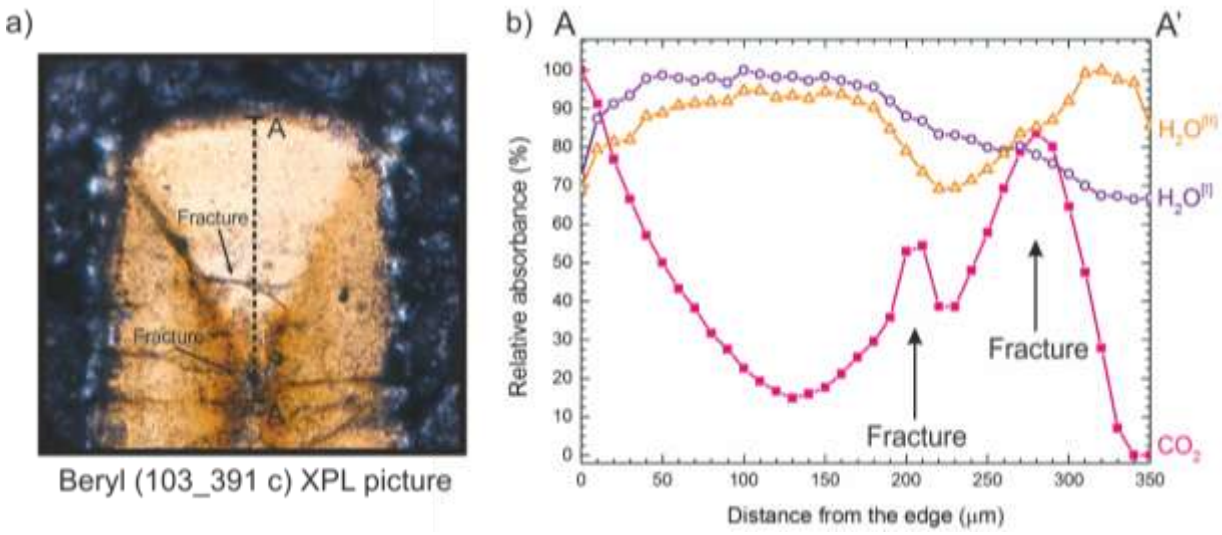

Figure 6 – (a) XPL image of the treated beryl. (b) Absorbance profiles along the AA' trace in (a) for $H_2O^{[I]}$ (open circles), $H_2O^{[II]}$ (open triangles) and CO_2 (solid squares); intensity data are expressed as % of the maximum intensity for each target molecule. A fracture is present about 200 μm from the grain edge and a hole at about 280 μm. Spot size 15x15 μm, step 10 μm.

4. Discussion

4.1 Hourglass zoning and CO_2 diffusion

During the experiments of CO_2 diffusion in beryl and cordierite (this Thesis, chapter 5) it was observed, in particular by high-resolution FPA imaging, that carbon dioxide diffusion in beryl is faster along the structural channels parallel to [001], and eventually along fractures presents in the grain. This behavior is in agreement with the diffusion mechanism of H_2O in beryl (Fukuda *et al.*, 2009). The spectroscopic image given in Figure 5d clearly demonstrates that the CO_2 diffusion proceeds from the (001) surface into the grain along the [001] direction. Single-spot, quantitative data collected on a traverse parallel to [001] (Figure 6b) in addition show that the CO_2 concentration profile follows the typical one dimensional diffusion trend (see for example Fukuda *et al.*, 2009, Zhang and Cherniak, 2010, and this Thesis, chapter 5) up to about 130 μm from the crystal edge.

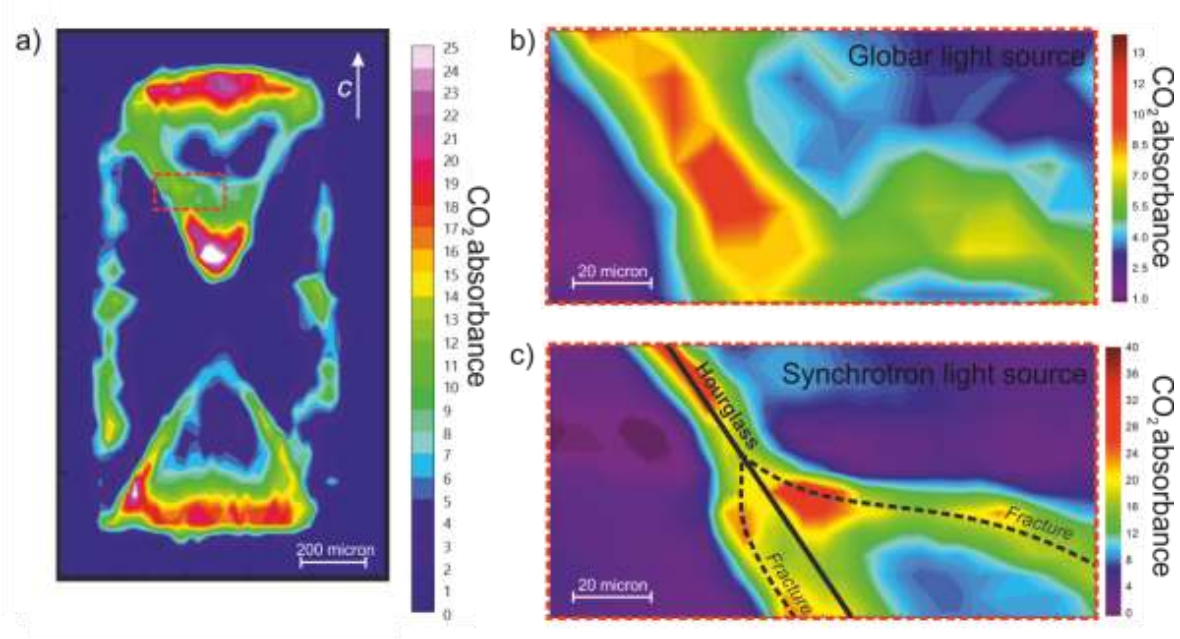

Figure 7 – Contour map of CO_2 distribution in the indicated (red broken-line box) portion of the beryl sample; spectra collected with synchrotron. The traces of the "hourglass" growth structure and the fractures are highlighted. The same image obtained using a Globar IR radiation is given for comparison. Chromatic scale is proportional to the CO_2 content, units are arbitrary.

However, Figure 5d shows a feature that has never been observed so far, *i.e.* a clear and significantly increased diffusion of CO_2 along the boundaries of the hourglass zoning of chromium. In other words, the FPA images show that the hourglass boundary acts as a preferential, fast pathway, for the CO_2 diffusion. Figure 7c displays a higher-resolution FPA image of the CO_2 distribution across the hourglass boundary. The image was collected using a synchrotron source, a spot size of 10 x 10 µm and a step of 5 µm, *i.e.* oversampling the analytical points by significant overlapping of the signal; accordingly, these conditions ensure both a very high spatial resolution and an excellent signal-to-noise ratio (Della Ventura *et al.*, 2014). Figure 7b gives also, for comparison, the FPA image obtained on the same area when using a conventional IR source; the gain in resolution due to the use of SR radiation is evident. From Figure 7c it is possible to distinguish two main directions of CO_2 diffusion: one parallel to the hourglass boundary (solid line) and a second along a fracture inside the grain (dashed line) that is well visible in the optical image in Figure 6a. To get a better insight into this issue we tried to check whether or not a physical discontinuity, *i.e.* a crack, was formed during the heat/pressure treatment, thus implying that the hourglass structure simply acted like a fracture in enhancing the CO_2 diffusion (this Thesis, Chapter 5).

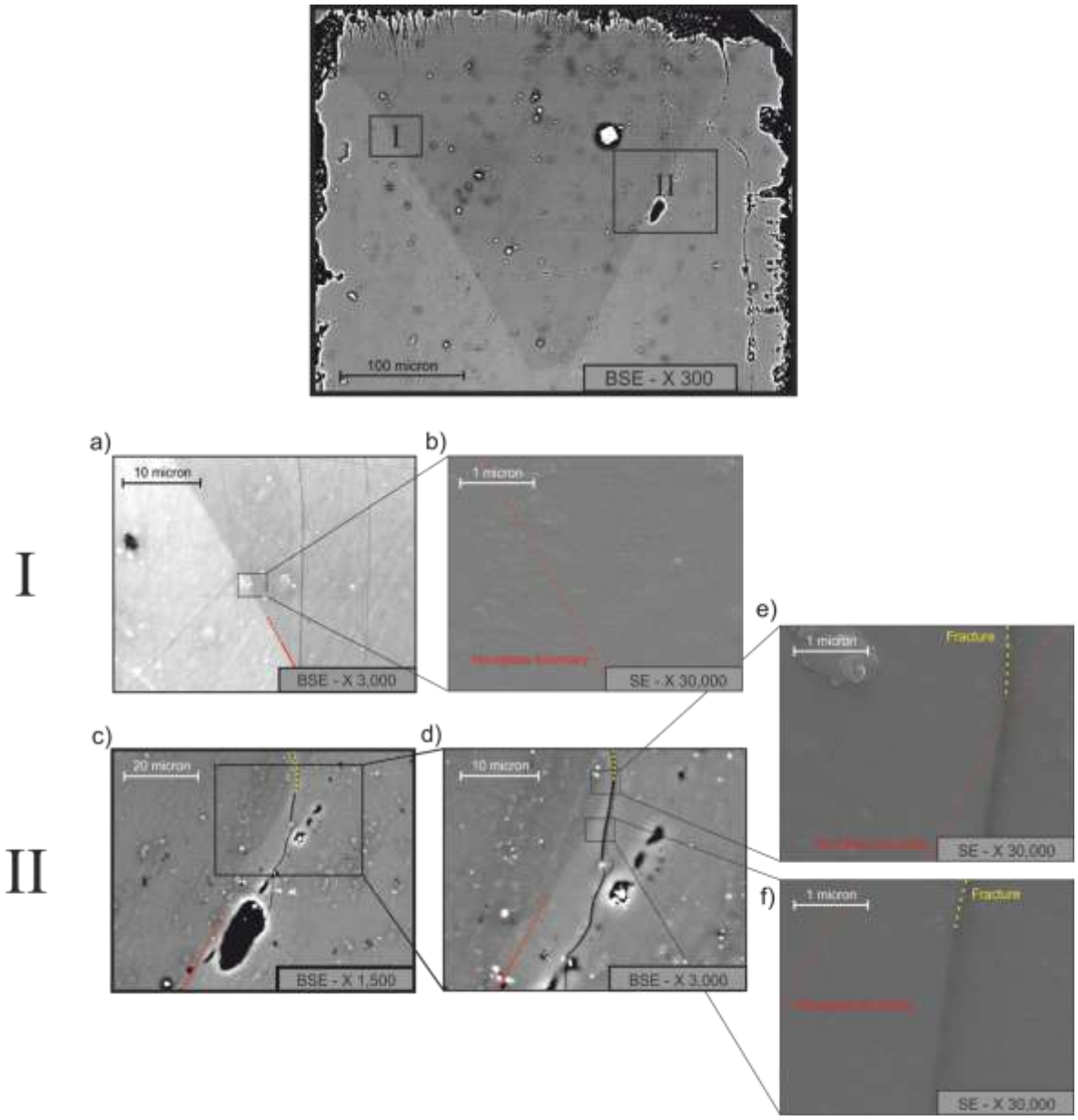

Figure 8 – FESEM pictures of the treated beryl sample in correspondence of the "hourglass" structure, in a fracture-free area (a and b) and in a fractured area (c, d, e and f). Note that in a, c and d the BSE compositional images of the investigated areas are given, while in b, e and f the morphological SE images are displayed. The red dashed line indicates the limit of the "hourglass" sector zoning and the yellow dashed line indicates a fracture in the grain.

Figure 8 shows high-resolution FESEM (Field-Emission SEM) images of selected areas of the studied sample. The areas were chosen across the hourglass boundary, both in a point optically clean and without fractures (Fig. 8a) and in a second point characterized the presence of a fracture (Fig. 8c). The BSE (back-scattered electron) pictures displayed in Figures 8a and 8b show how the higher magnification images given in Figures 8b, 8e and 8f were indeed collected across the hourglass boundary, *i.e.* across the compositional discontinuity due to the different Cr contents, and across a fracture (Fig. 8d) running semi-parallel to this boundary. High-resolution SE (secondary electrons) morphological images

collected in the area displayed in Figure 8a show a perfectly flat surface suggesting that no cracks are present along the hourglass boundary (Figure 8b, see red broken line), while in correspondence of the fracture optically visible in Figure 8c (yellow dashed line) a defined groove is clearly present (Figs. 8d to 8f). The FESEM images of Figure 8 thus allow the conclusion that, at least at the scale of tenths of nm, the hourglass structure is exclusively due to a compositional inhomogeneity, and that there is no physical discontinuity along the compositional boundary. This being the case, the diffusion path observed along this structure (Figs 5 and 6) cannot be explained on the basis of a fracture-enhanced diffusion mechanism, therefore the process responsible for the enrichment of CO_2 in specific directions of the sample (*i.e.* along the hourglass boundaries) is probably similar to a defect-enhanced mechanism.

Hollister (1970) showed that differences in growth rates of different crystal faces may causes a mismatch in the periodical structure, and concluded that this mechanism may be responsible for the formation of sector zoning in minerals. The mismatch is usually characterized by chemical zoning, which is controlled by the presence of particular ions in the supply material, by differences in local charge-balance and/or atomic geometrical conditions (Hollister, 1970, Bahat, 1974); for instance this process has been shown to be responsible for Pb zoning in synthetic cordierite (Wunder *et al.*, 1991), Cr zoning in Be-indialites (Mikhailov *et al.*, 2007) and can explain the Cr zoning in the crystals studied here (Fig. 5).

The images of Figure 7c suggest that the defects arising from the structural mismatch likely speed up the diffusion of CO_2, similarly to what observed along a fracture. Zhang *et al.* (2006) studied the oxygen diffusion in titanite under different experimental conditions and observed that planar defects may act as fast-path for diffusion inside the crystal lattice and that diffusion along these directions may be even 4 - 5 orders of magnitude faster than the lattice diffusion at the same PTt conditions. A similar mechanism could explain the penetration of CO_2 down to the core of the grain along the hourglass discontinuity. A consequence of this discussion is that, in experimentally treated samples, several diffusion mechanisms may locally act; for example, in the studied case, our spectroscopic data suggest the possible combination of (a) a fast-path defects diffusion, (b) a fracture-induced diffusion and (c) a structural-channel diffusion (this Thesis, Chapter 5). Therefore, in diffusion studies, a careful characterization of the possible inhomogeneous distribution of the target molecule

inside the matrix is mandatory because measurement of diffusion coefficients could be complicated by local effects.

4.2 The role alkali ions on the H_2O diffusion

The images displayed in Figures 5c and 5d suggest that the role of the hourglass zoning on the H_2O diffusion is extremely different to that so far discussed for CO_2. As a matter of fact, the FTIR-FPA data show that while type I H_2O diffusion is not affected by the chemical zoning (Fig. 5b), $H_2O^{[II]}$ incorporation/speciation is significantly decreased where CO_2 concentration is higher, and where Na has been locally replaced by K (compare Fig. 3c with Fig. 5c).

In Figure 1b we showed that both H_2O and CO_2 share the same crystallographic position (2a) in the channel, thus we would expect that areas with a higher concentration of CO_2 (like the hourglass traces) presented a lower global H_2O content. However, the FPA images show that only $H_2O^{[II]}$ is depleted along the hourglass traces, while $H_2O^{[I]}$ is unaffected. In the introduction we mentioned that $H_2O^{[II]}$ is strongly associated to the monovalent cations inside the channels (Wood and Nassau, 1968; Goldmann *et al.*, 1977), and we also mentioned that in beryl K^+ and other larger cations are located in the larger 2a site (Hawthorne and Černý, 1977), where $H_2O^{[II]}$ is also located; in Figure 3 we observe that along the hourglass boundary there is an increase in K^+ and a decrease of Na^+. Considering that $H_2O^{[II]}$ may be associated preferentially, if not exclusively, to Na^+, we conclude that the $H_2O^{[II]}$ depletion along the hourglass discontinuity may be the combined result of a paucity of Na (which is preferentially bound to H_2O) and an increase K^+ content at the 2a site (Fig. 1). In other words, the presence of K filling the 2a sites would prevent the occurrence of H_2O at the same site (compare Fig. 3c and 3d with Fig. 5c). Aines and Rossman (1984) in their high-T study of water and CO_2 in cordierite and beryl concluded that CO_2 probably acts as a partial plug for the diffusion of H_2O along the cordierite channels. The same feature was also observed by Johannes and Schreyer (1981) in their hydrothermal equilibration studies on cordierite. Additionally CO_2 may alter the local thermodynamic equilibrium of H_2O, affecting a particular speciation of water, similarly to the problem of diffusion and speciation of OH and H_2O in melt/glasses. Based on these considerations, we suggest that an additional reason for the depletion of $H_2O^{[II]}$ along the hourglass boundary could be simply connected with the increased amount of CO_2. As a final comment, Fukuda *et al.* (2008) observed in their

experiments that the dominant diffusive species along the beryl channels was type I H_2O relatively to type II H_2O, however the FTIR-FPA images of Figure 5 show that this is not the case in our samples, and clearly suggest that there is no major difference in the diffusivity of the two water types, which seems to be controlled only by the alkali content. We have no explanation at this moment for this discrepancy.

CHAPTER 7

SPECIATION AND DIFFUSION PROFILES OF H_2O IN WATER-POOR BERYL: COMPARISON WITH CORDIERITE

Abstract

This chapter reports the polarized FTIR study of two beryl samples treated in CO_2-rich atmosphere, at 700°C and 800°C, 700 MPa, respectively. The infrared spectra, as expected, show the presence of CO_2 but also of minor H_2O due to moisture present in the starting products used for the synthesis. FPA-FTIR images show that H_2O diffuses into the beryl matrix along the structural channels oriented parallel to [001]. Spectra collected along profiles parallel to the *c* crystallographic axis show subtle changes as a function of the distance from the crystal edge; these changes can be correlated to a progressive change in the H_2O coordination environment in the channel, as a response to the varying H_2O/alkali ratio. In particular, the data show that when $2 \cdot H_2O > Na^+$ apfu, H_2O can assume both type I and type II orientation; in the latter case, each Na cation coordinates two $H_2O^{[II]}$ molecules (doubly coordinated H_2O). If $2 \cdot H_2O < Na^+$ apfu, then $H_2O^{[II]}$ molecules are singly coordinated to each Na cation. The same type of feature is observed and commented for the structurally related cordierite.

1. Introduction

Beryl, ideally $Be_3Al_2Si_6O_{18}$, is an accessory mineral typical of pegmatitic and granitic rocks (*e.g.* Deer *et al.*, 2006). In the beryl structure, SiO_4 tetrahedra share common oxygens to form six-membered hexagonal rings with $[Si_6O_{18}]^{12-}$ composition (Fig. 1a); the stacking of these rings along the crystallographic *c* direction give rise to cages which are connected into open channels parallel to [001] (Fig. 1b). The cages diameter is about 5.0 Å (Gibbs *et al.*, 1968), while the bottle necks of the channels have a diameter of 2.8 Å (Fukuda and Shinoda, 2011). For this reason beryl, as well as the isostructural cordierite, are of interest as a model for microporous materials. It is known since the early work of Wood and Nassau (1967, 1968) that several atoms and molecular groups may be present in the structural voids of beryl.

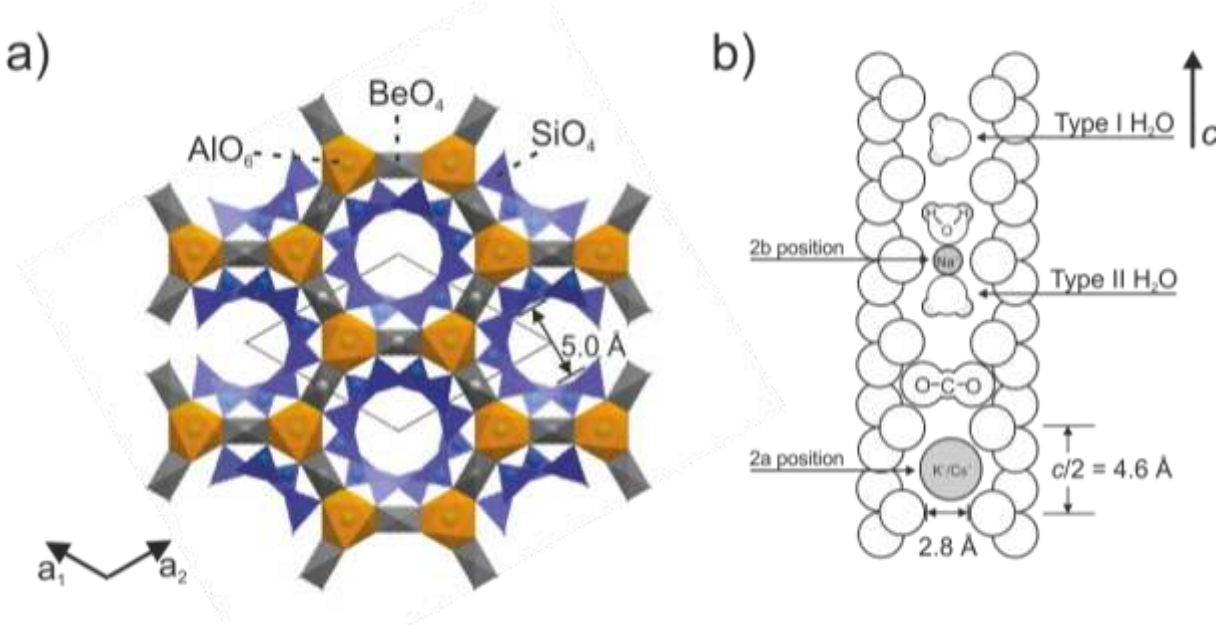

Figure 1 - Schematic representation of the crystal structures of beryl viewed down the crystallographic *c* axis (a) and parallel to the (100) plane (b). In blue the Si site, in orange the Al site and in gray the Be site. Mean distances in the crystal cages are reported. The position on CO_2 and H_2O molecules are shown (modified after Fukuda and Shinoda, 2011).

In particular, water and carbon dioxide (Wood and Nassau, 1968, Aines and Rossman, 1984) which are both located in the wider parts of the channels (2a position, Fig. 1b). Possible OH groups (Wickersheim and Buchanan, 1959, Aurisicchio *et al.*, 1994) and large ions such as Cs and K are almost exclusively located at the 2a position (Hawthorne and Černý, 1977) while smaller cations like Na^+ (Wood and Nassau, 1968) always occupy the

narrower 2b site (Fig. 1b). The linear CO_2 molecules are oriented orthogonally to the *c* axis (Wood and Nassau, 1968; Aines and Rossman, 1984). H_2O groups occur in the structural channels with the molecular plane parallel to (100) but with two different possible orientations (Fig. 1b): type I H_2O (hereafter $H_2O^{[I]}$) has with the H–H vector parallel to the *c* axis, while type II H_2O ($H_2O^{[II]}$) has the H–H vector perpendicular to the *c* axis (Wood and Nassau, 1968). H_2O molecules of the latter orientation are bonded locally to alkali cations at the 2b site in a 2:1 ratio (Goldmann *et al.*, 1977; Hawthorne and Černý, 1977), however, Fukuda and Shinoda (2008, 2011) showed recently that in a low-H_2O environment $H_2O^{[II]}$ may be bound to only one alkaline cation.

In the present PhD work, several volatile-free beryl single-crystals were treated in CO_2-rich environment at different *PTt* conditions, in order to study CO_2 diffusion in the structural channel (see Chapter 5). After the experimental runs, FTIR spectroscopy showed systematically the presence of weak amounts of H_2O in the samples. Due to the absence of water as a pressure medium during the experiments (see below), the H_2O trapped in the beryl is inferred to originate from the moisture adsorbed by the used materials during the tube preparation; because of this, diffused H_2O contents are very low. For this reason, a detailed polarized FTIR spectroscopic study was carried out to study the local environment of such trace amounts of water into the beryl structure, such as to contribute to the knowledge of the coordination environment and the physical state of H_2O in beryl, after the extensive studies of Kolesov (2008), Fukuda and Shinoda (2008, 2011) and Fukuda *et al.* (2009).

2. Experimental methods and studied materials

Experiments were carried out using synthetic H_2O and CO_2-free beryls (Hautefeuille and Perrey, 1888, 1890; Bellatreccia *et al.*, 2008, this Thesis, cap. 5) as starting materials. Single-crystals were packed into Pt tubes together with crushed Al_2O_3 powder as inert, and silver carbonate as a CO_2 source and treated at different *PTt* conditions. Two samples were selected for the present study, treated at the same *P* = 700 MPa and *T* = 700 °C (Pa_340 r) and 800 °C (Pa_340 o), respectively. Experiments were done using a non end-load piston-cylinder apparatus QUICKpress™ at the HP-HT Laboratory of Experimental Volcanology and

Geophysics of Instituto Nazionale di Geofisica e Vulcanologia (INGV, Rome, Italy). After the run, the recovered crystals were oriented along (hk0) using the external morphology.

FTIR spectra were acquired using a Bruker™ Hyperion 3000 microscope equipped with a conventional Globar IR source, a KBr broadband beamsplitter and a liquid nitrogen-cooled MCT detector, at Laboratori Nazionali di Frascati, Istituto Nazionale di Fisica Nucleare (LNF-INFN), in Frascati (Rome). The polarized spectra were collected using a gold-wire-grid polarizer. The nominal resolution was 4 cm^{-1} and 128 scans were averaged for both spectrum and background. FTIR images were collected with a 64 x 64 pixel focal-plane array (FPA) of liquid nitrogen-cooled MCT detectors coupled with a 15x Schwarzschild objective. The nominal resolution was set at 4 cm^{-1} and 64 scans were averaged for both spectrum and background; each image covers an area of 170 µm x 170 µm with a spatial resolution close to 5 µm (Della Ventura *et al.*, 2010, 2014). Polarized FTIR profiles were performed with a spot size 25 X 80 µm, collecting the data at steps of 20 µm.

Selected polarized FTIR spectra, collected on the crystal edge (see below) are given in Figure 2. The spectra show a sharp and very intense peak at 2360 cm^{-1} for E⊥c which is assigned to the antisymmetric stretching mode of CO_2, and a group of sharp peaks in the H_2O stretching region (3750-3500 cm^{-1}).

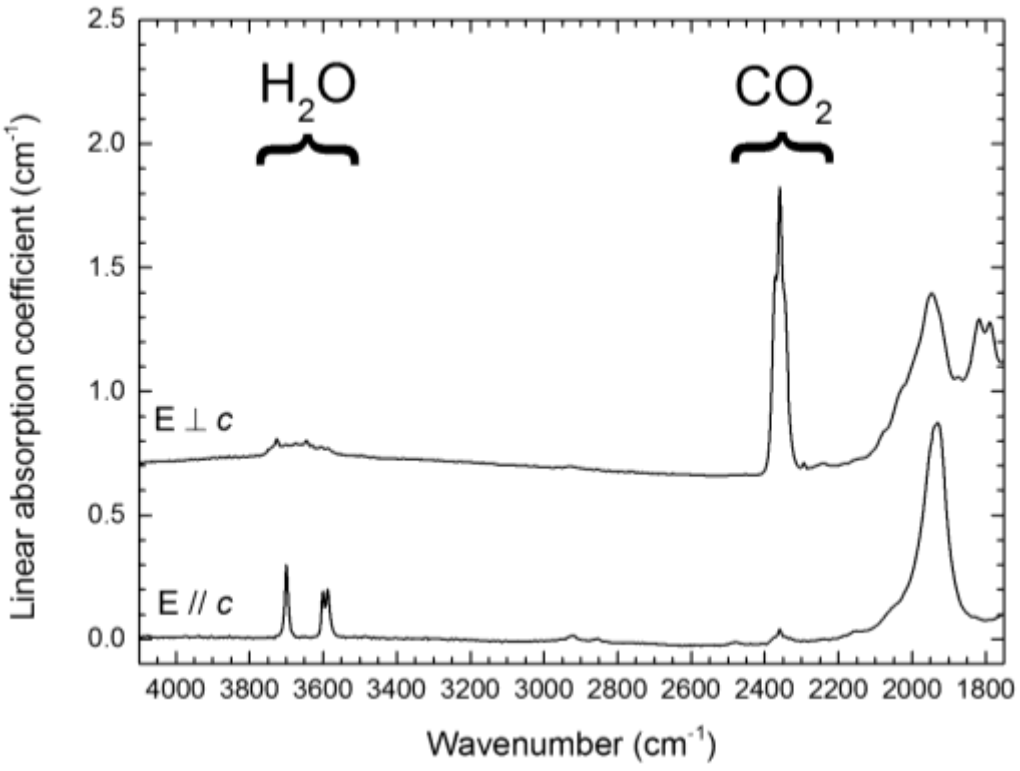

Figure 2. Polarized FTIR spectra of sample Pa 340_o collected on the crystal edge (see text for explanation).

Peak areas were determined using the routine built into the spectrometer software; the spectra were decomposed using Origin 9™ by using a Lorentzian shapes for all components except for the broad absorption at 3665 cm^{-1} which was modeled as a Gaussian band (Kolesov, 2008). Peak positions and widths were constrained to be constant and the background was modeled as linear; an example is given in Figure 3.

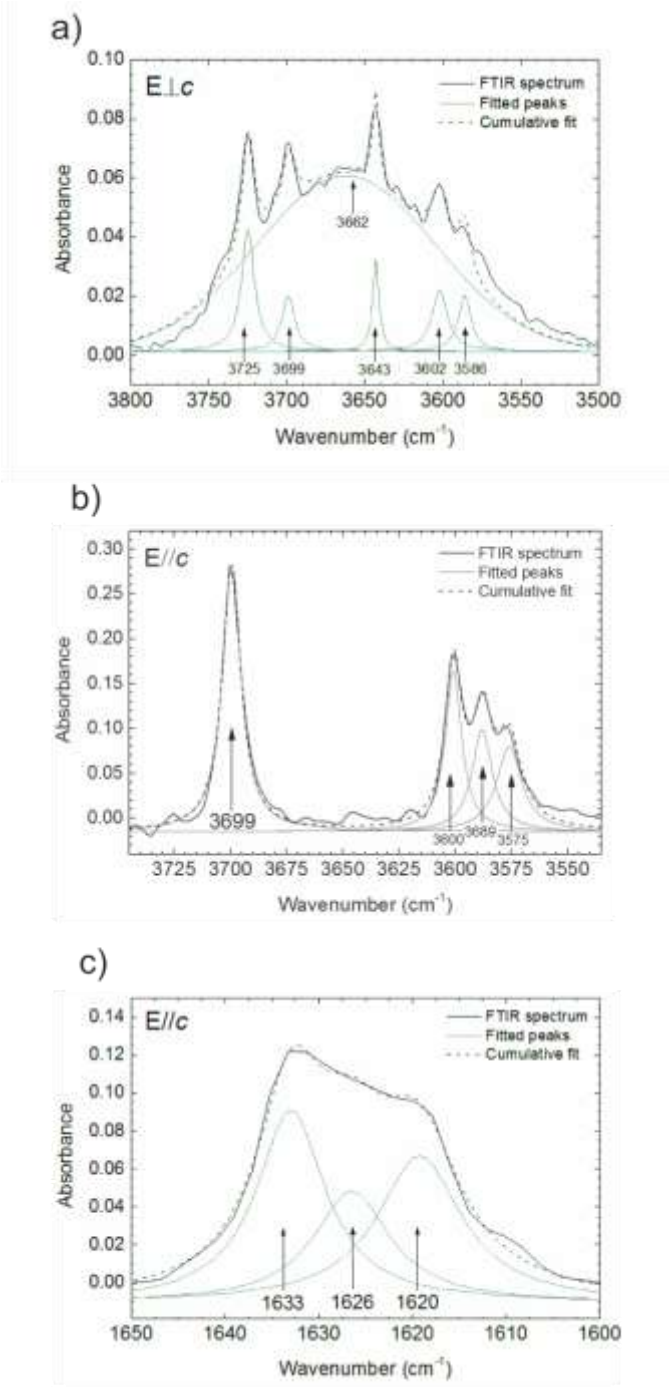

Figure 3 - Decomposed single-crystal polarized FTIR spectra of beryl Pa 340_r in H_2O stretching region for (a) E⊥c and (b) E // c, and in H_2O bending region (c). Experimental spectrum = black line, fitted peaks = gray line, calculated pattern = dashed black curve; peak position are reported.

The maximum amount of water and CO_2 incorporated into the sample were quantified, via the Beer-Lambert relationship, see this Thesis, cap 6. Absorbance values (A) were obtained from polarized data collected on the edge of the grain (see below); the used mode, type of absorbance and molar absorption coefficients are summarized in Table 1.

Table 1 – Used mode, method, absorption coefficients and resulting H_2O and CO_2 contents (ppm) for the studied beryl samples. For explanation, see text.

Linear abosorbance data; ε_i values from Charoy *et al.* (1996) for type I H_2O, and from Goldman *et al.* (1977) for type II H_2O				
Molecule	Mode, position and polarization	ε_i ($l \cdot mol^{-1} \cdot cm^{-1}$)	Pa_340_r	Pa_340_o
Type I H_2O	ν_3 at 3699 cm^{-1}, E//c	197	1215 ± 172	544 ± 77
Type II H_2O	ν_1 at 3602 cm^{-1}, E//c	256	725 ± 102	611 ± 86
Total H_2O				
Integrated absorbance data; ε_i values recalculated after Charoy *et al.* (1996), see also Chapter 5				
Molecule	Mode, position and polarization	ε_i ($l \cdot mol^{-1} \cdot cm^{-2}$)		
CO_2	ν_3 at 2360 cm^{-1}, E⊥c	70000±7000	1795 ± 276	1071 ± 159

3. FTIR-FPA imaging

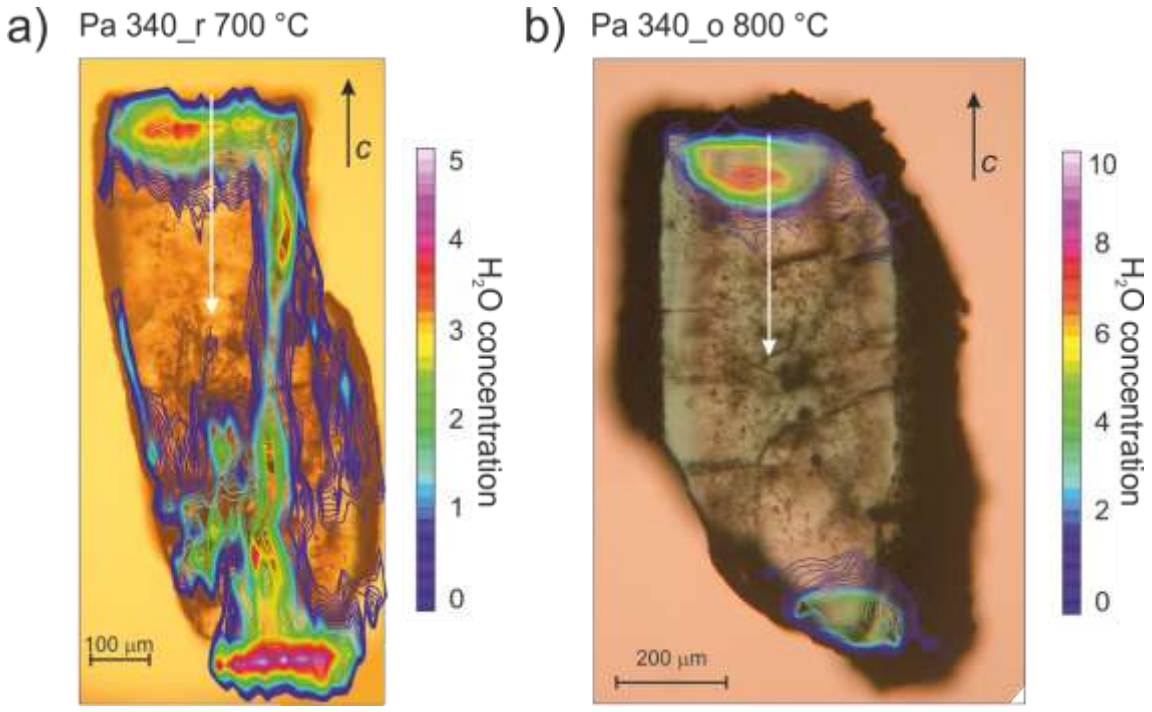

Figure 4 – FTIR-FPA images of the H_2O distribution for (a) sample Pa 340_r, (107 µm thick section) treated at 700 MPa, 700 °C for 24 hrs and (b) sample Pa 340_o (188 µm thick section) treated at 700 MPa, 800 °C for 10 hrs. Color scale is proportional to water concentration (integration range 3740-3565 cm^{-1}), units are cm^{-1}. The white arrows indicate the direction FTIR profile in Figure 5.

The FPA-FTIR maps of the H_2O distribution within the studied samples (Fig. 4) shows that the H_2O content is maximum at both edges of the crystal or in fractures along the sample (Fig. 4a, see also Chapter 5). Based on single-spot FTIR data Fukuda *et al.* (2009) inferred that the H_2O diffusion in beryl proceeds exclusively along the structural channels parallel to the *c* crystallographic axis, implying that the H_2O content must be maximum on the edge of the grain, then progressively decrease toward the crystal; this is what we actually observe using FPA imaging (Fig. 4), and, more generally, in all beryl and cordierite samples studied during this Thesis (chapters 5 and 6). The white arrows in Figure 4 indicate the profiles along which we collected FTIR single spot data used for the discussion presented below. Based on the FPA images, we thus assume that proceeding from the edge of the grain along the analytical profile, the H_2O content progressively decreases, providing the possibility to compare the FTIR patterns collected on points with different H_2O contents, in the same matrix. For each point, the H_2O content was quantified using the polarized data, as explained above.

4. Polarized FTIR measurements

Figures 3a and 3b show an enlargement of the fitted spectra of Figure 2 in the water stretching 3800-3500 cm^{-1} region. For E⊥c (Fig. 3a) a very broad and convolute absorption is observed, centered at 3665 cm^{-1}; relatively sharp and intense peaks are resolved at 3725, 3643, 3602 and 3586 cm^{-1}, and a minor peak is also visible at 3699 cm^{-1}. The 3665 cm^{-1} band is assigned to the ν_3 mode $H_2O^{[II]}$, while the 3602 cm^{-1} component is assigned to the ν_1 mode of type I H_2O (see Fukuda and Shinoda, 2008). The sharp peaks at 3725 and 3586 cm^{-1} have never been observed in the water region for beryl when E⊥c; based on the data for cordierite, these bands can be related to the $\nu_3 + \nu_1$ and $\nu_3 + 2\nu_2$ combination modes of CO_2, respectively (Della Ventura *et al.*, 2009, 2012). This assignment is confirmed by their polarization behavior and by the excellent correlation between their intensity with that of the ν_3 mode of CO_2 (see Chapter 5). Assignment of the sharp 3643 cm^{-1} peak will be discussed in a later section. The E//c spectrum (Fig. 3b) shows a sharp and intense peak at 3699 cm^{-1} which is assigned to the ν_3 mode $H_2O^{[I]}$ (Wood and Nassau, 1967); this band occurs also in the E⊥c spectrum with a very low intensity (Fig. 3a), possibly due to a slight

misalignment of the section. In Figure 3b two relatively intense peaks are resolved at 3600 and 3589 cm^{-1}, respectively. The former band is assigned to the v_1 mode of type I H_2O. The latter component can be assigned to the v_1 mode of a new water configuration in beryl, *i.e.* to the "singly coordinated" type II water (Fukuda and Shinoda, 2008); this point will be discussed in more details below. The E//c spectrum in the H_2O bending region (Fig. 3c) shows two components centered at 1633 and 1620 cm^{-1}. Based on the work of Fukuda and Shinoda (2008, 2011) these peaks can be correlated with the v_2 bending motion of $H_2O^{[II]}$.

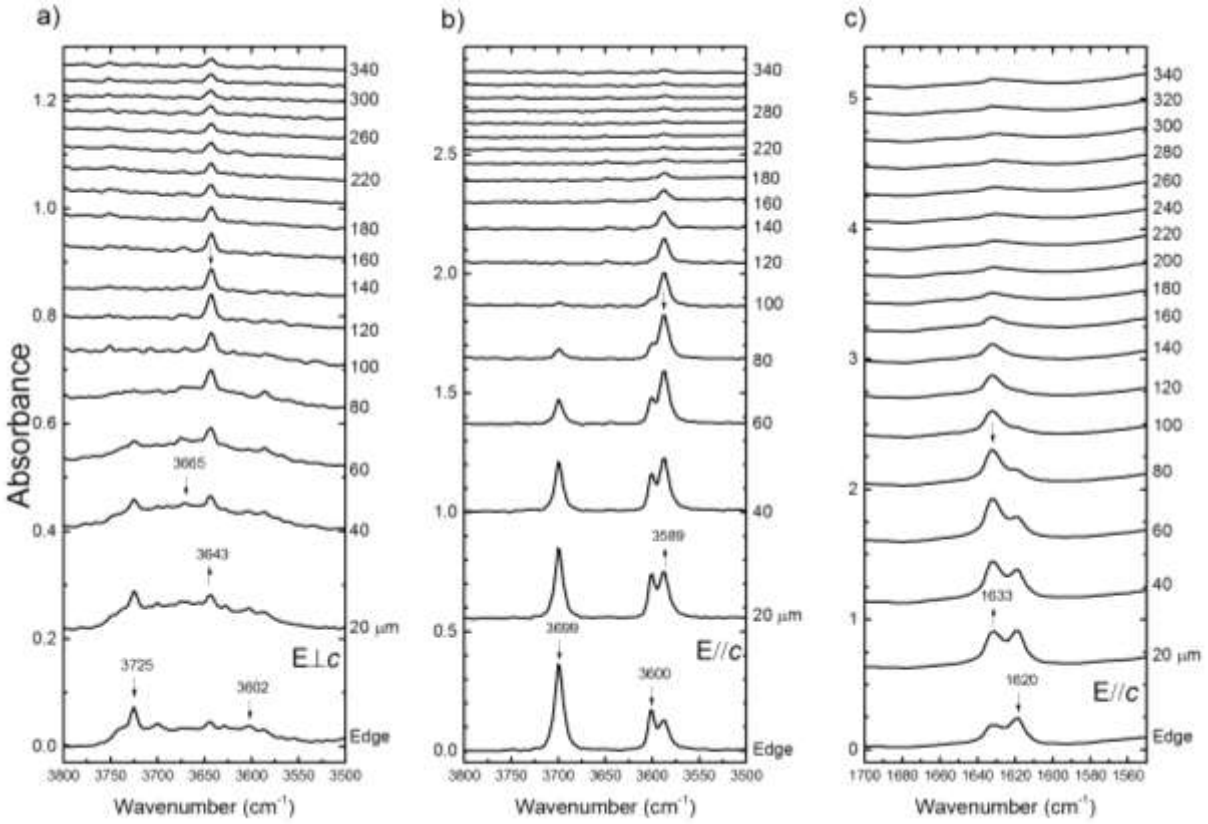

Figure 5 - Polarized IR spectra collected for sample Pa 340_r in the H_2O stretching region with (a) E⊥c and (b) E//c, and in the H_2O bending region (c) for E//c. The distance from the grain rim is indicated on the right. Upward and downward arrows indicate increase or decrease in the peak intensity.

The evolution of the polarized FTIR patterns of sample Pa 340_r, as a function of the distance from the crystal rim, is given in Figure 5; it is evident that several variations occur in the spectra, and, as explained above, these variations are connected with the progressive decrease in the H_2O content. In particular, the intense band at 3699 cm^{-1} rapidly decreases while progressing within the crystal, and disappears at a distance > 120 μm from the rim (see spectra for E//c in Figure 5b). The broad band at 3665 cm^{-1} (for E⊥c, Fig. 5a) and the sharp peak at 3600 cm^{-1} (for E//c, Fig. 5b) also decrease progressively in the same range. By

contrast, the sharp peak at 3643 cm^{-1} (E⊥c, Fig. 5a) and the 3589 cm^{-1} component (E//c, Fig. 5b) initially grow in intensity and then eventually decrease, but persist up to 340 µm from the rim. In the bending region (spectra collected for E//c, Fig. 5c), the 1620 cm^{-1} component follows the same intensity variation of the 3665/3600 cm^{-1} pair, while the trend of the 1633 cm^{-1} component is similar to that of the 3589 cm^{-1} band. No absorptions related to the $H_2O^{[I]}$ bending mode (1626, 1600, 1544 cm^{-1} after Charoy *et al.*, 1996) were present in the spectra, probably because of the low H_2O contents.

Figure 6 clearly shows that the measured absorbance of the 3600/1620 and 3589/1633 cm^{-1} pair of bands are strongly correlated, and this feature, coupled with the fact that both sets of bands occur with E polarized in the same direction, allows their assignment to two different water molecules, but oriented in a similar way.

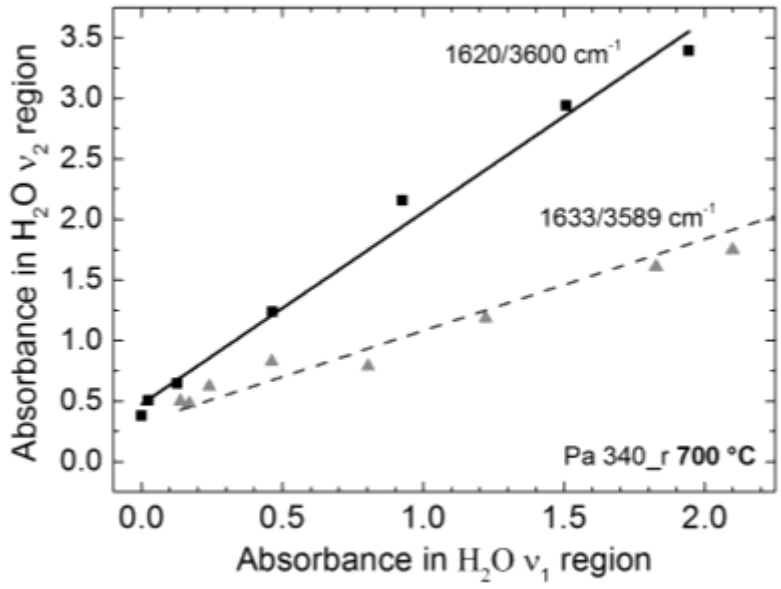

Figure 6 – Absorbance relationship between for the 1620/3600 cm^{-1} and 1633/3589 cm^{-1} peaks, sample Pa 340_r.

As discussed by Fukuda and Shinoda (2008) considering that these water molecules have different vibrational frequency, their coordination state in the structural channel must also be different. The 3643 cm^{-1} component, observed above in Figures 3a and 5a for E⊥c is also compatible with this scenario. From the recent work of Fukuda and Shinoda (2008, 2011) it is now clear that type II water occurs in the beryl channels with two bonding environments, called "doubly-coordinated" type II water, and "singly-coordinated" type II water in Fukuda and Shinoda (2008). The former molecule is characterized by a ν_3 mode

around 3660 cm^{-1} polarized for E⊥c, a ν_1 mode around 3600 cm^{-1} polarized for E//c, and a ν_2 mode around 1620 cm^{-1} polarized for E//c, while the latter molecule is characterized by a ν_1 mode around 3589 cm^{-1} polarized for E//c and a ν_2 mode around 1633 cm^{-1} polarized for E//c. The polarization direction and its behavior as a function of varying water contents, described above, allows assignment of the 3643 cm^{-1} to the ν_3 motion of singly-coordinated type II water. The spectra given in Figure 3 show in fact that the 3643 cm^{-1} peak is totally polarized for E⊥c, indicating that this peak is correlated with a water molecule having the H-H vector perpendicular to [001]. However, according to the extensive literature on the FTIR spectroscopy of beryl (*e.g.* Wood and Nassau 1967, 1968, Charoy *et al.*, 1996), the ν_3 mode of doubly-coordinated $H_2O^{[II]}$ is systematically observed at 3660 cm^{-1}, and typically in the form of a rather broad absorption (*e.g.* Adamo et al., 2008; see also Fig. 3 and 5). Bellatreccia *et al.* (2008) described the spectrum of a synthetic beryl containing a very low (~ 30 ppm) water content showing a very sharp peak at 3643 cm^{-1} polarized for E⊥c, paired with a less intense component at 3589 cm^{-1}, polarized for E//c.

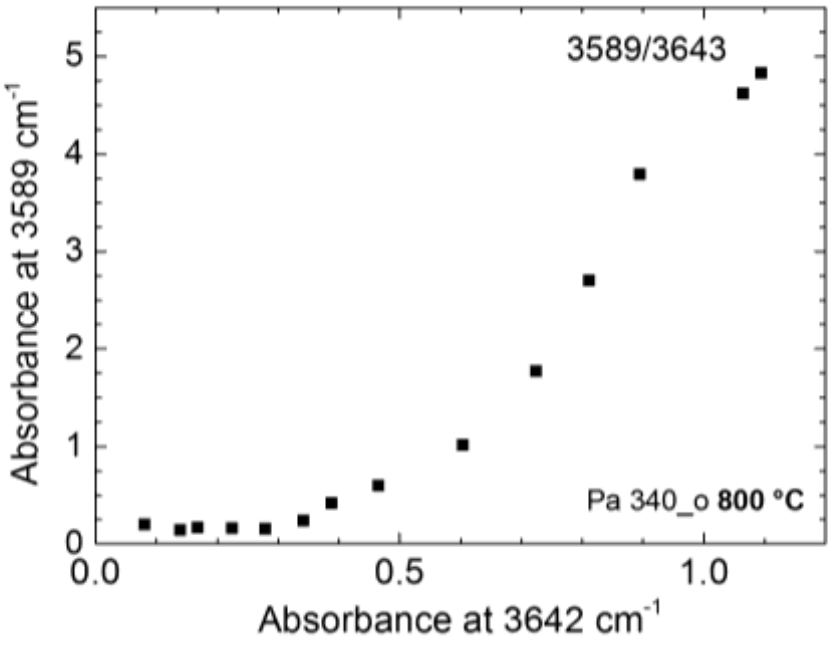

Figure 7 - Correlation between the measured intensity of the 3643 cm^{-1} and 3589 cm^{-1} bands in sample Pa 340_o.

Their pattern thus provides a definitive proof of the correlation between these two components, since no any other band appears in their spectra, and allows definitive assignment of the 3643 cm^{-1} band to the ν_3 mode of singly-coordinated type II water. In

agreement with this assignment, the intensities between the 3643 and 3589 cm^{-1} bands as a function of varying H_2O contents are also correlated, although there is some discrepancy at the very low concentrations due to the difficulties in the fitting procedure. Final band assignment is schematically displayed in Figure 8.

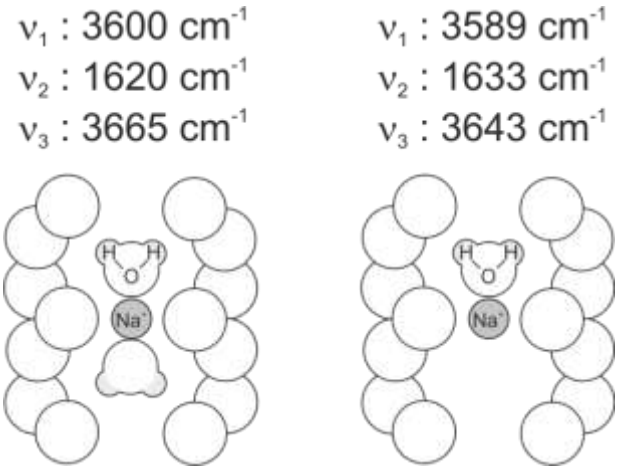

Figure 8 - schematic representation of the proposed band assignments (modified after Fukuda and Shinoda, 2008).

The integrated intensities of all bands in Figures 5 are plotted in Figure 9 as a function of the distance from the edge. Examination of Figure 9 shows that the $H_2O^{[II]}$ peaks at 3665, 3600 and 1620 cm^{-1}, all assigned to doubly-coordinated type II water are initially constant and then progressively decrease. The 3643, 3589, and 1633 cm^{-1} peaks, on the other hand, initially increase in intensity and then decrease progressively, but are still observed, although with a very low intensity, up to 340 μm from the rim. This behavior suggests that, while progressing within the crystal, because of the decreasing content in the channel $H_2O^{[II]}$ molecules modify their coordination environment from doubly-coordinated molecules to singly-coordinated molecules, the change occurring when the H_2O : Na apfu ratio becomes < 2 : 1.

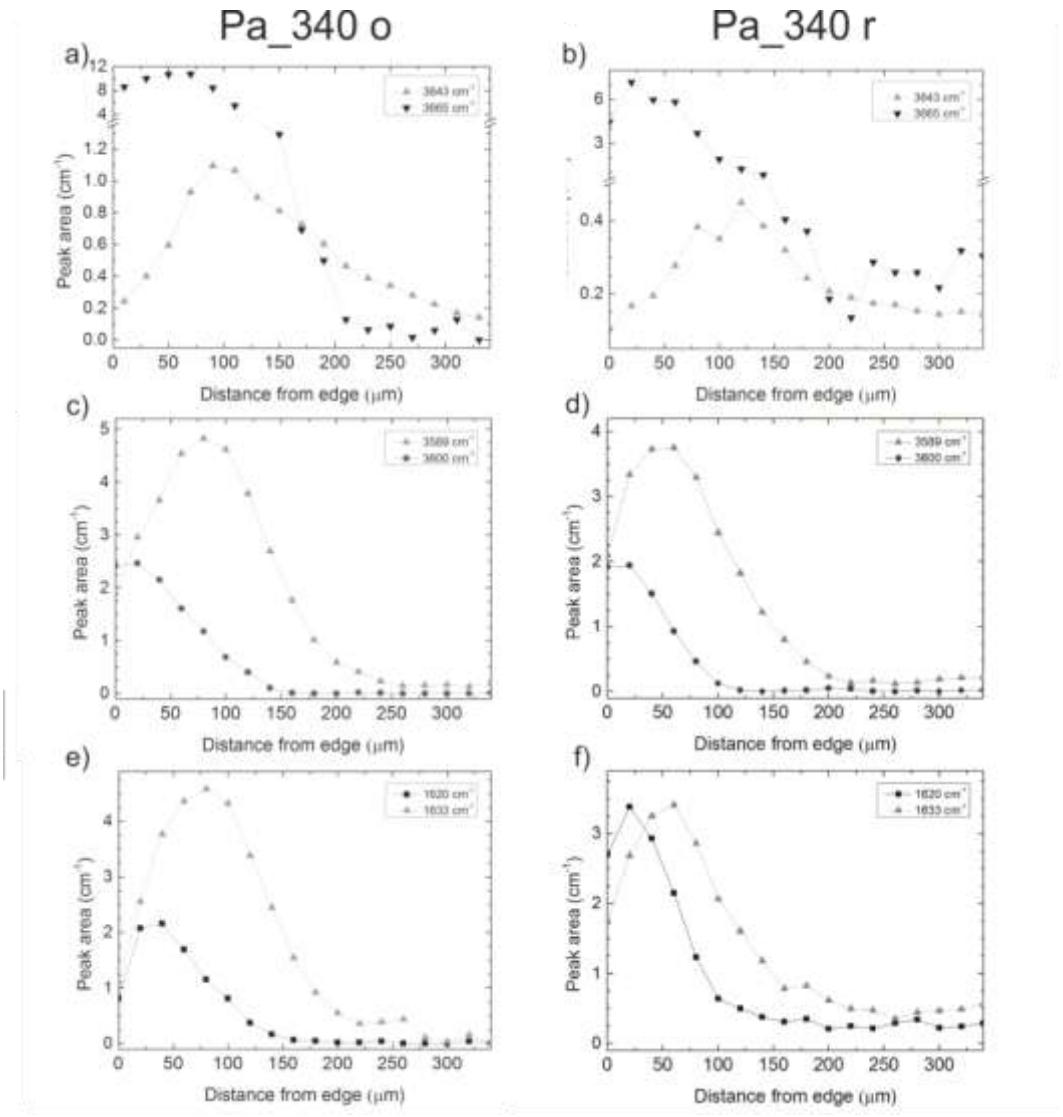

Figure 9 - Evolution of selected peak areas for sample Pa 340_o (a, c and e) and sample Pa 340_r (b, d and f).

5. The coordination of H_2O in beryl and cordierite

According to several studies, type II H_2O and alkali cations are typically in the ratio 2:1 in both beryl (*e.g.* Charoy *et al.*, 1996; Kolesov, 2008) and cordierite (*e.g.* Della Ventura *et al.*, 2010), suggesting that in both minerals each alkali cation is normally associated with two water molecules in the channel. However, both Fukuda and Shinoda (2008, 2011) and this work, provides evidence that in H_2O poor samples this relationship is no longer valid, and each alkali cation may coordinate to a single $H_2O^{[II]}$ molecule. The same point was also addressed by Kolesov (2008) in his analysis of Raman spectra collected on H_2O-poor beryl.

A theoretical approach to this feature has been provided by Bauschlicher *et al.* (1991) and Lee *et al.* (2004), who simulated the energy of $M(H_2O)_n^+$ clusters as a function of

increasing number of water molecules coordinating a metal cation (M). Accordingly, for increasing n, both the v_3 and v_1 stretching modes of H_2O shift to higher wavenumbers, while the frequency of the bending mode shifts to lower wavenumbers. The frequency shifts are related to changes in the geometry of the H_2O molecule, and can be explained by considering that changes in the electrostatic charge exchanged by the M cation (in the present case Na) and the hydroxyl oxygen in the $M(H_2O)_n^+$ cluster (Fig. 10), are translated into changes of the M-O bond distances. If n = 1, the fraction of the electrostatic charge of sodium exchanged with the hydroxyl oxygen (^{W}O) is maximum, the O-H bond is longer and the H-O-H angle decreases. When n = 2, the charge of Na is shared by two ^{W}O and the O-H bond shortens to compensate for the resulting charge deficit; the H-O-H angle simultaneously increases (Fig. 10). The geometrical changes of the water molecule, due to the described different coordination environments are evidenced by the observed shifts in frequency of the stretching and bending modes.

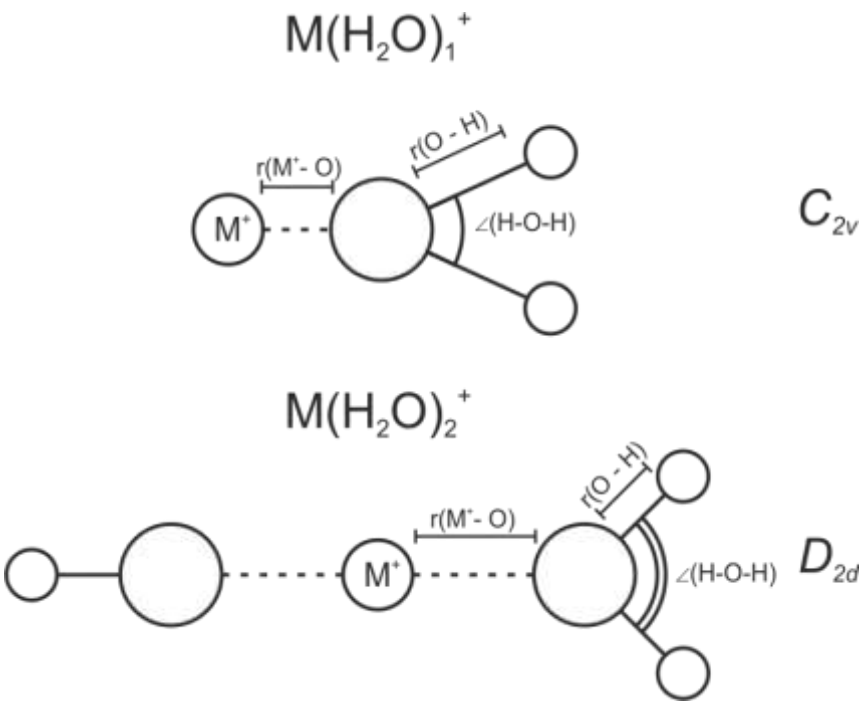

Figure 10 – Schematic representation of H_2O geometry around an alkaline cation for a singly coordinated (top) and a doubly coordinated (bottom) H_2O molecule. The symmetry of the cluster is reported on the side (after Bauschlicher *et al.,* 1991).

Similar shifts in frequency in response to the modified electrostatic environment in the $M(H_2O)_n^+$ cluster can be modeled by the GF matrix method (Wilson *et al.*, 1955); for type II H_2O in beryl the calculations are reported in Fukuda and Shinoda (2008, 2011).

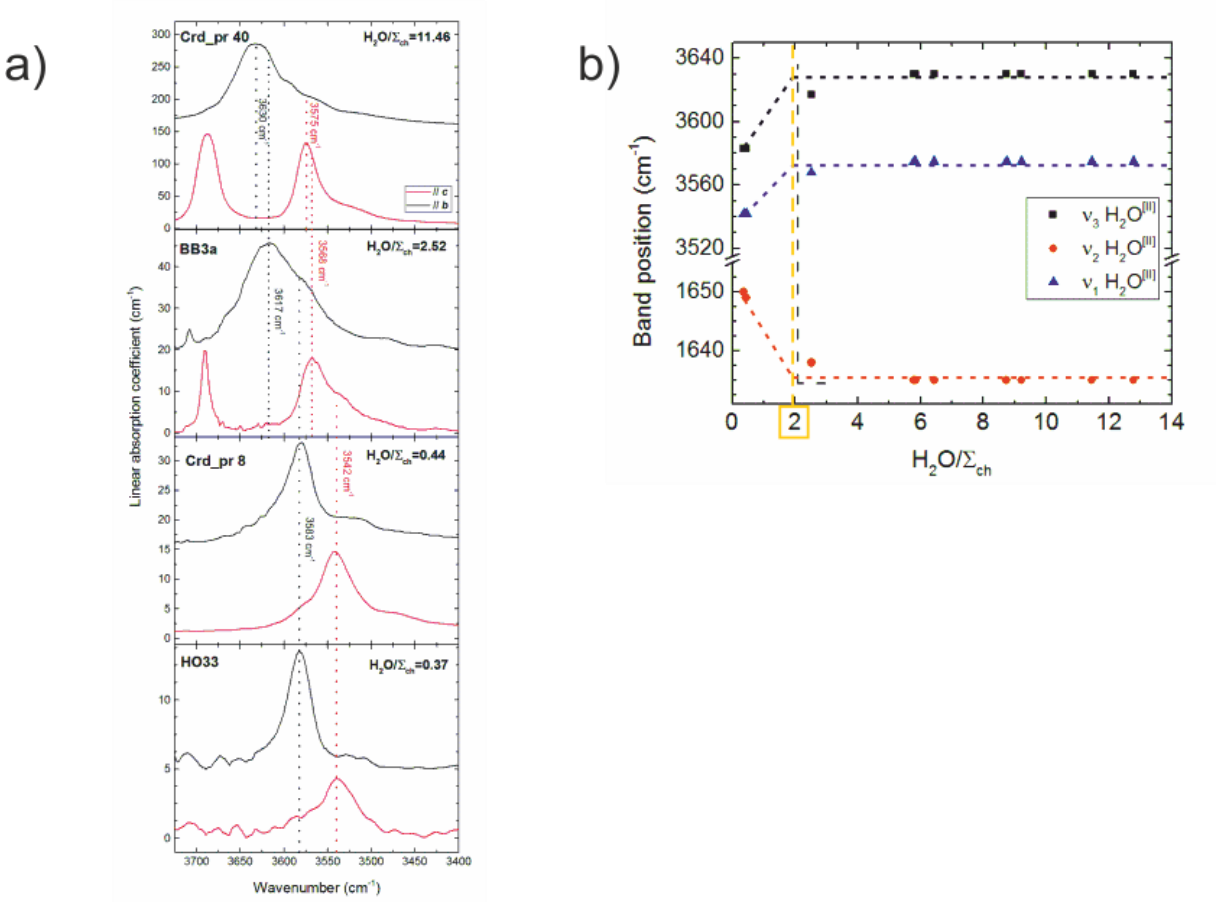

Figure 11 – (a) FTIR polarized light spectra for E//b (black line) and E//c (red line) crystallographic directions, for different cordierites. The H_2O/Σ_{ch} ratio is expressed as H_2O apfu over the total Na + K + Ca apfu. Compositional data for Crd_pr 40 are from Della Ventura *et al.* (2012), for BB3a from Della Ventura *et al.* (2012) and for HO33 from Della Ventura *et al.* (2009). (b) Frequency position of ν_3 antisymmetric stretching (black squares) ν_2 bending (red dots) and ν_1 symmetric stretching mode (blue triangles) as a function of H_2O/Σ_{ch} ratio. Lines are only a guide for the eye.

The mechanism so far described can be extended to explain the peak shifts observed in the FTIR spectra of the structurally-related cordierite. In Figure 11a we compare the E//b and E//c FTIR spectra of four cordierites (BB3a, from Della Ventura *et al.,* 2012; HO33, from Della Ventura *et al.,* 2009; Crd_pr 40 and Crd_pr 8 from this Thesis, cap 5) having a different H_2O to alkali cation ratio (H_2O/Σ_{ch} = H_2O over Na^++ K^+ + Ca^{++} apfu). Dotted lines indicate the peak position of the ν_3 and the ν_1 modes for $H_2O^{[II]}$. Examination of Figure 11a shows that both ν_3 and ν_1 peaks shift to lower energy as the H_2O/Σ_{ch} ratio decreases, similarly to what observed for beryl. Starting from sample Crd_pr 40 (H_2O/Σ_{ch} = 11.46) there is a progressive shift from the 3630/3575 cm^{-1} (Della Ventura *et al.,* 2012) to 3617/3568 cm^{-1} in sample BB3a (H_2O/Σ_{ch} = 2.52). The broad band in cordierite BB3a sample shows two pronounced shoulders at ~ 3583 cm^{-1} and 3542 cm^{-1}, respectively. These shoulders become the main peaks in the spectra with the lowest H_2O/Σ_{ch} ratio (Crd_pr 8 and HO33). In Figure 11b (top)

we plot the ν_3 (squares) and ν_1 (triangles) peak positions against the H_2O/Σ_{ch} ratio (data from Della Ventura *et al.*, 2012). As expected from the above discussion, the ν_2 bending mode (Fig. 11b, circles), shows an opposite trend for increasing H_2O/Σ_{ch} ratio, from 1634 cm^{-1} to 1650 cm^{-1}. Figure 11b emphasizes that there is a sudden shift in peak position for compositions with $H_2O/\Sigma_{ch} < 2$. This threshold value corresponds to the ratio of 2 $H_2O^{[II]}$ for each alkali cation atom in the channel: when this ratio is below 2 the 3583 – 3542 – 1650 cm^{-1} components prevail suggesting that $H2O^{[II]}$ is predominantly in a singly-coordinated state.

6. Conclusions

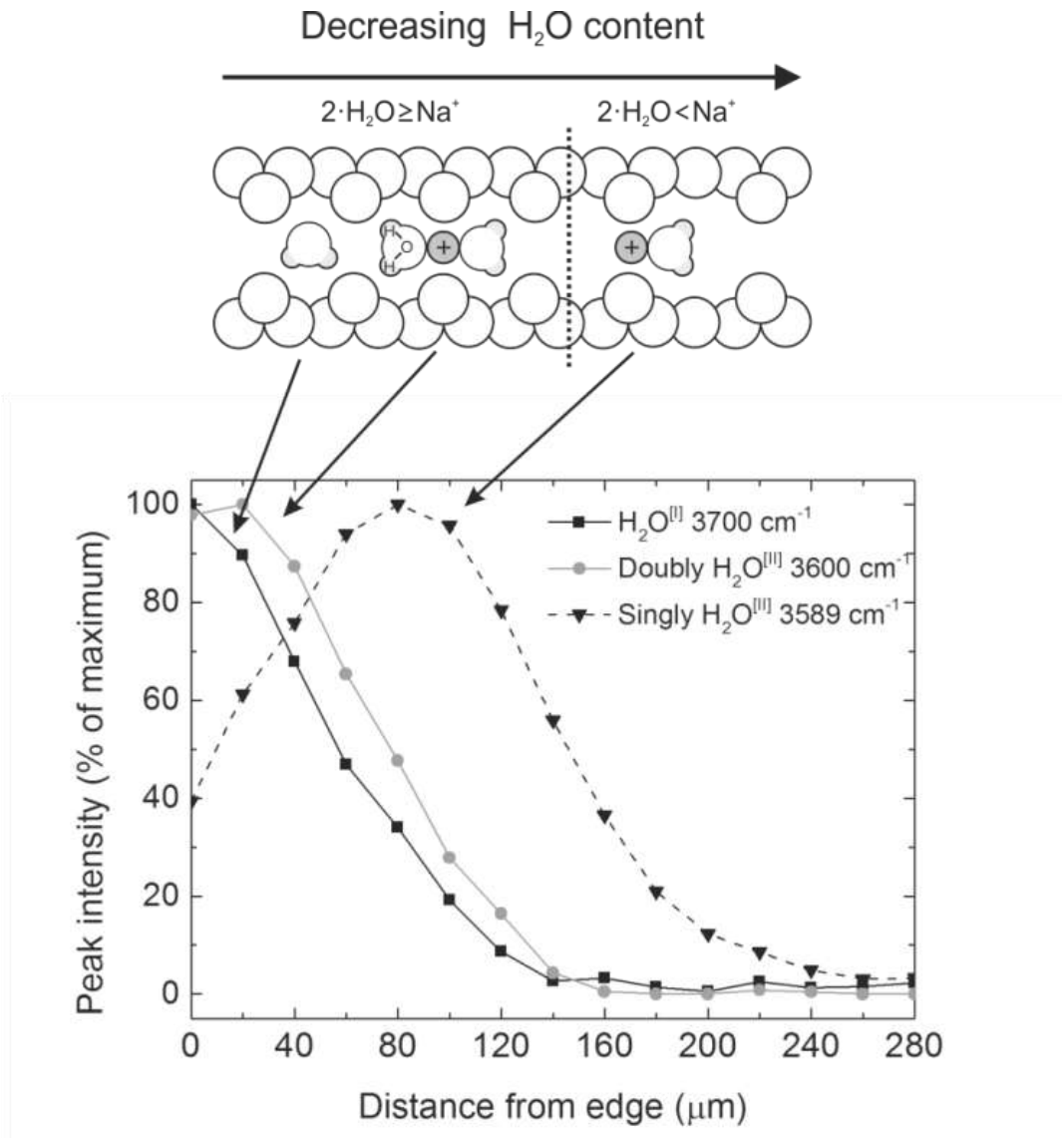

Figure 12 – Top: schematic representation of the configuration of water molecules inside the structural channels of beryl, as the overall water content decreases. Bottom: concentration trends of selected peaks in the FTIR spectra. Peak intensities are scaled to the maximum intensity value.

Figure 12 displays schematically the summary of the discussion presented so far, providing a sketch of the water molecules within the beryl channels as H_2O concentration progressively decreases, correlated with the plots relating the intensity variation of the antisymmetric stretching modes for each H_2O configuration. From the plot it is apparent that for higher water contents on the crystal edge, H_2O can assume both type I and type II orientations (black squares and gray circles curves close to the edge in Fig. 12) and this implies that $2{\cdot}H_2O > Na^+$ apfu. Proceeding within the channel, all H_2O molecules tend to assume the type II configuration (doubly $H_2O^{[II]}$, gray circle curve) implying that the water content approaches $2{\cdot}H_2O \approx Na^+$ apfu. Proceeding further within the channel, the water content reaches $2{\cdot}H_2O < Na^+$ apfu and singly coordinated $H_2O^{[II]}$ predominates (singly $H_2O^{[II]}$, black triangles curve).

The above FTIR data thus allow to conclude that H_2O diffuses across the structural channels as an unbounded molecule, then it changes its local bonding configurations as a function of the based on the Na/H_2O ratio. The diffusion coefficients for $H_2O^{[I]}$ and $H_2O^{[II]}$ (considering for simplicity the doubly and the singly coordinated $H_2O^{[II]}$ as a single molecule) were evaluated for both samples, using the monodimensional plane diffusion formalism (Crank, 1975, Zhang and Cherniak, 2010) as discussed in chapter 5. Profile data were obtained by integrating the $H_2O^{[I]}$ ν_3 anti-symmetric stretching mode at 3699 cm^{-1} polarized for E//c and the sum of both $H_2O^{[II]}$ ν_1 symmetric stretching modes at 3600 and 3589 cm^{-1} also polarized for E//c. The results are reported in Table 2. The calculated mean activation energy for $H_2O^{[I]}$ (E_a) is 135 kJ/mol with a pre-exponential ($-\log D_0$) factor of $10^{-6.61}$ (m^2/s) or $10^{-2.61}$ (cm^2/s), for $H_2O^{[II]}$ E_a = 90 kJ/mol and $-\log D_0 = 10^{-8.43}$ (m^2/s) or $10^{-4.43}$ (cm^2/s). The combined result for total H_2O is E_a = 111±54 kJ/mol and $-\log D_0 = 10^{-7.5}$ (m^2/s) or $10^{-3.5}$ (cm^2/s). It is to be noted that the results for $H_2O^{[I]}$ are in good agreement with those obtained by Fukuda *et al.* (2009), for the same molecular type.

Table 2 – Diffusion coefficients for $H_2O^{[I]}$ and $H_2O^{[II]}$ along the structural channels of beryl.

Sample	Pressure (MPa)	Temperature (°C)	Time (h)	D (m^2/sec)	1000/T (K)	Log D
Pa_340 r $H_2O^{[I]}$	700	700	24	1.8±0.1 E-14	1.03	-13.75±0.06
Pa_340 r $H_2O^{[II]}$	700	700	24	5.2±0.3 E-14	1.03	-13.28±0.05
Pa_340 o $H_2O^{[I]}$	700	800	10	8.3±0.6·E-14	0.93	-13.08±0.07
Pa_340 o $H_2O^{[II]}$	700	800	10	1.5±0.1·E-13	0.93	-12.83±0.07

PUBLISHED ON RENDICONTI ONLINE SOCIETÀ GEOLOGICA ITALIANA (2014)

DOI 10.1007/s00410-012-0779-8

CHAPTER 8

THE PERMANENT STORAGE OF CO_2 IN MESOPOROUS MINERALS: EXPERIMENTS WITH BERYL

Giancarlo Della Ventura[1], Francesco Radica[1], Fabio Bellatreccia[1] and Lidia Bellomo[1]

[1]Laboratorio di spettroscopia FTIR, Università di Roma Tre, Largo S. Leonardo Murialdo 1, 00146 ROMA

Abstract

In this short note we describe the recent experimental mineralogy work at University of Roma Tre focused on the diffusion of carbon dioxide within the structural channels of microporous silicates. The results obtained in the last few years for cordierite and beryl are briefly reported, as well as the developments of novel spectroscopic methods to characterize the volatile distribution across the studied materials.

KEY WORDS: CO_2 diffusion, HT/HP experiments, cordierite, beryl, FTIR-FPA spectroscopy and imaging, optical properties.

Carbon dioxide (CO_2) generated by the combustion of fossil fuels is by far the most abundant greenhouse gas; its reduction in the atmosphere is therefore a primary environmental concern. Due to several reasons, it can be easily understood that fossil fuels will continue to play a significant role in the world's economy at least in the following decades, thus emphasis must be placed on improving methods to decrease the amount of CO_2 dispersed in the environment. The reduction of CO_2 from the atmosphere can be achieved by efficiency improvements in power plants, use of alternative energy technologies, sequestration of CO_2, or some combination of these methods. Up to the present, several techniques have been considered, and these include: 1) forestation, where CO_2 is removed from the atmosphere by biological activity; 2) aquifer storage, in which CO2 is injected into terrestrial aquifers where it is trapped hydro-dynamically; 3) deep sea storage, where CO_2 is injected into the ocean at approximately 3,000 meter depths, where it is believed to remain stable; and 4) mineral carbonation, in which CO_2 is reacted with minerals to form solid carbonates. This final form of sequestration is the most permanent method, because the carbonates are stable over geologic time periods (millions of years), rather than the hundreds to thousands of years of stability expected for the first three forms of sequestration. This process is however highly expensive and energy consuming, therefore research in material science has focused in the last decade at developing technically feasible processes for mineral sequestration of carbon dioxide alternative to carbonation.

Actually, many minerals contain carbon as a major to trace constituent, however the carbon content analysed in naturally occurring silicates is traditionally assigned to CO_3^{2-} groups in the structure, whereas the possible presence of molecular CO_2 in these phases is almost completely ignored. Up to the present, the only accepted CO_2-bearing minerals are beryl (Wood and Nassau, 1967) and cordierite (Armbruster and Bloss, 1980, Della Ventura et al., 2009, 2012) two (structurally) closely related silicates characterized by open channels running along [001]; in these channels carbon dioxide is located together with H_2O and extra framework cations such as Na, Li or Cs. Recent research have shown that other silicate materials are able to host molecular CO_2 in their structural pores; these materials include some clay-like minerals (Zhang et al., 2005), some particular type of hydrous silica (Kolesov and Geiger, 2003) and several microporous, zeolite-type, feldspathoids (Bellatreccia, 2009, 2012, Bonaccorsi et al., 2007, Della Ventura et al., 2005, 2007, 2008).

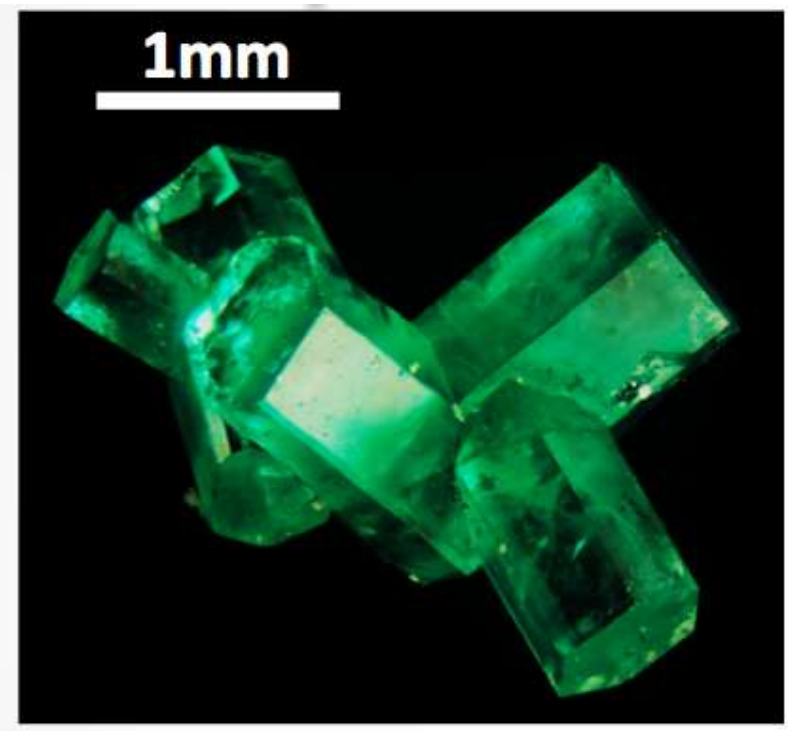

Figure 1 - Photo of the studied synthetic emeralds

We devoted significant efforts in the last years to the problem of CO_2 diffusion in microporous minerals, and in particular in cordierite and beryl. Cordierite is an extremely interesting material because it represents the only known case of a microporous structure (pore size under 2 nm) stable under extreme geological conditions and able to trap significant amounts of molecular H_2O and CO_2 (Armbruster and Bloss 1980). As a matter of fact, its occurrence extends from the amphibolite facies to ultra-high temperature metamorphism to crustal anatexis (Carrington and Harley, 1996; Harley *et al.*, 2002). Because of its thermal and mechanical properties cordierite is used in applications such as high-tech ceramics or as a catalyst in petroleum industry. Beryl is a pegmatitic mineral and has a lower thermal and baric stability; it is well known for providing some of the most notable gemstones, such as the varieties emerald (green), aquamarine (light-blue), heliodor (yellow) or bixbite (red). We used natural cordierite and synthetic emeralds (Fig. 1) as starting materials for CO_2 diffusion experiments under high P and T conditions; this research has been developed in the frame of two Master Thesis and a PhD project in collaboration with the INFN (Istituto Nazionale di Fisica Nucleare) and INGV (Istituto Nazionale di Geofisica e Vulcanologia).

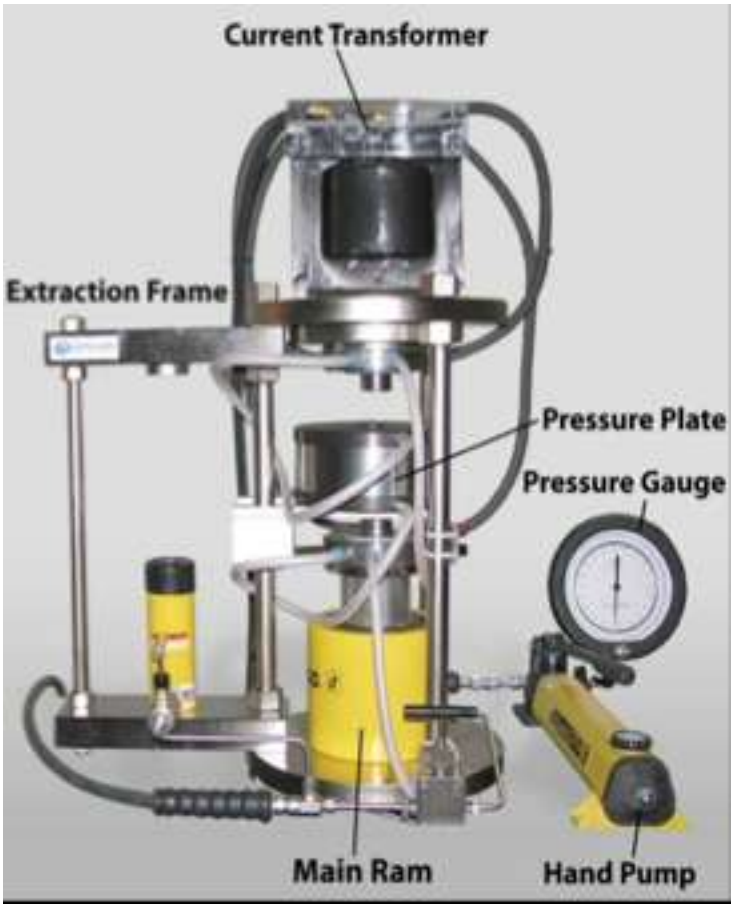

Figure 2 - The QUICK press™ pyston cylinder installed at INGV (Rome) and used for the described experiments.

Briefly, we equilibrated previously degassed cordierite fragments and synthetic volatile-free emeralds in CO_2 saturated atmosphere, at different T, P and time conditions. The research was aimed at studying the diffusion of gaseous CO_2 across the mineral matrix as a function of the above mentioned parameters. We stress that from a practical point of view nobody would ever use emeralds as starting materials for carbon dioxide sequestration, thus our study must be regarded as a fundamental science research; however, knowledge of the process by which a gas having important geological implications, like CO_2, diffuses throughout solids, may open new frontiers in future applied Science. The experiments were conducted using a variety of facilities (HT/HP press, Fig. 2, and Tuttle-type cold seal pressure vessels) and in different laboratories, including the HP/HT laboratory of INGV (Rome) and the Institut für Mineralogie of Leibniz Univerität Hannover (Germany). The starting materials were encapsulated in Pt tubes with Ag carbonate or Ca-oxalate as a source for CO_2; these compounds in fact decompose at relatively low T thus saturating the charge with carbon dioxide. The charge was equilibrated for T in the range 700-900°C and P in the range 200-700 MPa.

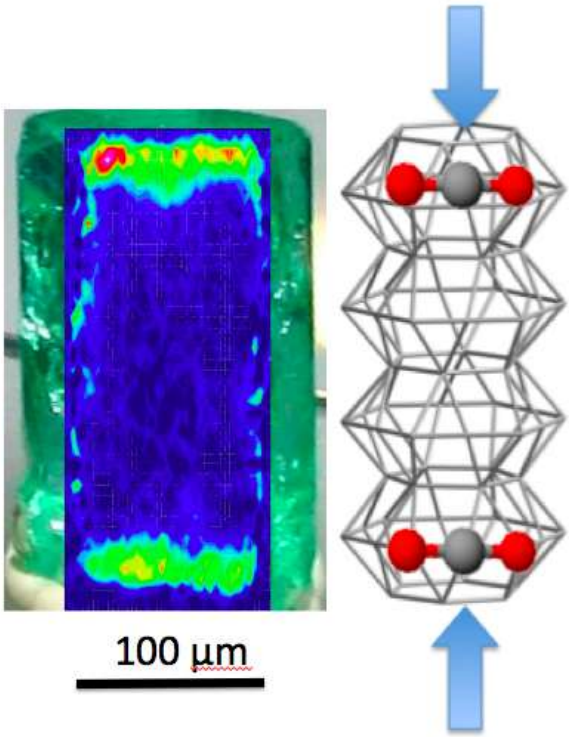

Figure 3 - Left: selected FTIR-FPA image of the CO_2 distribution within the emerald samples equilibrated at 700°C, 500 MPa in carbon dioxide saturated atmosphere. The spectroscopic image is oriented over the crystal image. The color from red to blue is proportional to the amount of CO_2. Right: schematic model for the CO_2 diffusion within the structural channels.

This short note is not intended to describe all obtained results, however, from a general point of view we observed that temperature has a very small effect on the CO_2 solubility in the studied minerals, while pressure has a significant effect; the effect of time is also negligible. To characterize the run products we used a novel technique in mineral spectroscopy (Della Ventura et al., 2014), which takes advantage of the focal-plane-array of detectors (FPA) to produce bi-dimensional images of the distribution of an absorber within a matrix, a concept very similar to the CCD detectors typically used in X-ray based methods. The extreme interest of these techniques in experimental studies is the possibility to probe the distribution of the target molecule, a piece of information that is crucial in diffusion studies where the homogeneity of the run product is rarely attained. Figure 3 shows a selected FTIR-FPA image of a beryl slice after the experiment, where the color intensity, from blue to red, is proportional to the CO_2 amount within the sample; the FPA image has been oriented onto the emerald crystal. The image clearly shows that the carbon dioxide diffused only for a short distance from the basal (pinacoidal) faces of the emerald along the channels; a schematic interpretation of the process is given on the right side of Figure 3.

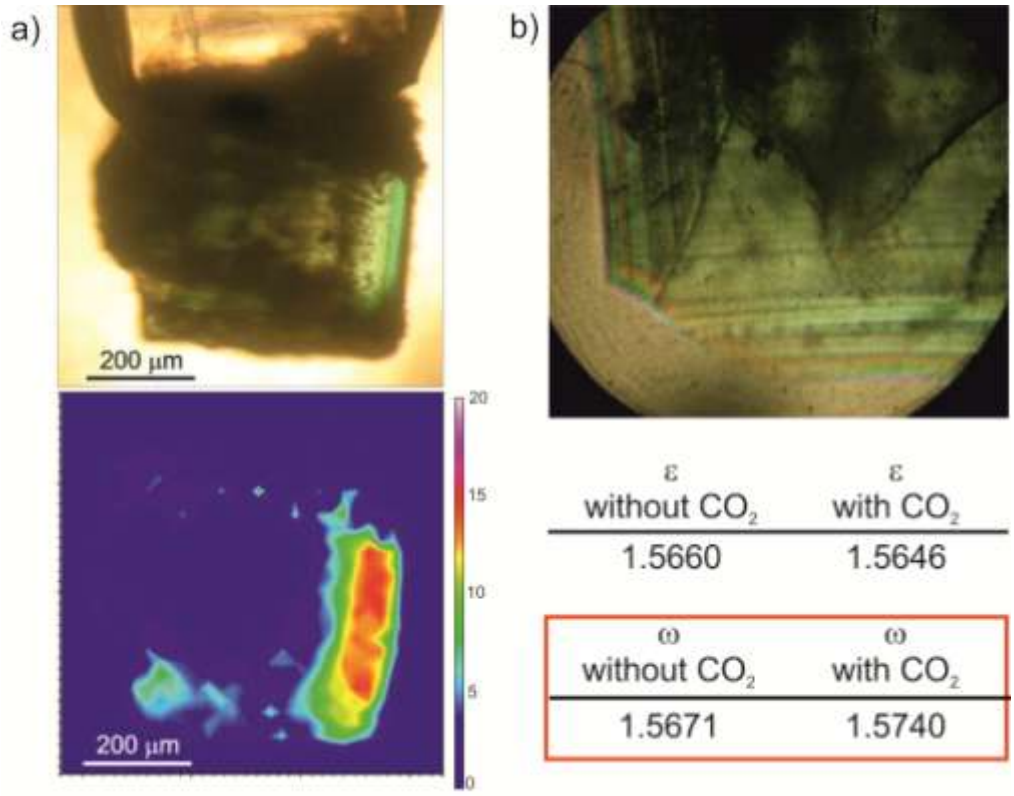

Figure 4 - (a) above: optical image of the experimental emerald fragment glued on the glass capillary for the spindle stage analysis; below: FTIR-FPA image of the same grain showing the CO_2 distribution. (b) above: optical image of the emerald sample in immersion within the Cargille liquid: the Becke line is visible; (below) final measured refractive indexes.

The refractive indexes of the emerald were measured using the spindle stage and the double variation method, by means of immersion liquids (Cargille liquids) of known refractive index under monochromatic light. For this analysis also, a map of the CO_2 distribution across the grain (Fig. 4) was essential to measure the correct optical property in different part of the crystal. Emerald is optically uniaxial negative, with a very low birefringence (0,005 to 0,009). It was found that the introduction of carbon dioxide into the structure has a significant effect on the ordinary ray value (ω), which increases one order of magnitude (Fig. 4), while the extraordinary ray value (ε) is unaffected. This is consistent with the alignment of the linear CO_2 molecule perpendicular to the ***c*** crystallographic axis. A point we would like to stress here is that almost no laboratories worldwide are equipped to measure optical properties of minerals and perform crystal-chemical studies (including non-ambient conditions studies) based on optical methods. Optical mineralogy is an extremely powerful technique in geology and also in material Science, because the macroscopic

property which is displayed by a change in refractive index (a measure of the speed of light across the mineral), or in birefringence, retardation, conoscopic figures or interference colors is a quick measure of structural properties which can be obtained only by using much more sophisticated methods. For more than a century, the use of optical methods has been one of the prerogatives of Earth Science but this knowledge is unfortunately going to be lost.

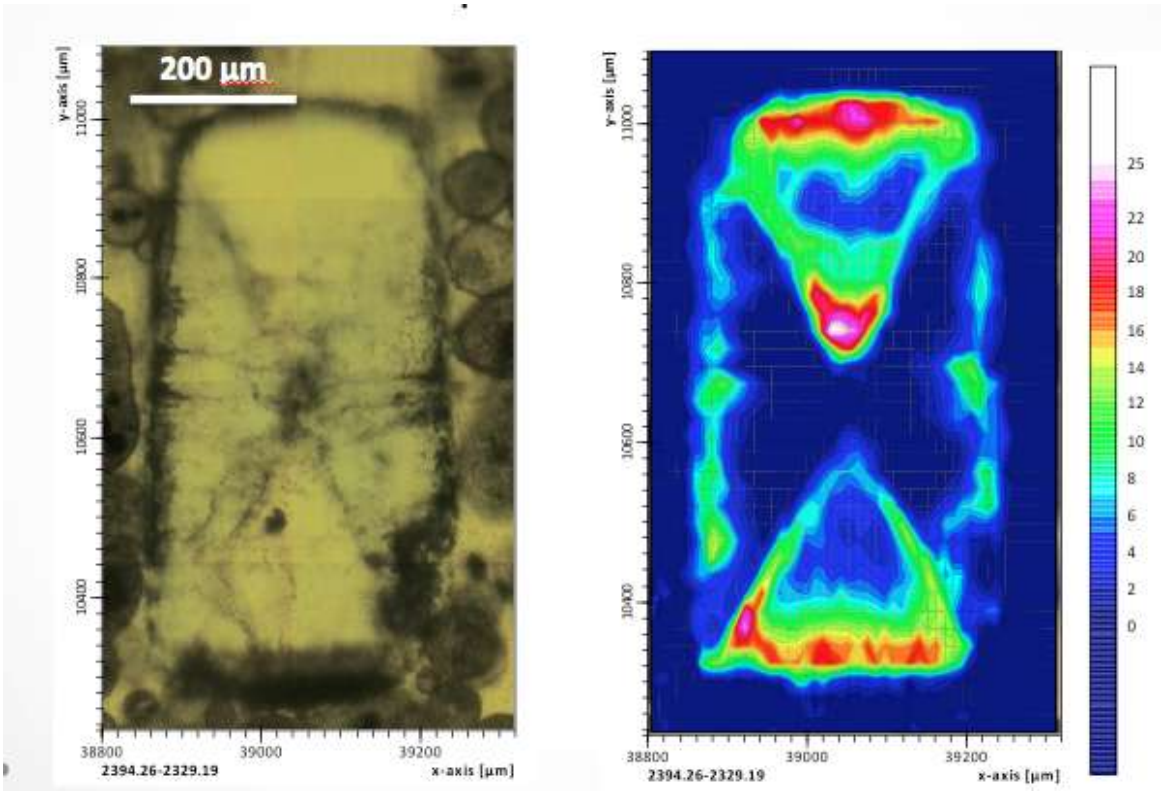

Figure 5 - Left: optical image of the studied emerald showing the evident hourglass texture. Right: FTIR-FPA image of the CO_2 distribution within the samples

A final, spectacular observation on the distribution of carbon dioxide within emeralds is shown in Figure 5 which displays the FPA image collected on a particular sample, characterized by a pronounced hourglass zoning of chromium (Cr is a dopant used during the emerald synthesis to give the beautiful green color to the gem). The spectroscopic image shows that the CO_2 diffusion during the HT/HP treatment is significantly controlled by the hourglass texture, and is greatly enhanced along the zone boundaries. The reasons for this behavior are still unclear and we are working to better constrain the phenomenon. It is however clear that experimental mineralogy is able to open promising frontiers in technology, most of which originate from researches driven just by the scientist's curiosity.

Acknowledgments

Thanks are due to S. Mollo, C. Freda and P. Scarlato (INGV, Rome) for providing both facilities and their personal expertise to solve most of the technical aspects of this research. The spectroscopic work has been done at Daϕne Laboratory of FTIR spectroscopy of INFN (Frascati, Rome), thanks to the scientific collaboration of Mariangela Cestelli Guidi and Augusto Marcelli.

FINAL REMARKS

This PhD Thesis was aimed at investigating the ability of cordierite and beryl, considered as a model for microporous materials, to diffuse and trap H_2O and CO_2 within their structural channels.

The work focused in particular on the CO_2 diffusion because of very few and controversial results so far available in the literature. In addition, CO_2 is considered one of the major cause of long-term climate change, thus knowledge of the conditions under which it diffuses into minerals may have interesting bearings for the design of new materials for the permanent storage of this gas. The study was done by combining different analytical techniques, however most data were based on micro-FTIR and FTIR-FPA imaging. Indeed, during this work novel applications of the FPA imaging were developed and tested for the first time in the study of Earth Science materials, in particular under polarized and synchrotron radiation.

The volatile-free crystals were treated at different pressure and temperatures in a CO_2 rich atmosphere using a non end-load piston–cylinder press, especially designed for short term experiments. The results showed that CO_2 diffusion inside beryl and cordierite proceeds exclusively along the structural channels running parallel to the *c* crystallographic axis (Chapter 5); the same mechanism occurs also during CO_2 expulsion from the matrix (Chapter 3). Thus the CO_2 loss from cordierite and beryl is strongly affected by both the particle size and shape of the crystal, *i.e.* the length of the escape path. To examine quantitatively this feature, in Chapter 3 we performed experiments with two different crystallographic orientations: a first (001), 77 μm thick slab, with a diffusion pathway of 34 μm to simulate the loss from small or tabular grains, and a second (010) slab to model the case of large or prismatic grains (typical growth habit of cordierite, Deer *et al.*, 2004). In this case, in fact, the mean diffusion pathway was about 120 μm, corresponding to half the slab

dimension along the *c* axis. In the (001) lamella or in thin and tabular cordierite grains both CO_2 and H_2O desorption proceeds smoothly even when T increases with a very fast rate; on the other side, for thicker or prismatic cordierite grains, as simulated by the (010) lamella, both CO_2 desorption and dehydration occur at higher temperatures, at least 50/100 °C higher than in the former sample. In other words, the data suggest that the difference in diffusion path length has a significant effect on the temperatures of CO_2 and H_2O desorption and longer heating time are necessary to extract all volatile molecules from the core of the grain (see also Chapter 4).

Fractures inside the grains also acted as additional pathways of inward and/or outward CO_2 diffusion, in accelerating the CO_2 diffusion across the grain (Chapter 3 and 5); this finding is in line with the general observation that grain-boundary diffusion and diffusion along interfaces, like cracks, can be several order of magnitude faster than lattice diffusion (Zhang and Cherniak, 2010). A third additional way of diffusion was observed in synthetic beryls (Chapter 6). The planar defect generated by the structural mismatch in correspondence of the hourglass zoning also acted as a fast-path for CO_2 diffusion (Zhang *et al.*, 2006). A direct conclusion is that the simultaneous occurrence of different diffusion mechanisms, i.e. (I) channel/lattice diffusion, (II) fracture induced diffusion and (III) fast path diffusion, may complicate the evaluation of diffusion coefficients of a molecular species, thus inspection of the distribution of a molecule inside the mineral via 2D imaging is mandatory in experimental work.

Differently to CO_2, which is always oriented normal to the *c* axis, H_2O may be oriented in different ways (Chapters 1, 2 and 7): relatively unbound $H_2O^{[I]}$, doubly coordinated $H_2O^{[II]}$ and singly coordinated $H_2O^{[II]}$. It follows that H_2O in different coordination environments may have different diffusion mechanisms and consequently diffusion coefficients. Based on the results discussed in Chapter 7, it is possible to infer that when the amount of H_2O in the channels is $2{\cdot}H_2O$ > Na apfu, than water may be present both as $H_2O^{[I]}$ and doubly coordinated $H_2O^{[II]}$; when $2{\cdot}H_2O$ < Na apfu, than water is present as doubly and/or singly coordinated $H_2O^{[II]}$. Characterization of the coordination state of H_2O in the structural channels is thus important for a proper interpretation of diffusion data in experimental studies.

A major result of the experiments described in chapter 5 is that pressure plays a major role in controlling the amount of CO_2 diffused in both cordierite and beryl, while

temperature and time have a minor effect, in line with data from natural occurrences (Thompson, *et al.*, 2001; Harley *et al.*, 2002). Surprisingly, however, the CO_2 contents introduced during the present study into cordierite were at least one order of magnitude lower than expected (Johannes and Schreyer, 1981; Armbruster and Bloss, 1982). One of the reasons for this discrepancy probably is related to the fact that the crystals used here as a starting material had significant amounts of alkali cations (Chapter 1). Vry *et al.* (1990) observed that in natural cordierite the total content of CO_2 + alkali may induce a volatile deficiency of both H_2O + CO_2 during equilibration with the surrounding fluid because of a plug effect hindering diffusion of the relatively large CO_2 molecule from the fluid into the mineral. A second, additional source of discrepancy may be looked for in the sample handling and preparation for the analyses; HT/HP treatment of the sample during the experiments were found to induce development of a series of micro-fractures close to the edges of the cordierite crystals. These micro-fractures may induce the formation of a CO_2-rich but fragile external layer which may be removed during sample slicing and polishing for FTIR analyses, thus distorting the final data relative to analyses done on bulk samples.

Cracks and fractures, produced during the thermal treatment, were found to enhance significantly the CO_2 diffusion across with contents up to 4 times higher than at the edge of the grain. This feature has a great relevance from a technological point of view, because it demonstrates that to trap faster and larger CO_2 amounts inside the material, the use of highly fractured or clusters of micron-sized grains is preferred over larger grains (Chapter 8).

Because of the well-developed hexagonal prismatic habitus, the beryl samples were excellent candidates to evaluate the inward diffusivity of CO_2 in microporous structures (Chapter 5); diffusion coefficients for cordierite, on the opposite, could be evaluated only for the outward diffusion (Chapter 3). Diffusion coefficients of volatile species in silicates are expected to be related to the dimension of the diffusing species and the diffusing structure. It is also widely accepted that for more compact silicate structures diffusing rates are smaller and activation energies larger. As we may observe from Figure 1 the diffusing rates calculated for CO_2 (Chapter 5) and H_2O (Fukuda *et al.*, 2009) in beryl are very close, even though CO_2 molecule are larger than the H_2O molecule. On the other hand, the inward CO_2 diffusion coefficients for beryl (see Figure 1 and Chapter 5) are greater than the diffusion coefficient calculated for the outward CO_2 diffusion in cordierite (see Figure 1 and Chapter 3)

even though the structures are very similar. Vry *et al.* (1990) observed that in cordierite inward diffusion is quicker than outward diffusion. These authors stated that the difference between inward and outward diffusion rates may be caused by alkali cations and CO_2 itself, that, acting as plugs in the channel, preferentially slows down outward volatile diffusions.

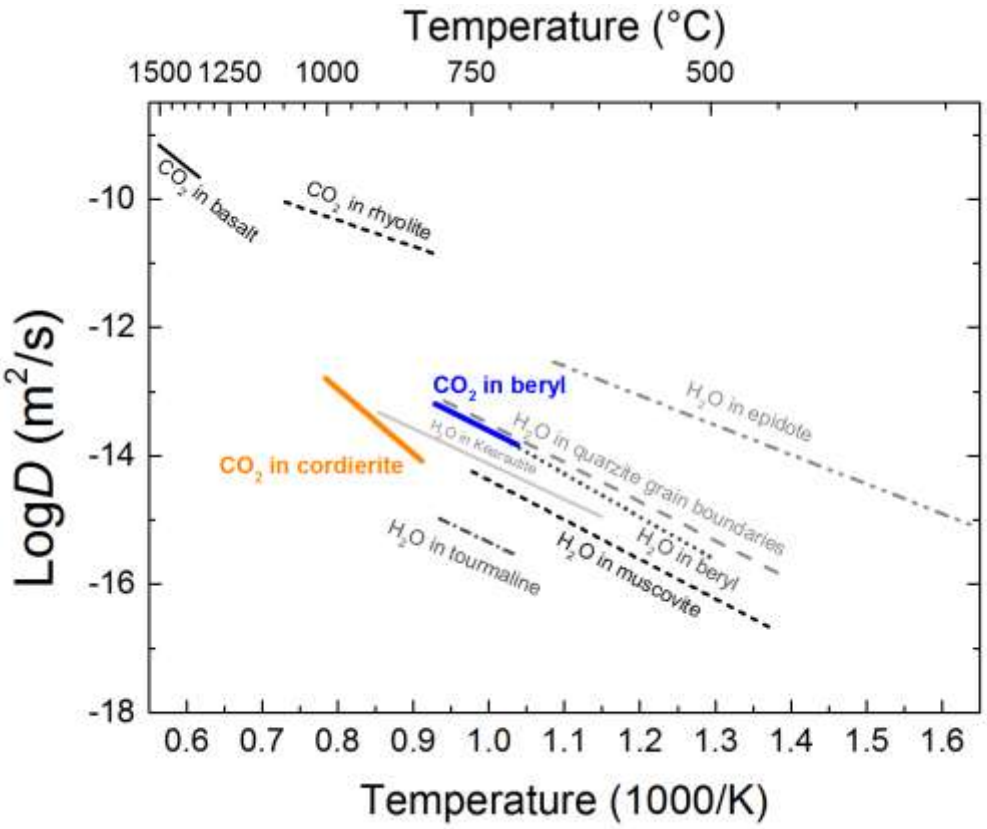

Figure 1 – Arrhenius diagram of various diffusion coefficients D for different silicates or silicate melts for H_2O and CO_2. D for beryl after diffusion profiles (Chapter 5), D for cordierite after isothermal heating experiments (Chapter 3).

Figure 1 give selected examples of diffusion rates for the most common hydrous minerals. In Figure 18 we may observe that the diffusion coefficients measured for CO_2 in beryl are close to the OH^- diffusion coefficients obtained in other ring silicates like tourmaline (Desbois and Ingrin, 2007), layer silicates like muscovite (Graham, 1981), amphiboles like kaersutite (Ingrin and Blanchard 2000), or in disilicates like epidote (Graham, 1981). However, it's important to note that structural OH^- probably diffuses inside these structures in the form of H^+ (Zhang *et al.*, 2010) thus the diffusing species is much smaller compared to molecular CO_2 and H_2O.

Our data suggest that the structural channels of cordierite and beryl act more likely as fast paths for the mobility of large molecular groups compared to similar silicate

structures, and for this reason the diffusing behavior is more similar (in terms of diffusion coefficients, not in the mechanism) to the one typically observed for grain boundary diffusion, such as, for example, H_2O in quartzite (Farver and Yund, 1991) or to the behavior of CO_2 in non-crystalline materials, like silicate melts (Watson *et al.*, 1982; Watson, 1991).

REFERENCES

Adamo I, Gatta GD, Rotiroti N,Diella V, Pavese A (2008) Gemmological investigation of a synthetic blue beryl a multi-methodological study. Mineralogical Magazine, 72, 799-808.

Aines RD, Rossman GR (1984) The high temperature behaviour of water and carbon dioxide in cordierite and beryl. American Mineralogist, 69, 319-327.

Anderson TF (1972) Self-diffusion of carbon and oxygen in dolomite. Journal of Geophysical Research, 77, 857-861.

Armbruster T (1985) Ar, N_2, and CO_2 in the structural cavities of cordierite, an optical and X-ray single-crystal study. Physics and Chemistry of Minerals, 12, 233-245.

Armbruster T, Bloss FD (1980) Channel CO_2 in cordierites. Nature, 286, 140-141.

Armbruster T, Bloss FD (1982) Orientation and effects of cannel H_2O and CO_2 in cordierite. American Mineralogist, 67, 284–291.

Armbruster, T (1986) Role of Na in the structure of low-cordierite: A single-crystal X-ray study. *American Mineralogist*, **71**, 746-757.

Armbruster, T, Irouschek, A (1983) Cordierites from the Lepontine Alps: Na + Be → Al substitution, gas content, cell parameters and optics. *Contribution to Mineralogy and Petrolology*, **82**, 389-396.

Aurisicchio C, Grubessi O, Zecchini P (1994) Infrared spectroscopy and crystal chemistry of the beryl group. Canadian Mineralogist, 32, 55–68.

Aurisicchio C., Fioravanti G, Grubessi O,Zanazzi PF (1988) Reappraisal of the crystal chemistry of beryl. American Mineralogist, 73, 826-837.

Avrami M (1939) Kinetics of Phase Change. I. General Theory. Journal of Chemical Physics, 7, 1103-1112.

Avrami M (1940) Kinetics of Phase Change. II. Transformation-Time Relations for Random Distribution of Nuclei. Journal of Chemical Physics, 8, 212-224.

Avrami M (1941) Kinetics of Phase Change. III. Granulation, Phase Change, and Microstructure. Journal of Chemical Physics,9, 177-184.

Bahat D (1974) Phase transformation and development of hourglass pattern in synthetic barium feldspar. American Mineralogist, 59, 139-142.

Baker DR (2004) Piston-cylinder calibration at 400 –500 MPa: a comparison of using water solubility in albite melt and NaCl melting. American Mineralogist, 89, 1553 –1556.

Bauschlicher CW, Langhoff SR, Partridge H, Rice JE, Komornicki A (1991) A theoretical study of $Na(H2O)^{+}_{n}$ (n = 1–4). Journal of Chemistry and Physics, 95, 5142–5148.

Behrens H (2010) Ar, CO_2 and H_2O diffusion in silica glasses at 2 kbar pressure. Chemical Geology. 272, 40-48.

Behrens H, Misiti V, Freda C, Vetere F, Botcharnikov R, Scarlato P (2009) Solubility of H_2O and CO_2 in ultrapotassic melts at 1200 and 1250 °C and pressure from 50 to 500 MPa. American Mineralogist, 94, 105-120

Bellatreccia F, Della Ventura G, Libowitzky E, Beran A (2005) The quantitative analysis of OH in vesuvianite: a polarized FTIR and SIMS study. Physics and Chemistry of Minerals, 32, 65–76.

Bellatreccia F, Della Ventura G, Piccinini M, Cavallo A, Brilli M (2009) H_2O and CO_2 in minerals of the haüyne-sodalite group: an FTIR spectroscopy study. Mineralogical Magazine, 73, 399-413.

Bellatreccia F, Della Ventura G, Piccinini M, Grubessi O (2008) Single-crystal polarized light IR study of an historical synthetic water poor emerald. Neues Jahrbuch für Mineralogie Abhandlungen, 185, 11-16.

Bellatreccia F, Della Ventura G, Gatta GD, Harley S (2012) Carbon dioxide in pollucite, a feldspathoid with the ideal composition $(Cs,Na)_{16}Al_{16}Si_{32}O_{96} \cdot nH_2O$. Mineralogical Magazine, 76, 903-911.

Bellatreccia F, Della Ventura G, Libowitzky E, Beran A (2005) The quantitative analysis of OH in vesuvianite: a polarized FTIR and SIMS study. *Physics and Chemistry of Minerals*, **32**, 65-76.

Beran A, Langer K, Andrut M (1993) Single crystal infrared spectrain the OH range fundamentals of paragenetic garnet, omphacite and kyanite in an eclogitic mantle xenolith. Mineralogy and Petrology, 48, 257–268.

Bertoldi C, Proyer A, Garbe-Schönberg D, Behrens H, Dachs E (2004) Comprehensive chemical analyses of natural cordierites: implications for exchange mechanisms. Lithos 78:389-409

Bish DL, Carey JW (2001) Thermal behavior of natural zeolites in: Natural zeolites: occurrence, properties, applications. Review in Mineralogy and Geochemistry, vol 45, The Mineralogical Society of America, Washington.

Bloss FD (1981) The spindle stage: principles and practice. Cambridge University Press, Cambridge.

Boberski C, Schreyer W (1990) Synthesis and water contents of Fe^{2+}-bearing cordierites. *European Journal of Mineralogy*, **2**, 565-584

Bonaccorsi E, Della Ventura G, Bellatreccia F, Merlino S (2007) The thermal behaviour and dehydration of pitiglianoite, a mineral of the cancrinite group. Microporous Mesoporous Materials, 99, 225-235

Bruno G, Vogel S (2008) Calculation of the Average Coefficient of Thermal Expansion in oriented Cordierite Polycrystals. Journal of American Ceramic Society, 91, 2646-2652.

Bulbak TA, Shvedenkova SV (2011) Solid solutions of (Mg, Fe^{2+})-cordierite: Synthesis, water content, and magnetic properties. *Geochemistry International*, **49**, 391-406.

Burla MC, Caliandro R, Camalli M, Carrozzini B, Cascarano GL, De Caro L, Giacovazzo C, Polidori G, Siliqi D, Spagna R (2007) IL MILIONE: a suite of computer programs for crystal structure solution of proteins. Journal of Applied Crystallography, 40, 609–613.

Burton WK, Cabrera N, Frank FC (1951) The Growth of Crystals and the Equilibrium Structure of their Surfaces, Philosophical Transactions of the Royal Society, 243, 299-358.

Carbone M, Ballirano P, Caminiti R (2008) Kinetics of gypsum dehydration at reduced pressure: an energy dispersive X-ray diffraction study. European Journal of Mineralogy, 20, 621-627.

Carey JW (1993) The Heat Capacity of Hydrous Cordierite Above 295 K. Physics and Chemistry of Minerals, 19, 578-583.

Carey JW (1995) A thermodynamic formulation for hydrous cordierite. Contribution to Mineralogy and Petrology, 119, 155–165.

Carrington DP, Harley SL (1995) Partial melting and phase relations in high-grade metapelites: an experimental petrogenetic grid in the KFMASH system. Contrib Mineral Petrol 120:270-291

Carrington DP, Harley SL (1996) Cordierite as a monitor of fluid and melt water contents in the lower crust: an experimental calibration. Geology, 24, 647–650.

Carslaw HS, Jeager JC (1959) Conduction of heat in solids. Oxford Science Publications, 510 pp.

Černý P, Chapman R, Schreyer W, Ottolini L, Bottazzi P, McCammon CA (1997) Lithium in sekaninaite from the type locality Dolni Bory, Czech Republic. The Canadian Mineralogist, 35, 167-173.

Cesare B, Maineri C, Baron Toaldo A, Pedron D, Acosta Vigil A (2007) Immiscibility between carbonic fluids and granitic melts during crustal anatexis: a fluid and melt inclusion study in the enclaves of the Neogene Volcanic Province of SE Spain. Chem Geol 237:433–449

Charoy B, de Donato P, Barres O, Pintho-Choelo C (1996) Channel occupancy in an alkali-poor beryl from Serra Blanca (Goias, Brazil): spectroscopic characterization. American Mineralogist, 81, 395–403.

Cohen, JP, Ross, FK, Gibbs GV (1977) An X-ray and neutron diffraction study of hydrous low cordierite. *American Mineralogist*, **62**, 67-78.

Coulomb CA (1776) Essai sur une application des regles des maximis et minimis a quelques problems de statique relatifs a la architecture. Mémoires de l'Académie Royale pres Divers Savants, 7, 343–387.

Crank J (1975) The Mathematics of Diffusion. Clarendon Press, Oxford. 414 pp.

Dachs E, Geiger CA (2008) Low-temperature heat capacity of synthetic Fe-and Mg-cordierite: thermodynamic properties and phase relations in the system FeO-Al_2O_3-SiO_2-(H_2O). European Journal of Mineralogy, 21, 971-983.

Daniels P (1992) Structural effects of the incorporation of large-radius alkalis in high cordierite. American Mineralogist, 77, 407-411.

Deer WA, Howie RA, Wise WS, Zussman J (2004). Rock-forming minerals. Volume 1B. Disilicates and ring silicates (2nd ed.). London, Geological Society of London. 982 pp.

Deer WA, Howie RA, Zussman J (1986) *Rock-forming minerals 1B: disilicates and ring-silicates, second edition.* The Geological Society, Bath (UK).

Della Ventura G, Bellatreccia F, Bonaccorsi E (2006) CO2 in minerals of the cancrinite-sodalite group: pitiglianoite. European Journal of Mineralogy, 17, 847-851.

Della Ventura G, Bellatreccia F, Cesare B, Harley S, Piccinini M (2009) FTIR microspectroscopy and SIMS study of water-poor cordierite from El Hoyazo, Spain: application mineral and melt devolatilization. Lithos, 113, 498–506.

Della Ventura G, Bellatreccia F, Marcelli A, Cestelli Guidi M, Piccinini M, Cavallo A, Piochi M (2010) Application of micro-FTIR imaging in the Earth sciences. Analytical and Bioanalytical Chemistry, 397, 2039-2049.

Della Ventura G, Bellatreccia F, Piccinini M (2008) Presence and zoning of hydrous components in leucite from the Albani Hills volcano (Rome, Italy). American Mineralogist, 93, 1538-1544.

Della Ventura G, Bellatreccia F, Rossi P (2007) The single-crystal, polarized-light, FTIR spectrum of stoppaniite, the Fe analogue of beryl. Physics and Chemistry of Mineral, 34, 727-731.

Della Ventura G, Marcelli A, Bellatreccia F (2014) SR-FTIR Microscopy and FTIR Imaging in the Earth Sciences. Reviews in Mineralogy and Geochemistry, 78, 447-479.

Della Ventura G, Radica F, Bellatreccia F, Cavallo A, Capitelli F, Harley (2012) Quantitative analysis of H_2O and CO_2 in cordierite using polarized FTIR spectroscopy. Contributions to Mineralogy and Petrology, 164, 881-894.

Della Ventura G, Bellatreccia F, Bonaccorsi E (2005) CO_2 in minerals of the cancrinite-sodalite group: pitiglianoite. European Journal of Mineralogy, 17, 843-851.

Della Ventura G, Bellatreccia F, Piccinini M (2008) Channel CO_2 in feldspathoids: a review of existing data and new perspectives. Rendiconti Accademia Lincei, 19, 141-159.

Della Ventura G, Bellatreccia F, Parodi GC, Cámara F, Piccinini M (2007) Single-crystal FTIR and X-ray study of vishnevite, ideally $[Na_6(SO_4)][Na_2(H_2O)_2](Si_6Al_6O_{24})$. American Mineralogist, 92, 713-721.

Della Ventura G, Rossi P, Parodi GC, Mottana A, Raudsepp M, Prencipe M (2000) Stoppaniite $(Fe,Al,Mg)_4(Be_6Si_{12}O_{36})*(H_2O)_2(Na,\square)$, a new mineral of the beryl group from Latium (Italy). European Journal of Mineralogy, 12, 121-127.

Desbois G, Ingrin J (2007) Anisotropy of hydrogen diffusion in tourmaline. Geochimica Cosmochimica Acta, 71, 5233-5243.

Duisenberg AJM, Kroon-Batenburg LMJ, Schreurs AMM (2003) An intensity evaluation method: EVAL-14. J. Appl. Crystall 36 :220-229

Erämetsä O, Nieminen K, Niinisto L (1973) Two transparent beryl varieties from the Kaatiala pegmatite. Finland. Bulletin of the Geological Society of Finland, 45, 125 130.

Farrell EF, Newnham RE (1967) Electronic and vibrational absorption spectra in cordierite. Am Min 52:380-388

Farver JR (2010) Oxygen and Hydrogen Diffusion In Minerals, in Diffusion in Minerals and Melts. Reviews in Mineralogy and Geochemistry, 72, 2010.

Farver JR, Yund RA (1991) Measurement of oxygen grain boundary diffusion in natural, fine grained, quartz aggregates. Geochimica Cosmochimica Acta, 55, 1597-1607.

Fediuk F (1971) Cordierite in the Moldanubian gneisses. Krystalinikum (Academia, Prague), 7, 183-204.

Ferraris G, Merlino S (2005) Micro- and Mesoporous Mineral Phases. Reviews in Mineralogy and Geochemistry, vol. 57, The Mineralogical Society of America, Washington

Fitzsimons ICW (1996). Metapelitic migmatites from Brattstrand Bluffs, East Antarctica – Metamorphism melting and exhumation of the mid crust. J Petrol 37:395-414

Freda C, Gaeta M, Misiti V, Mollo S, Dolfi D, Scarlato P (2008) Magma–carbonate interaction: an experimental study on ultrapotassic rocks from Alban Hills (Central Italy) Lithos, 101, 397–415.

Fukuda J, Shinoda K (2008) Coordination of water molecules with Na^+ cations in a beryl channel as determined by polarized IR spectroscopy. Physics and Chemistry of Minerals, 35, 347-357.

Fukuda J, Shinoda K (2011) Water molecules in beryl and cordierite: high-temperature vibrational behavior, dehydration, and coordination to cations. Physics and Chemistry of Minerals, 38, 469-481.

Fukuda J, Shinoda K, Nakashima S, Miyoshi N, Aikawa N (2009) Polarized infrared spectroscopic study of diffusion of water molecules along structure channels in beryl. American Mineralogist, 94, 981-985.

Gatta GD, Nestola F, Bromiley GD, Mattauch S (2006) The real topological configuration of the extra-framework content in alkali-poor beryl: A multi-methodological study. American Mineralogist, 91, 29-34.

Geiger CA, Armbruster T, Khomenko VM, Quartieri S (2000) Cordierite I: The coordination of Fe^{2+}. Am Min 85:1255-1264

Geiger CA, Kolesov BA (2002) Microscopic-macroscopic relationships in silicates: Examples from IR and Raman spectroscopy and heat capacity measurements. In:Gramaccioli CM (ed) Energy modelling in minerals. European Notes in Mineralogy 4, Eötrös University Press, Budapest, Hungary, pp 347-387

Geiger CA, Rager H, Czank (2000) Cordierite III: the site occupation and concentration of Fe^{2+}. Contribution to Mineralogy and Petrology, 140, 344-352.

Giampaolo C, Putnis A (1989) The kinetics of dehydration and order-disorder of molecular H_2O in Mg-cordierite. European Journal of Mineralogy, 1, 193-202.

Gibbs GV (1966) The polymorphism of cordierite I: the crystal structure of low cordierite. American Mineralogist, 51, 1068–1087.

Gibbs GV, Breck DW, Meagher EP (1968) Structural refinement of hydrous and anhydrous synthetic beryl, $Al_2(Be_3Si_6)O_{18}$ and emerald, $Al_{1.9}Cr_{0.1}(Be_3\ Si_6)O_{18}$. Lithos, 1, 275–285.

Goldman DS, Rossman GR, Dollase WA (1977) The channel constituents in cordierite. Am Min 62:1144-1157

Gottesmann, B. and Förster, H.J. (2004) Sekaninaite from the Satzung granite (Erzgebirge, Germany): magmatic or xenolithic? *European Journal of Mineralogy*, **16**, 483-491.

Graham CM (1981) Experimental hydrogen isotope studies III: Diffusion of hydrogen in hydrous minerals, and stable isotope exchange in metamorphic rocks. Contribution to Mineralogy and Petrology, 76, 216-228.

Grapes R, Korzhova S, Sokol E, Seryotkin Y (2010) Paragenesis of unusual fe-cordierite (sekaninaite)-bearing paralava and clinker from the kuznetsk coal basin, Siberia, Russia. *Contributions to Mineralogy and Petrology*, **162**, 253-273.

Griffin LJ (1950) Observation of unimolecular growth steps on crystal surfaces. Philosophical Magazine, 41, 196-199.

Guastoni A, Demartin F, Pezzotta F (2004) Sekaninaite delle pegmatiti granitiche di Feriolo e Baveno (VB). *Atti della Società Italiana di Scienze Naturali e Museo Civico di Storia Naturale Milano*, **145**, 59-68.

Gunter ME, Bandli BR, Bloss FD, Evans SH, Su SC, Weaver R (2004) Results from a McCrone Spindle Stage Short Course, a New Version of EXCALIBR, and How to Build a Spindle Stage. Microscope 52:23-39

Gunter ME, Downs RT, Bartelmehs KL, Evans SH, Pommier CJS, Grow JS, Sanchez MS and Bloss FD (2005) Optic properties of centimeter-sized crystals determined in air with the spindle stage using EXCALIBRW. American Mineralogist, 90, 1648–1654.

Hancock JD, Sharp JH (1972) Method of Comparing Solid-State Kinetic Data and Its Application to the Decomposition of Kaolinite, Brucite, and $BaCO_3$. Journal of the American Ceramic Society, 55, 74-77.

Hanson RC, Jones LH (1981) Infrared and Raman studies of pressure effects on the vibrational modes of solid CO_2. Journal of Chemical Physics, 75, 1102-1112.

Harley SL, Carrington DP (2001) The distribution of H_2O between cordierite and granitic melt: improved calibration of H_2O incorporation in cordierite and its application to high-grade metamorphism and crustal anatexis. Journal of Petrology, 42, 1595–1620.

Harley SL, Thompson P (2004) The influence of cordierite on melting and mineral-melt equilibria in ultra-high-temperature metamorphism. Transactions of the Royal Society of Edinburgh: Earth Sciences, 95, 87–98.

Harley SL, Thompson P, Hensen BJ, Buick IS (2002) Cordierite as a sensor of fluid conditions in high-grade metamorphism and crustal anatexis. Journal of Metamorphic Geology, 20, 71-86.

Hautefeuille P, Perrey A (1888) Sur la reproduction de la phenacite e de l'emeraude. Comptes Rendus de l'Académie des Sciences, 106, 1800–1802.

Hautefeuille P, Perrey A (1890) Sur la combinaisons silicatèes de la glucine. Annales de chimie et de physique, 6, 447-435.

Hawthorne FC, Oberti R, Della Ventura G, Mottana A (2007) Amphiboles: Crystal Chemistry, Occurrence, and Health Issues. Reviews in Mineralogy and Geochemistry, vol. 67, The Mineralogical Society of America, Washington.

Hawthorne, F.C. and Cěrný, P. (1977) The alkali-metal positions in Cs-Li beryl. The Canadian Mineralogist, 15, 414-421.

Herzberg G (1956)Infrared and Raman Spectra of Polyatomic Molecules. D. Van Nostrand Company, New York

Hochella MFjr, Brown GE jr (1986) Structural Mechanisms of Anomalous Thermal Expansion of Cordierite-Beryl and Other Framework Silicates. Journal of the American Ceramic Society, 69, 13-18.

Hochella MFjr, Brown GE jr, Ross FK, Gibbs GV (1979) High-temperature crystal chemistry of hydrous Mg- and Fe-Cordierite. American Mineralogist, 64, 337-351.

Hollister LS (1970) Origin, mechanism, and consequences of compositional sector zoning in staurolite. American Mineralogist, 55, 742-766.

Holtz F, Becker A, Freise M, Johannes W (2001) The water-undersaturated and dry Qz-Ab-Or system revisited. Experimental results at very low water activities and geological implications. Contributions to Mineralogy and Petrology, 141, 347–357.

Iezzi G, Liu Z, Della Ventura G (2006) High pressure synchrotron infrared spectroscopy of synthetic $Na(NaMg)Mg_5Si_8O_{22}(OH)_2$ up 30 GPa: a possible high-pressure new amphibole polymorph. American Mineralogist, 91, 479-482

Iezzi G, Liu Z, Della Ventura G (2009) The role of B-site on the compressional behaviour of synthetic P21/m amphiboles in the system $^{A}Na^{B}(Na_xLi_{1-x}Mg_1)\ ^{C}Mg_5\ Si_8\ O_{22}\ (OH)_2$ (with x=1, 0.6, 0.2 and 0): an high pressure synchrotron infrared study. Physics and Chemistry of Minerals, 36, 343-354

Ingrin J, Blanchard M (2000) Hydrogen mobility in single crystal kaersutite. EMPG VIII, Journal of Conference Abstracts, 5, 52.

Ingrin J, Blanchard M (2006) Diffusion of hydrogen in minerals. Reviews in Mineralogy and Geochemistry, 62, 291-320.

Ingrin J, Hercule S, Charton T (1995) Diffusion of hydrogen in diopside: results of dehydration experiments. Journal of Geophysical Research: Solid Earth, 100, 15489-15499.

Jakobsson S (2012) Oxygen fugacity control in piston-cylinder experiments. Contribution to Mineralogy and Petrology, 3, 397-406.

Johannes W, Schreyer W (1981) Experimental introduction of CO_2 and H_2O into Mg-cordierite. American Journal of Science, 281, 299-317.

Kalt A (2000) Cordierite channel volatiles as evidence for dehydration melting: an example from high-temperature metapelites of the Bayerische Wald (Variscan belt, Germany). European Journal of Mineralogy, 12, 987–998.

Keppler H, Bagdassarov NS (1993) High-temperature FTIR spectra of H_2O in rhyolite melt to 1300 °C. American Mineralogist, 78, 1324-1327.

Keppler H, Smyth JR (2006) Water in Nominally Anhydrous Minerals. Reviews in Mineralogy and Geochemistry, vol. 62, The Mineralogical Society of America, Washington

Khomenko VM, Langer K (1999) Aliphatic hydrocarbons in structural channels of cordierite: a first evidence from polarized single-crystal IR-absorption spectroscopy. American Mineralogist, 84, 1181–1185

Khomenko VM, Langer K (2005) Carbon oxides in cordierite channels: determination of CO_2 isotopic species and CO by single crystal IR spectroscopy. American Mineralogist, 90, 1913–1917.

Khosrovani N, Sleight AW (1999) Strong anisotropic thermal expansion in oxides. The International Journal of Inorganic Materials, 1, 3-10.

Kitamura M, Hiroi Y (1982) Indialite from Unazuki schist, Japan, and its transition texture to cordierite. Contributions to Mineralogy and Petrology, 80, 110-116.

Koch-Müller M, Dera P, Fei Y, Reno B, Sobolev N, Hauri E, Wysoczanski R (2003) OH– in synthetic and natural coesite. American Mineralogist, 88, 1436-1445

Kolesov B (2008) Vibrational states of H_2O in beryl: physical aspects. Physics and Chemistry of Mineral, 34, 727-731.

Kolesov BA, Geiger CA (2003) Molecules in the SiO_2-clathrate melanophlogite: a single-crystal Raman study. American Mineralogist, 88, 1364-1368.

Kolesov BA, Geiger CA (2000) Cordierite II: the role of CO_2 and H_2O. American Mineralogist, 85, 1265–1274

Kolesov BA, Geiger CA (2000) The Orientation and Vibrational State of H2O in Synthetic Alkali-Free Beryl. Physics and Chemistry of Mineral, 27, 557-564.

Kolesov N (2008) Vibrational states of H_2O in beryl: physical aspects. Physics and Chemistry of Minerals, 35, 271-278.

Kurepin VA (1985) H_2O and CO_2 contents of cordierite as an indicator of thermodynamical conditions of formation. Geochemistry International, 22, 148–156.

Kurepin VA (2010) Cordierite as an indicator of thermodynamic conditions of petrogenesis. Contribution to Mineralogy and Petrology, 160, 391–406.

Labotka TC, Cole DR, Riciputi LR (2000) Diffusion of C and O in calcite at 100 MPa. American Mineralogist, 85, 488-494.

Lal RK, Akermand D, Raith M, Raase P, Seifert F (1984). Sapphirine-bearing assemblages from Kiranur, Southern India. A study of chemographic relationships in the Na_2O–FeO–MgO–Al_2O_3–SiO_2–H_2O system. Neues Jb Miner Abh 150:121-152

Le Breton N (1989) Infrared investigation of CO_2-bearing cordierites. Contribution to Mineralogy and Petrology, 103, 387–396.

Le Breton N, Schreyer W (1993) Experimental CO_2 incorporation into Mg-cordierite: nonlinear behavior of the system. European Journal of Mineralogy, 5, 427-438.

Lee HM, Tarakeshwar P, Park J, Kolaski MR, Yoon YJ, Yi HB, Kim WY, Kim KS (2004) Insights into the structures, energetics, and vibrations of monovalent cation-$(water)_{1-6}$ clusters. Journal of Physical Chemistry, A108, 2949–2958.

Lepezin GG, Melenevsky VN (1977) On the problem of water diffusion in the cordierites. Lithos, 10, 49-57.

Libowitzky E, Rossman GR (1996) Principles of quantitative absorbance measurements in anisotropic crystals. Physics and Chemistry of Minerals, 23, 319–327.

Libowitzky E, Rossman GR (1997) An IR absorption calibration for water in minerals. American Mineralogist, 82, 1111–1115.

Liedl A, Polese C, Hampai D, Della Ventura G, Dabagov SB, Marcelli A, Bellatreccia F, Cavallo A (2014) X-Ray µCT and µXRF Mapping of Synthetic Emerald by using a laboratory PolyCO-X-ray Tube Layout (submitted).

Łodziński M, Sitarz M, Stec K, Fojud Z, Jurga S (2005) ICP, IR, Raman, NMR investigations of beryls from pegmatites of the Sudety Mts. Journal of Molecular Structure, 744, 1005-1015.

Malcherek T, Domeneghetti MC, Tazzoli V, Ottolini L, McCammon C, Carpenter MA (2001) Structural properties of ferromagnesian cordierites. American Mineralogist, 86, 66–79.

Masotta M, Freda C, Gaeta M (2012) Origin of crystal-poor, differentiated magmas: insights from thermal gradient experiments. Contributions to Mineralogy and Petrology, 163, 49-65.

Masotta M, Freda C, Paul TA, Moore G, Gaeta M, Scarlato P, Troll VR (2012) Low pressure experiments in piston cylinder apparatus: calibration of newly designed 25 mm furnace assemblies to P = 150 MPa. Chemical Geology, 312-313, 74-79.

McCusker LB (2005) IUPAC Nomenclature for Ordered Microporous and Mesoporous Materials and its Application to Non-zeolite Microporous Mineral Phases. Reviews in Mineralogy and Geochemistry, 57, 1-16

McCusker LB, Liebau F, Engelhardt G (2001) Nomenclature of structural and compositional characteristics of ordered microporous and mesoporous materials with inorganic hosts - (IUPAC recommendations 2001), Pure and Applied Chemistry, 73, 381-394.

Mikhailov MA, Demina TV, Belozerova OY (2007) Partitioning of species-forming and impurity cations among growth pyramids of pinacoid and prism faces in crystals of beryl, cordierite, and beryllian Indialite. Russian geology and geophysics, 48, 923-932.

Mirwald PW, Maresch WV, Schreyer W (1979) Der Wassergehalt von Mg-Cordierit zwischen 500° und 800 °C sowie 0.5 und 11 Kbar. Fortschritte der Mineralogie, 57, 101-110.

Mirwald PW, Schreyer W (1977) Die stabile und metastabile Ab-baureaktion von Mg-Cordierit in Talk, Disthen und Quarz und ihre Abhiingigkeit vom Gleichgewichtswassergehalt des Cordierits. Fortschritte der Mineralogie, 55, 95-97.

Moore G, Roggensack K, Klonowski S (2008) A low-pressure-high-temperature technique for the piston-cylinder. American Mineralogist, 93, 48–52.

Morosin B (1972) Structure and thermal expansion of beryl. Acta Crystallographica, B28, 1899–1903.

Mottana A, Fusi A, Bianchi Potenza B, Crespi R, Liborio G (1983) Hydrocarbon-bearing cordierite from the Dervio-Colico road tunnel (Como, Italy). Neues Jahrbuch für Mineralogie Abhandlungen, 148, 181–199

Newton RC, Wood BJ (1979) Thermodinamics of water in cordierite and some petrological consequances of cordierite as hydrous phase. Contributions to mineralogy and petrology, 68, 391-405.

Nonius (1998) COLLECT. Nonius BV, Delft, The Netherlands.

Olijnyk H, Däufer H, Jodl HJ, Hochheimer HD (1988) Effect of pressure and temperature on the Raman spectra of solid CO_2. Journal of Chemical Physics, 88, 4204-4212.

Orlandi P, Pezzotta F (1994) La sekaninaite dei filoni pegmatitici elbani. *Atti della Società Toscana di Scienze Naturali, Memorie*, **100**, 85-91.

Paterson M (1982) The determination of hydroxyl by infrared absorption in quartz, silicate glasses and similar materials. Bulletin de Mineralogie, 105, 20-29

Paukov IE, Kovalevskaya YA, Rahmoun NS, Geiger CA (2007) Heat capacity of synthetic hydrous Mg-cordierite at low temperatures: thermodynamic properties and the behavior of the H_2O molecules in selected hydrous micro and nanoporous silicates. American Mineralogist, 92, 388–396.

Pistorius AMA, DeGrip WJ (2006) Deconvolution as a tool to remove fringes from an FT-IR spectrum. Vibrational Spectroscopy, 36, 89-95.

Pouchou JL, Pichoir F (1985) A new model for quantitative X-ray microanalysis. Rech. Aerosp., 3 13–38.

Prasad PSR, Shiva Prasad K, Ramana Murthy S (2005) Dehydration of natural stilbite: An in situ FTIR study. American Mineralogist, 90, 1636-1640

Putnis A (1992) Introduction to mineral science. Cambridge University Press, 457 pp.

Putnis A, Winkler B, Fernandez-Diaz L (1990) In situ IR spectroscopic and thermogravimetric study of the dehydration of gypsum. Mineralogical Magazine, 54, 123-128.

Radica F, Capitelli, F, Bellatreccia F, Della Ventura G, Cavallo A, Piccinini M, Hawthorne FC (2013) Spectroscopy and X-ray structure refinement of sekaninaite from Dolní Bory (Czech Republic). Mineralogical Magazine, 77, 485-498.

Rigby MJ, Droop GTR, Bromiley GD (2008) Variations in fluid activity across the Etive thermal aureole, Scotland: evidence from cordierite volatile contents. J Metam Geol 26:331–346

Rossman GR (2006) Analytical methods for measuring water in nominally anhydrous minerals. In:Keppler H, Smith JR (eds) Water in nominally anhydrous minerals. Reviews in Mineralogy, Mineralogical Society of America 62, pp 1-28

Rouquerol J, Avnir D, Fairbridge CW, Everett DH, Haynes JM, Pernicone N, Ramsay JDF, Sing KSW, Unger KK (1994) Recommendations for the characterization of porous solids (Technical Report), Pure and Applied Chemistry, 66, 1739–1758.

Ryback G, Nawaz R, Farley E (1988) Seventh supplementary list of British Isles Minerals (Irish). *Mineralogical Magazine*, **52**, 267-274.

Sarkar S, Santosh M, Dasgupta S, Fukuoka M (2010) Very high density CO_2 associated with ultrahigh-temperature metamorphism in the Eastern Ghats granulite belt, India. Geology, 34, 51-54.

Schreyer W (1985) Experimental studies on cation substitutions and fluid incorporation in cordierite. Bulletin of Mineralogy, 108, 273–291.

Schreyer W, Gordillo CE, Werding G (1979) A new sodian-beryllian cordierite from Sato, Argentina, and the relationship between distortion index, Be content, and state of hydration. Contrib Mineral Petrol 70:421-428

Schreyer W, Yoder HS (1964) The system Mg-cordierite—H_2O and related rocks. Neues Jahrbuch für Mineralogie Abhandlungen, 101, 271–342.

Sekanina J (1928) Minerals of Moravian pegamtites. *Acta Musei Moraviae, Scientie Naturales*, **26**, 113-224 (in Czech).

Selkregg KR, Bloss FD (1980) Cordierites: compositional controls of Δ, cell parameters, and optical properties. *American Mineralogist*, **65**, 522-533.

Sharygin VV, Sokol EV, Belakovskii DI (2009) Fayalite-sekaninaite paralava from the Ravat coal fire (central Tajikistan). *Russian Geology and Geophysics*, **50**, 703-721.

Sheldrick GM (1996) SADABS. Absorption correction program. University of Göttingen, Germany.

Sheldrick GM (1997) SHELXL-97. Program for the Refinement of Crystal Structures. University of Gottingen, Germany

Sheldrick, GM (2008) A short history of SHELX. *Acta Crystallographica.* **A64**, 112-122.

Sherriff BL, Grundy HD, Hartman JS, Hawthorne FC, Černý P (1991) The incorporation of alkalis in beryl, a multinuclear MAS-NMR and crystal structure study. *Canadian Mineralogist*, **29**, 271-285.

Smith CH (1996) H_2O-CO_2 contents of cordierite in migmatites of the Fosdick Mountains, Marie Byrd Land. Terra Antartica 3:11-22

Sokol EV, Seryotkin YV, Bul'bak TA (2010) Na-Li-Be-rich cordierite from the Murzinka pegmatite field, Middle Urals, Russia. Euro J Miner 22:565–575

Staněk, J, Miškovský j (1964) Iron-rich cordierite from the Dolní Bory pegmantite. *Casopis pro mineralogii a geologii*, **9**, 191-192 (in Czech).

Staněk J, Miškovský j (1975) Sekaninaite, a new mineral of the cordierite series, from Dolní Bory, Czechoslovakia. *Scripta Facultatis Scientiarum Naturalium Universitatis Purkynianae Brunensis; Geologia 1*, **5**, 21-30.

Su SC, Bloss FD, Gunter ME (1978) Procedures and computer programs to refine the double variation method. *American Mineralogist*, **72**, 1011-1013.

Thompson P, Harley SL, Carrington DP (2001) The distribution of H_2O-CO_2 between cordierite and granitic melt under fluid-saturated conditions at 5 kbar and 900□C. Contrib Mineral Petrol 142:107-118

Tokiwai K, Nakashima S (2010) Dehydration kinetics of muscovite by in situ infrared microspectroscopy. Physics and Chemistry of Minerals. 37, 91-101.

Tokiwai K, Nakashima S (2010) Integral molar absorptivities of OH in muscovite at 20 to 650 °C by in-situ high-temperature IR microspectroscopy. American Mineralogist, 95, 1052-1059.

Tuttle OF (1949) Two Pressure Vessels for Silicate-Water Studies. Geological Society of American Bulletin 60, 1727-1729.

Visser D, Kloprogge JT, Maijer C (1994) An infrared spectroscopic (IR) and light element (Li, Be, Na) study of cordierites from the Bamble Sector, South Norway. Lithos 32:95-107

Vry JK, Brown PE, Valley JV (1990) Cordierite volatile content and the role of CO_2 in high-grade metamorphism. American Mineralogist, 75, 71–88.

Watson EB (1991) Diffusion of dissolved CO_2 and Cl in hydrous silicic to intermediate magmas. Geochimica Cosmochimica Acta, 55, 1897-1902.

Watson EB, Baxter EF (2007). Frontiers: Diffusion in solid-Earth systems. Earth and Planetary Science Letters, 253, 307-327.

Watson EB, Sneeringer MA, Ross A (1982) Diffusion of dissolved carbonate in magmas: experimental results and applications. Earth Planet Science letters, 61, 346-358.

Welch MD, Cámara F, Della Ventura G, Iezzi G (2007) In situ non-ambient studies of amphiboles. Reviews in Mineralogy, 67, 223-260

Wickersheim KA, Buchanan RA (1959) The Near Infrared Spectrum of Beryl. American Mineralogist, 44, 440-445.

Wilson EB, Decius JC, Cross PC (1955) Molecular vibrations: the theory of infrared and Raman vibrational spectra. McGraw-Hill, New York, pp 174–177.

Winkler B, Coddens G, Hennion B (1994) Movement of channel H_2O in cordierite observed with quasi-elastic neutron scattering. American Mineralogist, 79, 801-808.

Wood DL, Nassau K (1967) Infrared Spectra of Foreign Molecules in Beryl. The Journal of Chemical Physics, 47, 2220-2228.

Wood DL, Nassau K (1968) The characterization of beryl and emerald by visible and infrared absorption spectroscopy. American Mineralogist, 53, 777–780.

Wunder B, Sahl K, Schreyer W (1991) Abrupt high/low-transition in flux-grown Mg-cordierite single crystals with hour-glass structure. European Journal of Mineralogy, 3, 809-817.

Yakubovich OV, Massa W, Pekov IV, Gavrilenko PG and Chukanov NV (2004) Crystal structure of the Na-, Ca-, Be-cordierite and crystallochemical regularities in the cordierite-sekaninaite series. Crystallography Reports, 49, 953-963.

Yamagishi H, Nakashima S, Ito Y (1997) High temperature infrared spectra of hydrous microcrystalline quartz. Physics and Chemistry of Minerals, 24, 66-74.

Zhang M, Hui Q, Lou J, Redfern SAT, Salje EKH, Tarantino SC (2006) Dehydroxylation, proton migration and structural changes in heated talc: An infrared spectroscopic study. American Mineralogist, 91, 816-825.

Zhang M, Salje EKH, Carpenter MA, Wang JY, Groat LA, Lager GA, Wang L, Beran A, Bismayer U (2007) Temperature dependence of IR absorption of hydrous/hydroxyl species in minerals and synthetic materials. American Mineralogist, 92, 1502-1517.

Zhang M, Wang L, Hirai S, Redfern SAT, Salje EKD (2005) Dehydroxylation and CO_2 incorporation in annealed mica (sericite): an infrared spectroscopic study. American Mineralogist, 87, 90, 173-180.

Zhang XY, Cherniak DJ, Watson EB (2006) Oxygen diffusion in titanite: lattice diffusion and fast-path diffusion in single crystals. Chemical Geology, 235, 105–123.

Zhang Y, Cherniak DJ (2010) Diffusion in Minerals and Melts. Reviews in Mineralogy and Geochemistry, vol. 72, The Mineralogical Society of America, Washington.

Zimmermann JP (1981) La libération de l'eau, du gaz carbonique et des hydrocarbures des cordiérites. Cinétigue des mécanismes. Determination des sites. Intéret pétrogénétique. Bulletin de la Société française de minéralogie et de cristallographie, 104, 325-338.